TECHNISCHE UNIVERSITÄT ILMENAU
Faculty of Electrical Engineering and Information Technology

Dissertation

For the attainment of the academic degree
Doctor of Engineering (Dr.-Ing.)

Lightning Protection of Floating Roof Tanks

Submitted by: Aderibigbe Israel Adekitan

Day of submission: 27. 06. 2022

Day of the oral examination: 15. 12. 2022

Field of study: Lightning and surge protection

Reviewer: Prof. Dr.-Ing. Michael Rock
Prof. Dr.-Ing. Ottmar Beierl
Dr.-Ing. Martin Hannig

DOI: 10.22032/dbt.55201

urn:nbn:de:gbv:ilm1-2022000440

Abstract

In tropical regions of the world, floating roof tanks can be struck by more than 200 kA lightning peak currents. Without adequate measures to ensure the safe flow of the high energy transient current to the earth, the lightning strike can result in lightning-induced tank fires.

A floating roof tank has a floating roof that reduces volatile vapour emissions by more than 90%. The gap separating the tank shell and the roof creates an electrical discontinuity which causes a significant voltage differential when lightning strikes. About 95% of all lightning-induced floating roof tank fires start around this air gap. Available methodologies to provide a direct electrical connection using shunts and bypass cables are inadequate.

This dissertation seeks to examine the various impact of the lightning current on the steel sections of the tank and identify high-risk strike points. Ultimately lightning protection systems for floating roof tanks using conventional approaches will be proposed and evaluated.

Using a numerical simulation to identify differences in the likelihood of a direct strike to the meshed points on a structure offers a significant advantage instead of the rolling sphere method. The numerical concept is investigated, and sources of numerical errors and superfluous space points were eliminated to create an improved dynamic electro-geometrical model (IDEGM) with a significant reduction in computation time from over one hundred hours to below thirty minutes. The probability of lightning directly striking a floating roof tank is influenced by its height and diameter. For the cases considered, the probability of a direct strike to the air gap region is about 73% to 95% when the roof is at its topmost height. A lightning strike simulation of the tank steel shells in Simulink on MATLAB shows that the voltage at the strike point on the tank can reach 55 kV with a very low grounding resistance of 0.225 Ω, which is sufficient to ignite flammable vapours. The highest risk of a tank fire occurs when the lightning current terminates on the roof with the air gap voltage reaching 211 kV even with the recommended maximum grounding resistance of 10 Ω for lightning protection.

Nine lightning protection system models are proposed using various arrangements of air terminals and catenary wires above the tank. Their strike interception capability is evaluated, and parallel catenary wires had the best performance, with an interception efficiency of 99.93% when the roof is at the top.

Kurzfassung

In tropischen Regionen der Welt können Schwimmdachtanks von Blitzentladungen mit Scheitelwerten von mehr als 200 kA getroffen werden. Ohne geeignete Maßnahmen zur sicheren Ableitung des hochenergetischen Blitzstoßstroms zur Erde kann der Blitzeinschlag zu katastrophalen Tankbränden führen.

Ein Schwimmdachtank hat ein Schwimmdach, das den Austritt flüchtiger Dämpfe um mehr als 90% reduziert. Der Spalt zwischen dem Dach und der Tankhülle erzeugt eine elektrische Diskontinuität, an dem bei Blitzeinschlägen eine erhebliche Spannungsdifferenz aufgebaut wird. Etwa 95% aller blitzinduzierten Schwimmdachtankbrände entstehen an diesem Spalt, der mit entzündlichen Dämpfen angereichert ist. Verfügbare Methoden zur Bereitstellung einer direkten elektrischen Verbindung (Potentialausgleich) unter Verwendung von Shunts und Bypass-Kabeln sind unzureichend.

Ziel dieser Dissertation ist es, die verschiedenen Auswirkungen des Blitzstroms auf Schwimmdachtanks zu untersuchen und risikoreiche Einschlagstellen zu identifizieren. Abschließend werden Blitzschutzsysteme für Schwimmdachtanks mit konventionellen Ansätzen vorgeschlagen und bewertet.

Die Anwendung einer numerischen Simulation zur Ermittlung von Unterschieden in der Wahrscheinlichkeit eines direkten Blitzeinschlages auf die vernetzten Punkte einer modellierten Struktur bietet Vorteile gegenüber der Methode der rollenden Blitzkugel. Das Konzept wurde untersucht sowie Quellen numerischer Fehler und überflüssige Raumpunkte eliminiert, um ein verbessertes dynamisches elektrogeometrisches Modell (IDEGM) mit einer signifikanten Reduzierung der Rechenzeit von über hundert Stunden auf unter dreißig Minuten zu erhalten. Die Wahrscheinlichkeit eines direkten Blitzeinschlages in einen Schwimmdachtank wird durch dessen Höhe und Durchmesser beeinflusst. Für die betrachteten Fälle beträgt die Wahrscheinlichkeit eines direkten Einschlags in den Spaltbereich des Tanks etwa 73% bis 95%, wenn sich das Dach in seiner höchsten Position befindet. Die Simulation der Stahlwand des Tanks beim Blitzeinschlag in MATLAB Simulink zeigte, dass die Spannung am Einschlagpunkt auf dem Tank 55 kV bei einem sehr niedrigen Erdungswiderstand von 0,225 Ω erreichen kann, was ausreicht, um brennbare Dämpfe zu entzünden. Das höchste Risiko eines Tankbrandes besteht, wenn der Blitzstrom auf dem Dach eingespeist wird und dabei die Spannung über dem Luftspalt 211 kV erreicht, selbst bei dem für den Blitzschutz empfohlenen maximalen Erdungswiderstand von 10 Ω.

Es werden neun Ausführungen des Blitzschutzsystems vorgeschlagen, bei denen verschiedene Anordnungen von Blitzfangstangen und Blitzfangseilen am Tank verwendet werden. Ihre Fähigkeit, Blitzeinschläge aufzufangen, wurde bewertet. Parallele Fangseile zeigten die beste Wirksamkeit mit einer Einfangeffizienz von 99,93%, wenn sich das Schwimmdach in der höchsten Position befindet.

Acknowledgement

I am very much grateful for the gift of life and God's protection, especially during this Covid 19 period. I am thankful for the grace to get to yet another milestone in my academic pursuit.

I sincerely appreciate my doctoral supervisor, Prof. Dr.-Ing. habil. Michael Rock for his interest in my topic from the initial stage and his continuous support, technical suggestions and commitment to helping me improve my research.

I thank Prof. Dr.-Ing. Ottmar Beierl and Dr.-Ing. Martin Hannig for taking precious time to review my dissertation and for their expert opinions.

I must also appreciate Christian Drebenstedt and Wolfram Sven, who are members of my research cluster at the Group for Lightning and Surge Protection at Technische Universität Ilmenau, for their assistance in setting up and fixing issues on my computer systems.

This doctoral study would not have been possible without the postgraduate scholarship I received from the Nigerian Petroleum Technology Development Fund (PTDF) in partnership with the German Academic Exchange Service (DAAD). I am grateful for the initiative of the PTDF in providing funds for research studies towards the development of innovative solutions to technological challenges facing the petroleum industry in Nigeria.

I must express my heartfelt gratitude to my parents, Mr and Mrs Adekitan, and my siblings for their regular calls, encouragement and motivation, which kept me strong and focused during trying times. Thank you all for your support.

Finally, I must express my utmost appreciation to everyone whom I may not be able to mention individually. I thank everyone for their support, either administratively or otherwise, which brought me to this phase of my study. I am very grateful, and I acknowledge you all.

Table of Content

List of Formula Symbols, Constants and Abbreviations

List of formula symbols

ArcA	The length of the flattened arc for $r = 0$ to h
ArcB	The length of the flattened arc for $r = 0$ to ∞
ArcD	The length of the flattened arc for $r = 0$ to h_{Int} when the roof is lowered
ArcE	The length of the flattened arc for $r = h_{Int}$ to ∞ when the roof is lowered
BorderA	The chord of the flattened collection surface touching the FRT
BorderB	The chord of the flattened collection surface external to the FRT for $r = 0$ to h
BorderC	The chord of the flattened collection surface external to the FRT for $r = 0$ to ∞
BorderD	The chord of the flattened collection surface internal to the FRT for $r = 0$ to h_{Int} when the roof is lowered
BorderE	The chord of the flattened collection surface internal to the FRT for $r = h_{Int}$ to ∞ when the roof is lowered
C	Capacitance
CDF(I)	Cumulative distribution function in terms of lightning current I
CDF(r)	Cumulative distribution function in terms of striking distance r
D_n	Distance to a meshed point n
D_{nG}	Striking distance to a meshed point n on the ground
D_{nR}	Striking distance to a meshed point n on the FRT's roof
D_{nW}	Striking distance to a meshed point n on the FRT's cylindrical wall
erf	Error function
f	Frequency
f_f	Virtual front frequency
ft	Virtual tail frequency
h_{Int}	Internal height of roof below the FRT's rim

i_{LH}	Lightning pulse current
$\hat{i}_{LH}$	Peak lightning pulse current
K_{P2C}	PDF to CDF conversion factor
l	Length
LengthA	The horizontal length of the curved section for $r = 0$ to h
LengthB	The horizontal length of the curved section for $r = h$ to ∞
LengthD	The horizontal length of the curved section for $r = 0$ to h_{Int} when the roof is lowered
LengthE	The horizontal length of the curved section for $r = h_{Int}$ to ∞ when the roof is lowered
n	Negative (subscript)
n	Steepness factor
p	Positive (subscript)
$P(SU_{nG})$	Cumulative probability for a surface point n on the ground
$P(SU_{nR})$	Cumulative probability for a surface point n on the roof
$P(SU_{nW})$	Cumulative probability for a surface point n on the cylindrical wall
$PMCV_{FRT}$	Total probability modulated collection volume for the FRT
r_{int}	Effective striking distance for the internal strike due to the lowered roof
r_{max}	Maximum vertical striking distance for any point on the lowered roof
R_{sp}	Rolling sphere radius
R_{len}	Radial distance of a point n on the roof from the edge of the roof
SD_r	Effective striking distance
SP_1CL_1	Space point 1 on cloud layer 1
SP_1CL_2	Space point 1 on cloud layer 2
SP_nCL_1	Space point n on cloud layer 1
SP_nCL_2	Space point n on cloud layer 2
SU_{1CW}	Surface point 1 on the cylindrical wall
SU_{1G}	Surface point 1 on the ground

SU_{2G}	Surface point 2 on the ground
SU_{nCW}	Surface point n on the cylindrical wall
SU_{1R}	Surface point 1 on the roof
SU_{nR}	Surface point n on the roof
w	Width
Y	Admittance
Z	Impedance
δ	Skin depth
η	Pulse current peak factor
μ_{rst}	Permeability of steel
ρ_{st}	Resistivity of steel
τ_1	Front time constant
τ_2	Tail time constant
ρ_g	Soil resistivity
σ	Standard deviation of the log (I) distribution
σ_n	Standard deviation of the negative lightning log (I) distribution
σ_p	Standard deviation of the positive lightning log (I) distribution
σ_{st}	Conductivity of steel
μ	Median value of the lightning current distribution
μ_n	Median value of the negative lightning current distribution
μ_p	Median value of the positive lightning current distribution

List of constants

ε_0	8.854×10^{-12} F/m	Permittivity of free space
μ_0	$4\cdot\pi\cdot10^{-7}$ H/m	Permeability of free space

List of abbreviations

3D	Three-dimensional
AC	Alternating Current
ANSYS	Analysis System
API	American Petroleum Institute
API-RP	American Petroleum Institute Recommended Practice
CAGE	Chemically Activated Grounding Electrode
CDF	Cumulative Distribution Function
CTS	Charge Transfer System
CVM	Collection Volume Method
DAS	Dissipation Array System
DC	Direct Current
DL	Data Line
EGM	Electro-geometrical Model
ESE	Early Streamer Emission
FastHenry	A Three-Dimensional Inductance Extraction Program
FBE	Fusion Bonded Epoxy
FDTD	Finite Difference Time Domain
FEM	Finite Element Method
FOPO	Fall-off Potential
FreeCAD	Free Parametric Three-dimensional Computer-Aided Design Modeler
FRT	Floating Roof Tank
GCC	Ground Charge Collector
IDEGM	Improved Dynamic Electro-Geometrical Model
IEC	International Electrotechnical Commission
DEGM	Dynamic Electro-Geometrical Model
IEEE	Institute of Electrical and Electronics Engineers

LEL	Lower Explosive Limit
LEMP	Lightning ElectroMagnetic Pulse
LHD	Linear Heat Detector
LPS	Lightning Protection System
MATLAB	Matrix Laboratory
MDB	Main Distributions Board
M-file	MATLAB file (script or function)
MTL	Multi Transmission Line
MSP	Motor Surge Protection
NFPA	National Fire Protection Association
nFS	Negative First Stroke
nSS	Negative Subsequent Stroke
PDF	Probability Density Function
PE	Protective Earth
pFS	Positive First Stroke
PMCV	Probability Modulation Collection Volume
Q3D	Quasi-Static Three-dimensional
RC	Resistance and Capacitance
RFL	Roof Lowered
RGA	Retractable Grounding Arrays
RL	Resistance and Inductance
SDB	Sub-Distribution Board
SGD	Scalable Grounding Device
Simulink	Block diagram simulation environment of MathWorks
SLE	Semiconductor Lightning Extender
SPD	Surge Protective Device

List of Figures

List of Tables

1 Introduction

1.1 Preamble

Scientists have investigated the potent power of lightning to cause damage to structures and facilities over centuries [1]. A lightning strike on installations can induce fires and create disruptive magnetic fields that can affect the functionality of sensitive devices or induce dangerous voltage levels in nearby conductive paths. Power transmission lines and buildings [2] were the initial focus of lightning protection research studies. Still, reality has shown the dangers posed by lightning to other structures such as nuclear power plants [1], refineries and hydrocarbon storage facilities [3, 4], military facilities [5, 6], aircraft and airports [7-9], photovoltaic systems [10, 11], wind turbines [12, 13], etc.

Crude oil and related hydrocarbon by-products are stored in storage tanks in the petroleum industry. Storage tanks can be atmospheric or pressure tanks. Atmospheric tanks are for storing stabilised hydrocarbon products and are made of a fixed roof or the floating roof. Fire incidents on external floating roof tanks (FRT) are more frequent than on fixed roof tanks [14, 15]. The petroleum industry is prone to the hazard of lightning fires due to the flammable nature of the products handled. Cases of lightning-induced FRT fires have been reported in various regions of the world [15, 16], resulting in firefighting, clean-up and rebuilding costs, production losses, environmental pollution, litigation and a bad public image for the operators of such facilities.

Lightning protection systems (LPS) are required to safeguard buildings and structures from the negative effects of lightning by serving as a safe alternative pathway for the lightning current to flow to the earth rather than through the protected structure, thereby reducing the likelihood of structural damage [2, 17]. A LPS must be designed per approved standards to be effective and adequate. This standard-based design will help to prevent lightning bypass cases and unwanted flashes to unintended structural parts. It is vital to determine high-risk points on a facility or building when installing a LPS for optimal positioning of air terminals. Likewise, random effects [18] and the proximity effects of neighbouring air terminations are other factors that influence the performance of a LPS [19].

The International Electrotechnical Commission (IEC) 62305 code [20, 21] is a key guideline on lightning protection that classifies LPS into four classes from Class I to Class IV and specifies the requirements for each class. An effective LPS for a FRT must be based on the behavioural interaction of lightning with a FRT.

This study investigates the issue of lightning-induced FRT fires and proposes LPS designs for FRTs. The designs are appraised for effectiveness by applying the dynamic electro-geometrical model (DEGM). The DEGM is built on IEC 62305 standard. The DEGM as a methodology is first reviewed, and modifications for performance improvement with regard to the computation time and accuracy were implemented. Then the interception probabilities

of conventional LPS models developed for FRTs were evaluated and compared. Relevant operational guidelines are recommended to promote lightning safety within FRT storage facilities.

1.2 Research background

The floating roof tank comprises two parts, the tank shell and the floating roof made of buoyant pontoons or double-decks [22]. FRTs are majorly used as storage for gas condensate and crude oil, and as such, FRTs contain flammable vapour [23]. An annular space of about 20 cm exists, which separates the floating roof and the tank shell. This space, referred to as the rim seal region, allows the roof to move without friction with changing crude oil levels. This gap breaks the electrical continuity between the roof and the FRT's shell, both made of steel. FRTs are constructed in the open space exposed to the environment and, as such, are susceptible to peak lightning currents of 200 kA depending on the lightning severity in that geographical location. Lightning pre-strike charge build-up or a direct lightning strike on the FRT can create a dangerous potential difference between the floating roof and the tank shell, resulting in the electrical breakdown of the volatile air-gas dielectric.

FRTs store hydrocarbons and flammable vapour can accumulate around the tank and within the gap separating the tank shell and the roof [23, 24]. The vapour can be ignited when lightning strikes the FRT, resulting in a lightning-induced FRT fire [25, 26]. About 15–20 tank fires are recorded yearly in various facilities [15]. A study of accident cases shows an ignition probability of 82% due to lightning strikes on atmospheric hydrocarbon storage tanks [27], [28]. More than 33% of FRT fires are due to lightning strikes [26], and 95% of these strikes are initiated at the annular air gap region [29, 30]. Strikes to a FRT can be direct or indirect. Studies have shown that direct strikes to a FRT create a significant risk of inducing fires due to the inherent energy dissipated at the strike point [31]. However, indirect strikes to the nearby ground are more frequent [32] but are less severe. Studies have found various modes of protection via bypass cables and stainless-steel shunts for bridging the rim seal gap to be inadequate [33]. Therefore, a lightning protection system (LPS) designed based on the conventional approach must be developed, evaluated and recommended to protect FRTs from the harmful effects of lightning strikes. Lightning-induced tank fire is a very potent threat that requires a research intervention.

1.3 Research aim

This dissertation takes a further look at the problem of lightning-induced FRT fires. It highlights the FRT fire formation process and the aggravating factors. The study identifies historical interventions that have been inadequate, and ultimately, various conventional lightning protection system models for FRTs will be developed. Their performances will be evaluated in terms of their interception probability by means of an improved dynamic electro-geometrical model (IDEGM).

1.4 Research objectives

This dissertation seeks to achieve the following:

1. To develop a description of the FRT, particularly to establish the lightning threat and the importance of installing adequate LPS.
2. To conduct a state-of-the-art review of lightning protection of FRTs.
3. To modify the lightning current distribution functions, i.e., the Probability Density Function (PDF) and the Cumulative Distribution Function (CDF) towards simplifying DEGM simulation algorithms.
4. To improve the performance of the numerical DEGM by eliminating numerical errors and reducing the computation time.
5. To develop novel analytical DEGM models for a FRT.
6. To investigate the lightning impulse voltage distribution on critical points on the FRT under lightning current flow via simulations.
7. To propose and evaluate the performance of various lightning protection systems for FRTs based on IEC-approved conventional methodologies.

1.5 Research Contributions

This dissertation takes a holistic view of lightning-induced FRT fires by investigating the concepts behind the causal factors and the fire initiation process toward identifying and providing mitigations for FRT fire prevention. The study identifies the pattern of voltage and current distributions along the steel plates of a FRT towards determining the extent of the risk of flammable vapour ignition by lightning strikes using an RL model. The likelihood of a direct strike to various meshed points on the surface of the FRT is investigated to identify high-risk points, and this is important for designing an efficient LPS for the FRT. The main contributions of this dissertation to the body of knowledge on lightning protection of FRT are summarized as follows:

1. Novel concepts and equations are developed for linearising the discontinuity of the cumulative distribution function and the probability density function of the lightning current at 20 kA to reduce the complexity of analytical DEGM simulation.
2. A presentation in detail of the concepts of numerical DEGM simulation with easy-to-interpret diagrams as a visual interpretation of what DEGM computer codes implement. The diagrams illustrate the various span of the collection volume and the computation of the probability modulated collection volume using striking distance intervals.
3. A novel modification of the traditional numerical DEGM is implemented by eliminating numerical errors and superfluous space points to create an improved DEGM, which lowered the simulation time from over one hundred hours to below thirty minutes for the case of a FRT.

4. This study developed novel analytical DEGM models and equations for a FRT with the roof at the top and when the roof is lowered.
5. A novel evaluation of the effects of the dimension of the FRT and the position of the floating roof on the exposure and the probability of a direct lightning strike to various parts of a FRT using IDEGM.
6. Detailed and improved modelling of the steel sheets of a FRT using resistance and inductance values extracted from ANSYS Q3D with novel evaluations of the effects of frequency on the voltage and current distributions and the effect of an extended length of pipes on a FRT when lightning strikes. A new model is implemented to ascertain the difference between the effects of a direct strike to the tank shell and a strike to the roof.
7. This study created LPS designs and implemented a performance evaluation of the probability of a direct strike to nine different conventional LPS configurations for a FRT.

1.6 The structure of the dissertation

The ultimate goal of developing an effective LPS for FRTs first necessitates an in-depth knowledge of lightning-induced tank fire incidents. The study begins with an introduction and a state-of-the-art review of the subject matter.

Chapter 2 covers the theoretical principles of lightning formation, highlighting the conventional and non-conventional lightning protection systems. The chapter introduces the floating roof tank, which is the main subject of this study, by discussing its structure and parts and how lightning fires are induced and can escalate into a full surface fire. A thorough literature review of vital studies on various aspects of a FRT is also presented in a summary section.

Chapter 3 provides a holistic analysis of the dynamic electro-geometrical model by describing the concept and how to implement it using the lightning current distribution functions. Two alternatives are discussed using either the numerical approach or novel analytical equations for a FRT. The chapter presents a modification to the lightning current distribution functions to remove the discontinuity effect at 20 kA. The chapter identifies opportunity areas for improving the computational accuracy and reducing the simulation time of the numerical model, which resulted in the creation of an improved numerical model using a conversion factor termed K_{P2C}.

Chapter 4 presents the results obtained using the dynamic electro-geometrical model to evaluate FRTs of various radii lengths and heights. The probability of a direct lightning strike to different parts of the FRT is also discussed. A comparison is provided of both the numerical and the analytical approaches.

Chapter 5 provides an extensive simulation and analysis of the voltage and current distributions on the sectional steel plates of the FRT's shell and roof using Simulink on

MATLAB. The steel plates are modelled using their resistance and inductance values obtained from the Ansys Q3D Extractor.

Chapter 6 presents the results of the conventional LPS models evaluated for a FRT. Nine arrangements of air terminals, masts, and catenary wires are considered, analysed, and compared in terms of their interception efficiency and the maximum value of the lightning currents that can strike the roof and the tank shell.

Chapter 7 concludes the dissertation by focusing on the maintenance issues in a typical FRT facility. It highlights the importance of surge protection devices and the different types available. Finally, the chapter provides recommendations for ensuring a lightning-safe FRT facility.

2 Theoretical background

2.1 Lightning

Across the world, there are about 40-100 lightning flashes per second, with most lightning flashes occurring over land due to the lower updrafts speed of 10 m/s in oceanic thunderstorms compared with 50 m/s in inland regions. This results in intensive cloud charging in the inland regions. More lightning activities are measured in terms of thunderstorm days in the tropics than in any other region of the world [34]. This fact implies that structures such as hydrocarbon storage facilities in tropical regions in Africa, South America and Asia are more likely to be struck by lightning. Lightning is naturally associated with thunderclouds. Lightning can also be triggered by volcanoes and desert sandstorms. The global distribution of the lightning flash rate is illustrated in Figure 2.1. In Appendix A, a similar image captured by the lightning imaging sensor is presented in Figure A.1:.

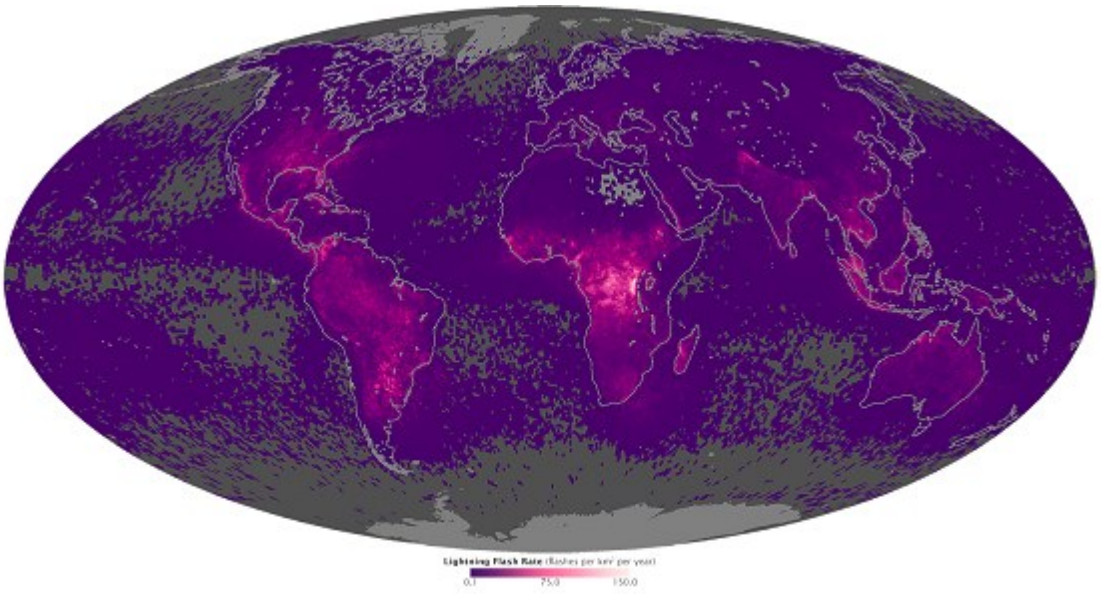

Figure 2.1. Global lightning flash rate [35]

Lightning is a commonly known natural occurrence with its associated beautiful display of bright flare arcs across this sky. Lightning strikes can be hazardous and destructive if not well managed. Lightning is the discharge of atmospheric charges [36, 37], leading to the flow of high-energy electric current through the strike path.

The polarity of a lightning flash can either be positive or negative. On average, a negative lightning bolt transmits an electric current of 30 kA in the first return stroke, but generally, the peak current may reach amplitudes of 100 kA with a step leader speed of 3×10^5 m/s. The first return stroke transfers an electric charge of about 5 coulombs, and about 40 – 60 ms are between strokes. The magnitude of the continuing current varies from ten to hundreds of amperes and flows for 10 – 100 ms. About 30% to 50% of all lightning flashes support the

flow of continuing lightning current. The cumulative electrical charge transmitted by a negative lightning flash varies from 2 to about 200 C. About 10% of all lightning strikes to the earth are positive cloud to ground lightning strikes. A positive lightning bolt transmits a peak current of about 200 – 300 kA [34, 38] or more in some cases [39] (this is about ten times the average current of negative lightning), and this current flows for several milliseconds far longer than the typical duration of a negative return stroke. Research studies have shown that 99% of lightning strikes have a current that is lower than 200 kA [40]. Positive polarity lightning flashes often contain a single stroke as they rarely support subsequent return strokes [34]. The lightning current and associated electromagnetic energy are sufficient to cause strong electrostatic and electromagnetic pulse (LEMP), fire or damage to equipment and facilities [38, 39, 41, 42]. Lightning-induced electromagnetic fields can trigger inductive or capacitive voltage build-up in nearby systems causing damage or disruptions [43].

2.1.2 Lightning formation

Charge build-up in the cloud continues until a critical potential is reached, which causes electric charges to suddenly start descending towards the earth with a corona radius of about 10 m. Due to environmental factors and arbitrary variations of air conditions, the stepped leader moves via a random irregular path. As the lightning-stepped leader moves towards the ground, the background electric field around structures on the ground increases. At a critical distance from the structures, the tip of grounded objects under the effect of this field will emit upward streamers. Some of these will change to upward leaders with only one successfully connecting with the stepped downward leader, thereby creating a low resistance channel for the flow of charges from the cloud through the attachment point to the ground. As the electrical charges flow to the ground, it tries to pass through the lowest resistance pathway to the ground [44, 45]. The electro-geometrical model (EGM) is one of the prominent models for explaining the lightning leader development and interception process.

Once the stepped leader is within a distance of about a few hundred meters from the earth [38], the electric field intensity close to the ground will sharply rise to about $5 – 20 \times 10^3$ V/m. This electric field will be intensified at the tip of objects within the region and may attain 3×10^6 V/m at sea level [46]. For negative streamers, at about $1 – 2 \times 10^6$ V/m at the tip of grounded objects, the electric field on tall structures around the lightning cloud region will become sufficient to launch an upward leader (upward emission of opposite charge particles to that of the downward leader) in the direction of the downward leader tip. As illustrated in Figure 2.2, almost simultaneously, multiple upward leaders will ascend from grounded structures on the earth, but only one of these will effectively attach to the downward leader. Therefore, a low resistance pathway is created to discharge the stepped leader channel, thereby completing the first return stroke. After the first return stroke, a subsequent return stroke may follow with current peaks of 12 kA. Lightning strikes within striking distance of 50 – 250 m have been reported by various studies [47]. Several models are available for studying the return stroke distribution and its effects [48].

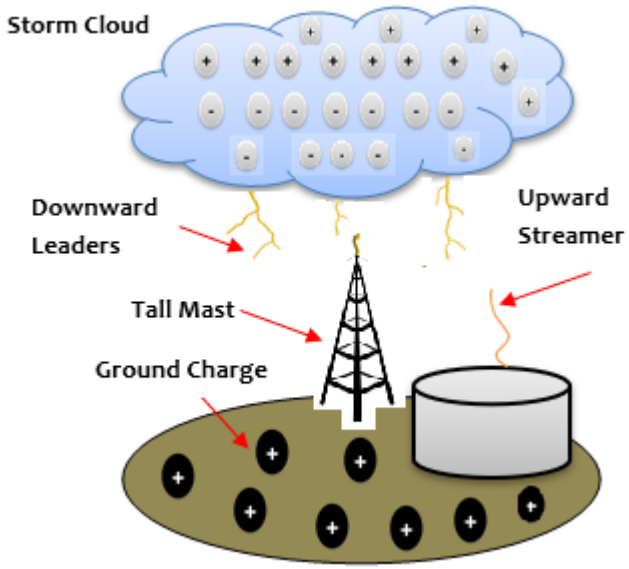

Figure 2.2. Streamers and upward leaders emitted from structures on the ground

The components of a negative cloud to ground lightning current are shown in Figure 2.3. Table A.1: in Appendix A also shows the lightning parameters according to the American Petroleum Institute (API). The temperature within the lightning channel can rise to 30,000 K [34]. This high temperature is indicative of the level of energy of the charged particles within the channel. Therefore, to protect structures against the impact of lightning, adequate mitigations in the form of protective systems must be put in place.

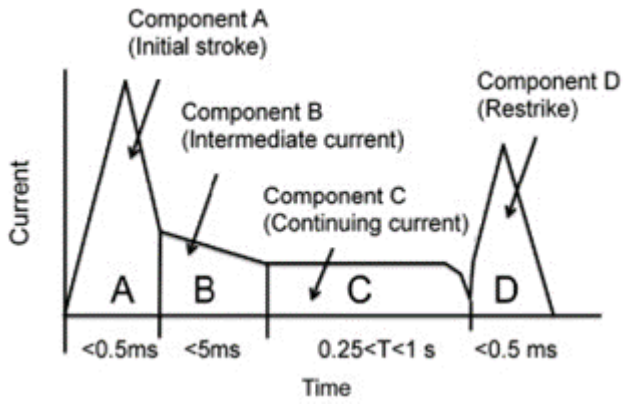

Figure 2.3. Negative cloud to ground lightning stroke current component [49-51]

2.1.3 Lightning Protection Systems

The efficacy of a LPS is dependent on the design and the nature of the materials used. The use of high-quality materials for a poorly designed LPS will result in lightning bypass and other forms of protective failures. While a LPS may not guarantee absolute protection, especially for lightning strikes with small first stroke currents, the use of appropriate air terminations coupled with surge protective devices for sensitive electronics can offer a

significant level of protection. This section looks at the LPS products currently available in the market irrespective of their general acceptability by the lightning research community.

A LPS is set up to shield a structure of interest from destruction by lightning strikes by safely diverting the associated high-energy lightning currents to the ground [34, 52-54]. Lightning protection of structures and facilities is a broad field of study with respect to the dynamics of how lightning interacts with different objects based on their ability to emit an upward leader. The efficiency of a LPS depends on its ability to interact with the lightning formation process. Concerning the available products, LPS offers protection by either serving as a preferential attachment point (sacrificial attachment) or by preventing charge accumulation (Charge Transfer System). These devices can be grouped globally into two types, i.e., conventional LPS and unconventional LPS [46, 55, 56]. The variations in the opinions of the scientific community and approved standards on lightning protection on the different types of LPS are presented in this section.

2.1.3.1 Conventional LPS

A conventional LPS serves as a preferred attachment point for a lightning strike and safely conducts the lightning current to the earth, thereby protecting the structure on which it is installed. This protection is generally in the form of a conductive rod or catenary wire, and it works based on the principle of the age-long Franklin rod. There are four key elements in a conventional LPS.

1) Air terminations

These refer to the array of conductive rods and shield wires typically installed above the protected structure to intercept the lightning strike before it touches the structure below it. The air termination rods may have a blunt tip and must be installed around at-risk points on a structure in line with appropriate guidelines.

2) Down conductors

Down conductors are the conductive cables, copper tapes or structural parts of a structure that conducts the lightning current safely from the air terminals to the earth. An adequate number of down conductors installed with the necessary separation distance must be ensured to prevent side flashes and unwanted electromagnetic effects on sensitive devices nearby.

3) Grounding system

This consists of ground electrodes of various types such as rods, pipes, rings, plates etc. The grounded electrodes transmit the lightning current safely to the earth. The electrodes can be copper or stainless steel and must be designed to ensure a low-impedance pathway for the lightning current [57].

4) Equipotential bonding

It is essential to safeguard against significant potential differences between the metallic parts of equipment and structures that are near the conductive LPS components when lightning strikes. This is achieved by ensuring adequate

equipotential electrical bonding to prevent flashes to such metallic objects [58]. Grounding electrodes and nearby metallic pipes should also be bonded together.

The performance validation of the conventional LPS:

a) The statistical study by [59] shows that conventional LPS prevent direct strikes to structures, and the cases of lightning fires recorded were due to improper installation of the LPS.

b) A performance study between 1905 through 1930 shows that farm buildings protected with the traditional lightning rod were less prone to lightning-induced fire incidents [1, 60].

c) Two research studies that meticulously explored this subject have verified the lightning interception capability of the Franklin rod [61, 62].

d) The study by [63] on buildings struck by lightning reveals that 90% of buildings with lightning rods were shielded from lightning strikes.

e) Standards on lightning protection (IEC 62305 series, NFPA 780 etc.) and bodies such as International Conference on Lightning Protection (ICLP) approve the conventional approach to lightning protection and have developed guidelines for effective implementation based on years of research findings.

The potential issues with the use of the conventional LPS:

a) The lightning rod's effectiveness depends on the placement of the air terminals and associated components at potential strike points. Ineffective design or installation may result in lightning bypass to the protected structure. Also, with proper placement, there still exists a low probability of strike to the protected structure [64, 65] due to the probabilistic nature of lightning, and no lightning protection system is 100% efficient.

b) Metallic down conductors used with traditional LPS may be prone to side flash [38] if proper analysis is not done to ensure adequate side clearances and a parallel current flow path through multiple down conductors.

c) Conventional LPS without additional surge protective devices for sensitive electronics may create a risk for such electronics or electric devices too when high lightning current flows through down conductors associated with the LPS with the attendant LEMP effects.

2.1.3.2 Non-conventional LPS

This class of LPS is of three different categories based on the principles of operation [66]. These are the Dissipation Array System (DAS), also called Charge Transfer System (CTS), and according to the inventors, DAS can prevent a lightning strike, the Early Streamer Emission (ESE) air terminal that wants to have an increased protective range, and Semiconductor Lightning Extender (SLE) that wants to reduce the magnitude of the lightning current.

A) Dissipation Array System (DAS)

The manufacturers of the DAS devices specify that they can shield a structure from a direct strike by lightning which implies that lightning cannot terminate on the DAS itself and the structure on which it is installed. The DAS device, which was invented in 1973 [67], has three essential parts:

1) The DAS ioniser

The ioniser is an array of multi-point air terminations, as shown in Figure 2.4, and they are installed above the protected structure.

Figure 2.4. The DAS Ionizer

The ionisers are designed to interact with storm cells by leaking the charges from the protected area unto air molecules above.

2) The interconnecting wire

The interconnecting wires create a low-impedance connection between the ground electrodes and the special ionisers above the protected structure. The tank shell of a FRT can also serve as the interconnecting wire.

3) The Ground Charge Collector (GCC)

This GCC consists of interconnected electrodes. The electrodes are chemically activated to reduce the grounding resistance. A GCC is shown in Figure 2.5.

Figure 2.5. Chemically activated grounding electrode (CAGE)

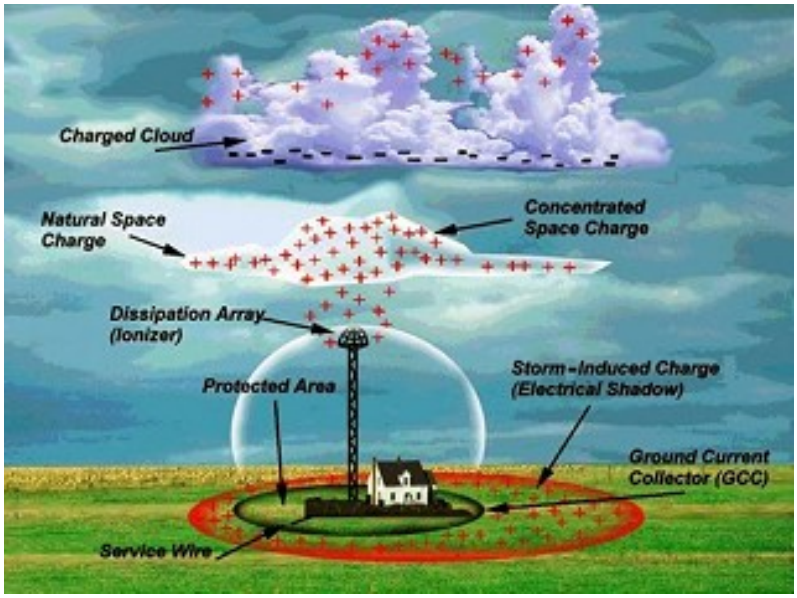

Figure 2.6. An illustration of the working principle of a DAS device [68]

The downward descent of charged particles during lightning strikes requires an optimal potential difference between the storm cloud cell and structures on the earth's surface. The DAS is designed to reduce this differential voltage such that the resulting voltage will be below the required value of about 10^8 V [69]. The DAS leaks charges within the protected site to such a level that the formation of upward streamers becomes unattainable [70]. This concept is termed the corona cloud theory or the bleed-off theory, as illustrated in Figure 2.6.

The performance validation of the DAS:

a) A large radius hemispherical surface can influence the lightning formation process by preventing structures from emitting upward streamers, thereby preventing lightning strikes to protected structures [71].

b) The redistribution of the electric field that occurs by releasing space charge via corona discharge at the peak of tall structures limits the ability of such structures to emit upward streamers during thunderstorms [72-74].

c) DAS can be effectively deployed for mitigating power stations and transmission lines' direct and indirect lightning strikes and transient current anomalies [75].

Counter-claims on the performance of the DAS:

a) For a field intensity of 10 – 50 kV/m heavy ions drifts vertically at a speed of 1.4 – 7.5 m/s. The horizontal movement of a gentle breeze of about 3.4 – 5.4 m/s around the DAS ioniser will blow away any accumulated shielding ions over the protected structure, which will prevent the DAS from offering any shielding protection.

b) The DAS failed the test conducted at Orlando Airport in 1989, which was set up to determine its efficacy. The DAS was severely struck by lightning, and electronic equipment was damaged [38, 76]. The Federal Aviation Authority set up the test.

c) The multi-point ioniser is said to emit several ions in multiplicity, but a laboratory analysis shows that the magnitude of current measure from an 80-point ioniser array was only twice that of a single point. The study by Bent and Llewellyn [77], Mousa [78] shows that multiple point arrays emit the same corona as a single point. According to Bent and Llewellyn [77], a single-point source emits more corona than a multi-point array at 50 ft.

d) The research by NASA in the 1970s shows that the number of strikes to a DAS-protected tower and another tower in the same area without any protection was about the same. This finding indicates that DAS does not remarkably reduce the number of strikes and neither does it prevent lightning strikes [46, 79, 80].

e) The study by the U.S. Air Force [81] on the operation of point charge arrays, without making any categorical conclusion on the overall effectiveness of these devices, the study states that using corona discharge as a basis for explaining lightning prevention is a forlorn hope.

f) According to Mousa [78], when critiqued, the manufacturers of these devices have repeatedly changed their explanation of how the device eliminates lightning.

g) Manufacturers of DAS devices recommend extensive equipotential bonding and good grounding practices coupled with the use of surge protective devices. Researchers claim that these factors account for any effectiveness demonstrated by DAS devices [77] just like any other conventional LPS and not because DAS prevents lightning. The studies by Uman and Rakov [56], Carpenter and Auer [75], Mousa [82] further support this position.

h) From 1989 to 2004, the manufacturers of DAS devices proposed a preliminary lightning protection standard, and this proposal was declined five times by the National Fire Protection Association (NFPA) due to the lack of an adequate scientific basis. Likewise, a similar standard presented to IEEE in 2000, titled PAR 1576, was also rejected in 2004 [83].

i) A study claims that, even if the principle of operation of the DAS device was valid, the electrical charges that are required to neutralise a leader need ionisers with at least 25,000 points as opposed to 1,500 points design[79].

B) Early Streamer Emission (ESE)

ESE devices are said to have the ability to emit upward streamers faster than other objects within their vicinity due to an enhanced field intensity at the tip of the rods. An ESE device is shown in Figure 2.7.

Figure 2.7. A sample ESE device [84]

Due to its ionising capabilities, this time advantage enables ESE terminals to intercept downward leaders faster than nearby objects, thereby acting as the preferential attachment point [67]. The ESE devices originally utilised radioactive elements, but other methods were deployed in the 1980s after the ban on the use of radioactive substances. The installation design of the ESE is based on the Collection Volume Method (CVM) [47]. The integrity and efficacy of this practice have been challenged by researchers over the years [85].

The performance validation of the ESE devices:

a) The ESE offers a protection radius of 100 m per electrode.

b) The upward streamer launched by the ESE terminal attains a speed of 1×10^6 m/s.

c) The ESE down conductor consists of a specially made Triax-cable with multi-layer protective shields, which prevents slide flash to nearby structures [38].

d) Experimental analysis by [86] indicates that the ESE device has a small-time advantage with respect to breakdown (sphere gap) as compared to the Franklin rod. However, the ability of the ESE exciter to generate pulses at a rate that is commensurate with the increase in the field of the downward leader was not verified. Determining this capability is essential to show that the ESE has a substantial time advantage in early streamer emission.

e) According to one of the manufacturers, INDELEC has conducted several performance tests under laboratory and natural lightning conditions in three continents over decades to verify the efficacy of the ESE device, and the results of the analysis have been presented at conferences. Also, about 70% of buildings in Hong Kong are protected by ESE devices, and with installations in over 80 countries and no history of damages and casualties coupled with the increasing market of ESE devices, all these factors further justify the performance efficacy of the ESE [87].

Counter-claims on the performance of the ESE devices:

a) Studies have established that laboratory experiments are inadequate to justify the efficacy of the ESE device. This is because the development of positive leaders under laboratory conditions using switching impulse waveforms differs from the reality under natural lightning [34, 88].

b) Even if emitted early, an upward streamer cannot propagate towards the downward leader without adequate energy from the electric field to support this. The functionality of the ESE device and the operating principle has only been confirmed and advocated by the manufacturers, but analysis by independent researchers contradicts this position. The lightning physics community has also demonstrated that the ESE claims are largely exaggerated [89, 90].

c) Various lab studies have shown cases of ESE devices failing to intercept lightning strikes [91]. Examples are the USA's New Mexico mountain top research studies [46, 67].

d) Manufacturers of low-impedance coaxial down conductors claim that it has a lower inductive drop than a typical wire when conducting lightning current, and as a result, it efficiently prevents slide flash, reduces the stress on the cable insulation, and also reduces the required separation distance. The result of the simulation analysis carried out by Beierl and Brocke [92] found this claim untrue. The connection of the shield conductor to the protected structure generates induced currents which can induce high voltages. Hence, the flow of heavy and rapidly changing lightning current is not reduced using a coaxial cable.

e) The study by Rison [46] asserts that, at best, the ESE device functions as a lightning rod with no enhanced performance capabilities as regards lightning capture and wide protection zone [93-95]. An example is the Rome incident where lightning struck the Papal crest even though it was protected by a radioactive lightning device [38, 94, 96], although the nearest rod to the strike point is about 150 m [38, 96]. Also, the bell tower incident at Sigolsheim in France is another case where lightning struck a point just 6 m away from the ESE device [97].

f) A scientific study states that the speed of the ESE upward steamer is about 10^4 - 10^5 ms^{-1}. This speed is ten times slower than the speed claimed by manufacturers [56].

g) The lightning strike counters of some ESE devices indicate more strikes than the normal lightning activity at the place of installation, and this makes them unreliable [67].

C) Semiconductor Lightning Current Duration Extender (SLE)

The Semiconductor Lightning Extender (SLE) is a device designed to reduce the magnitude of lightning current up to 99%. Invented in 1978, it has a 3-dimensional fan shape comprising highly resistive rods, as illustrated in Figure 2.8. The SLE reduces the inductive impact of

lightning by reducing the rate of change of the lightning current and by increasing the discharge time from microseconds to milliseconds [98]. The device has nine to twenty-five rods [99], and each rod of the SLE can withstand 1500 kV. When this threshold is exceeded on one rod, the lightning current will jump to the next rod until the capacity of all the rods is surpassed. By this point, a flashover may occur to nearby objects, but the magnitude of the lightning current would have been reduced to about 0.4% of the initial value.

Figure 2.8. A semiconductor lightning extender [100]

The performance validation of the SLE:

a) The SLE can significantly reduce lightning current, and this makes it suitable for protecting flammable products and sensitive electronics [101].

b) An experimental study that captured pictures of lightning strikes on both conventional and SLE devices with current waveform measurements confirms the current reducing capability of the SLE device [102].

c) Current-limiting SLE devices can adequately protect sensitive devices in high-rise structures from the effects of lightning [103].

Counter-claims on the performance of SLE devices:

a) Experiments conducted in 1999 state that SLE did not demonstrate the current reducing ability when tested [99]. Also, the device suffers from parallel discharges during the initial stages of lightning, making it unsuitable for flammable zones.

b) Extreme variations have been observed between the number of strikes counted by SLE dedicated lightning counters and the actual strikes to such locations [67].

c) The lightning-reducing effect of the SLE was also not observed when rocket-triggered lightning experiments were conducted by researchers at the Chinese Academy of Sciences [67, 104].

Currently, experimental data and theory do not adequately support non-conventional LPS as being fit for the claimed purpose [56]. The scientific community does not generally agree on

the basis and efficacy of the non-conventional LPS. According to IEC 62305-1:2010 [20], Bouquegneau [94], “There are neither devices nor methods capable of modifying the natural weather phenomena to the extent that they can prevent lightning discharges.” Therefore, it is essential to apply lightning protection measures.

2.2 The floating roof tank

A floating roof tank (FRT) is a specialised, welded-steel storage tank used in industries for storing stabilized hydrocarbons. In the petroleum industry, it is used for storing crude oil and gas condensate. As implied by the tank's name, the FRT has a movable roof that moves with the level of the liquid content in the tank [105]. It can be described that the roof floats within the tank.

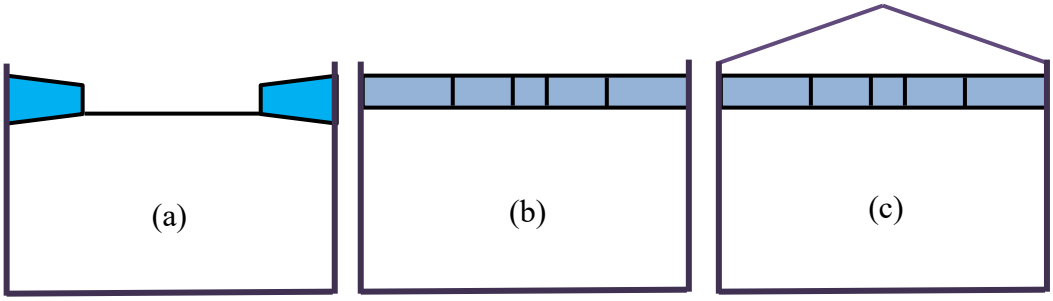

Figure 2.9. FRT roof types (a) Single deck pontoon roof (b) Double deck roof (c) Internal FRT with double-deck roof

The FRT comprises the cylindrical tank shell and the floating roof. The FRT can be of the external or internal type. The internal FRT is specially used for very volatile liquids. It has a cover such as a geodesic dome above the floating roof, which prevents vapour escape and protects the floating roof from environmental elements. The floating roof is of two types: the pontoon or the single-deck roof and the double-deck roof, as displayed in Figure 2.9. The double-deck roof has a lower and upper membrane with a radial bulkhead positioned in between the two. The air gap between the two layers helps to reduce solar radiation reaching the liquid stored in the tank [22].

Figure 2.10 shows a FRT with the main components identified. An air gap separates the roof and the tank shell, and this eliminates the friction that could inhibit the roof’s movement. The rim seal air gap is covered by seals to prevent vapour escape and keep rainwater out of the tank. Appropriate vents are installed to regulate vapour build up within the tank. When tank temperature rises or during a product transfer operation, the vents are likely to exhale flammable vapours, which can be ignited by lightning strikes. Flame arrestors can be deployed on vents, but these arrestors can also result in vent blockage without adequate maintenance [106]. Inverted U-shaped vents can be deployed to minimize the risk of vent ignition by lightning [33].

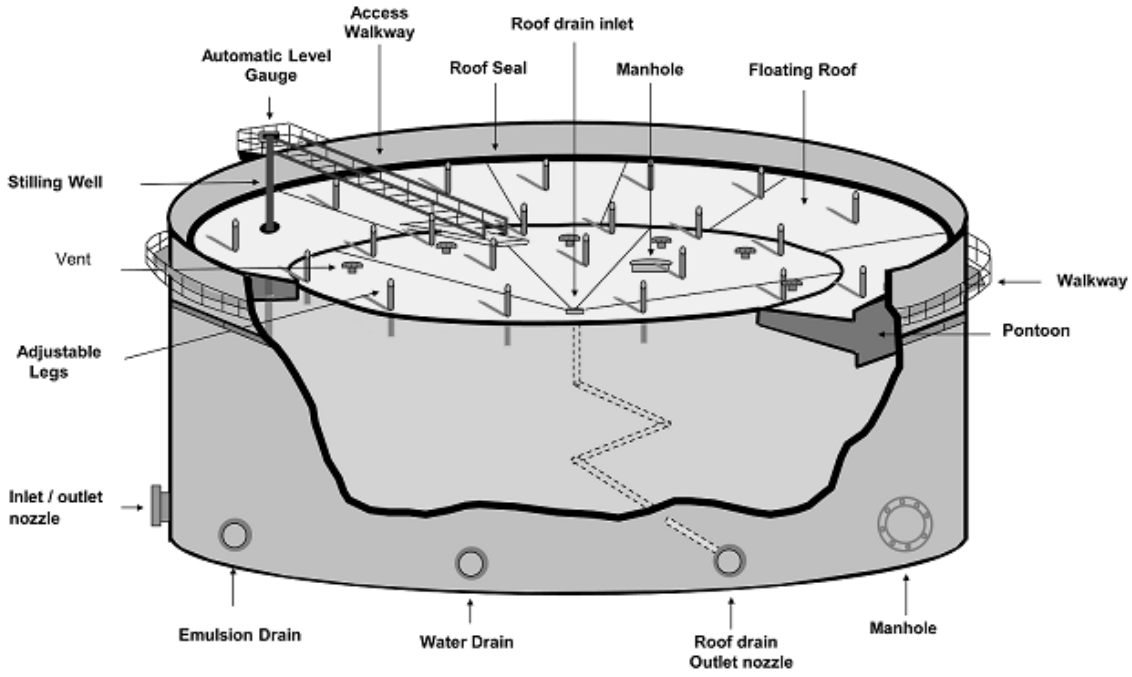

Figure 2.10. A floating roof tank [107]

The height of the FRT varies from 10 m to 20 m, with a diameter of about 30 m to 60 m, and in some cases, as much as 100 m. The roof is movable to ensure that it sits on top of the liquid, thereby eliminating the vapour space above the liquid, and this reduces the evaporation of light hydrocarbons by 90% - 98% [108]. Fire suppression systems are usually installed on and around a FRT to ensure a rapid response to any eventualities. The roof of the tank can be accessed via an access walkway that has two wheels at its base resting on the roof.

The tank has a roof drain system for rainwater and another at the base for draining water from crude oil. The roof has adjustable legs which can be raised from the high to the low position for maintenance activities. The tank base typically rests on compacted sand and gravel [107]. Double-wall designs are also possible as a means of additional containment in the event of a spill or leakage, as illustrated in Figure 2.11. Double-wall tanks can be deployed as a replacement for dikes, especially when there is a space constraint.

Liquids stored in storage tanks can be classified into the flammable or combustible class. A liquid is flammable if it has a vapour pressure that is less than 40 psi at 37.8 °C with a cup flash point that is less than 38 °C, e.g., gasoline, Ethanol and kerosene. These are class I liquids. Combustible liquids are those with a cup flash point that is ≥ 37.8 °C and are further classified into three. For class II, the cup flash point is < 60 °C, e.g., camphor oil, paint thinner and diesel fuel. For class IIIA, the cup flash point is 93 °C, e.g., pine oil and formaldehyde. For class IIIB liquids, the cup flash point is > 93 °C, e.g. lubricating, transformer oils and vegetable oils [109, 110].

Figure 2.11. Double-wall external FRT [111]

Different types and combinations of seals are possible for the rim seal region to prevent vapour escape. This may include a primary seal in combination with separate secondary or tertiary seals [23]. Sample rim seal arrangements are shown in Figure 2.12.

An operational failure such as tank overfilling, seal and tank damage can increase vapour escape from a FRT. A critical level of emission that exceeds the lower explosive limit (LEL) must be prevented at all times to ensure lightning safety within a tank farm. A study by Zinke, et al. [23] shows that areas with emissions above the LEL are only likely on the roof. Emissions from external FRT can be slightly affected by wind [24], and the level of emissions from measurements during normal tank operation is usually very small [112].

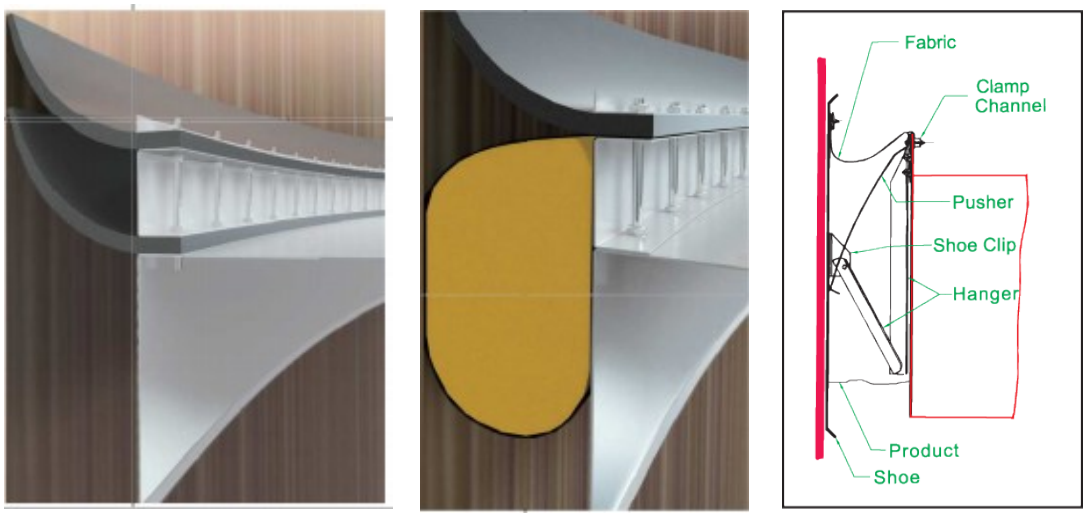

(a) (b) (c)

Figure 2.12. Rim seal configurations (a) Double wiper seal (b) Double (foam & wiper) seal arrangement [113] (c) Mechanical shoe seal [114]

2.2.2 Hazardous areas classification

The area around a FRT can be classified into potentially explosive atmospheres based on the concentration of flammable vapour, i.e., flammable Ex. Zones as illustrated in Figure 2.13.

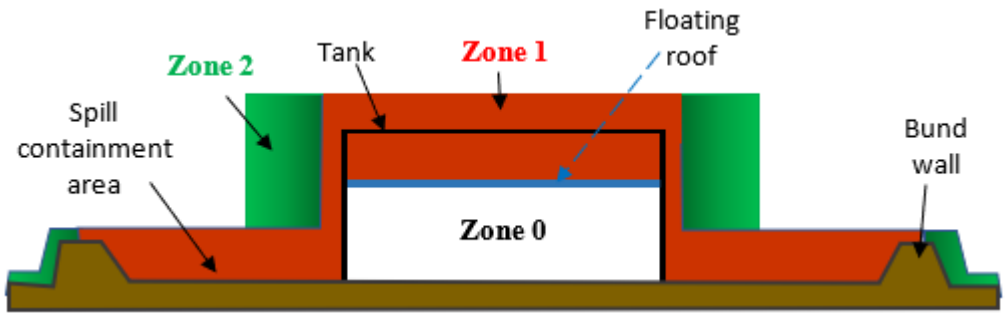

Figure 2.13. Flammable Ex. Zones around a FRT [112]

Zone 0 refers to the region where an explosive atmosphere is continuously present during normal operation. Zone 1 refers to the space where flammable vapour may occasionally exist during normal operation. In contrast, Zone 2 refers to the space within which the release of flammable vapour is unlikely to occur [112, 115].

2.3 The impact of lightning on the FRT

2.3.1 Lightning-induced tank fires

When lightning strikes a FRT, the gap separating the tank shell from the floating roof creates a problem [116]. This gap creates a difference in potential between the tank shell and the roof. If this voltage rises beyond the withstand voltage of the air-gap dielectric strength, it will break down, and this may result in ignition leading to tank fire. The risk of a lightning-induced fire significantly increases with the level of flammable vapour available around the lightning strike point. Since the fire triangle requires oxygen, a source of ignition and fuel, it becomes apparent that to prevent tank fires, either the sources of ignition or flammable vapours must be eliminated since oxygen is readily available in the atmosphere. Adequate vapour control must be ensured on a FRT by the use of seals and breather valves. The production team must ensure that crude oil with high true vapour pressure (TVP) is not routed to the FRT because this will result in high vapour emission, and it may also jam the roof at the top [25]. The NFPA 550, a guide to the fire safety concepts tree, offers two alternatives to fire management; one is to avert fire by removing sources of ignition and fuel or by adequately managing the fire after ignition by regulating the combustion process or through the use of firefighting systems.

Figure 2.14. Buncefield oil terminal fire [117]

Dependence on just firefighting systems can flop if the tank's linear heat detectors (LHD) which ought to sense the fire and activate an alarm fails. Often, manual fighting systems are preferred due to the likelihood of automatic systems failing during fires. When alarms are triggered after fire detection, the response of the firefighting system and the arrival of firefighters at the location of the fire must be prompt. A target response time of less than 5 min is typical.

Approximately 33% of tank fires have been associated with lightning strikes [26], with 95% of such strikes occurring at the shell-roof air gap area [30], i.e. the rim seal region of the FRT [29], [118]. Lightning is a natural phenomenon that, as of today, its formation and occurrence cannot be prevented. A study by [119] shows that 65 out of 107 FRT fires studied in China were due to direct lightning strikes [31]. Research on the rate of lightning ignition of flammable products that are stored in atmospheric tanks shows a likelihood of 82% [27], [28]. This emphasizes the significant risk of lightning strikes to FRTs that are typically used to store gasoline, crude oil, etc. The Buncefield oil storage facility mishap at Hertfordshire in the UK due to tank overfilling, which destroyed over 20 tanks, is a typical example of how dangerous and destructive tank fires are, as shown in Figure 2.14. The cost of the damage was over one billion Pounds.

Lightning-induced fires can be triggered on a FRT in three major ways [120]:

a) Electrostatic charging of the surface of the roof before a lightning strike can result in the build-up of charges on the roof, which can set up transient currents.

b) There are many welded joints and metallic contacts on a FRT, and some of these create unwanted spark gaps. When lightning strikes a FRT, sparks can erupt from

any of such gaps existing on the FRT. This may be in the form of a thermal spark creating incendiary components or a voltage spark due to the electrical breakdown of the flammable vapour between the gap.

c) The flow of lightning current through thin steel materials will result in heating, and this may cause such materials (< 5 mm thickness) to melt.

2.3.2 Direct and indirect strikes to FRT

A lightning strike to a FRT may be direct if the lightning terminates on either the roof or the tank shell, and it may be indirect if it terminates on the nearby ground or connected appurtenances.

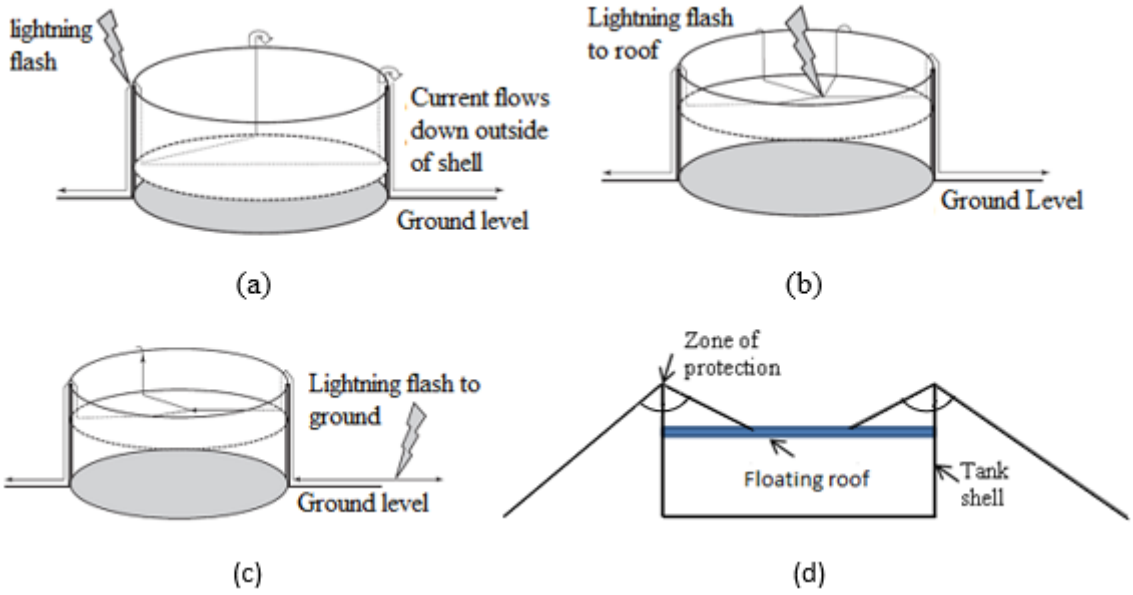

Figure 2.15. A lightning strike to a FRT (a) Direct strike to the tank shell (b) Direct strike to the roof (c) Indirect strike [120] (d) The region of the roof protected from direct strike based on roof height within the tank [25]

A direct strike to a FRT creates the highest level of risk of fire due to the energy dissipated, particularly at the point of strike. Without an early and sufficient fire-control intervention after ignition on a FRT, it can lead to a full-blown tank fire with various financial, environmental and health implications.

The likelihood of a direct lightning strike to the floating roof depends on its position within the tank, and it is highest when the roof is at its peak height [121]. As illustrated in Figure 2.15, when lightning terminates on the tank shell, a significant part of the lightning current will flow down to the ground via the tank shell, while the rest of the current will flow via nearby shunts to the roof. When lightning terminates on the roof, all the lightning current must flow through shunts, if available, to the tank shell and then to the ground. This creates the highest tendency of a spark formation at the shunt-shell interface.

A low resistance grounding and adequate equipotential bonding on a FRT reduce the risk posed by indirect strikes. Sensitive devices may be destroyed by electric fields of 1.15 kV/m created by indirect lightning [122]. A lightning current of 30 kA at less than 1200 m from the FRT may affect sensitive electronics. According to the simulation by Liu, et al. [123], an indirect strike of 30 kA within a 30 m distance from the outside of the FRT may induce an electric field magnitude of 200 kV/m in the FRT's steel sheet. Surge protective devices (SPD) can be installed to manage the impacts of an indirect strike on instrumentation and sensitive devices around the FRT. Sueta, et al. [124] emphasised that research studies should focus on hot spot formation and direct lightning strikes.

2.3.3 Tank fire escalation scenario

Preventing ignition on a FRT is the utmost option because fire can progress quickly. Fire can start on the roof when lightning strikes, especially if there is a spill on the roof. Ignition can also occur at the rim seal area or on the pontoon and within the bund wall. A full surface fire can result if the fire is sustained for a while without a successful attempt at quenching it [4]. A full surface FRT fire can cause the floating roof to collapse and fall into the tank, thereby exposing the crude oil to the burning fire. The crude oil surface will heat up quickly, and the heat will gradually descend downwards to the bottom of the tank. This process is illustrated in Figure 2.16. When the heated crude oil gets to the water interface, it will transfer the heat to the water. The heat quickly converts the water to steam, expanding in volume and generating sufficient pressure to push the crude oil further out of the tank into the burning blaze at the top [125, 126].

Above the tank, the hot crude oil will burn rapidly (boil over), producing more vapour and smoke, which can spread further, thereby increasing the scale of the fire even to nearby structures. The bund wall at this point will serve as a physical barrier, limiting the spread of the burning crude oil. If the bund wall is not of appropriate size and design, and if the fire burns for too long, even the bund wall can collapse, releasing the burning crude oil all over the facility. FRTs should be adequately spaced in a tank farm so that in the event of a fire incident, radiant heat from a burning tank cannot impinge on nearby tanks, thereby eliminating the risk of escalating fires. The deluge system on nearby tanks must be activated during tank fires to cool down the tanks and prevent heat build-up.

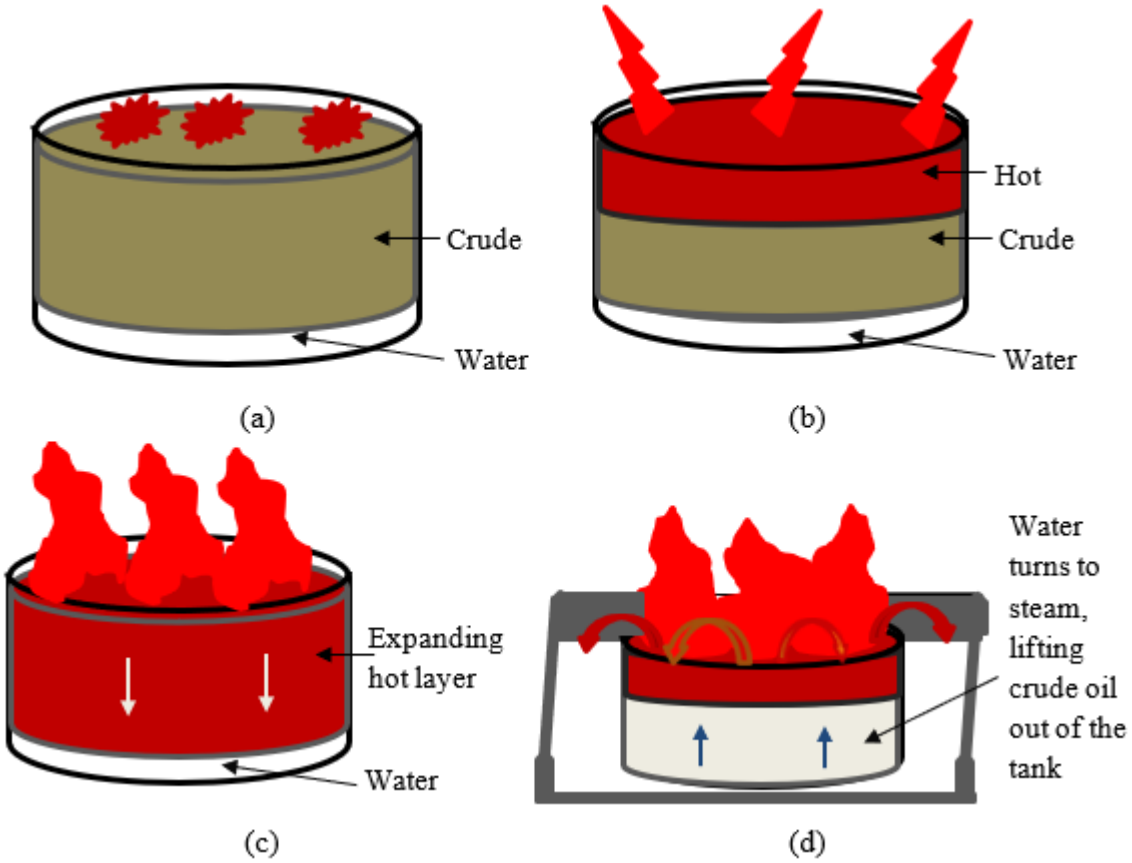

Figure 2.16. FRT fire escalation stages (a) Full surface fire initiation (b) Hot layer of crude oil expands downwards (c) The heated crude oil touches the water interface (d) Steam pressure propels the hot crude oil upwards [125, 126].

According to the Institute of Petroleum (IP) refining safety code, individual FRT in a tank farm or storage facility are to be separated from each other by a recommended distance of 0.3 times the diameter of the larger tank, and this should not be lower than 10 m for crude oil tanks [106]. According to HSG176 [127], a separation distance of 10 m is recommended for tanks with a diameter D ≤ 45 m and 15 m for D > 45 m. The inadequate separation between tanks increases the risk of fire spreading across tanks due to the heat flux radiating from the burning tank to other tanks. This risk will be further aggravated if there is a wind blowing in the direction of the tanks resulting in a direct flame impingement on nearby tanks [106]. A rim seal fire can lead to the explosion of the pontoon. An example of this occurred in 1979, which led to the death of a firefighter [16]. Firefighters should not go on top of the roof to fight rim fires, and adequate arrangement via piping should be in place to pump away firewater to prevent roof collapse, which may lead to a full surface fire.

2.4 Lightning protection of FRT - The state of the art

Preventing lightning-induced tank fires requires a compound effort incorporating operation safety guidelines and adequate lightning protection systems. Operational failures such as

tank overfilling, rapid filling of tanks which triggers charge build-up [128], unsafe hot-work practices, bypassing control systems, design errors [129], poor maintenance culture, and a collapsing roof [4] which may be due to heavy snow [108], etc. increase the risk of fire when lightning strikes. Several protective measures have been considered over time to safely conduct the lightning current from the roof to the tank shell, but all of these have proved inadequate over time.

2.4.1 Shunts, bypass cable, retractable grounding array (RGA)

As shown in Figure 2.17, stainless steel shunts are short stainless conductors with at least a 20 mm^2 cross-sectional area. Shunts were recommended by the American Petroleum Institute (API) to be installed at every 3 m interval across the circumference of the FRT [120, 130]. Shunts can also be installed submerged at a depth of 0.3 m below the surface of the crude oil.

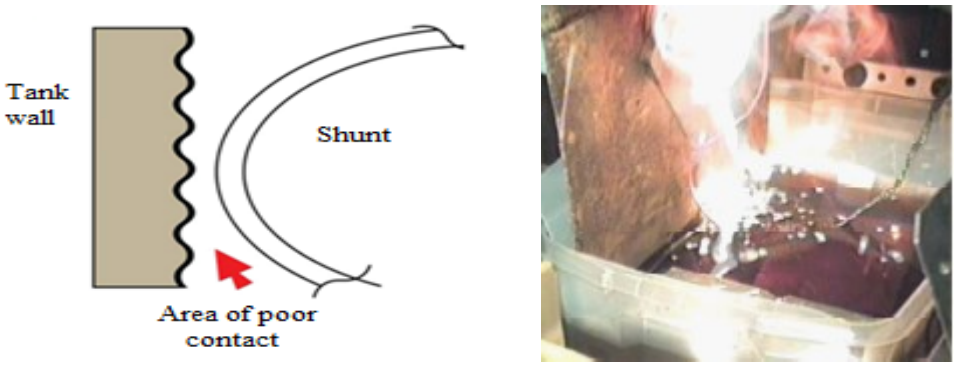

(a) (b)

Figure 2.17. FRT Shunts (a) Shunt not in contact with tank shell (b) Shunt emitting sparks under impulse test [120]

Sparks have been observed at the shunt shell interface during lab tests [120], [131]. Also, insulating thick oil components that coat the tank shell surface, especially in cold climates, impair the electrical contact between the shunt and the tank shell, and this increases the electrical resistance that the lightning current flows through. Over time shunts often lose their physical contact with the tank shell, particularly when there is tank subsidence as the tank becomes out-of-round. The study by Hu and Liu [132] suggested that mechanical seals and shunts should not be fitted on a FRT because they create spark gaps. Submerged shunts offer some advantages in spark prevention, and flammable vapours are also not readily available in the liquid crude oil itself. Arc pressure from a submerged shunt can cause liquid eruption [133]. Challenges with the inspection and oil coating of submerged shunt conductors have prevented the implementation of this recommendation.

Bypass cables have also been used to connect the floating roof directly to the tank shell. These cables are installed at every 30 m distance across the circumference of the tank. Each cable should have a maximum resistance of 0.03 Ω and is designed to conduct the long-duration lightning current components. Due to the large dimensions of most tanks, these cables are very long and as the roof moves upward, the cables spread in loops on the roof,

as illustrated in Figure 2.18. This creates a risk of high inductive voltage when lightning current flows. As an improvement to the bypass cables, retractable grounding arrays (RGA) were deployed, as shown in Figure 2.19.

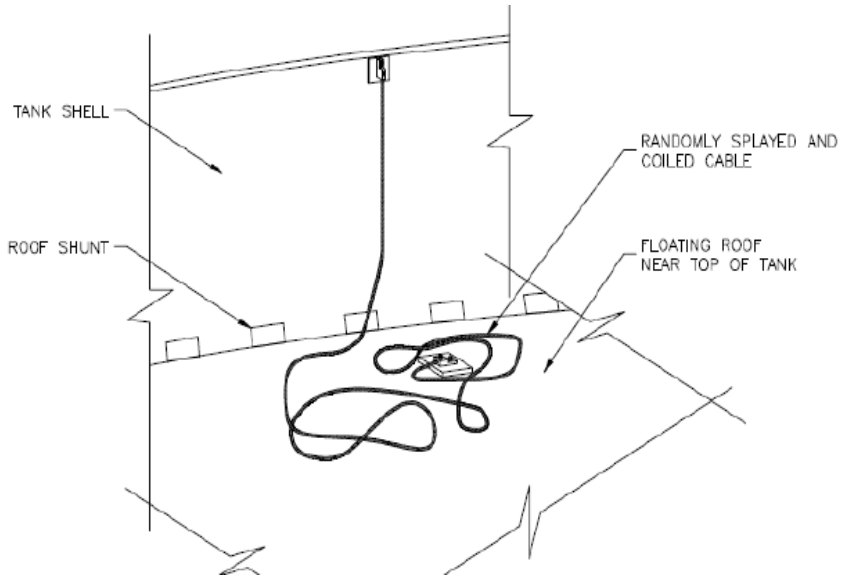

Figure 2.18. Bypass cable spreading in coils on the roof surface [134]

Figure 2.19. A RGA installed on a FRT [135]

The RGA ensures an optimal length of the cable connecting the roof to the tank shell by expanding and retracting based on the position of the roof [132]. According to Denov and Zoro [136], RGA reduces the effective resistance of bonding cable but does not reduce the inductance. RGA installations, over time, tend to break off, and this is often due to mechanical fatigue and possible corrosion by hydrogen sulphide.

The steel accessway from the tank shell to the roof shown in Figure 2.20 has also been considered as a possible means of safely conducting the lightning current from the tank roof to the tank shell. The base of the stairway makes contact with the roof via rollers, and these do not provide a good and solid electrical connection. When oil spills on the roof, the poor electrical connection of the rollers will be further degraded, thus creating a high impedance path for lightning current.

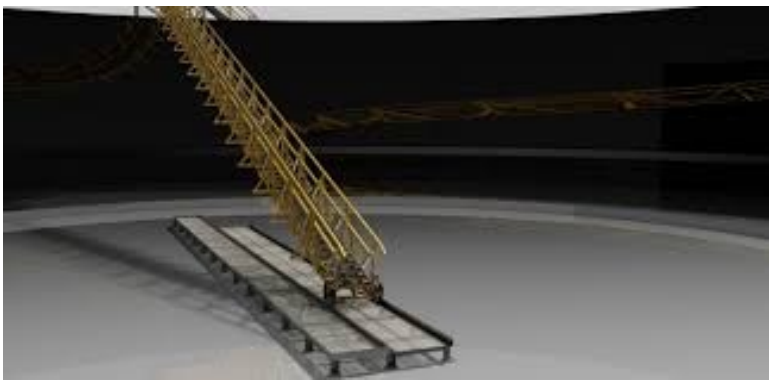

Figure 2.20. The steel access way from the tank shell to the roof [137]

2.4.2 Dissipation Array System (DAS) and non-availability of approved conventional LPS for FRT

As shown in Figure 2.21, DAS is installed on FRT in some storage facilities to avert a direct lightning strike to the tank by creating a cloud of ions that shields the protected site. Unfortunately, cases of a lightning strike to the FRT resulting in a fire have been recorded. For example, in Nigeria, DAS-protected floating roof tanks in two major oil and gas terminals were struck by lightning which triggered the fire detection system. This shows that the DAS installation did not prevent lightning strikes to the FRT in this case. Also, the validity of the effectiveness of the DAS is not generally agreed on by the lightning protection research community.

Figure 2.21. DAS protected FRT

Lightning protection standards such as API RP 545 [130] and chapter seven of NFPA 780 [138] only talk about shunts, the recommended thickness of tank sheets and the application of surge protective devices. These standards do not provide any approved conventional LPS design that can be deployed on a FRT. This creates a research gap to explore possible conventional air termination systems that can be deployed to intercept the lightning current on a FRT and safely pass it to the ground via appropriate down conductor systems.

2.4.3 The summary of the extensive literature review

Summarized here is an extensive literature review of relevant studies that have worked on different aspects of lightning protection and safety analysis related to the floating roof tank using experimental analysis, simulations and analytical calculations. The testing of crude oil wax-coated tank sheet by Haigh, et al. [33] with 12 kA (15/50 μs) fast current and long duration current of 800 A flowing for 5 ms and submerged shunts shows that the shoe plates of the primary seal should be isolated to prevent sparking. Also, increasing the contact tension between the shunts and the rusty shell surface did not affect the severity of the sparking. Little can be done to improve the performance of shunts for achieving spark elimination. Lightning strikes to nearby areas are more frequent than direct strikes to the FRT [139]. An experimental investigation of indirect strikes to a FRT using a model tank and a raised circular disk as a thundercloud by applying 7.0 kV DC to the disk induced a maximum of 1.84 V and 1.88×10^{-8} C on the model tank [139]. Nitrogen gas can be applied as an inert gas supplied to the tank seals via an annular pipe network to reduce the concentration of oxygen and destroy free radicals. This can be incorporated with early lightning warning systems to achieve a safe oxygen level in 60 minutes [140].

An experimental study found that tank sheets greater than 4 mm can withstand perforation by lightning strikes, but the temperature on the face of the sheet may pose an ignition risk [141]. According to Degaev and Korolchenko [142], fighting FRT fires by injecting foam from the bottom of the tank is ineffective when the floating roof has collapsed and tilted within the tank, preventing the foam from reaching the other side of the tank roof. A method is proposed to improve FRT's firefighting efficiency by subsurface injection of foam into the tank's base by modifying the roof configuration. A lab study confirmed that the presence of a conductive film or shunts on the floating roof tank when lightning strikes will always result in contact discharge and will generate sparks [143]. An investigation of the impact of the number and the diameter of the scalable grounding device (SGD) on overall effectiveness found that the transient voltage across the spark gap reduces with an increasing number of SGDs [144]. An examination of the effect of a direct lightning strike on the materials used for the roof covers of geodesic domes of FRTs using aluminium and carbon steel found that the arc voltage can vary for different voltage polarities. Heated areas remain at the same temperature after the initial expansion, and then slowly, the temperature will decay [145].

Analysis of the field strength of lightning strike at various distances from the FRT using a monopole antenna lightning current channel model with the application of the finite difference time domain (FDTD) found that strikes within a radius of 500 m can affect sensitive electronics [32]. According to [123], indirect strikes with current magnitudes less than 17 kA may not be a threat to large FRT. The study by Galván and Gomes [146] asserts that the use of air terminations increases the chances of lightning terminating around the storage tank but reduces the likelihood of hot spot formation on the tank's metallic sheets. A charge of 200 C can puncture steel of 2.5 mm thickness.

The installation of an array of sensors and cameras for automatic and intelligent fire monitoring, detection, alarm and firefighting will solve the challenges of traditional static

foam pourers on FRT, which may take up to 9 minutes to fill the annual foam channel on large FRTs [147]. A causal factor analysis using the bowtie diagram shows that 90% of all case study accidents involve fire and explosion, and 95% of FRT fires are related to the rim seal region [30]. FRT reduces evaporation losses by as much as 90%. While in service, various light hydrocarbon component escapes as vapours from the FRT. The evaporative losses consist of withdrawal or working losses and breathing or standing losses. The withdrawal losses from a FRT increase with the roughness of the wall surface (corrosion) during pumping due to the increased adhesion. Double seals significantly reduce evaporation losses [148].

The extensive review of the body of literature on lightning-induced FRT fires has revealed key aspects of the issue. The American Petroleum Institute (API) conducted extensive research on the suitability of thin stainless-steel conductors called shunts and the tendency and severity of sparks at the shunt shell interface. The results were compiled into standards API-RP 545 and API-RP 545-A [120, 130]. Further works and various experiments by researchers have further confirmed API's findings and identified the impracticability of the recommendation of API regarding submerged shunts. Key highlights of the body of knowledge on lightning-induced tank fires are focused on sparking at the shunts [132], the effects of wax coating on the tank shell [33], and the difference in frequency between direct strikes and indirect strikes to FRTs [139], melting of thin steel sheets [141], the suitability of various types of rim seals, calculation of the breakdown voltage at the shunts, and the use of retractable conductors [143].

The following have been established:

1. Shunts are ineffective for preventing roof-shell sparks due to bending, sheet coating and tank subsidence.
2. Submerged shunts are difficult to inspect, and contact with the shell is not guaranteed.
3. Tank shell thickness greater than 5 mm can withstand melting when struck by lightning.
4. Retractable conductors reduce the length of the bonding cable, but cases of conductor snaps have been recorded.
5. Indirect strikes are more frequent, but their effect can be significantly reduced by proper equipotential bonding at various points and the use of surge protective devices.
6. No non-conventional lightning protection system (LPS) design has been approved by lightning standards for protecting FRT.

3 Materials and Methods

3.1 The dynamic electro-geometrical model (DEGM)

The rolling sphere method has been demonstrated by many research studies and also in practice for identifying likely strike points on a structure. It is based on the concepts of the EGM [149, 150], which defines a striking radius as the interval between the point of the final jump of the upward counter leader and the point of strike on the object or building. By rolling an imaginary sphere of a specific radius (Appendix A: Table A.2:) based on the lightning current peaks, points where the sphere touches are identified as likely strike points, and air termination must be installed at such points to avert a direct lightning strike to the protected object. Although the technique identifies a possible strike point and is easy to apply in practice, it does not differentiate between the type of points on a structure, i.e., flat points, edges, sharp points, etc. This is a challenge to the sufficiency of this method for adequately classifying high-risk points on a structure [151].

Field observation and field intensity measurements have revealed that there are more lightning strikes to the sharp points and edges of buildings than to any other part [152, 153]. The study by Becerra, et al. [151] has also shown that the interception distances based on the rolling sphere technique were overestimated for grounded structures. The rolling sphere method cannot be applied to quantify the probability of a direct strike to the different parts of a building or object in terms of strike probability. The relation linking the striking distance radii (r) and the strike probability has been explored [154], and this led to the development of the numerical DEGM by Kern, et al. [155]. The DEGM considers various orientation points around the structure under study, and this is used to develop a probability modulated collection volume for all the points on the structure. The lightning current probability functions are required to implement the DEGM. The computations in this section will be implemented on MATLAB running on WINDOWS 10.

3.1.1 The Probability Density Function (PDF) and Cumulative Distribution Function (CDF) of lightning current – The improved continuous version

The electro-geometrical model defines a relationship between the lightning current (I) and the striking distance (r) as defined by IEC 62305-1 and is shown in equations 3.1 and 3.2.

$$r(m) = 10 \times I(kA)^{0.65} \tag{3.1}$$

$$I(kA) = \left[\frac{r(m)}{10}\right]^{\frac{1}{0.65}} \tag{3.2}$$

The lognormal distribution function expressed in equation 3.3 describes the probability density function (PDF) of the lightning current (I), and equation 3.4 describes the PDF in terms of r. Equations 3.5 and 3.6 give the cumulative distribution function (CDF) in terms of I and r, respectively [156, 157]. The median value of the lightning current distribution is given as μ and σ is the standard deviation of the $\log(I)$ distribution.

$$PDF(I) = \frac{1}{\sigma I(kA)\times\sqrt{2\pi}} e^{\frac{-\left(\ln\frac{I(kA)}{\mu}\right)^2}{2\sigma^2}} \tag{3.3}$$

$$PDF(r) = \frac{10^{\frac{-1}{0.65}}}{0.65} r(m)^{\frac{0.35}{0.65}} \frac{1}{\sigma\left(\frac{r(m)}{10}\right)^{\frac{1}{0.65}}\sqrt{2\pi}} e^{\frac{-\left\{\ln\frac{\left(\frac{r(m)}{10}\right)^{\frac{1}{0.65}}}{\mu}\right\}^2}{2\sigma^2}} \tag{3.4}$$

$$CDF(I) = \int_0^{\infty} PDF(I)\,dI = \int_0^{\infty} \frac{1}{\sigma I(kA)\sqrt{2\pi}} e^{\frac{-\left\{\ln\frac{I(kA)}{\mu}\right\}^2}{2\sigma^2}} dI \tag{3.5}$$

$$CDF(r) = \int_0^{\infty} \frac{10^{\frac{-1}{0.65}}}{0.65} r(m)^{\frac{0.35}{0.65}} \frac{1}{\sigma\left(\frac{r(m)}{10}\right)^{\frac{1}{0.65}}\sqrt{2\pi}} e^{\frac{-\left\{\ln\frac{\left(\frac{r(m)}{10}\right)^{\frac{1}{0.65}}}{\mu}\right\}^2}{2\sigma^2}} dr \tag{3.6}$$

Lightning facts have already established that ninety percent of all lightning strikes are negative (n) and the remaining are of a positive (p) charge. Based on this, new probability functions are generated as a weighted sum of the 10% value of the positive probability function and the 90% value of the negative probability function. For the DEGM computations, the weighted PDF(r) and CDF(r) are defined as a function of the striking distance. These parameters are plotted in Figure 3.1 and Figure 3.2, respectively.

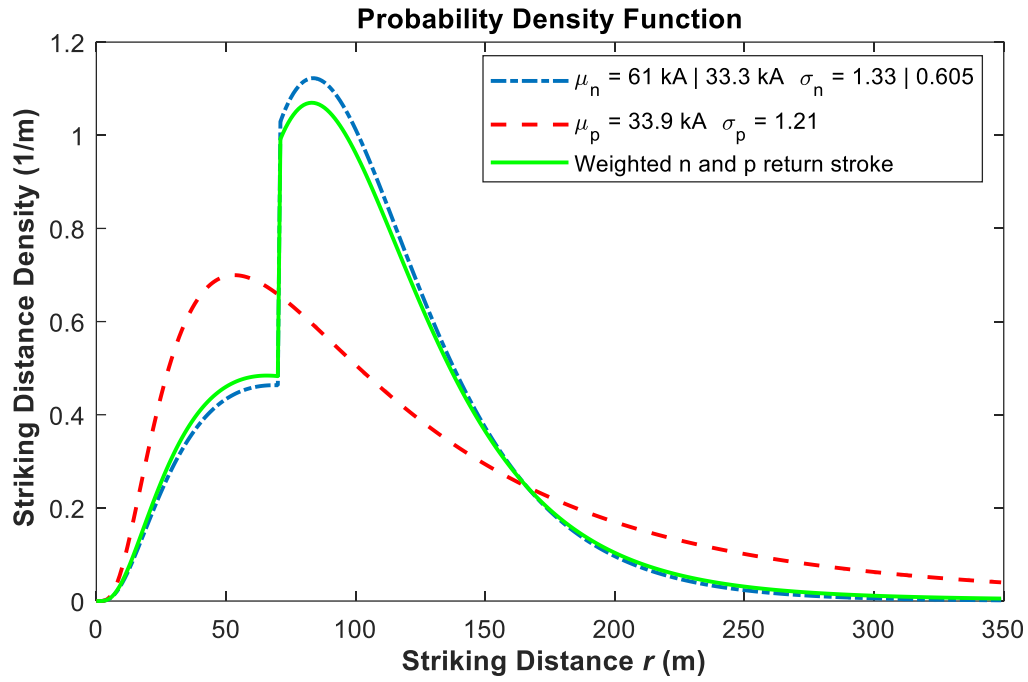

Figure 3.1. A plot of the PDF(r) function

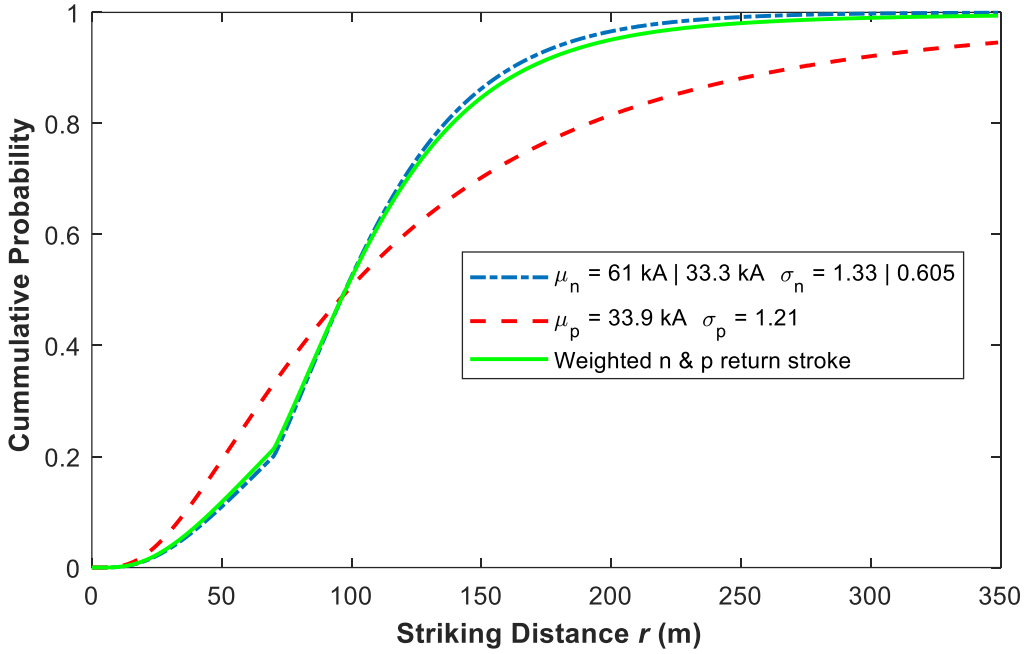

Figure 3.2. A plot of the CDF(*r*) function

3.1.1.2 The modified continuous PDF and CDF

As shown in Figure 3.3 for the CIGRE line plot, the lightning current distribution has a discontinuity at the value of 20 kA, i.e., at 70.1 m in terms of striking distance. This discontinuity has been attributed to the combination of lightning current measurements using 100 direct measurements and supplementary data from indirect methods such as magnetic links [158] from various parts of the world in the current dataset, which has now increased

to 408 samples [158, 159]. This discontinuity does not have an impact on the numerical implementation of DEGM, but it makes the analytical computation complex due to the number of loops required for switching the values of σ_n and μ_n for currents greater or less than 20 kA, which may be tricky to implement accurately. In response to this issue, which was identified during DEGM studies, modified probability functions have been developed by this study to eliminate the effect of discontinuity by introducing a continuous step function at the point of discontinuity.

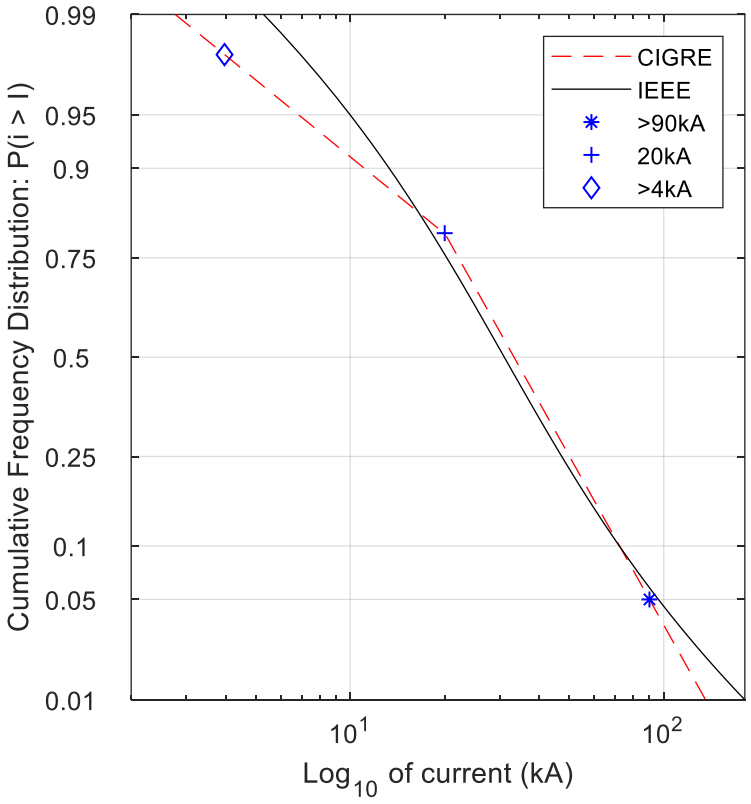

Figure 3.3. The CIGRE and IEEE lightning current distributions [160]

The distribution functions for the negative lightning current are modified and the following variables are defined as follows: $\mu_1 = 61$ kA, $\sigma_1 = 1.33$, $\mu_2 = 33.3$ kA, and $\sigma_2 = 0.605$ and for the positive lightning current $\mu_p = 33.9$ kA and $\sigma_p = 1.21$ [126, 160].

$$\mu_n = \frac{1}{2}\left[\mu_1 + \mu_2 - (\mu_1 - \mu_2)\cdot erf\left(\frac{3}{\pi}(I(kA) - 20\ kA)\right)\right] \tag{3.7}$$

$$\sigma_n = \frac{1}{2}\left[\sigma_1 + \sigma_2 - (\sigma_1 - \sigma_2)\cdot erf\left(\frac{3}{\pi}(I(kA) - 20\ kA)\right)\right] \tag{3.8}$$

$$\mu_n = \frac{1}{2}\left[\mu_1 + \mu_2 - (\mu_1 - \mu_2)\cdot erf\left(\frac{3}{\pi}(r(m) - 70.092\ \mathrm{m})\right)\right] \tag{3.9}$$

$$\sigma_n = \frac{1}{2}\left[\sigma_1 + \sigma_2 - (\sigma_1 - \sigma_2)\cdot erf\left(\frac{3}{\pi}(r(m) - 70.092\ \mathrm{m})\right)\right] \tag{3.10}$$

$$PDF(I) = 0.9 \times \frac{e^{\frac{-\ln^2\left(\frac{I(kA)}{\mu_n}\right)}{2\sigma_n^2}}}{\sigma_n I(kA)\sqrt{2\pi}} + 0.1 \times \frac{e^{\frac{-\ln^2\left(\frac{I(kA)}{\mu_p}\right)}{2\sigma_p^2}}}{\sigma_p I(kA)\sqrt{2\pi}} \tag{3.11}$$

$$PDF(r) = 0.9 \times \frac{e^{\frac{-\ln^2\left(\frac{\left(\frac{r(m)}{10}\right)^{\frac{1}{0.65}}}{\mu_n}\right)}{2\sigma_n^2}}}{0.65\sigma_n\sqrt{2\pi} \times r(m)} + 0.1 \times \frac{e^{\frac{-\ln^2\left(\frac{\left(\frac{r(m)}{10}\right)^{\frac{1}{0.65}}}{\mu_p}\right)}{2\sigma_p^2}}}{0.65\sigma_p\sqrt{2\pi} \times r(m)} \tag{3.12}$$

$$CDF(I) = \int_0^\infty PDF(I)\, dI \tag{3.13}$$

$$CDF(r) = \int_0^\infty PDF(r)\, dr \tag{3.14}$$

The analyses from equations 3.7 to 3.14 using the error function generate a continuous version of the density functions as shown in Figure 3.4, Figure 3.5, Figure 3.6, and Figure 3.7. Visually, this weighted discontinuous plot and the modified continuous version look similar, except that the continuous version has a slight slope at the point of discontinuity rather than a vertical line in the PDF plots.

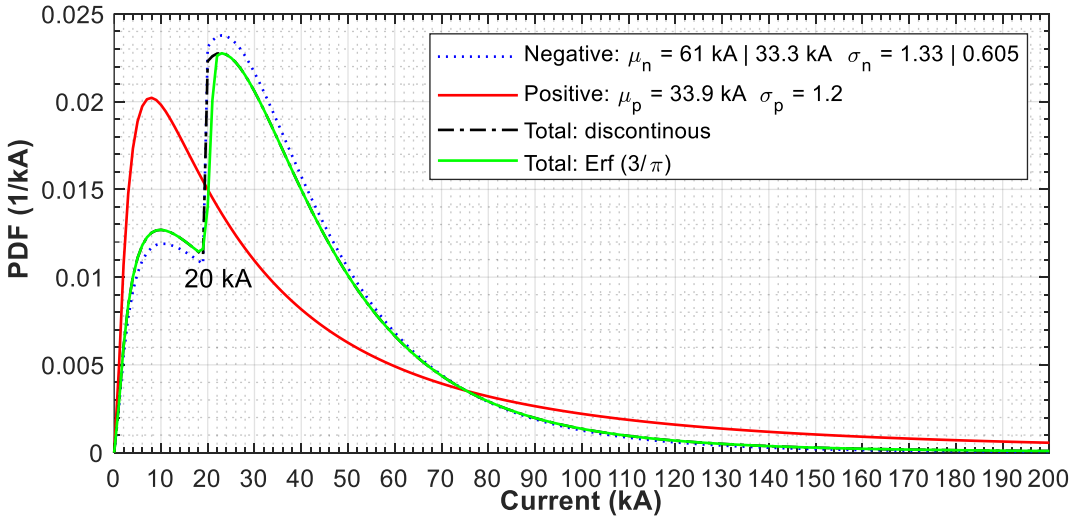

Figure 3.4. Continuous PDF plot against the current in kA

For the continuous version, the appropriate values of μ and σ are automatically selected based on the value of the lightning current without having to use loops in the code to achieve this, as illustrated in Figure 3.8.

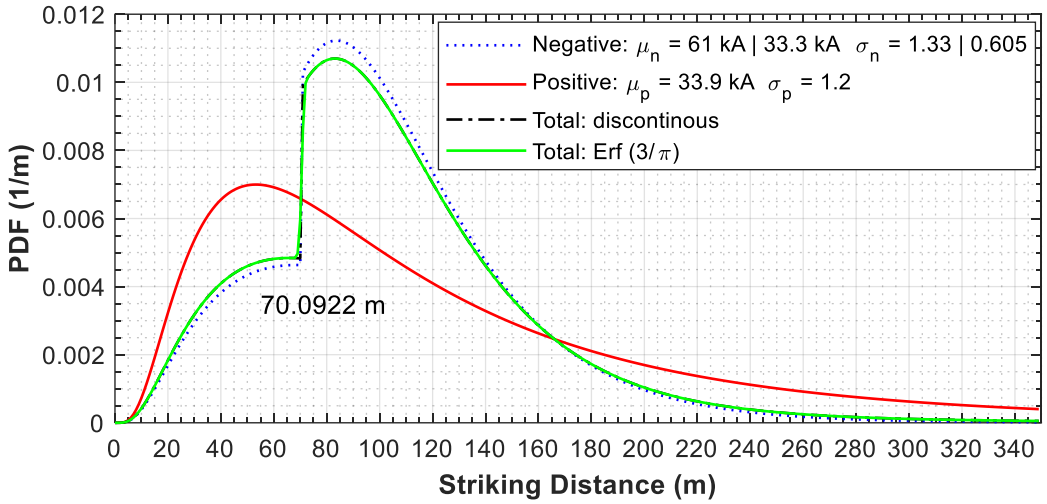

Figure 3.5. Continuous PDF plot against striking distance in m

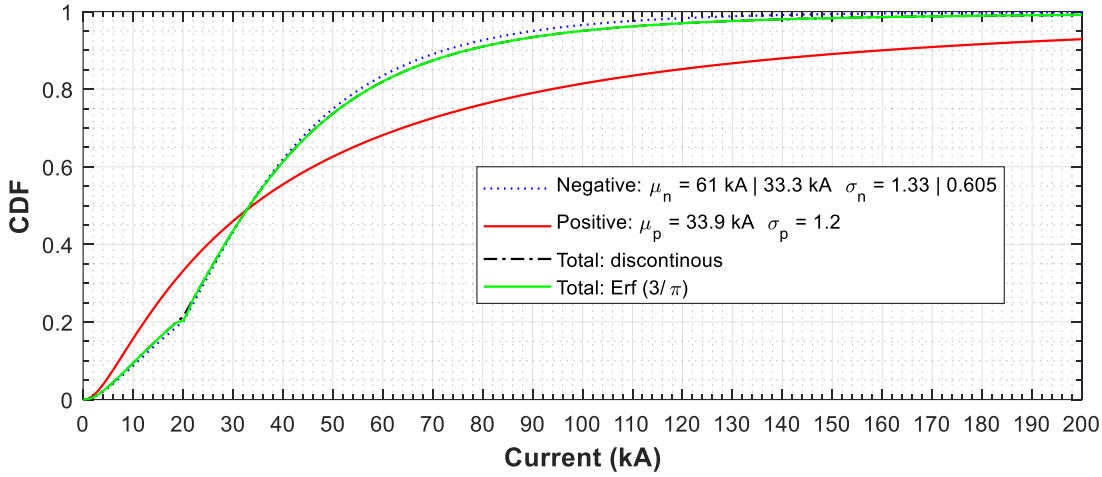

Figure 3.6. Continuous CDF plot against the current in kA

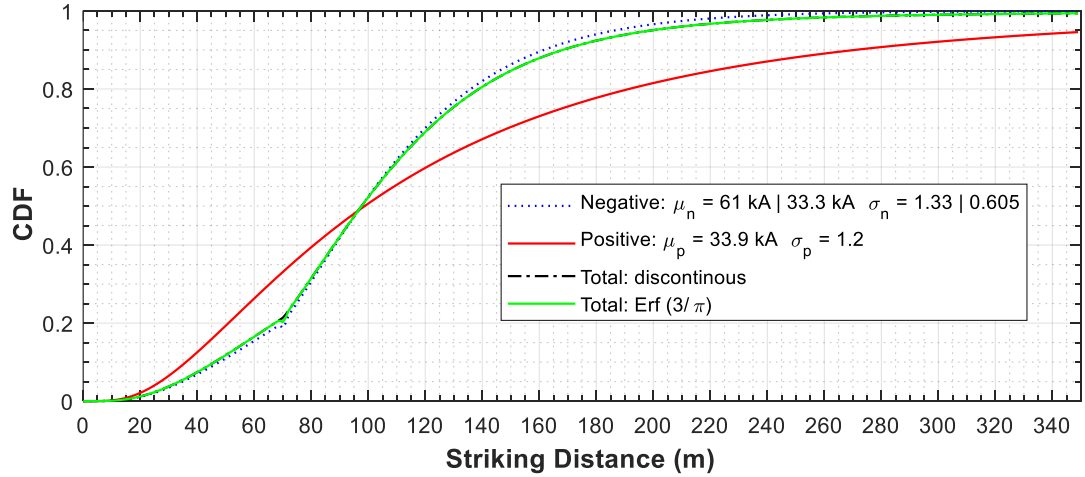

Figure 3.7. Continuous CDF plot against striking distance in m

The benefit of the continuity applied is illustrated in Figure 3.9. A two-step iteration is required to apply analytical DEGM to compute, for example, the probability modulation collection volume (PMCV) for the corner of cuboid structures of heights 1 m to 100 m, using

the modified functions, but with the discontinuous function, several intricate loops and decisions will be required which is more challenging to implement.

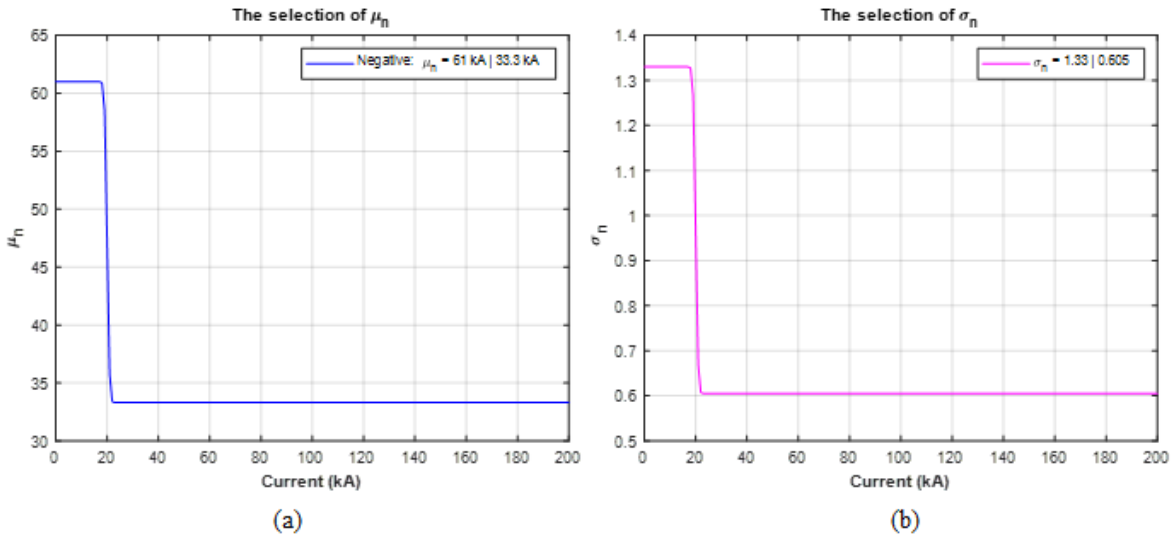

Figure 3.8. Automatic selection of (a) μ (b) σ

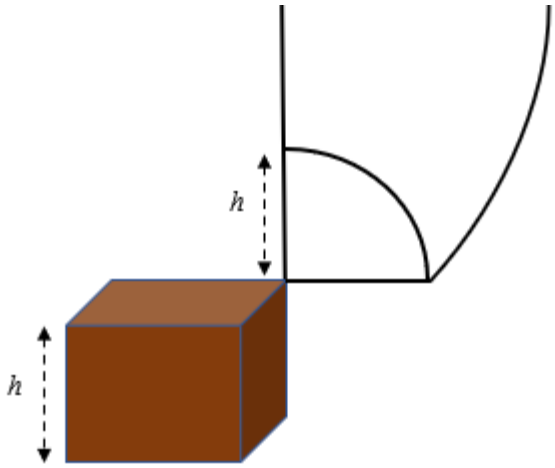

Computation of the PMCV for the corner of cuboids of height 1 m to 100 m

Continuous PDF

H = 0
Volume Equation 1
H = 70
Volume Equation 2
H = ∞

Discontinuous PDF

Structure < 70 m

H = 0
Volume Equation 1
H = h
Volume Equation 2
H = 70
Volume Equation 2
H = ∞

Structure > 70 m

H = 0
Volume Equation 1
H = 70
Volume Equation 1
H = h
Volume Equation 2
H = ∞

Figure 3.9. The benefit of the continuous density functions

3.1.2 The implementation of the numerical DEGM

The numerical DEGM requires surface discretisation of the structure and the nearby space. Discretisation size of 1 m × 1 m and 2 m × 2 m has been applied by studies on cuboid structures and discretisation at 1 m intervals along air terminal rods and catenary wires [155, 161]. This creates surface points on the structure and space points around the structure, as shown in Figure 3.10. The space points are the lightning orientation points, and for each space point around and above the structure, the nearest surface point on the ground or the structure as a function of geometric distance will be identified. This distance is the actual striking distance to the identified strike point on the ground or structure. The equivalent lightning current can also be determined using equation 3.2. Likewise, this distance r can also be probability-modulated by substituting it into the PDF(r) and CDF(r) equations.

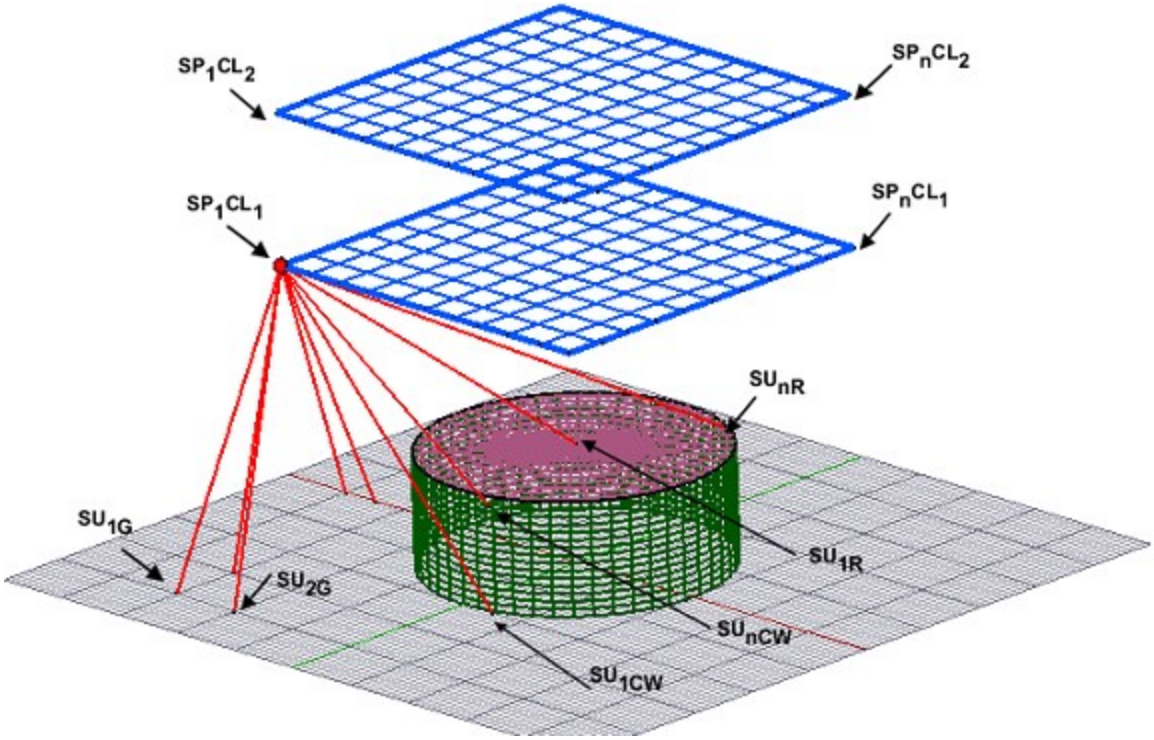

Figure 3.10. Surface discretisation in DEGM implementation

This computation is then performed iteratively for all the space points, and the probability values for each strike to each point are summed. Finally, the total strike probability for all the points will be cumulated as the probability PMCV for the whole structure, and the values for each point can then be expressed as a percentage of this total value. DEGM helps to identify high-risk points as it clearly expresses the strike probability of all the points in percentage.

Considering the case of a tank, to apply DEGM, the following are defined:

The spatial striking distance between a space point and a point on the roof of the tank is D_{nR}, D_{nG} for a point on the ground, and D_{nW} for points on the cylindrical wall. Where n increases

from one, i.e., the first to the last surface point. The effective striking distance for each strike is defined as SD_r.

$$SD_r = \min\left[D_{1G} : D_{nG}, D_{1R} : D_{nR}, D_{1W} : D_{nW} \right] \tag{3.15}$$

The rolling sphere radii R_{sp} are computed within the range of 0 m to 300 m vertically above the roof.

For any space point, a radii interval is defined from r_1 on the lower space layer and r_2 on the current space layer.

For each iteration, a distance D_n is identified from D_{nG}, D_{nW}, and D_{nR} such that $D_n = SD_r$.

For any surface point n on the ground, the cumulative probability for that point is:

$$P(SU_{nG}) = \sum_{r=0}^{r=300} \int_{r_1}^{r_2} PDF(r)\, dr \quad \forall\, D_{nG} = SD_r, \forall\, r(m) \in R_{sp} \tag{3.16}$$

For any surface point on the cylindrical wall of the tank, the cumulative probability for that point is:

$$P(SU_{nW}) = \sum_{r=0}^{r=300} \int_{r_1}^{r_2} PDF(r)\, dr \quad \forall\, D_{nW} = SD_r, \forall\, r(m) \in R_{sp} \tag{3.17}$$

For any surface point on the roof, the cumulative probability for that point is:

$$P(SU_{nR}) = \sum_{r=0}^{r=300} \int_{r_1}^{r_2} PDF(r)\, dr \quad \forall\, D_{nR} = SD_r, \forall\, r(m) \in R_{sp} \tag{3.18}$$

Given n_1 total number of surface points on the roof of the tank and n_2 total number of surface points on the cylindrical wall, the total PMCV for the tank is given by

$$PMCV_{\text{FRT}} = \sum_{n=1}^{n_1} P(SU_{nR}) + \sum_{n=1}^{n_2} P(SU_{nW}) \tag{3.19}$$

3.1.3 Improving the performance of the numerical DEGM – errors, computation time, and computation without ground points

The numerical DEGM described in section 3.1.2 has some limitations, which will be addressed in this section. Numerical DEGM requires surface discretisation, and due to the thousands of points generated by this discretisation and the need for repeated iterations for each point, numerical DEGM simulation is typically slow and may run for several days for large-dimension structures. There is a need to improve the computation time and the accuracy of the DEGM simulations by eliminating sources of numerical errors [162].

3.1.3.1 Factors that influence the numerical accuracy of DEGM simulations

1) The surface and space point discretisation size

The discretisation size determines how the length of surfaces is defined. Consider a 5 m linear length on the surface of a cuboid discretised in two ways using 1 m and 0.5 m, as illustrated in Figure 3.11. Two corner points remain constant irrespective of the discretisation size, but the number of internal points changes with discretisation. The PMCV for this cuboid side length is equal to the length multiplied by the PMCV for one point. There are 4 points representing a 5 m length using a 1 m discretisation size which means 1 m is lost. For the case of 0.5 m discretisation size, there are 9 points representing 5 m which means 0.5 m is lost. The accuracy of the model improves with decreasing discretisation size, but the simulation becomes slower.

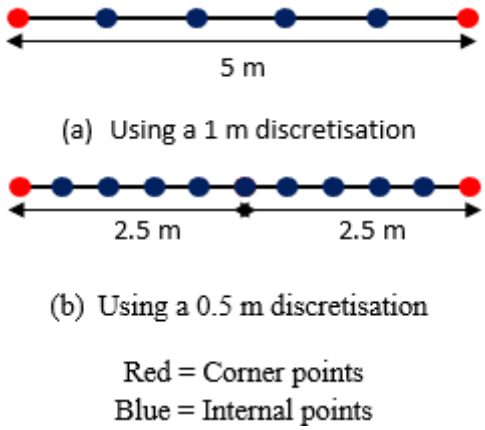

Figure 3.11. The difference in surface length definitions based on the discretisation size

2) Discontinuity along the striking distance path

A striking distance is the shortest straight line connecting the orientation point to the strike point. As a result of several vertical layers of space points with the computation performed between the intervals of these layers as expressed in equation 3.20, the striking path becomes discontinuous for some points. This vertical discontinuity is illustrated in Figure 3.12, and this introduces a little error in the accuracy for affected points. Since the PMCV is cumulated for all points, ultimately, the impact of the errors also becomes cumulative.

$$CDF_{\text{interval}} = \int_{r_1}^{r_2} PDF(r)\, dr \tag{3.20}$$

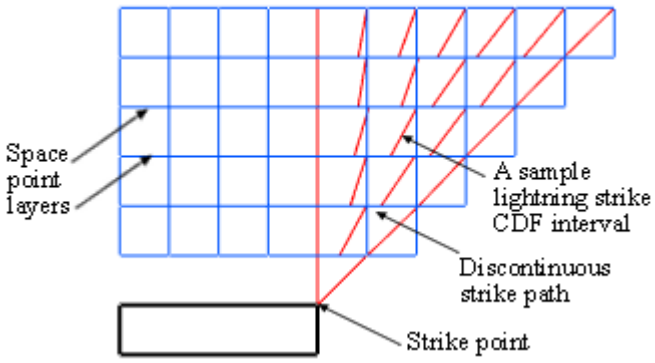

Figure 3.12. Discontinuity along the striking distance path

3) Superfluous space points within the collection volume

The pioneering works on numerical DEGM applied equally spanned space point layers [155, 161] from the ground upwards, as illustrated in Figure 3.13. Computing DEGM with this space point spread will take a very long time.

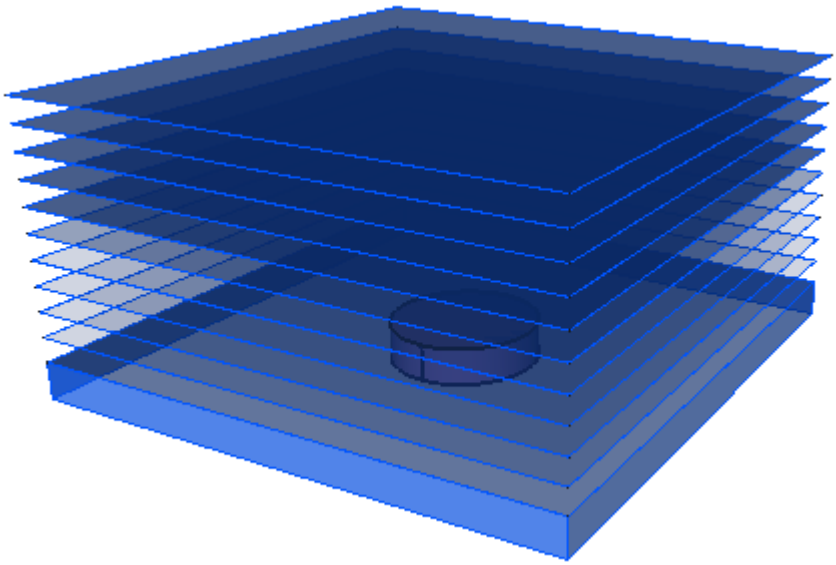

Figure 3.13. Equal spanned space point model [157]

The authors applied a discretisation of 2 m × 2 m to reduce the computation time, but this will, in turn, reduce the model accuracy. Further works by Adekitan and Rock [157] on numerical DEGM reduced the span of the rectangular space point layers by using linearly increasing space points [156] using a discretisation size of 1 m × 1 m, as shown in Figure 3.14 as model A. The rectangular space point layers have now been further constrained within the actual collection volume of the structures as shown in Figure 3.15 as model B. The span of each layer increased vertically with height, and this greatly reduced the computation time, but at the corner points of the space point layers, the model still has excess space points.

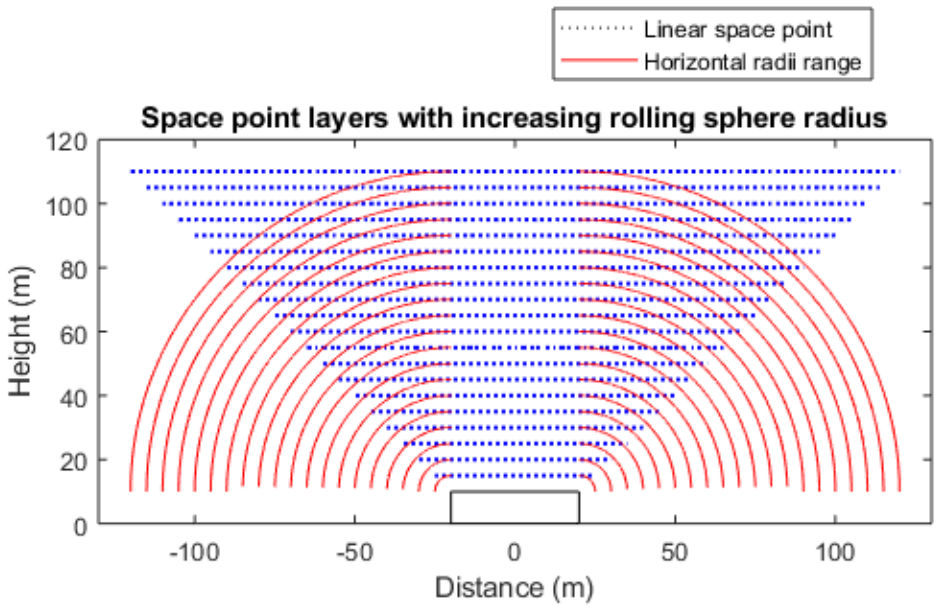

Figure 3.14. Linearly increasing space point layers

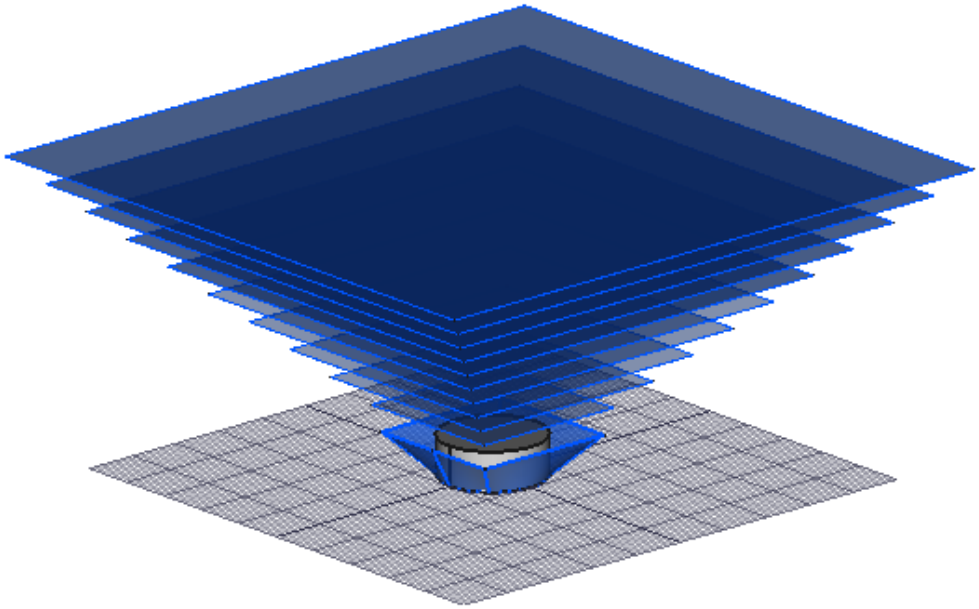

Figure 3.15. Reduced space point span with additional excess space points at corner points

3.1.3.2 Modifications to improve the accuracy of numerical DEGM simulations

The space point definition will be modified to enhance the performance of the numerical DEGM simulations, and an approach using PDF rather than CDF will be deployed.

1) Direct computation using PDF rather than CDF

Computing the PMCV at intervals requires CDF, which is the integration of PDF, and this is achieved at vertical intervals of the striking distance, i.e., r_1 to r_2. A method is proposed in this study to eliminate the errors created by the discontinuity in the striking distance by directly applying the PDF multiplied by a conversion factor. This method applies pointwise computation rather than at intervals, as shown in Figure 3.16. On a straight vertical path from 0 m to 300 m, the CDF is 0.9902, while the PDF computed at vertical intervals of 10 m is 0.0966. Based on this, a conversion factor from PDF to CDF termed K_{P2C} is generated as a ratio of these two values. The K_{P2C} is dependent on the vertical distance applied. For 2.5 m, $K_{P2C} = 2.51$; for 5 m, $K_{P2C} = 5.06$; and for 10 m, $K_{P2C} = 10.25$. This factor will be applied to space points above the roof structure at intervals of 10 m in this study. For space points by the side of the structure, K_{P2C} is not necessary, as vertical intervals of 1 m can be applied in this case, except for very tall structures, just to speed up the computation.

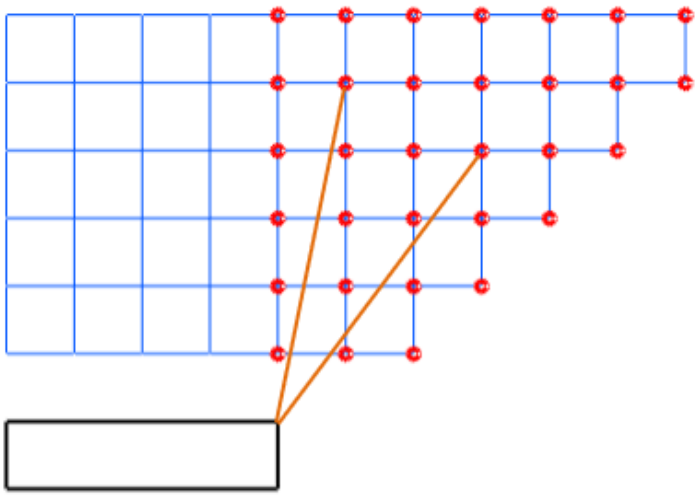

Figure 3.16. PMCV computation using PDF for each point

2) Improved space point definition

The space point layers in model C will be defined as confined within the collection volume to eliminate superfluous space points, especially at corner points for cuboid structures using the quarter-circle point, as shown in Figure 3.17 and Figure 3.18. The total space points within the quarter circles are approximately $\pi/4$ times that in square-shaped corners. Likewise, for FRTs, space points confined to the lightning collection volume of the FRT will be applied, as displayed in Figure 3.19. With the application of the confined space points, ground surface points are no longer needed in the model and will be removed. This is because strikes from space points that are outside the collection volume of any structure will hit the ground in DEGM simulation, but since all the space points are now confined, the ground surface points are no longer needed, and this will give a significant computation time advantage.

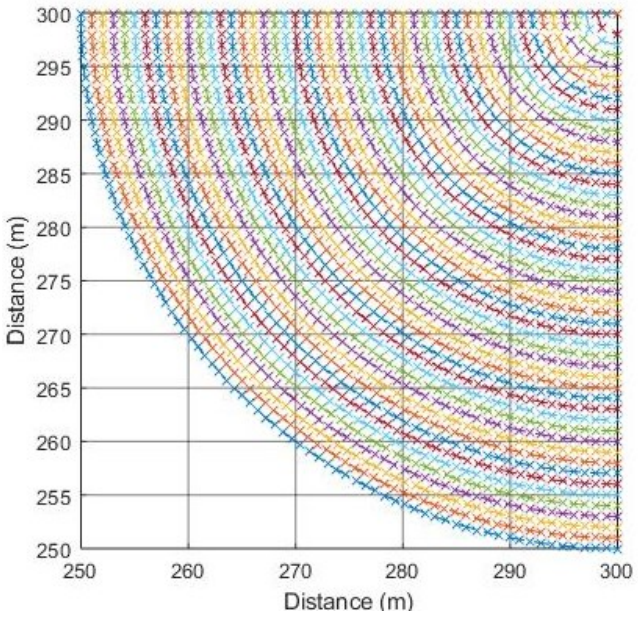

Figure 3.17. Quarter circle corner definition of space points

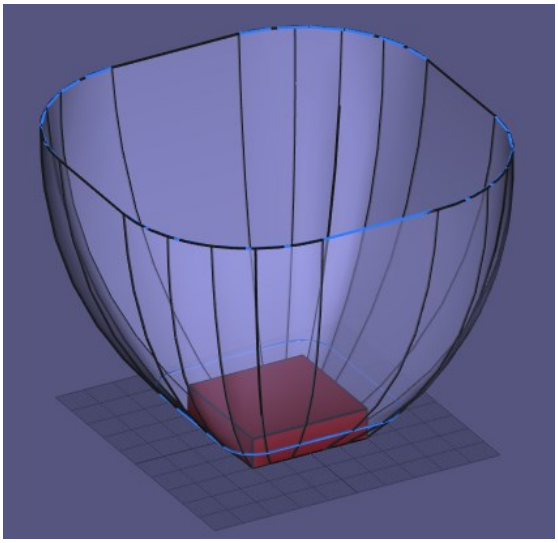

Figure 3.18. The effective space point volume for a cuboid using quarter-circle corners

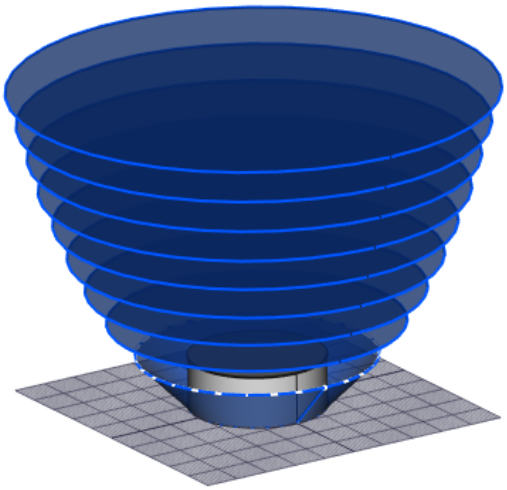

Figure 3.19. The space points around the FRT are confined within the collection volume

3.1.3.3 The effect of the proposed modifications on DEGM accuracy

The improved dynamic electro-geometrical model (IDEGM) showed improved accuracy in the result and a notable decrease in computation time for the few cases considered, as illustrated in Figure 3.20, Figure 3.21, Figure 3.22, and Figure 3.23.

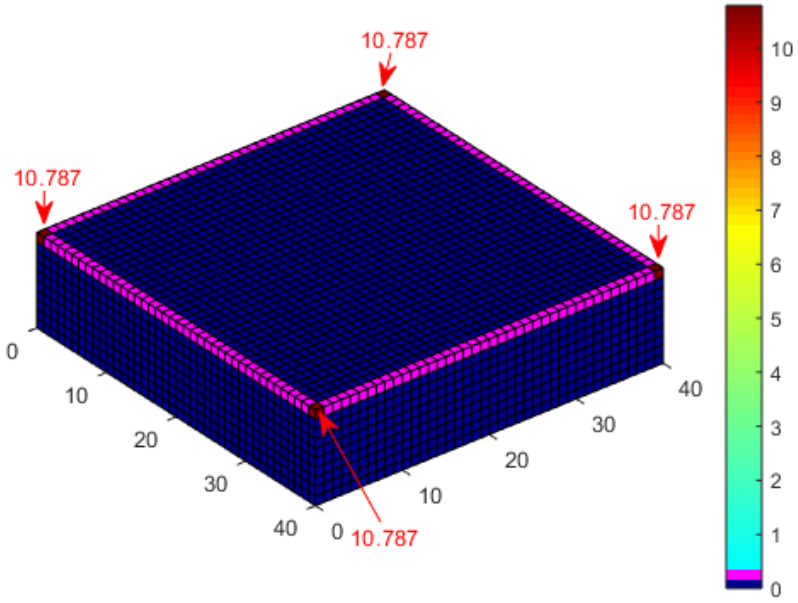

Figure 3.20. A cuboid and strike probability

The summary of the result is presented in Table 3.1. For the cuboid structure using K_{P2C}, there is an improvement in the accuracy of the corner strikes to 10.79% (1663.2 m^2) for the case without ground, and this result is close to the published result of 10.77% (1669.51 m^2) using an analytical method [156]. For the cuboid case with a central air termination of 10 m in height, the strike probability of 60.99% is very close to the published result of 61.49% [163]. In Table 3.1, the results from model C are preferred in terms of accuracy.

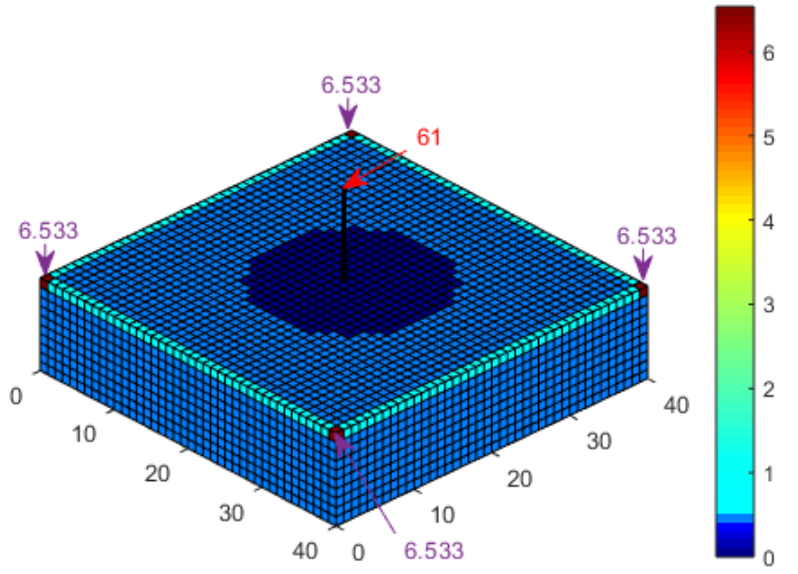

Figure 3.21. A cuboid with an air terminal and strike probability

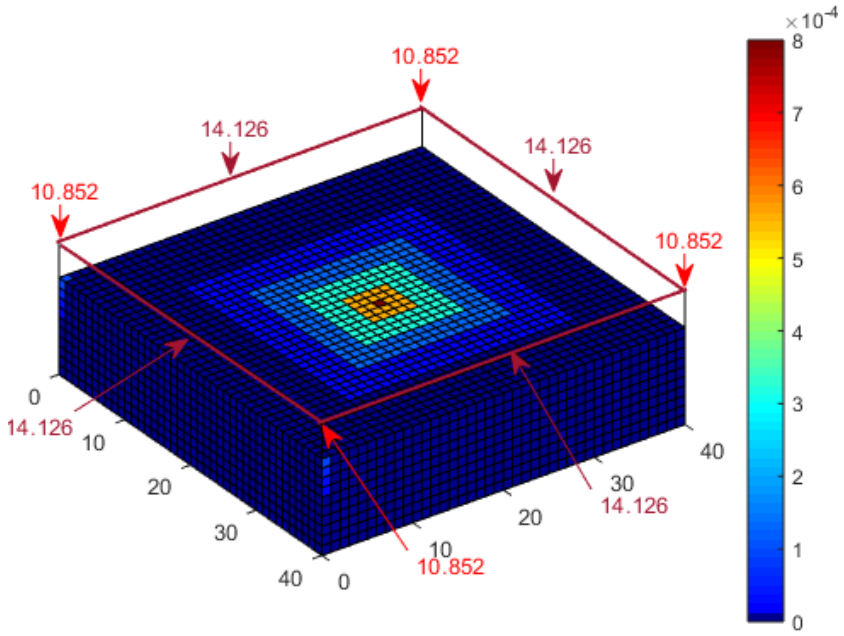

Figure 3.22. A cuboid with catenary wires and strike probability

A further comparison of the result for the cuboid case with published results is presented in Table 3.2. The IDEGM using K_{P2C} shows consistency with existing results, and the major advantage of this improvement is the reduced computation time, as shown in Table 3.3.

Using a confined collection of space points that enabled the removal of the ground surface points, the simulation time was reduced drastically without losing accuracy. The case for the catenary wires showed a strike percentage of 12.045% for the wire corners when the ground was included and 10.852% without the ground (Figure 3.22). This is because the catenary wires above the roof enable it to intercept more strikes outside the collection volume of the structure, and these external strikes do not exist when the analysis was computed using only the actual collection volume of the cuboid, i.e., for the case without ground. However, the total interception efficiency of the catenary wire system is 99.92% and 99.91%, respectively.

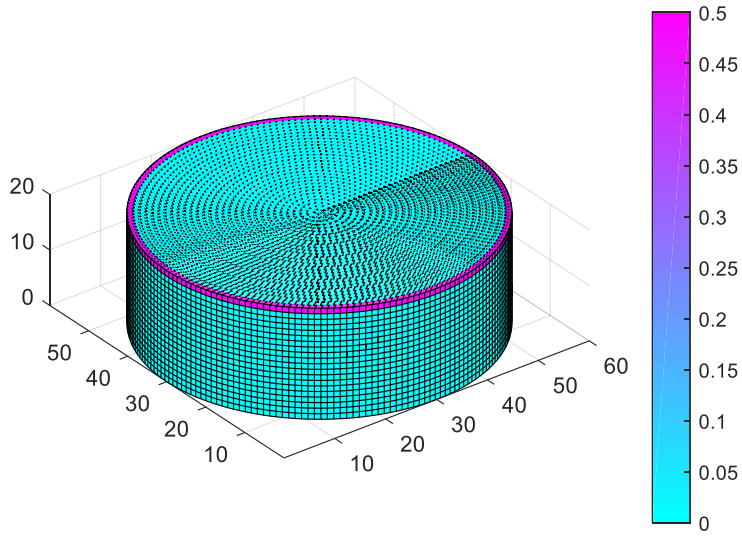

Figure 3.23. A FRT with colour-coded strike probabilities

Table 3.1. A comparison of the results and strike probabilities obtained for the different space point definitions for a cuboid and FRT

	Model A - Linearly increasing space point with ground points (%)	**Model B - Collection volume with ground points and K_{P2C} (%)**	**Model C - Collection volume without ground and with K_{P2C} (%)**
	Cuboid		
Corner strikes	11.232	10.918	10.79
	Cuboid and central air terminal		
Corner strikes	6.316	6.453	6.533
Air terminal strikes	63.607	61.215	60.999
	Cuboid and catenary wires		
Catenary wire corner strikes	12.379	12.045	10.852
Catenary wire length strikes	12.609	12.935	14.126
Total for the catenary wire	99.95	99.92	99.91
	Floating Roof Tank (FRT)		
Rim edge strikes	90.152	90.305	90.586
Roof strikes	9.803	9.651	9.362
Cylindrical wall strikes	0.044	0.044	0.052

For both cases, there is a redistribution in the percentages. The computation is also illustrated in Figure 3.24 for a FRT with lightning protection masts around it. The collection volume of the masts is bigger than that of the protected tank.

Table 3.2. A comparison of the result for the cuboid case

	Model A	Model B	Model C	Hannig et al. [156]	Kern et al. [155]
PMCV (m^2)	1814.3	1698.3	1663.2	1669.51	—
PMCV (%)	11.232	10.918	10.787	10.774	11.52

Table 3.3. A comparison of the simulation time

	Cuboid	**Cuboid and central air terminal**	**Cuboid and catenary wires**	**FRT**
Linearly increasing space point layers (h)	86.8	114.7	115.62	113.28
Collection volume with ground (h)	14	13.7	13.51	27.38
Collection volume without ground (min)	5.75	5.64	5.9	28.8

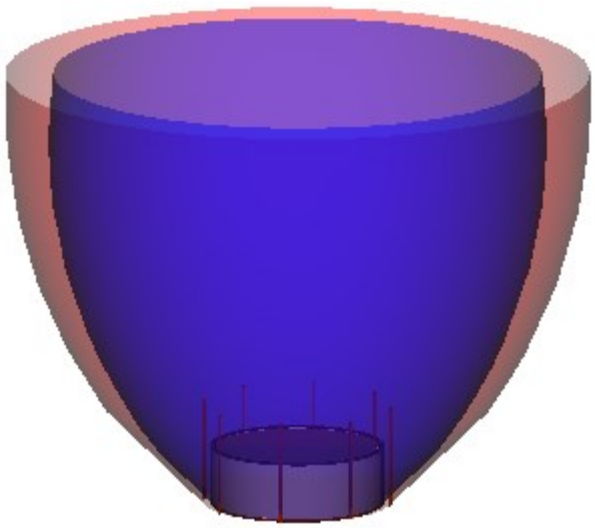

Figure 3.24. The collection volume of a FRT versus that of the masts around it

3.1.4 Analytical DEGM for FRT

The DEGM requires developing a probability modulated collection volume for the structure being analysed, and this can be achieved using a numerical or an analytical approach. The difference between the numerical and the analytical DEGM is illustrated in Figure 3.25, which shows a surface point that is exposed to a discretised space point volume and strikes to the surface point are considered per space point, and this is the numerical approach. For the analytical method, as illustrated in Figure 3.26, the space point volume is analysed as a composite volume using a geometrical equation to define the volume.

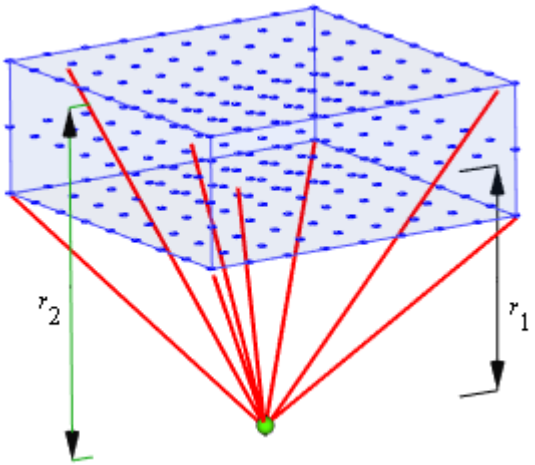

Figure 3.25. A surface point exposed to a discretised or continuous space point volume

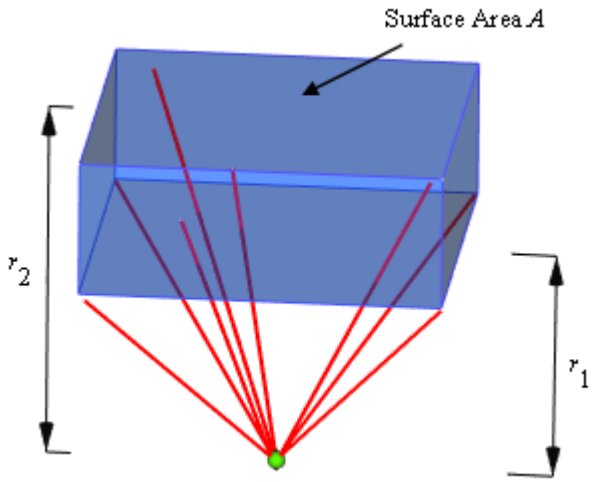

Figure 3.26. A surface point exposed to a composite space point volume

The numerical and analytical DEGM implementations can be further distinguished with simplified equations, as displayed in equations 3.21 and 3.22, to show the difference between the methods. The analytical approach implements the integration for the collection volume, while the numerical approach performs the integration for discretized elements in the volume and then sums everything.

$$Analytical = \int_{r1}^{r2} PDF(r)\ A(r)\, dr \tag{3.21}$$

$$Numerical = \sum_{1}^{n} \int_{r_1}^{r_2} PDF(r_n)\ dr \tag{3.22}$$

3.1.4.2 The application of analytical DEGM to a FRT

The surface of the FRT will be divided into three that is the rim, the roof and the cylindrical wall. Each of these parts has a unique lightning collection volume that must be separately analysed when the roof is at the top and when it has descended into the tank.

For the novel analysis, the tank has a radius of *R* in m with a height of *h* in m. The lightning striking distance *r* is also in m. For the first case, the roof of the FRT is positioned at the top.

A) The cylindrical sidewall of the FRT

For the cylindrical sidewall of the FRT, the collection volume extends laterally at any height *h,* as illustrated in Figure 3.27. For the sidewall, to compute the probability modulated collection volume, the idea of a unit sectional collection area (A_{wall} / unit) will be introduced, and this concept is illustrated in Figure 3.28.

$$\text{Striking distance } (r) = h \tag{3.23}$$

$$\text{The horiontal radial span } (R^*) = R + r = R + h \tag{3.24}$$

A unit angular span in radians is defined for an arc of length 1 m on the circumference of the FRT.

$$\theta_{unit} = \frac{2\pi}{2\pi R} = \frac{1}{R} \tag{3.25}$$

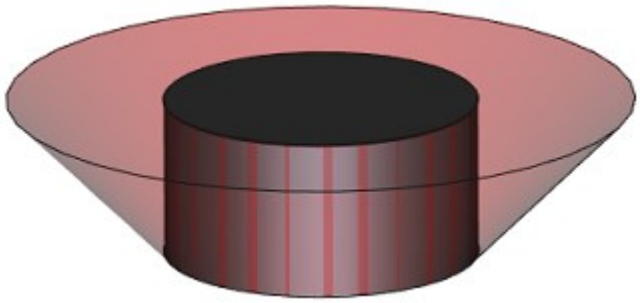

Figure 3.27. The symmetrical collection volume around the FRT's sidewall

$$\text{The radial arc area } A(r) = \frac{R^*}{R} = 1 + \frac{r}{R} \tag{3.26}$$

For a point at a height (h), the corresponding PMCV for a unit sectional area on the wall is

$$\mathrm{A}_{\mathrm{wall}} = \int_{r=0}^{r=h} PDF(r) \cdot \left(1 + \frac{r}{R}\right) dr. \tag{3.27}$$

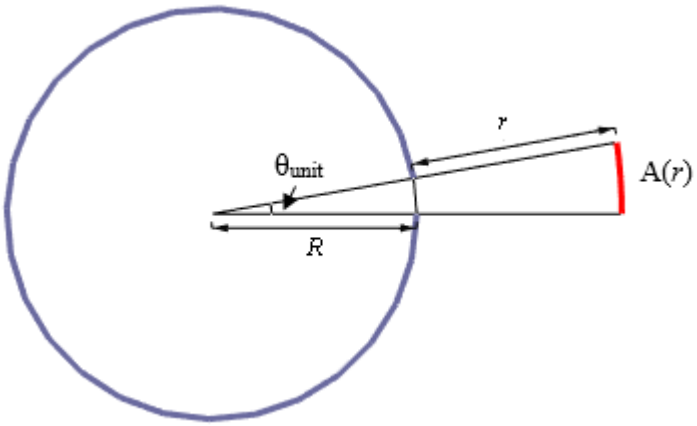

Figure 3.28. A unit sectional side flash area on the tank wall

Considering a lateral vertical unit from the bottom of the tank to h,

$$\mathrm{PMCV}_{\mathrm{wall}} / \text{unit} = \sum_{r=0}^{r=h} \int_{r=0}^{r=h} PDF(r) \cdot \left(1 + \frac{r}{R}\right) dr \tag{3.28}$$

The PMCV in m^2 for the cylindrical wall up to h is:

$$\mathrm{PMCV}_{\mathrm{wall}} = 2\pi R \times \mathrm{PMCV}_{\mathrm{wall}} / \text{unit} = 2\pi R \sum_{r=0}^{r=h} \int_{r=0}^{r=h} PDF(r) \cdot \left(1 + \frac{r}{R}\right) dr \tag{3.29}$$

B) The rim edge of the FRT

For the rim edge of the FRT, the collection volume is based on the depiction in Figure 3.29. From the rim edge, the horizontal span of the volume increases upwards. For a 1 m arc on the rim edge, a unit sectional area with a collection volume is generated as illustrated in Figure 3.30 with a horizontal angular span of θ_1 and a vertical angular spread of θ_2. Both angles are in radians. The curve's surface area expands with increasing height into the sky. The integral equation required to compute this is quite complex to solve, and as such, a simplification is required, and this is achieved by flattening the curved surface layer, as illustrated in Figure 3.31.

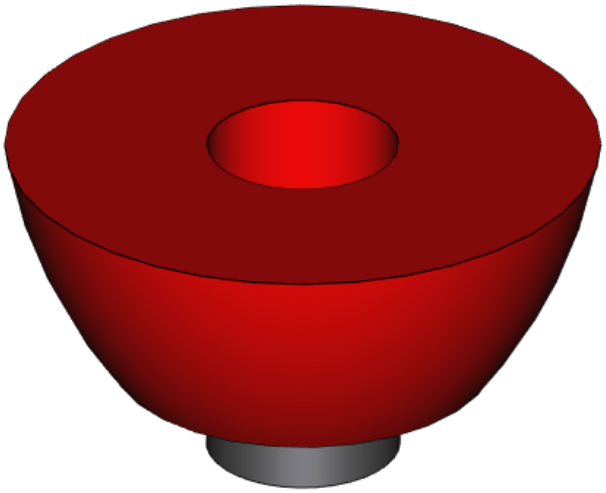

Figure 3.29. The FRT's rim edge lightning collection volume

$$\theta_1 = \theta_{unit} = \frac{2\pi}{2\pi R} = \frac{1}{R} \tag{3.30}$$

$$\theta_2 = \cos^{-1}\left(1 - \frac{h}{r}\right) \tag{3.31}$$

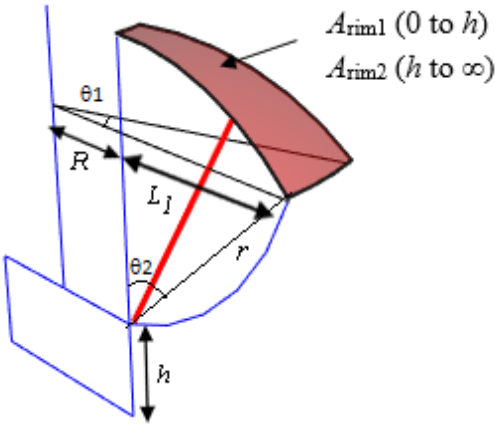

Figure 3.30. The collection surface of the rim edge per unit sectional area

For the rim edge, the computation is in two parts. The first part is computed starting from the rim edge itself up to the tank's height h above the rim, and the second part is from h above the rim to infinity in the sky. For the flattened surface, there are two chords or border

lengths in m. One touches the FRT's shell while the second border is at the opposite end. For the first part, the analysis is developed as follows with striking distance r increasing from 0 to h above the rim:

$$BorderA = 2R\sin\left(\frac{1}{2R}\right) \tag{3.32}$$

$$BorderB = 2(r+R)\cdot\sin\left(\frac{1}{2R}\right) \tag{3.33}$$

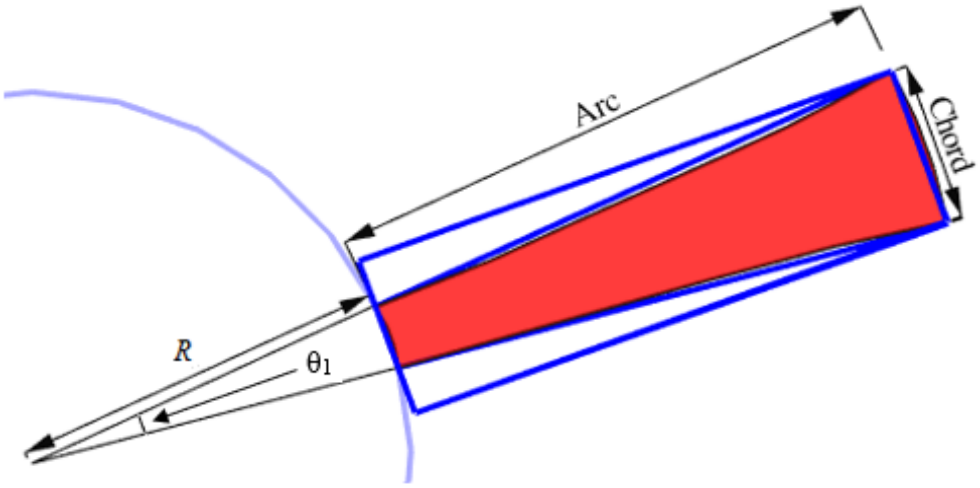

Figure 3.31. The corresponding flattened collection area for a span θ_1 along the rim

The length of the flattened arc in m is defined as

$$ArcA = \frac{\pi r}{2}. \tag{3.34}$$

The horizontal length of this section in m can be obtained as follows:

$$LengthA = ArcA \times \cos\left(\frac{1}{R}\right) \tag{3.35}$$

The flattened model is a simplification of the curved surface for integration. A relationship between the simplified model and the actual surface as implemented in FreeCAD was determined. This is illustrated in Figure 3.32, and a correction factor of 0.725 is required as applied in equation 3.36 to correct the effect of the flattened surface approximation of the actual curved surface. A comparison of the results for striking distance $r = 0$ to h for sample striking distance values of 10 m and 20 m for a FRT of height 20 m and four different diameters are presented in Table 3.4. These results confirm the accuracy of the simplified model.

$$A_{\text{rim1}} = \left(LengthA \times BorderB\right) - \left(\frac{BorderB - BorderA}{2} \times 0.725 \times LengthA\right) \tag{3.36}$$

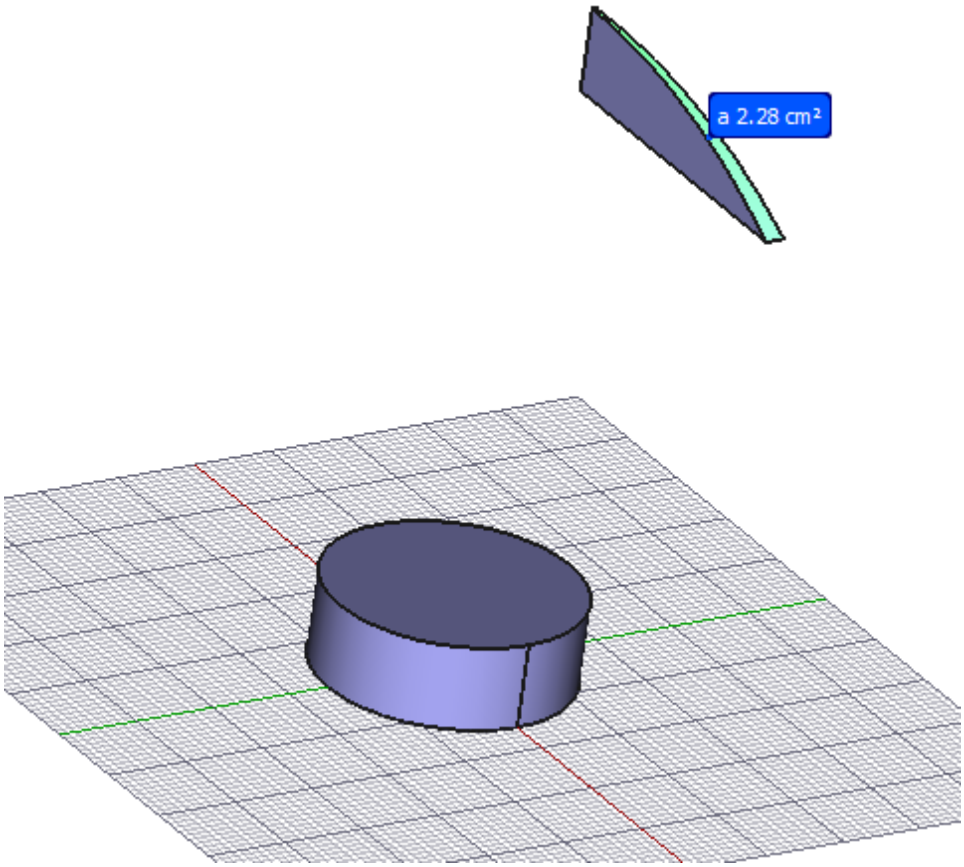

Figure 3.32. FreeCAD model of the curved surface area

For $r = 0$ to h above the cylindrical rim, the PMCV for a unit sectional area in m^2 is

$$\text{PMCV}_{\text{rim}} \text{ / unit} \Big|_{0 \text{ to } h} = \int_{r=0}^{r=h} PDF(r) \cdot A_{\text{rim1}} \, dr. \tag{3.37}$$

For the whole cylindrical rim, the PMCV for $r = 0$ to h in m^2 is

$$\text{PMCV}_{\text{rim}} \Big|_{0 \text{ to } h} = 2\pi R \times \text{PMCV}_{\text{rim}} \text{ / unit} \Big|_{0 \text{ to } h} = 2\pi R \int_{r=0}^{r=h} PDF(r) \cdot A_{\text{rim1}} \, dr \tag{3.38}$$

Table 3.4. Comparison of the areas A_{rim1} and A_{rim2} from FreeCAD and the simplified model in m^2

	Striking Distance									
	10 m		20 m		50 m		150 m		300 m	
Radius	**CAD**	**Model**	**CAD**	**Model**	**CAD**	**Model**	**CAD**	**Model**	**CAD**	**Model**
20 m	20.71	20.69	51.42	51.37	96.36	98.11	228.00	228.21	410.00	406.68
30 m	19.04	19.03	44.75	44.74	79.70	80.92	178.00	178.42	310.00	308.16
40 m	18.21	18.21	41.42	41.42	71.36	72.30	153.00	153.45	260.00	258.75
50 m	17.71	17.71	39.42	39.42	66.36	67.12	138.00	138.45	230.00	229.07

For $r = h$ to ∞ above the rim, the computation will also be initiated from the basics. For this case, the chord length BorderB will be reformulated as BorderC in m.

$$BorderC = 2(L_1 + R)\cdot \sin\left(\frac{1}{2R}\right) \tag{3.39}$$

$$ArcB = r\,\theta_2 \tag{3.40}$$

The length of the rectangular section in m is defined as

$$LengthB = ArcB \times \cos\left(\frac{1}{R}\right) \tag{3.41}$$

For $r = h$ to ∞, a correction factor of 1.02 will be applied as shown in equation 3.42 based on results from FreeCAD. The comparison of the results in m^2 for this simplified model with FreeCAD computation is presented in Table 3.4 for r = 50 m,150 m, and 300 m.

$$A_{\text{rim2}} = \left(LengthB \times BorderC\right) - \left(\frac{BorderC - BorderA}{2} \times 1.02 \times L_1\right) \tag{3.42}$$

For $r = h$ to ∞ above the cylindrical rim, the PMCV in m^2 for a unit sectional area is

$$\text{PMCV}_{\text{rim}} \text{ / unit} \Big|_{h \text{ to } \infty} = \int_{r=h}^{r=\infty} PDF(r)\cdot A_{\text{rim2}}\, dr \tag{3.43}$$

For the whole cylindrical rim, the PMCV for $r = h$ to ∞ in m^2 is

$$\text{PMCV}_{\text{rim}} \Big|_{h \text{ to } \infty} = 2\pi R \times \text{PMCV}_{\text{rim}} \text{ / unit} \Big|_{h \text{ to } \infty} = 2\pi R \int_{r=h}^{r=\infty} PDF(r)\cdot A_{\text{rim2}}\, dr \tag{3.44}$$

For r = 0 to ∞ the PMCV in m^2 for a unit sectional area is defined as

$$\text{PMCV}_{\text{rim}} \text{ / unit} = \text{PMCV}_{\text{rim}} \text{ / unit} \Big|_{0\ to\ h} + \text{PMCV}_{\text{rim}} \text{ / unit} \Big|_{h\ to\ \infty} \tag{3.45}$$

For r = 0 to ∞, the PMCV for the whole cylindrical rim in m^2 is defined as

$$\text{PMCV}_{\text{rim}} = \text{PMCV}_{\text{rim}} \Big|_{0 \text{ to } h} + \text{PMCV}_{\text{rim}} \Big|_{h \text{ to } \infty} \tag{3.46}$$

C) The floating roof

For the roof of a FRT, the collection volume is cylindrical, as shown in Figure 3.33, and it extends upwards from the roof up to infinity.

For a 1 m^2 area on the surface of the roof when the roof is at the top of the tank, the PMCV per unit area in m^2 is defined as:

$$\text{PMCV}_{\text{roof}} \text{ / unit} \Big| = \int_{r=0}^{r=\infty} PDF(r)\, dr \tag{3.47}$$

For the whole surface of the roof, the PMCV in m^2 is defined as:

$$\text{PMCV}_{\text{roof}} = \pi R^2 \int_{r=0}^{r=\infty} PDF(r)\, dr \tag{3.48}$$

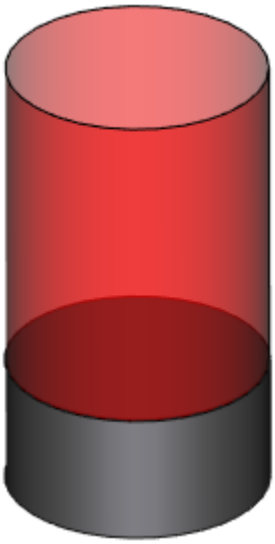

Figure 3.33. The lightning collection volume for when the roof of the tank is at the top

3.1.4.3 Analytical DEGM computation when the FRT's roof is lowered

Before lightning strikes, pre-strike charges accumulate on the FRT, especially on the roof and nearby grounds. According to Dodd [164], the charges accumulate on the external surface of the tank shell and none within the tank itself because electrical charges are self-repellent. This is similar to the Faraday cage effect using solid or mesh-type cages. The discharge of these charges, even when there is no direct strike to the tank, can result in electrostatic sparks.

When the roof of a FRT is lowered within the tank, as illustrated in Figure 3.34, a space volume is created above the roof, up to the rim of the tank. The top rim of the FRT's shell creates a zone of protection both internally and externally for the lower parts of the tank shell, as illustrated in Figure 3.35. Since lightning descends from above, strikes descending within the internal tank area toward the lowered roof of the FRT must pass through the collection reach of the top rim or head directly for the roof. If the Faraday cage effect proposition by Dodd [164] is valid, and there are no charges within the internal surface of the tank's shell, then an upward streamer cannot be formed, and as such, no strike can terminate on the internal surface of the tank shell. Strikes above the roof that are not intercepted by the rim edge will ultimately hit the tank roof. This may explain why reported cases of lightning strikes are always to the rim or the roof of the FRT.

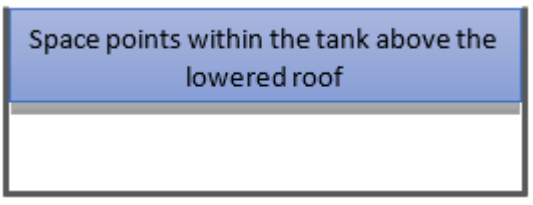

Figure 3.34. A FRT with lowered roof

Excluding this space volume above the roof in DEGM simulations for FRTs with a lowered roof is a demonstration of the expected practical realities that the critical lightning orientation volumes are those outside the FRT, both above and beside it. Also, strikes from this space are of currents that are ≤ 3 kA with no significant fire risk. The DEGM results consider the cases when the space above the roof is ignored and when it is added to the total collective volume of the FRT for lowered roof cases.

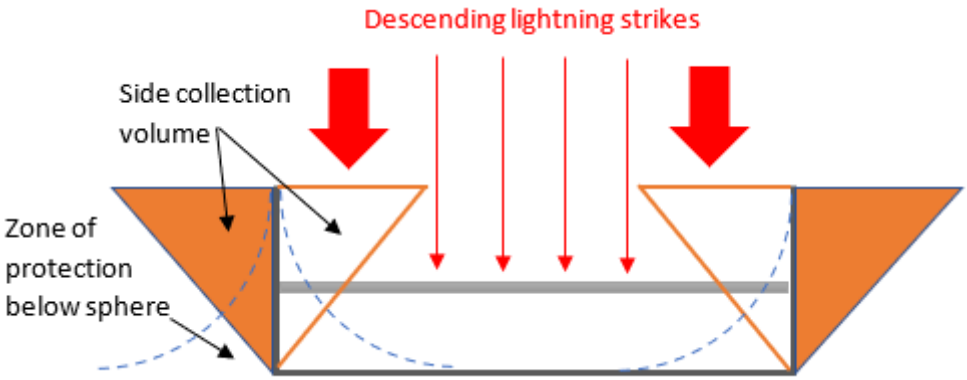

Figure 3.35. Potential lightning strikes to a lowered FRT's roof

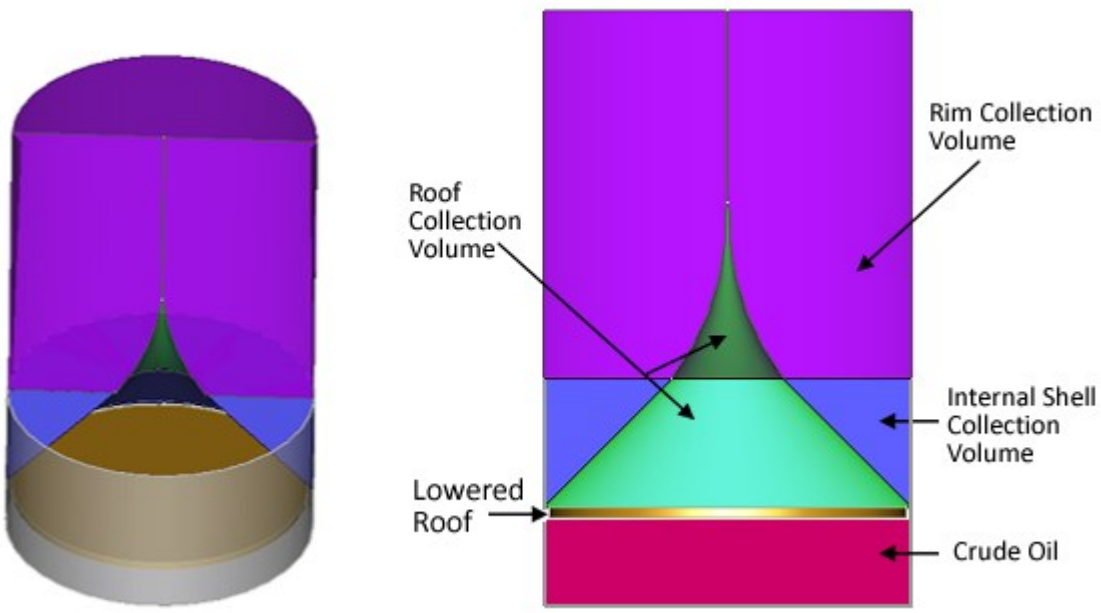

Figure 3.36. The division of the collection surface above a lowered roof into three parts

When the floating roof is lowered from its apex height to a height h_{Int} below the rim, the collection volume above the roof changes, and it becomes segmented into three parts, as shown in Figure 3.36. The collection volume for the roof significantly reduces, while additional volumes are created for the rim and internal side flashes for the tank shell, which must be added to the values calculated for the rim and cylindrical wall when the roof is at the top. The effective striking distance for the internal strike due to the lowered roof is r_{int}.

The following analysis is due to the sectional volumes created above the lowered roof.

A) The FRT's sidewall with the roof lowered (RFL)

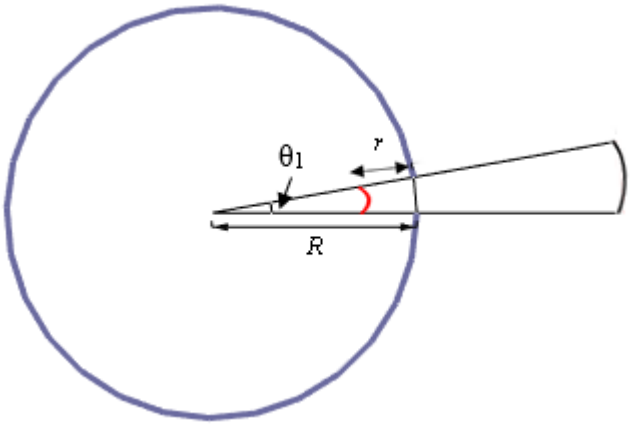

Figure 3.37. A unit sectional area of the tank wall with span θ_1 due to the lowered roof

$$\text{Effective radial span for the internal volume } R^* = R - h_{\text{Int}} = R - r_{\text{Int}} \tag{3.49}$$

The PMCV for a unit sectional area on the tank shown in Figure 3.37 can be obtained for a given height h as follows:

$$\text{A}_{\text{wall\_RFL}} = \int_{r=0}^{r=h} PDF(r)\cdot\left(1+\frac{r}{R}\right)dr + \int_{r=0|from\ h-h_{\text{Int}}}^{r=h_{\text{Int}}} PDF(r)\cdot\left(1-\frac{r_{\text{Int}}}{R}\right)dr \tag{3.50}$$

Considering the lateral sectional unit vertically from the ground to the reference height,

$$\begin{aligned}\text{PMCV}_{\text{wall\_RFL}}\ /\ \text{unit} = &\sum_{r=0}^{r=h}\ \int_{r=0}^{r=h} PDF(r)\cdot\left(1+\frac{r}{R}\right)dr + \\ &\sum_{r=0|from\ h-h_{\text{Int}}}^{r=h_{\text{Int}}}\ \int_{r=0|from\ h-h_{\text{Int}}}^{r=h_{\text{Int}}} PDF(r)\cdot\left(1-\frac{r_{\text{Int}}}{R}\right)dr.\end{aligned} \tag{3.51}$$

The total PMCV in m^2 for the cylindrical wall up to h is:

$$\begin{aligned}\text{PMCV}_{\text{wall\_RFL}} = 2\pi R\times\text{PMCV}_{\text{wall}}\ /\ \text{unit} = &\ 2\pi R\sum_{r=0}^{r=h}\int_{r=0}^{r=h} PDF(r)\cdot\left(1+\frac{r}{R}\right)dr + \\ &2\pi R\sum_{r=0|from\ h-h_{Int}}^{r=h_{\text{Int}}}\ \int_{r=0|from\ h-h_{Int}}^{r=h_{\text{Int}}} PDF(r)\cdot\left(1-\frac{r_{\text{Int}}}{R}\right)dr\end{aligned} \tag{3.52}$$

B) The FRT's rim edge with the roof lowered

The following analysis is for a striking distance $r_{\text{Int}} = 0$ to h_{Int} in m above the rim edge. The curved surface in Figure 3.38 has two border lengths, with one touching the tank's wall and the other at the interior end of the collection surface. This concept is shown in Figure 3.39 with the flattened equivalent of the curved surface. This analysis is for strikes to the rim due to collection layers vertically above the roof region, i.e., within the horizontal span L_2. These are internal (above the roof) strikes to the rim.

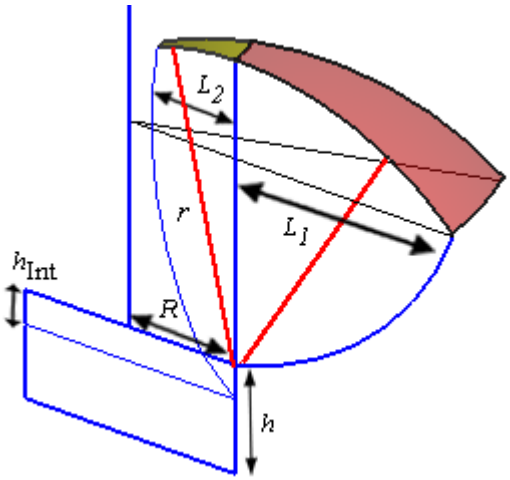

Figure 3.38. The collection surface of the rim edge per unit sectional area when the roof is lowered

$$BorderA = 2R\sin\left(\frac{1}{2R}\right) \tag{3.53}$$

$$BorderD = 2(R - r_{Int})\cdot\sin\left(\frac{1}{2R}\right) \tag{3.54}$$

The length of the flattened arc in m is defined as:

$$ArcD = \frac{\pi r_{Int}}{2} \tag{3.55}$$

For the rectangular section, the horizontal length *LengthD* in m can be obtained using equation 3.56:

$$LengthD = ArcD \times \cos\left(\frac{1}{R}\right) \tag{3.56}$$

$$A_{rim3} = \left(LengthD \times BorderA\right) - \left(\frac{BorderA - BorderD}{2} \times 0.725 \times LengthD\right) \tag{3.57}$$

For $r = 0$ to h_{Int} above the roof, the PMCV in m^2 per unit sectional area of the rim edge is

$$\text{PMCV}_{rim\_Int} \text{ / unit} \Big|_{0 \text{ to } h_{Int}} = \int_{r=0}^{r=h_{Int}} PDF(r)\cdot A_{rim3}\, dr \tag{3.58}$$

The total PMCV in m^2 for the rim edge up to height (h_{Int}) above the roof is:

$$\text{PMCV}_{rim\_Int}\Big|_{0 \text{ to } h_{Int}} = 2\pi R \times \text{PMCV}_{rim\_Int} \text{ / unit}\Big|_{0 \text{ to } h_{Int}} = 2\pi R \times \int_{r=0}^{r=h_{Int}} PDF(r)\cdot A_{rim3}\, dr \tag{3.59}$$

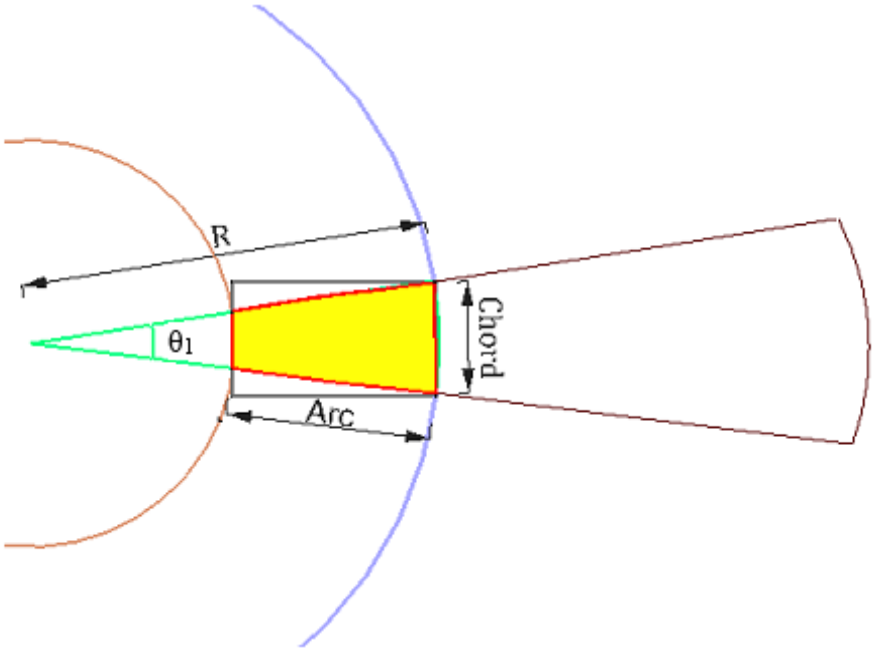

Figure 3.39. The Flattened equivalent of the collection surface area of the rim edge per unit sectional area of span θ_1 when the roof is lowered

The horizontal span of the internal collection volume for the rim will reach the centre of the FRT at a striking distance value of r_{centre}.

For $r < r_{centre}$, θ_2 is as defined in equation 3.61, while for $r \geq r_{centre}$, equation 3.62 applies.

$$r_{centre} \text{ is the value of } r \text{ for which } \sqrt{2rh_{Int} - h_{Int}^{\ 2}} = R \tag{3.60}$$

$$\theta_2 = \cos^{-1}\left(1 - \frac{h_{Int}}{r}\right) \tag{3.61}$$

$$\theta_2 = \sin^{-1}\left(\frac{R}{r}\right) \tag{3.62}$$

The following analysis considers the striking distance r from h_{Int} to infinity above the rim. The length BorderD of the chord in m is defined as BorderE in this instance.

$$BorderE = 2(R - L_2) \cdot \sin\left(\frac{1}{2R}\right) \tag{3.63}$$

The length of the flattened arc in m can be obtained from equation 3.64.

$$ArcE = r_{Int}\,\theta_2 \tag{3.64}$$

The horizontal length of the section in m can be obtained using:

$$LengthE = ArcE \times \cos\left(\frac{1}{R}\right) \tag{3.65}$$

$$A_{rim4} = \left(LengthE \times BorderA\right) - \left(\frac{BorderA - BorderE}{2} \times 1.02 \times L_2\right) \tag{3.66}$$

For $r = h_{\text{Int}}$ to ∞ above the roof, the PMCV per unit sectional area of the tank's rim is

$$\text{PMCV}_{\text{rim\_Int}} \text{ / unit} \Big|_{h_{\text{Int}} \text{ to } \infty} = \int_{r=h_{\text{Int}}}^{r=\infty} PDF(r) \cdot A_{\text{rim4}}\, dr \tag{3.67}$$

Considering a unit sectional area of the rim edge, the PMCV in m^2 from $r = 0$ to ∞ due to strikes vertically above the roof is:

$$\text{PMCV}_{\text{rim\_Int}} \text{ / unit} = \text{PMCV}_{\text{rim\_Int}} \text{ / unit} \Big|_{0 \text{ to } h_{\text{Int}}} + \text{PMCV}_{\text{rim\_Int}} \text{ / unit} \Big|_{h_{\text{Int}} \text{ to } \infty} \tag{3.68}$$

For the whole cylindrical rim, the PMCV in m^2 for $r = h_{\text{Int}}$ to ∞ due to strikes vertically above the roof is defined as follows:

$$\text{PMCV}_{\text{rim\_Int}} \Big|_{h_{\text{Int}} \text{ to } \infty} = 2\pi R \times \text{PMCV}_{\text{rim\_Int}} \text{ / unit} \Big|_{h_{\text{Int}} \text{ to } \infty} = 2\pi R \int_{r=h_{\text{Int}}}^{r=\infty} PDF(r) \cdot A_{\text{rim4}}\, dr \tag{3.69}$$

For the whole cylindrical rim, the total PMCV in m^2 for $r = 0$ to ∞ due to strikes vertically above the roof is:

$$\text{PMCV}_{\text{rim\_Int}} = \text{PMCV}_{\text{rim\_Int}} \Big|_{0 \text{ to } h_{\text{Int}}} + \text{PMCV}_{\text{rim\_Int}} \Big|_{h_{\text{Int}} \text{ to } \infty} \tag{3.70}$$

The total strike to the rim when the roof is lowered is the sum of strikes due to the collection layers external to the FRT (i.e., rim analysis when the roof is at the top) and those vertically above the roof region when the roof is lowered, i.e., within the horizontal span L_2.

The total PMCV for the FRT's rim edge for $r = 0$ to ∞ when the roof is lowered is the sum of equations 3.46 and 3.70.

$$\text{PMCV}_{\text{rim\_RFL}} = \text{PMCV}_{\text{rim}} + \text{PMCV}_{\text{rim\_Int}} \tag{3.71}$$

C) The FRT's roof with the roof lowered

This section analyses the curved conical shape of the collection volume above the roof when the roof is lowered. This area extends from the surface of the floating roof (i.e., 0 m) at the roof edge up to the point of highest exposure at the centre, as illustrated in Figure 3.40.

The maximum vertical striking distance r_{max} for any point on the roof is a function of the radial length R_{len} of that point from the edge of the roof. The equivalent PMCV for a unit sectional area of the roof for radial points from the edge of the roof up to h_{Int} in length (i.e., $R_{\text{len}} = 0$ to h_{Int}) is:

$$PMCV_{\text{len}} = \int_{r=0}^{r=R_{len}} PDF(r)\, dr \tag{3.72}$$

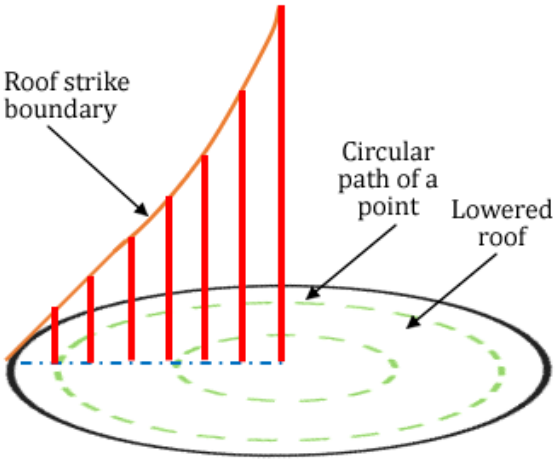

Figure 3.40. The strike boundary above the roof when the roof is lowered

The equivalent PMCV in m^2 for the full circumferential path along R_{len} is:

$$\text{PMCV}_{\text{circa}} = 2\pi(R - R_{\text{len}}) \int_{r=0}^{r=R_{len}} PDF(r)\, dr \tag{3.73}$$

The equivalent PMCV for a unit sectional area of the roof for radial points that are longer than h_{Int} in length (i.e., $R_{\text{len}} > h_{\text{Int}}$) is obtained as follows:

$$r_{\max} = \frac{R_{\text{len}}{}^2 + h_{\text{Int}}{}^2}{2 \times h_{\text{Int}}} \tag{3.74}$$

$$\text{PMCV}_{\text{len}} = \int_{r=0}^{r=r_{\max}} PDF(r)\, dr \tag{3.75}$$

The equivalent collection area in m^2 for the full circumferential path along R_{len} is:

$$\text{PMCV}_{\text{circa}} = 2\pi(R - R_{\text{len}}) \int_{r=0}^{r=r_{\max}} PDF(r)\, dr \tag{3.76}$$

The total PMCV in m^2 for the floating roof is defined as:

$$\text{PMCV}_{\text{roof\_RFL}} = \sum_{R_{len}=0}^{R_{len}=h_{\text{Int}}} 2\pi(R - R_{\text{len}}) \int_{r=0}^{r=R_{len}} PDF(r)\, dr + \sum_{R_{len}>h_{\text{Int}}}^{R_{len}=R} 2\pi(R - R_{\text{len}}) \int_{r=0}^{r=r_{\max}} PDF(r)\, dr \tag{3.77}$$

3.1.4.4 The limitations of analytical DEGM for complex structures and those with air terminations

The analytical computation of the DEGM is very fast, just like the IDEGM, and results can be obtained in a few minutes for most simulations. With this advantage, there is, unfortunately, a major challenge due to the need to accurately define the geometrical volume of each collection volume in the analysis.

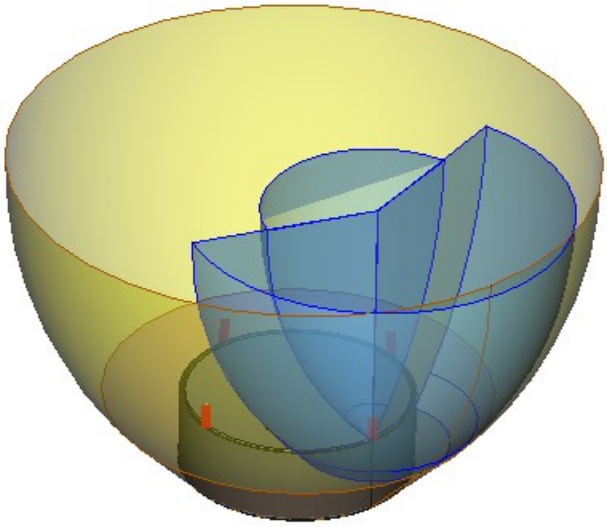

Figure 3.41. The collection volume of a FRT and for one of four air terminals

The collection volume for a simple structure may be easy to define mathematically, but it gradually becomes complex with the addition of air terminals. For example, the collection volume of the tank in Figure 3.41 is quite symmetric around the tank. Two sections emerge considering the collection volume of one air terminal on top of the rim, one above the roof and the other beside the tank. Each of these volumes must be mathematically defined even though the shapes may not necessarily be common shapes with existing equations. Also, the effective collection volume of the FRT is the symmetrical collection volume around the tank minus that of the air terminal, and this is also not easy to implement. To consider how the protection of the air terminal affects each part of the cylindrical tank is even more complex. For any section of the tank under consideration, the collection volume of the air terminal within that section must be removed geometrically. While this seems difficult, it becomes even more complex if the collection volumes of four air terminals are considered, as shown in Figure 3.42. The collection volumes of the air terminals are interwoven, forming complex shapes. A mathematical analysis of each of these sections will be a daunting task.

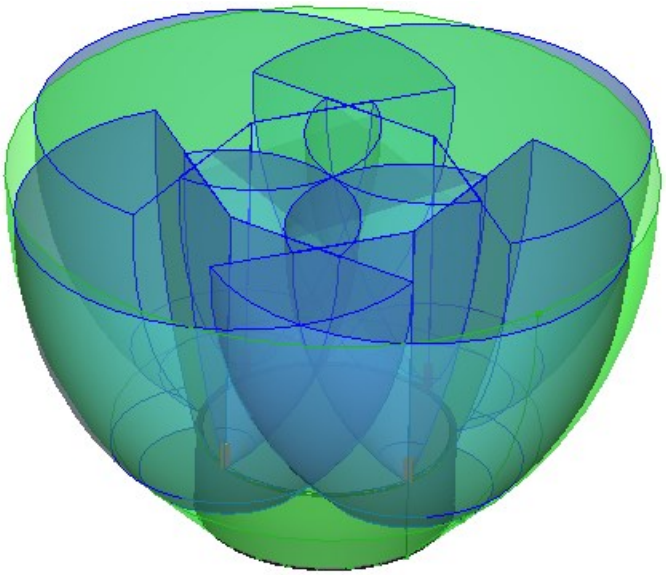

Figure 3.42. The collection volume of a FRT and four air terminals

Due to these challenging realities in the analytical computation of DEGM, the evaluation of the effects of various conventional LPS on a FRT can only be implemented using the numerical DEGM.

4 The results from numerical and analytical DEGM simulations

The exposure of the FRT component parts is influenced by the position of the floating roof within the tank. Although the roof may be at any height, three cases are considered in this simulation. For the first case, the floating roof is at the top. For the second case, the roof is in the middle position, and for the third case, the roof is at the bottom, just 0.5 m from the bottom plates. In practical operations, the roof usually will not touch the bottom of the tank where water and sediments typically accumulate. Three FRTs of height 10 m, 20 m, and 30 m were studied with seven different tank radii ranging from 20 m to 50 m.

4.1 Numerical simulation for FRT without air terminals

As shown in Figure 4.1, the likelihood of a direct strike to the FRT's rim with the roof at the top is approximately 95% for a 20 m high FRT with a radius of 20 m. The likelihood of a direct strike to the FRT's rim edge decreases as the FRT's radius increases and increases as the FRT's height increases.

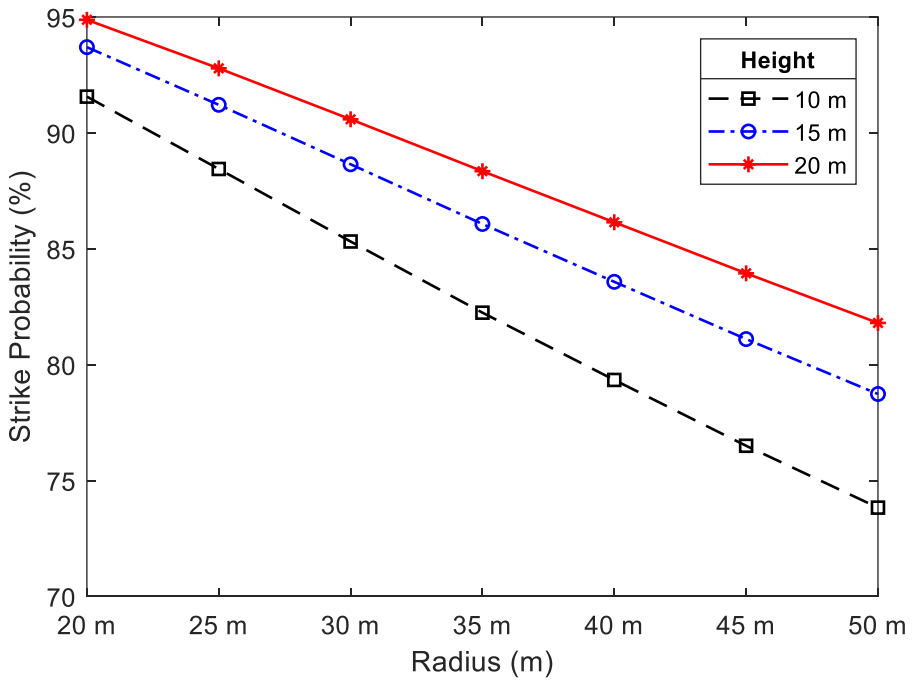

Figure 4.1. Strikes to the rim with the roof at the top

The highest likelihood of a direct strike to the roof occurs when the floating roof is at the apex position. The diagram in Figure 4.2 highlights the fact that the exposure of the roof to a direct lightning strike increases as the tank radius increases and reduces as the tank height increases. The exposure of the sidewall of a FRT increases slightly with increasing tank height, and it is relatively constant for a given tank height with increasing radius when the roof is at the top, as illustrated in Figure 4.3.

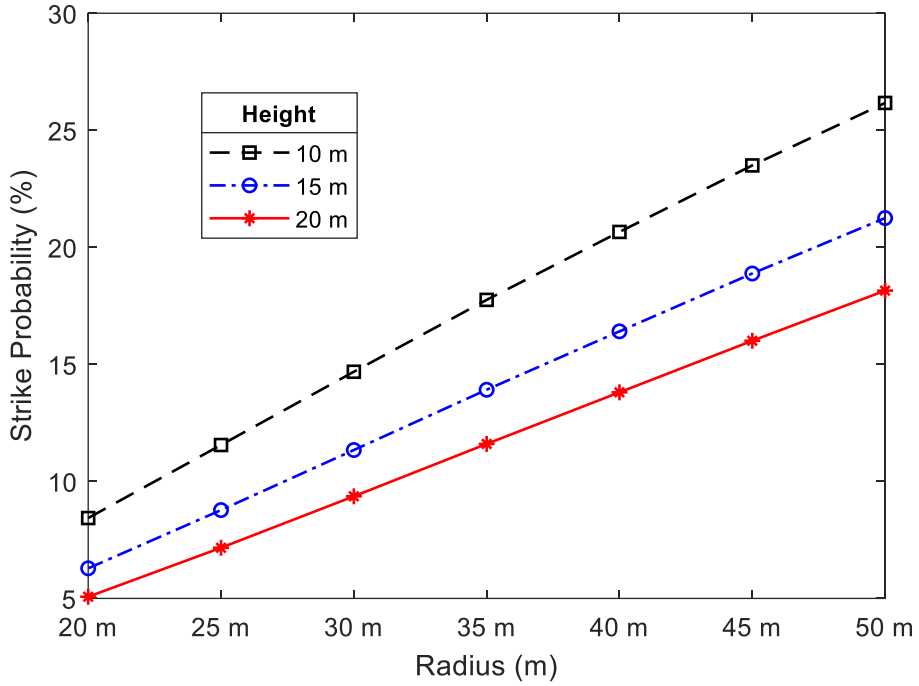

Figure 4.2. Strikes to the roof with the roof at the top

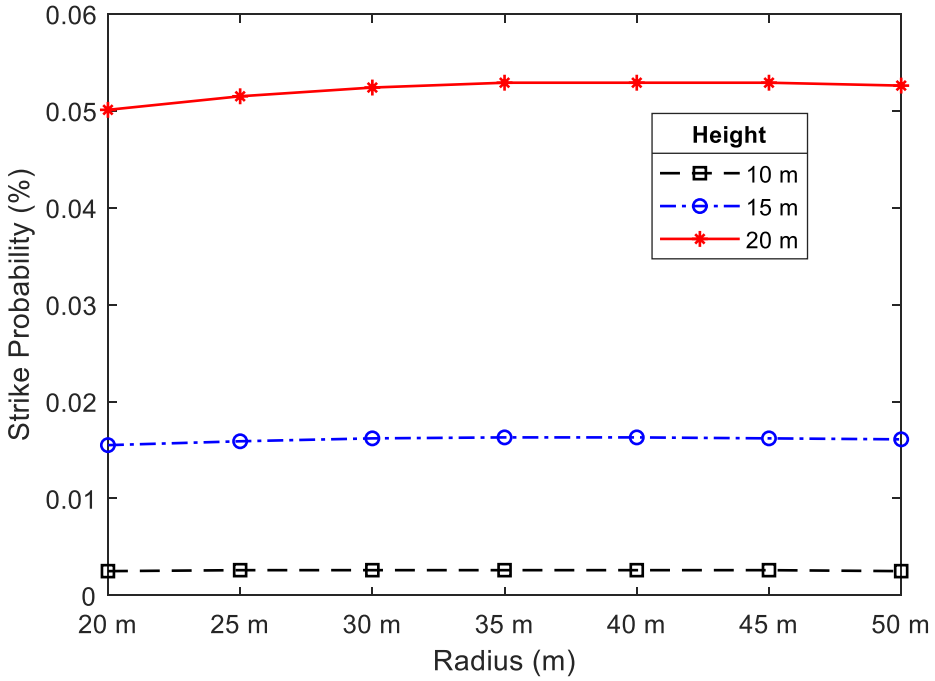

Figure 4.3. Strikes to the tank wall with the roof at the top

A summary of the case with the roof at the top is presented in Figure 4.4, which shows the probability of a lightning strike to the roof, the rim and the tank's sidewall in percentage ranges.

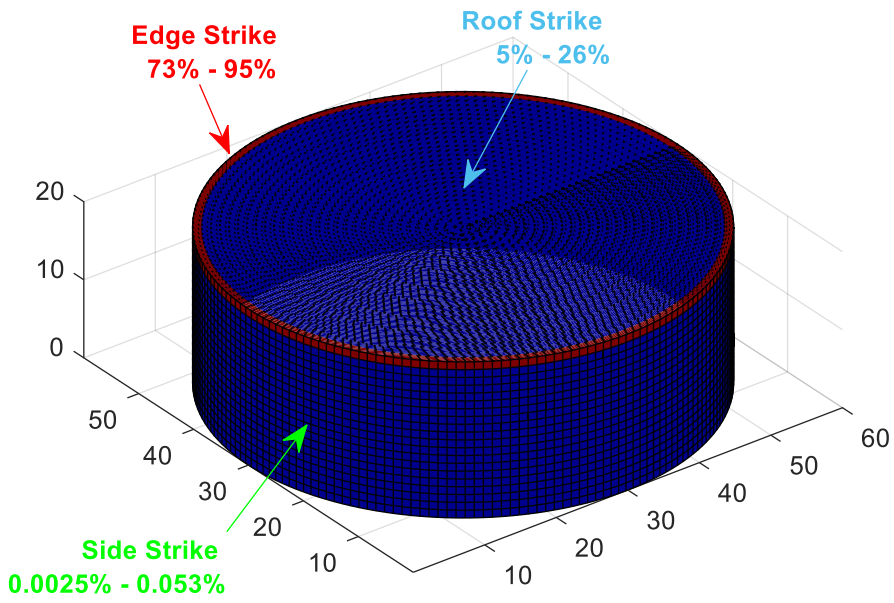

Figure 4.4. A summary of the case with the roof at the top

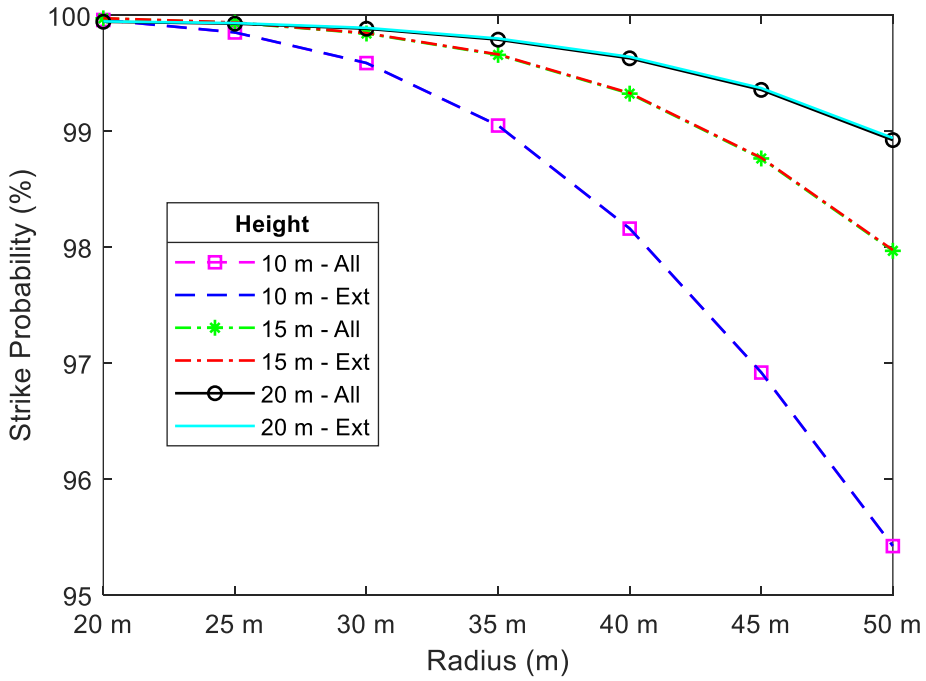

Figure 4.5. Strikes to the rim with the roof in the middle

When the roof is at the middle and bottom positions, two cases will be considered. For the first case, only the external collection volume will be considered (Ext case), while in the second case, the space above the roof but within the tank created by the lowering of the roof will also be considered as a part of the collection volume (All case). As shown in Figure 4.5, the likelihood of a direct strike to the rim area when the roof is in the middle is approximately 99% for a FRT with a radius of 20 m both for the Ext and All cases. The risk of a lightning strike to the FRT's rim area reduces as the tank radius increases, and it increases with increasing tank height. There is no significant difference between the Ext and All cases for the radii values analysed.

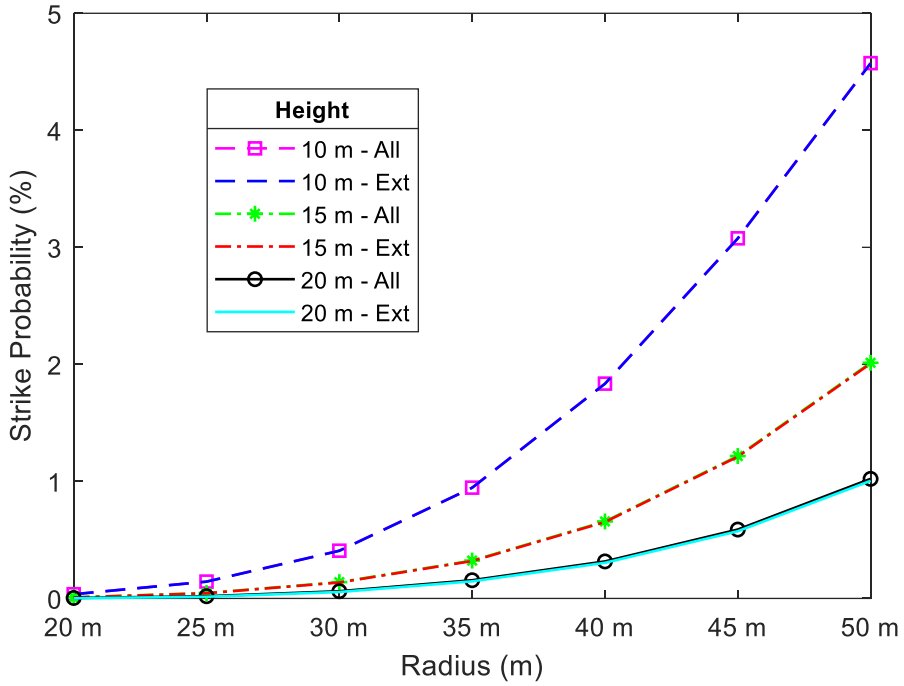

Figure 4.6. Strikes to the roof with the roof in the middle

The chart in Figure 4.6 shows that the exposure of the roof to a direct lightning strike increases with increasing tank radius and reduces with increasing tank height when the roof is at the middle position. The exposure of the sidewall for this case increases slightly with increasing tank height, and it is relatively constant for a given tank height with increasing radius when the roof is at the top, as presented in Figure 4.7. There is no major variation between the Ext and All cases for the radii values analysed.

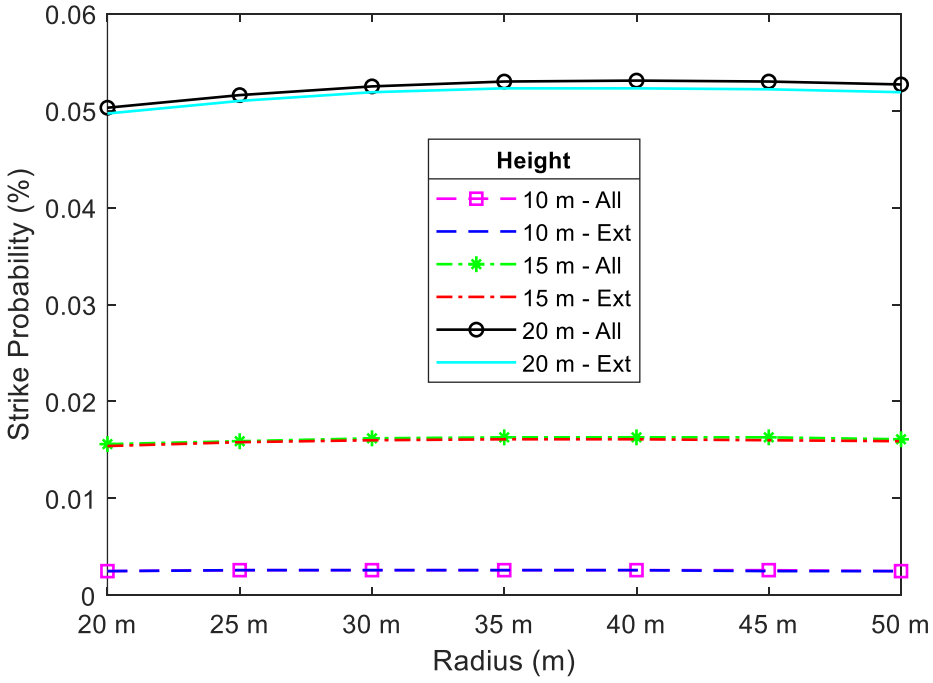

Figure 4.7. Strikes to the tank wall with the roof in the middle

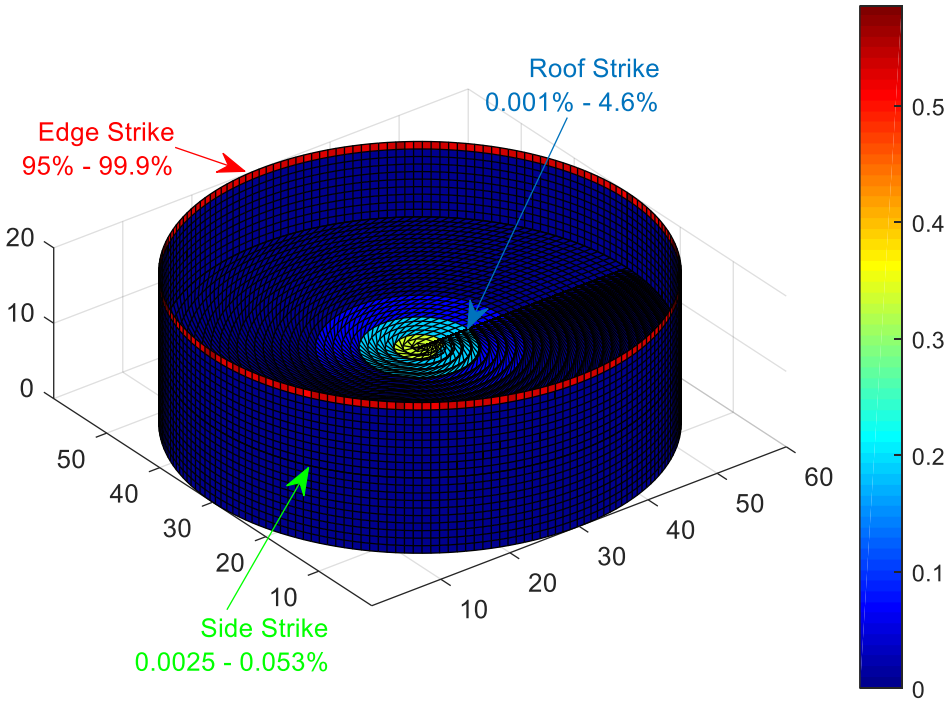

Figure 4.8. A summary of the case with the roof in the middle

A summary of the case with the roof in the middle is presented in Figure 4.8, which shows the probability of a lightning strike to the roof, the rim and the FRT's sidewall in percentage ranges.

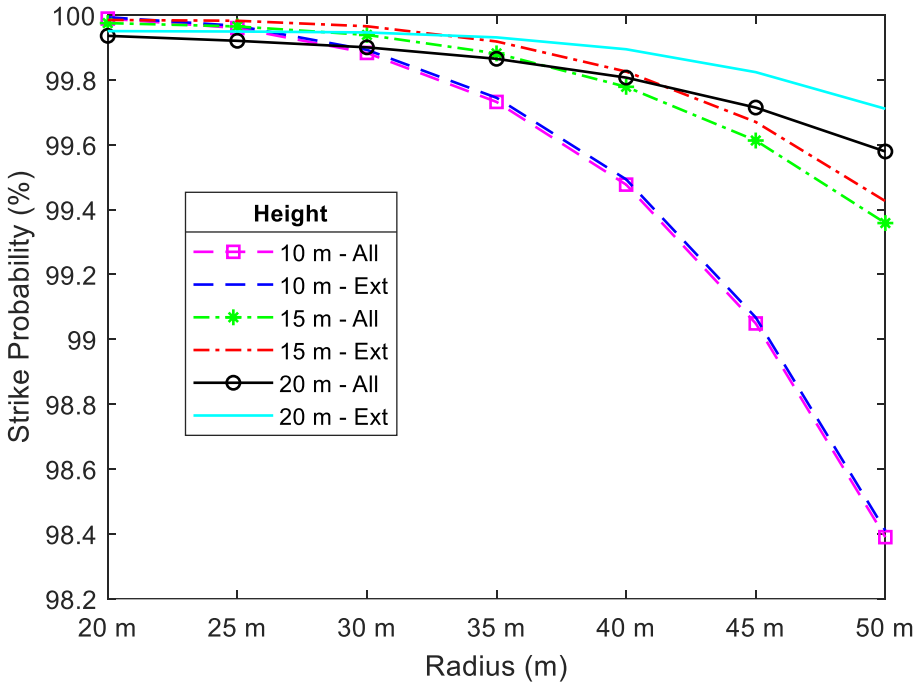

Figure 4.9. Strikes to the rim with the roof at the bottom

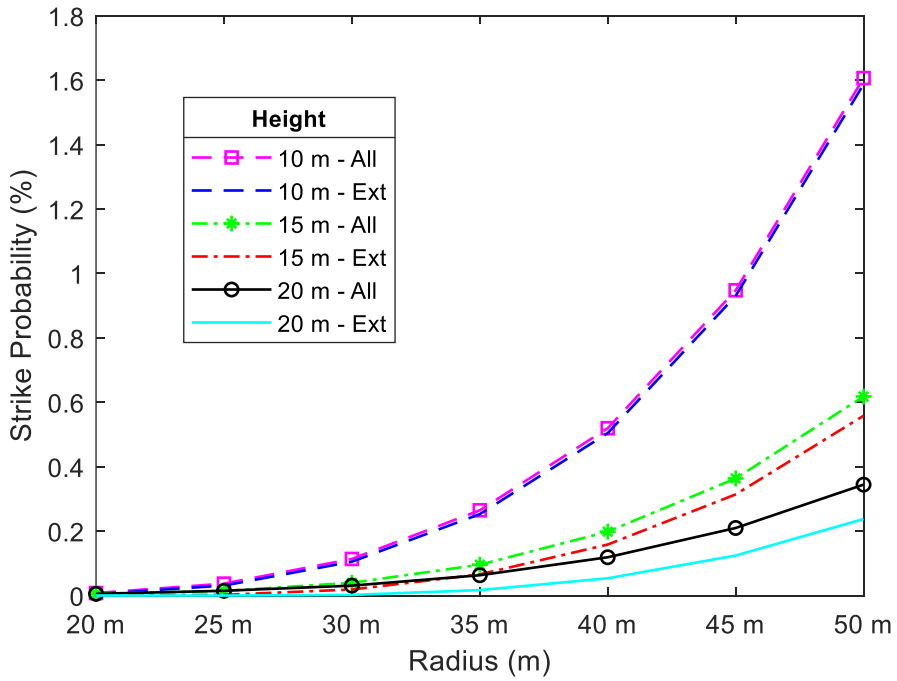

Figure 4.10. Strikes to the roof with the roof at the bottom

As shown in Figure 4.9, when the roof of the FRT is at the bottom, within the FRT, there is a significant space above the roof, and this created a little difference in the result for the Ext and All cases for the 15 m high and 20 m high FRTs. The likelihood of a strike to the FRT's rim also reduces as the tank radius increases. Figure 4.10 shows the probability of a direct strike to the floating roof. For the 15 m and 20 m high FRTs, there is a slightly higher likelihood of a strike to the roof for the All case. Although, it is important to note the highest difference is just about 0.025% for the 20 m high tank.

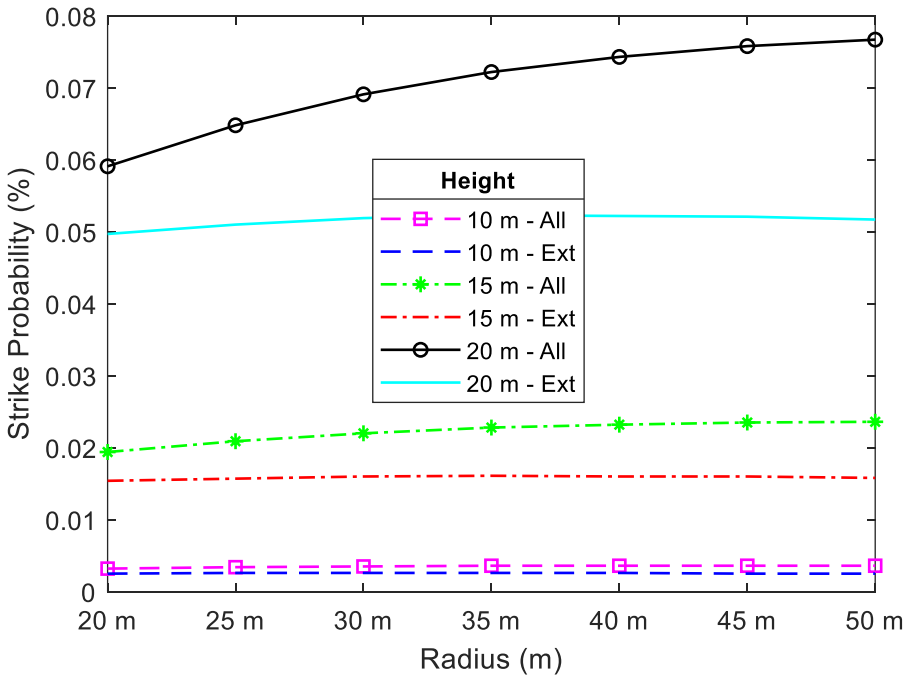

Figure 4.11. Strikes to the tank wall with the roof at the bottom

The percentage strike to the tank wall with the roof at the bottom is shown in Figure 4.11, and there is a slight difference in values between the Ext and All cases for the 15 m and 20 m cases due to internal volume within the tank when the roof is lowered. In terms of the severity of the strike to the sidewall, this may not have any practical effect. A direct lightning strike to the lower sidewall of a FRT is typically unlikely.

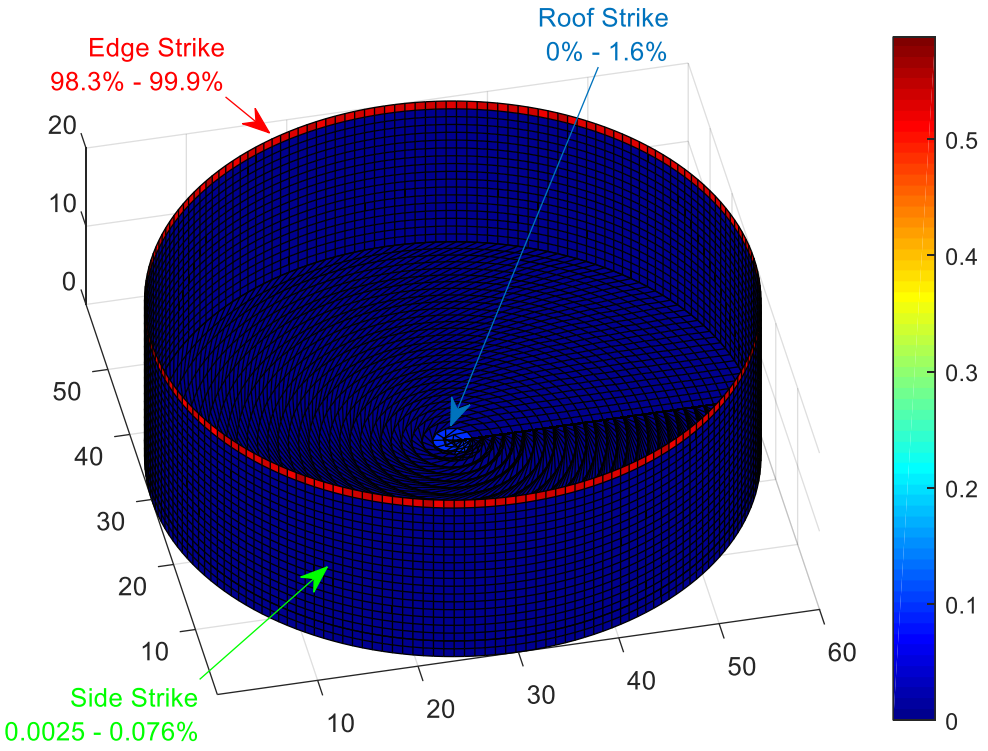

Figure 4.12. A summary of the case with the roof at the bottom

A summary diagram for the case with the roof at the bottom is presented in Figure 4.12.

4.2 Analytical simulation

The analytical equations developed in section 3.1.4.2 for the case when the roof is at the top and equations in section 3.1.4.3 for when the roof is lowered. The middle position will be analysed for the scenario where the roof is lowered.

When the roof is at the top, the effects of discretisation size can be easily observed when using analytical techniques. The analytical results computed will be compared with results from the numerical model using a discretisation size of 1 m. This means that in the numerical model, the height of the cylindrical sidewall is shortened by 1 m (0 to h-1) because the apex height represents the rim edge, and likewise, the radial length of the roof is also shortened by 1 m because the point also represents the edge of the rim and the area of the roof will be $\pi(r\text{-}1)^2$. Two analytical calculations will be developed for when the roof is at the top, the first will consider the effect of the discretisation in the numerical model, and the other will be computed based on the actual lengths of the components part. Four radii lengths of 20 m, 30 m, 40 m, and 50 m will be considered for two FRTs of the height of 15 m and 20 m, respectively.

Table 4.1. Analytical results with the roof at the top

		Strike Probability (%)		
		Numerical	**Analytical - Discretisation**	**Analytical - Actual**
Radius = 20 m Height = 20 m	Cylindrical Wall	0.050	0.045	0.056
	Rim Edge	94.880	94.959	94.438
	Roof	5.071	4.996	5.506
Radius = 20 m Height = 15 m	Cylindrical Wall	0.016	0.013	0.018
	Rim Edge	93.699	93.736	93.103
	Roof	6.286	6.250	6.879
Radius = 30 m Height = 20 m	Cylindrical Wall	0.052	0.047	0.059
	Rim Edge	90.586	90.610	90.009
	Roof	9.362	9.343	9.932
Radius = 30 m Height = 15 m	Cylindrical Wall	0.016	0.014	0.019
	Rim Edge	88.645	88.578	87.870
	Roof	11.339	11.408	12.111
Radius = 40 m Height = 20 m	Cylindrical Wall	0.053	0.048	0.059
	Rim Edge	86.142	86.091	85.466
	Roof	13.805	13.861	14.475
Radius = 40 m Height = 15 m	Cylindrical Wall	0.016	0.014	0.019
	Rim Edge	83.574	83.390	82.673
	Roof	16.410	16.596	17.308
Radius = 50 m Height = 20 m	Cylindrical Wall	0.053	0.047	0.059
	Rim Edge	81.799	81.685	81.065
	Roof	18.149	18.267	18.876
Radius = 50 m Height = 15 m	Cylindrical Wall	0.016	0.014	0.019
	Rim Edge	78.734	78.465	77.771
	Roof	21.250	21.521	22.210

Table 4.1 shows that slight difference in the results when the discretisation effect is implemented in the analytical calculations and when it is not. This further confirms that the discretisation size used in numerical models truly affects the results to some extent. When the roof is lowered, as considered in the second case, the results presented in Table 4.2 show that there is no notable difference when the discretisation effect is considered and when it is not. This is because when the roof is lowered within the tank, the edge of the roof, which is affected by the r-1 factor, is protected by the tank shell, and as such, it does not contribute to the PMCV of the tank, so its removal or addition does not affect the results.

Table 4.2. Analytical results with the roof in the middle

		Strike Probability (%)		
		Numerical	**Analytical - Discretisation**	**Analytical - Actual**
Radius = 20 m Height = 20 m	Cylindrical Wall	0.050	0.045	0.057
	Rim Edge	99.946	99.948	99.936
	Roof	0.004	0.007	0.007
Radius = 20 m Height = 15 m	Cylindrical Wall	0.016	0.013	0.019
	Rim Edge	99.975	99.973	99.968
	Roof	0.009	0.014	0.014
Radius = 30 m Height = 20 m	Cylindrical Wall	0.053	0.047	0.060
	Rim Edge	99.886	99.876	99.864
	Roof	0.062	0.076	0.076
Radius = 30 m Height = 15 m	Cylindrical Wall	0.016	0.014	0.020
	Rim Edge	99.845	99.835	99.829
	Roof	0.139	0.151	0.151
Radius = 40 m Height = 20 m	Cylindrical Wall	0.053	0.047	0.059
	Rim Edge	99.631	99.606	99.594
	Roof	0.316	0.347	0.347
Radius = 40 m Height = 15 m	Cylindrical Wall	0.016	0.019	0.014
	Rim Edge	99.326	99.285	99.290
	Roof	0.658	0.696	0.696
Radius = 50 m Height = 20 m	Cylindrical Wall	0.053	0.048	0.060
	Rim Edge	98.926	98.856	98.844
	Roof	1.022	1.096	1.096
Radius = 50 m Height = 15 m	Cylindrical Wall	0.016	0.014	0.019
	Rim Edge	97.970	97.887	97.882
	Roof	2.014	2.099	2.099

5 Simulation of the lightning impulse voltage on critical points on the FRT

This chapter is dedicated to studying the flow of lightning current on the welded steel sheets of a FRT. A model of a FRT with steel sections is implemented in Simulink on MATLAB, and lightning current is applied at various points to evaluate the voltage and current distribution along the steel sections. Towards implementing an effective LPS for a FRT, it is vital first to understand the effects of lightning current flow on voltage distributions on the FRT, which is responsible for air gap breakdown. The analysis carried out for a 60 m diameter and 20 m high FRT is extensive, and it considers steel plate resistance-inductance (RL) parameter extraction using FastHenry software and Ansys Q3D. Also, various computations were performed on MATLAB and simulations of lightning current flow, and the air gap capacitive effect was implemented using Simulink.

5.1 FRT resistance-inductance (RL) model using Ansys Q3D, Fast Henry and Simulink

A typical steel storage tank shell is made of various steel plates welded together in sections, as illustrated in Figure 5.1.

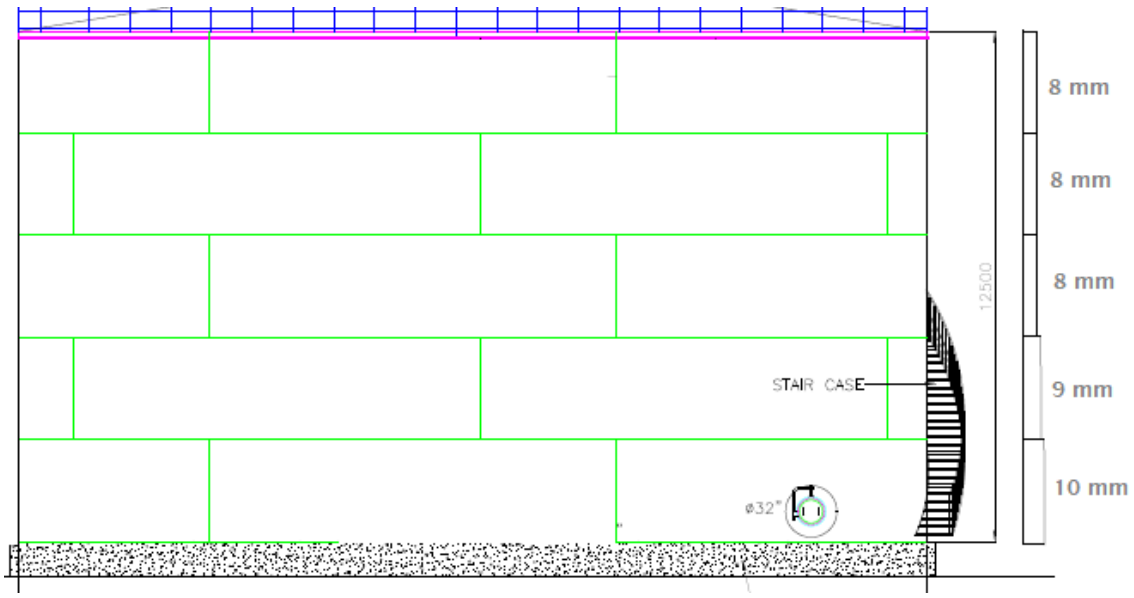

Figure 5.1. Steel sections on a FRT with the thickest steel layers at the base

The flow of current through the various tank steel plates can be evaluated using mesh impedance analysis. For this purpose, the tank shell sections will be divided into horizontal and vertical steel sheets as a representation of the possibility of current flow vertically and horizontally along the shell plates. The tank parameters for this analysis are defined as follows:

Tank diameter (D) = 60 m

Tank height (H) = 20 m

The circumference of the tank = $\pi \cdot D$ = 188.5 m

A tank sheet's typical length and breadth are about 10 m by 2.5 m. Hence, the circumference of the tank for this case is divided into 20 equal sections.

The circumferential length of steel plate = l = 9.424775 ≈ 9.425 m

The vertical height of each steel plate = w = 2.5 m

The steel plates are usually a little ticker at the base to support the weight of the upper steel sections, as shown in Figure 5.1. Three shell thicknesses will be applied in this model, i.e., 8 mm for the upper shell sections, 9 mm for the second to the last shell layer, and 10 mm for the base section. The thicknesses of the steel plates are t = 0.008 m, 0.009 m, and 0.01 m, respectively, and this complies with the minimum thank shell thickness requirement as shown in Table 5.1.

Table 5.1. Minimum tank shell thickness requirement – API 650 [165]

Nominal tank diameter *D*	**Nominal plate thickness *t***
< 15 m	≥ 5 mm
15 m – 36 m	≥ 6 mm
36 m – 60 m	≥ 8 mm
> 60 m	≥ 10 mm

Although NFPA 780 specifies that tank sheets with a minimum thickness of 4.8 mm are inherently self-protecting against melting by lightning current, but analysis by Budisatrio, et al. [166] has shown that a lightning current of 33.07 kA is the withstand limit of a 4.8 mm thick sheet for a 2 ms long-stroke current and this may be inadequate for tropical regions which have a 50% probability of lightning current greater than 40 kA [167]. A similar analysis for an 8 mm thick plate indicates a current withstand of 163.8 kA. This emphasises the importance of an adequate LPS for tanks, especially in tropical regions.

The tank model has 20 steel plates in the horizontal direction along the circumference and eight steel plates in the vertical direction. This gives a total of 160 mild steel sheet plates. The resistance and inductance of the steel sheet are affected by the direction of current flow through the sheet. For this case, the horizontal and vertical flow of current through the sheet will be considered, as illustrated in Figure 5.2 (a) and 5.2 (b).

The steel type analysed is mild steel with resistivity $\rho_{st} = 1.7 \cdot 10^{-7}\ \Omega \cdot m$, and relative permeability μ_{rst} = 300. The skin effect is considered, and it increases the current density near the skin of a conductor as frequency increases, resulting in different resistance and inductance values at different frequencies. According to the FastHenry user's guide, the conductor area where current flows, referred to as the skin depth δ, is defined as follows:

$$\delta = \sqrt{\frac{1}{\pi \cdot f \cdot \sigma \cdot \mu}} \tag{5.1}$$

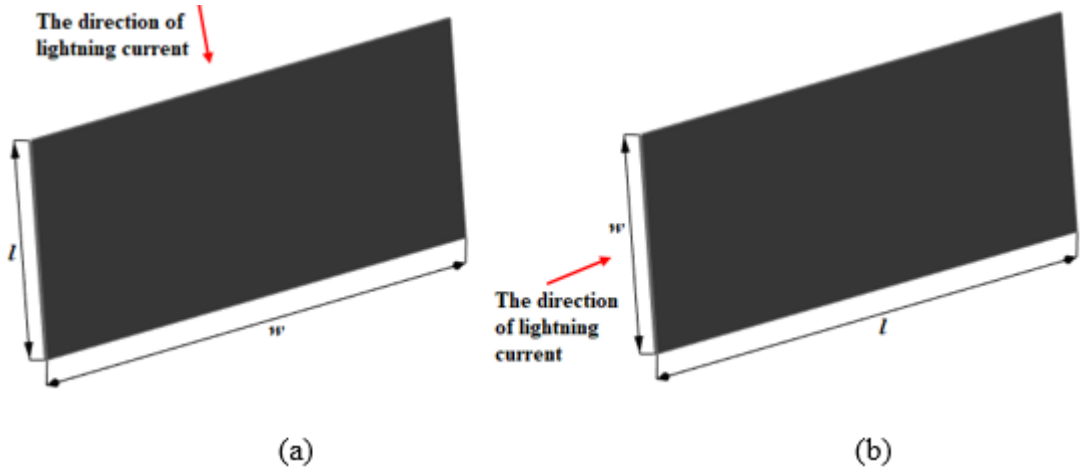

Figure 5.2. Single steel sheet illustrating current flow vertically and horizontally (a) Current flow vertically down (b) Current flow horizontally

For mild carbon steel, as calculated in Table 5.2,

$$\delta = \sqrt{\frac{\rho_{st}}{\pi \cdot f \cdot \mu_0 \cdot \mu_{rst}}} = \frac{0.01198}{\sqrt{f}} \text{ m} \tag{5.2}$$

f is frequency

The conductivity of steel $\sigma_{st} = 1/\rho_{st}$

The permeability $\mu = \mu_0 \cdot \mu_{rst}$

μ_{rst} is the relative magnetic permeability of steel

The permeability of free space $\mu_0 = 4 \cdot \pi \cdot 10^{-7}$ H/m

Table 5.2. Skin depth at different frequencies

***t* (mm)**	***f* (Hz)**	**δ (mm)**
8, 9, 10 mm	250	0.758
	437.5	0.573
	25000	0.076
	250000	0.024
	1000000	0.012

The front frequency f_f and tail frequency f_t of the lightning pulse are defined as follows:

$$f_f = \frac{1}{4 \cdot T_1} = \frac{0.25}{T_1} \tag{5.3}$$

$$f_t = \frac{7}{80 \cdot T_2} = \frac{0.0875}{T_2} \tag{5.4}$$

Where T_1 is the virtual front time, and T_2 is the virtual time to half-peak-value on the tail.

The front f_f and tail f_t frequencies for the positive First Stroke (pFS), 200 kA (10/350 µs) peak pulse lightning current, the negative First Stroke (nFS) 100 kA (1/200 µs) peak pulse lightning current and the negative Subsequent Stroke (nSS) 50 kA (0.25/100 µs) peak pulse lightning current are presented in Table 5.3. Where i_{LH} and $\hat{\imath}_{LH}$ are the lightning pulse current and the peak value, τ_1 is the front time constant and τ_2 is the tail time constant, n is the steepness factor (typically $n = 10$), and η is the pulse current peak factor.

Table 5.3. Lightning current parameters for the Heidler-time function [168]

Parameter	pFS	nFS	nSS
T_1/T_2	10/350 µs	1/200 µs	0.25/100 µs
t_i	31.02 µs	3.563 µs	0.945 µs
τ_1	18.8 µs	1.83 µs	0.454 µs
τ_2	480 µs	285 µs	143.4 µs
$\hat{\imath}_{LH}$	200 kA	100 kA	50 kA
η	0.934	0.988	0.993
f_f	25 kHz	250 kHz	1 MHz
f_t	250 Hz	437.5 Hz	875 Hz

$$i_{LH}(t) = \frac{\hat{\imath}_{LH}}{\eta} \times \frac{e^{\frac{-t}{\tau_2}}}{1 + \left(\frac{\tau_1}{t}\right)^n} \tag{5.5}$$

The impedance extraction for the steel sheet will be performed using FastHenry and Finite Element Method (FEM) on Ansys Q3D. Ansys Q3D Extractor is software for fast 3D parasitic extraction. The conductor volume modelled using FastHenry must be appropriately discretised into filaments to ensure result accuracy [169]. The smallest filament should not be bigger than the skin depth at the highest frequency. For this case, the highest frequency is 1 MHz. The steel sheet will be discretised in thickness and width direction using the following values for the FastHenry parameters: *nhinc* = 19, *nwinc* = 19, *rh* = 4, *rw* = 2.

The impedance extraction was first implemented using $\mu_{rst} = 1$ on FastHenry and Q3D, and the resistance and inductance (*RL*) result is presented in Figure 5.3 and Figure 5.4 for a few frequency points between 1 Hz to 1 MHz for an 8 mm thick steel sheet. The results from the two applications are reasonably close in this particular case. FastHenry has a default relative permeability μ_r of 1, which cannot be altered. Using FastHenry for analysing mild steel with $\mu_{rst} = 300$ is impossible. For this case, the analysis is performed in Q3D using $\mu_{rst} = 300$, and an approximate estimation is developed in FastHenry for comparison.

The relationship between electrical resistivity and permeability for most materials is not necessarily linear, but for simplification, we assume a simple linear relationship for analysis in FastHenry at $\mu_{rst} = 300$.

A modified resistivity $\rho_{st}^* = 1.7 \cdot 10^{-7} / 300 = 5.667 \cdot 10^{-10}\ \Omega \cdot m$

This will be used for computation in FastHenry as an approximation of the resistivity at $\mu_r = 1$. The R* and L* obtained from FastHenry will be modified as follows for an approximate estimation of the $\mu_{rst} = 300$ equivalent.

$$R = 300 \times R^* \tag{5.6}$$

$$R = 300 \times (L^* - L_{hf}) \times 300 + L_{hf} \tag{5.7}$$

L_{hf} is the smallest value of inductance at a very high frequency ($f \to \infty$), which is almost constant. For this case, at L_{hf}, $f = 1 \times 10^{155}$ Hz.

The RL values from Q3D and the estimated result for $\mu_{rst} = 300$ using FastHenry are presented in Figure 5.5 and Figure 5.6 for horizontal and vertical 8 mm thick steel sheets, Figure 5.7 and Figure 5.8 for 9 mm thick steel sheets, and Figure 5.9 and Figure 5.10 for 10 mm thick steel sheets. Values from Q3D, as shown in Table 5.4 and illustrated in Figure 5.11, will be used for further computation in MATLAB Simulink.

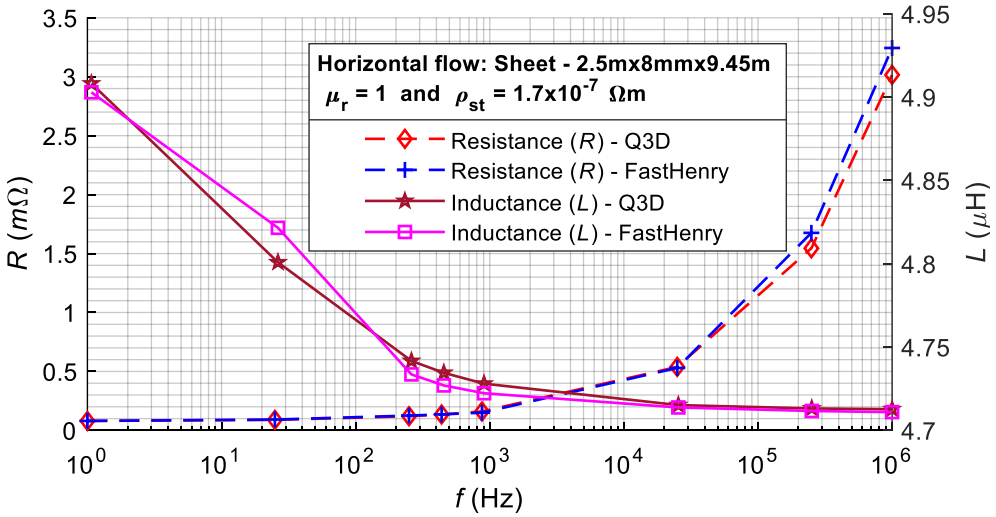

Figure 5.3. RL parameters of the 8 mm sheet for $\mu_r = 1$ (Horizontal current flow)

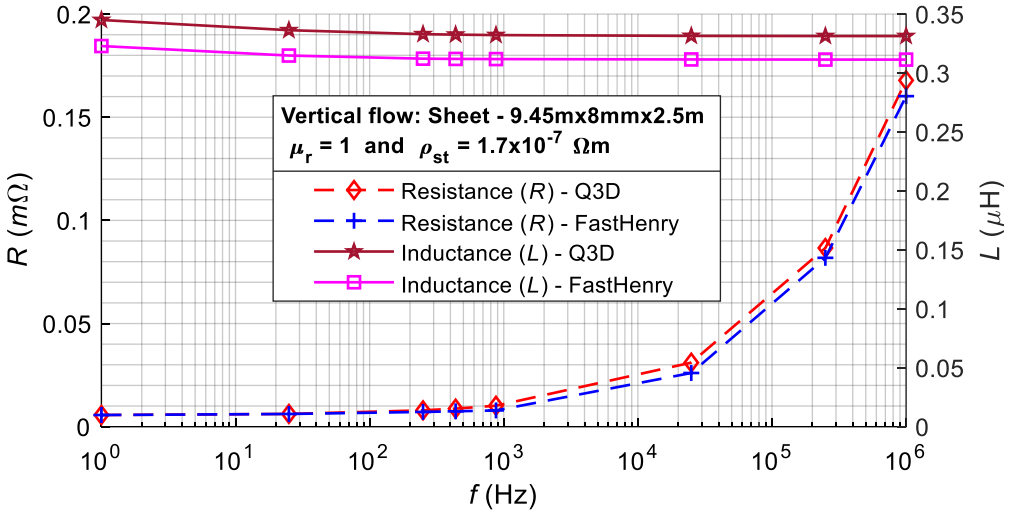

Figure 5.4. RL parameters of the 8 mm sheet for $\mu_r = 1$ (Vertical current flow)

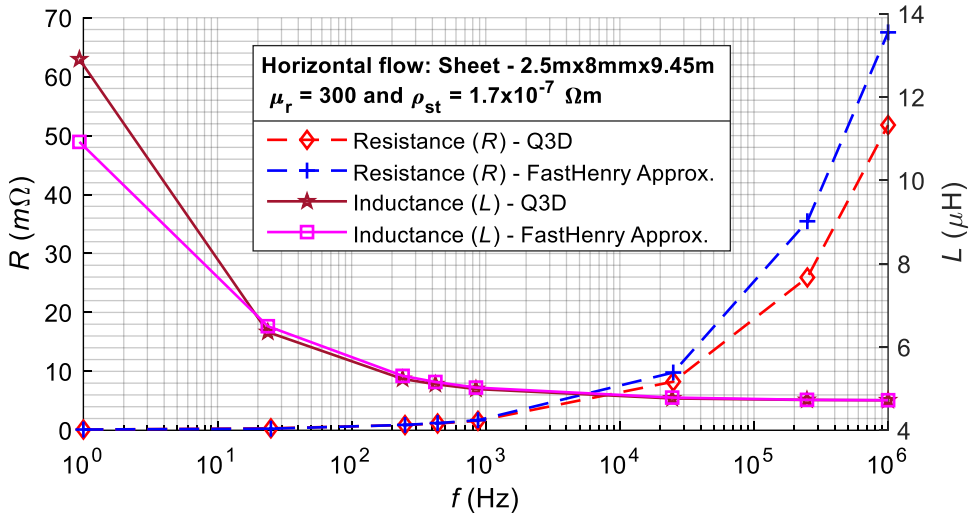

Figure 5.5. RL parameters of the 8 mm sheet for $\mu_{rst} = 300$ (Horizontal current flow)

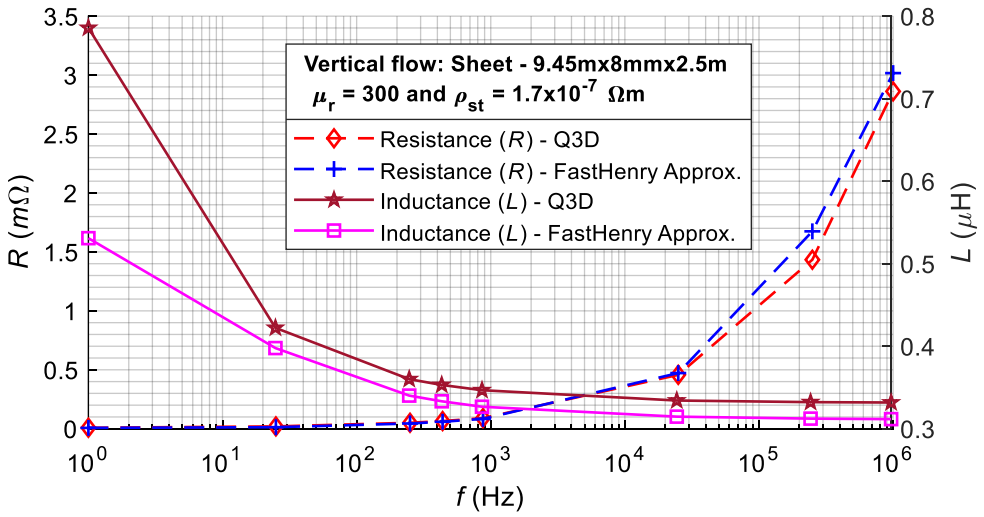

Figure 5.6. RL parameters of the 8 mm sheet for $\mu_{rst} = 300$ (Vertical current flow)

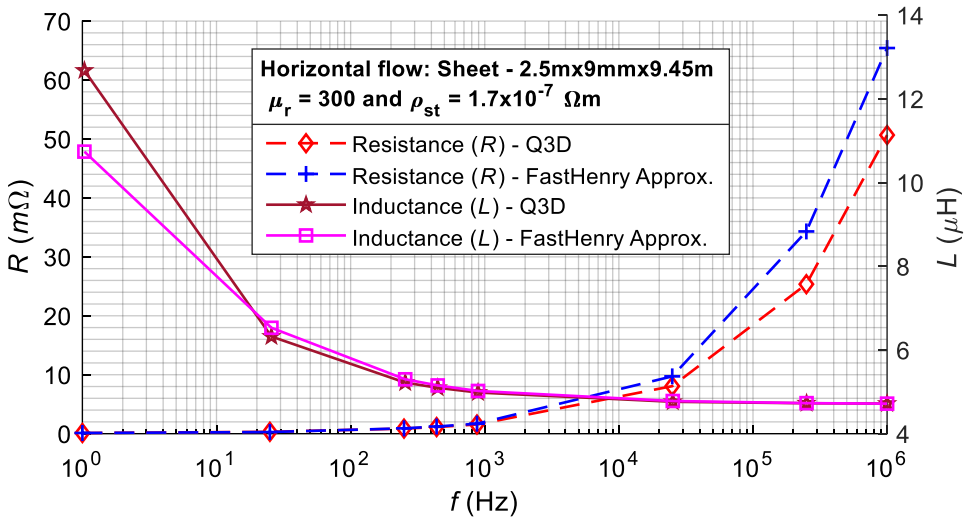

Figure 5.7. RL parameters of the 9 mm sheet for μ_{rst} = 300 (Horizontal current flow)

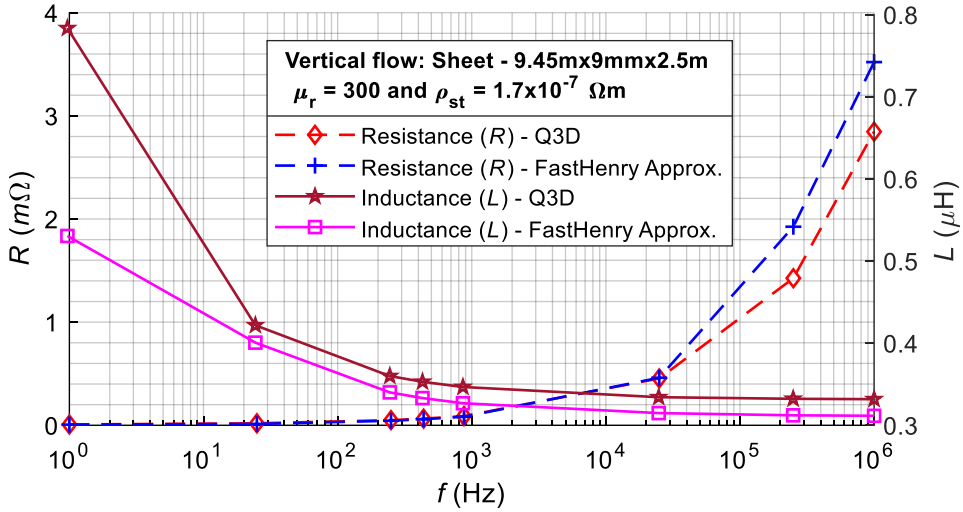

Figure 5.8. RL parameters of the 9 mm sheet for μ_{rst} = 300 (Vertical current flow)

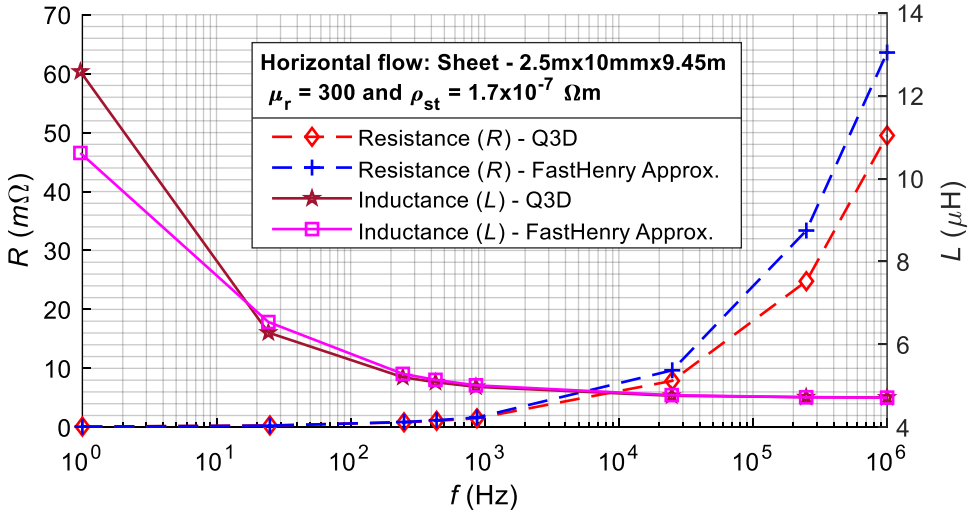

Figure 5.9. RL parameters of the 10 mm sheet for μ_{rst} = 300 (Horizontal current flow)

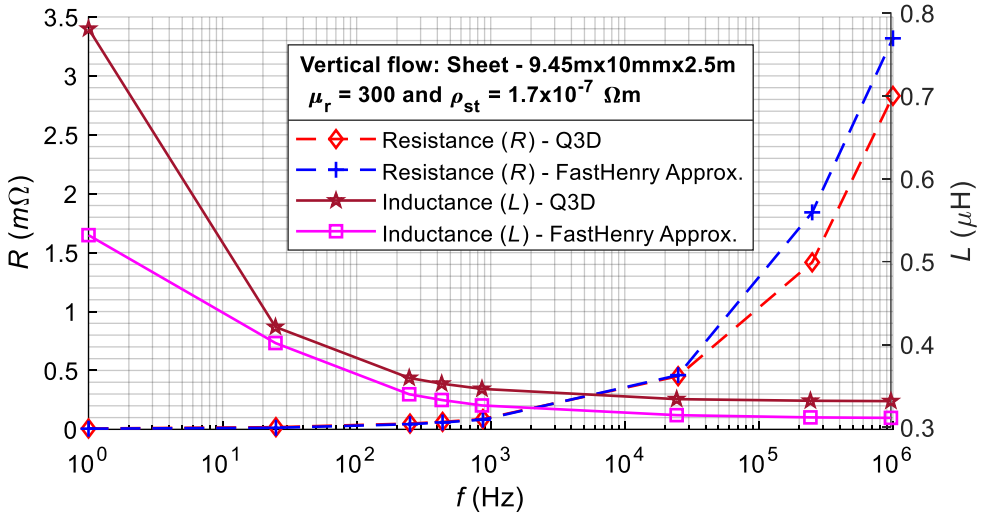

Figure 5.10. RL parameters of the 10 mm sheet for μ_{rst} = 300 (Vertical current flow)

Table 5.4. Single sheet resistance and inductance values from Ansys Q3D

		Resistance (mΩ)		Inductance (μH)	
t **(mm)**	***f*** **(Hz)**	**Horizontal**	**Vertical**	**Horizontal**	**Vertical**
8	250	0.891	0.051	5.233	0.360
	437.5	1.155	0.065	5.106	0.353
	25000	8.251	0.457	4.764	0.334
	250000	25.933	1.434	4.729	0.332
	1000000	51.793	2.862	4.721	0.332
9	250	0.861	0.050	5.220	0.360
	437.5	1.119	0.064	5.096	0.353
	25000	8.062	0.454	4.762	0.334
	250000	25.362	1.426	4.727	0.332
	1000000	50.663	2.847	4.719	0.332
10	250	0.846	0.049	5.208	0.360
	437.5	1.098	0.064	5.087	0.353
	25000	7.882	0.451	4.760	0.334
	250000	24.787	1.417	4.726	0.332
	1000000	49.509	2.830	4.719	0.332

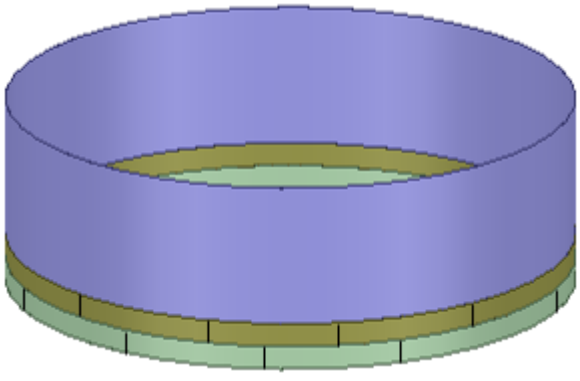

Figure 5.11. The three thickness layers of FRT shell steel sheets

5.2 Evaluating the overall tank shell impedance

The study by Buccella [170] evaluated the transient effect of lightning current on a small metallic oil container of 6.4 m in diameter on PSPICE simulator using the multi-transmission line (MTL) ground model with an arrangement of circular conductors. The effect of frequency and shell thickness was not considered. This study implements transient current analysis on a FRT shell modelled from first principles with vertical and horizontal steel plate parameters extraction from Ansys Q3D. The simulation at various lightning frequencies is implemented on Simulink for a FRT of 60 m in diameter.

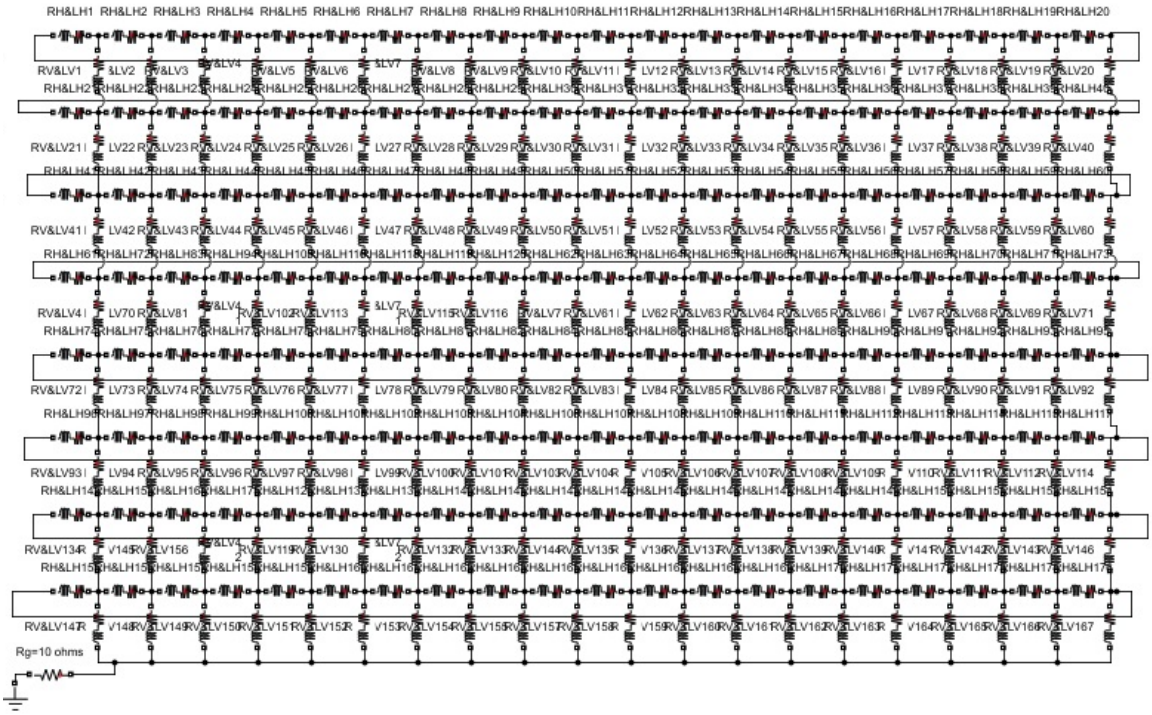

Figure 5.12. RL mesh tank model in Simulink

The FRT has three different layers of steel thickness, i.e., 8 mm at the top, 9 mm, and 10 mm, as illustrated in Figure 5.11. The tank model has 20 steel plates in the horizontal direction along the circumference and 8 steel plates in the vertical direction. The tank's shell plates are modelled in Simulink, as illustrated in Figure 5.12.

The overall impedance of the RL tank mesh network can be determined by applying an AC voltage source of any magnitude and frequency to a point at the top of the tank shell, as illustrated in Figure 5.13. The impedance of the network will be determined at specific frequencies set in a code implemented in an M-file on MATLAB. The parameters (A, B, C, D) of the state-space model of the RL mesh are first evaluated to compute the impedance by using the command power_analyze. The network's total admittance and phase magnitude are then determined using the Bode function. The impedance can be obtained as the inverse of the admittance.

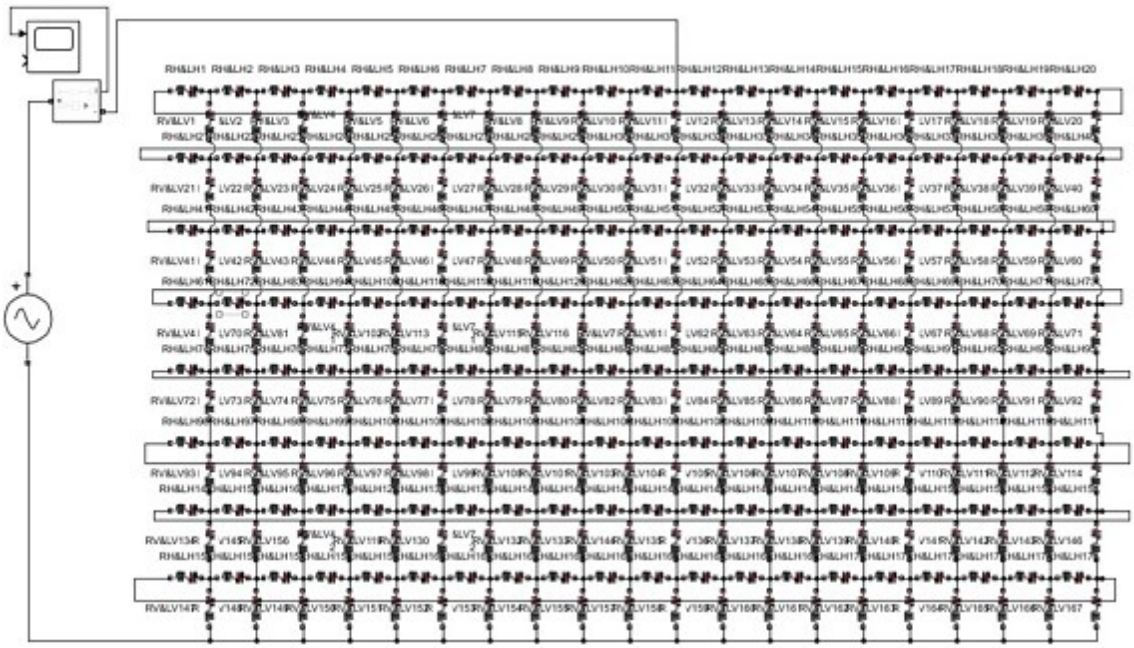

Figure 5.13. RL mesh impedance evaluation setup

In the Laplace domain, the admittance (Y) and impedance (Z) are defined as follows:

$$Y(s) = \frac{I(s)}{U(s)} \tag{5.8}$$

$$Z(s) = \frac{1}{Y(s)} \tag{5.9}$$

An approximate solution of the overall impedance can also be computed using analytical equations proposed by Tan [171] such that:

$$Z = R_{\mathrm{hz}} + \mathrm{j}\omega L_{\mathrm{hz}} \tag{5.10}$$

$$Z_0 = R_{\mathrm{v}} + \mathrm{j}\omega L_{\mathrm{v}} \tag{5.11}$$

In equations 5.10 and 5.11, subscripts *hz* and *v* represent horizontal and vertical components, as detailed in Table 5.4. Since the shell sheets have three different thicknesses, i.e., 8 mm (15 m high), 9 mm (2.5 m high) and 10 mm (2.5 m high). There is a need for an average value which is defined as

$$R = \frac{6 \times R_{8mm} + 1 \times R_{9mm} + 1 \times R_{10mm}}{8} \tag{5.12}$$

$$L = \frac{6 \times L_{8mm} + 1 \times L_{9mm} + 1 \times L_{10mm}}{8} \tag{5.13}$$

$$h = \frac{Z}{Z_0} \tag{5.14}$$

m = 8 (number of vertical *v* impedances)

n = 20 (number of horizontal *hz* impedances)

$p = m$ (node on top)

q = 0 (node on bottom)

$$\vartheta_i = \frac{2 \cdot i - 1}{2 \cdot m + 1} \cdot \pi \tag{5.15}$$

$$\lambda_i = 1 + h - h \cdot \cos\vartheta_i + \sqrt{(1 + h - h \cdot \cos\vartheta_i)^2 - 1} \tag{5.16}$$

$$\bar{\lambda}_i = 1 + h - h \cdot \cos\vartheta_i - \sqrt{(1 + h - h \cdot \cos\vartheta_i)^2 - 1} \tag{5.17}$$

$$Z_{m,n}(p,q) = \frac{4 \cdot Z}{2 \cdot m + 1} \cdot \sum_{i=1}^{m} \left[\left(\sin(p \cdot \vartheta_i) - \sin(q \cdot \vartheta_i)\right)^2 \cdot \frac{\coth\left(n \cdot \ln\left(\sqrt{\lambda_i}\right)\right)}{\lambda_i - \bar{\lambda}_i} \right] \tag{5.18}$$

In this case, the computation needed is

$$Z_{8,20}(8,0) = R_T + j\omega L_T \tag{5.19}$$

The overall mesh impedance, i.e., the total resistance (R_T) and the total inductance (L_T) obtained using Simulink and the analytical approach, are presented in Table 5.5 at four different lightning current frequencies.

Table 5.5. The tank's overall resistance and inductance values

	Simulink		Analytical	
***f* / Hz**	**R_T / mΩ**	**L_T / μH**	**R_T / mΩ**	**L_T / μH**
250	0.173	1.143	0.172	1.143
437.5	0.224	1.119	0.222	1.119
25000	1.582	1.054	1.576	1.053
250000	4.967	1.047	4.947	1.047
1000000	9.917	1.045	9.879	1.045

5.3 The grounding resistance of a FRT

The base plate of a FRT is usually installed on the ground. The tank bottom plates have multiple sections welded together, as shown in Figure 5.14, and this can be modelled as a single circular sheet. It is usually placed on top of a layer of concrete and compacted soil and bitumen to prevent corrosion, and a polythene membrane may be added. The foundation can be 2 m deep into the soil. The circular concrete edges are made of reinforced concrete, and the reinforcing bars of foundations and driven piles, where applicable, are usually interconnected to form an earth termination network. Therefore, the large diameter bottom plate usually has a very low resistance to current flow to the ground.

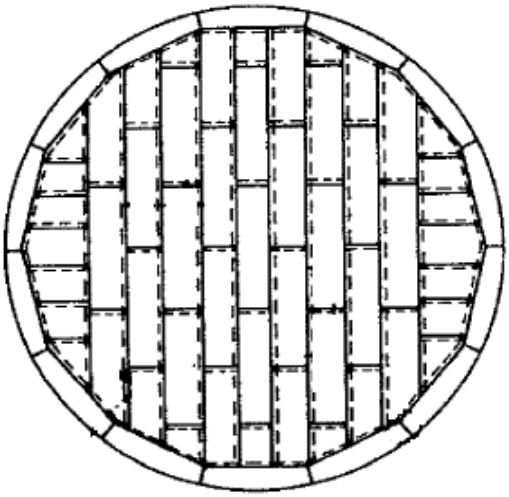

Figure 5.14. Typical sheet arrangement of tank bottom layer

The grounding resistance of a circular plate (tank bottom plates) placed directly on the earth's surface can be calculated using R_{g1} as defined by IEEE Std 80-2013 [172] or R_{g2} according to BS 7430:2011 [173]. The resulting values are plotted in Figure 5.15 over a resistivity span of 0 to 1200 Ωm. The tank diameter is 60 m.

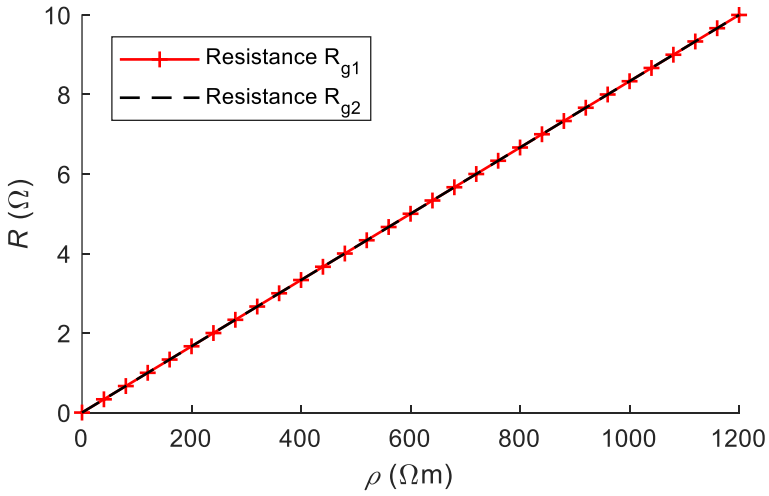

Figure 5.15. The resistance of a circular plate with increasing soil resistivity

$$R_{g1} = \frac{\rho_g}{2 \cdot D} \tag{5.20}$$

$$R_{g2} = \frac{\rho_g}{4} \sqrt{\frac{\pi}{A}} \tag{5.21}$$

ρ_g – soil resistivity (Ωm)

D – plate diameter (m)

A – plate surface area (m^2)

It is observed from Figure 5.15 that even at 1200 Ωm, the resistance of the base plate is just 10 Ω. A number of crude oil storage facilities are usually located in riverine areas, e.g. the Niger Delta crude oil storage facilities in Nigeria. In such areas, the soil resistivity can be very low and less than 50 Ωm, such that the resistance is ≤ 0.4167 Ω. The recommended grounding resistance for lightning current dissipation is 10 Ω or lower, and this can therefore be achieved on a FRT without any additional grounding rods. This emphasizes the view of API RP 545 [130] that flat-bottom tanks placed on the ground do not require additional grounding via separate rods, and as such, the lightning safety of tanks is not affected by grounding. According to Dodd [164], adding extra external grounding to the tank has no benefit whatsoever.

External grounding rods, if installed, are usually positioned around the tank's base. There are variations in the inter-electrode spacing from different sources. Some petroleum companies recommend a maximum inter-electrode spacing of 15 m around the tank circumference, while some use 20 m. For this case, 13 rods will be installed around the FRT, and the rods can be positioned 1 m away from the tank shell.

The overall resistance of n grounding rods arranged in a circle can be evaluated by R_{g3} [174]. The resulting values using R_{g3} are plotted in Figure 5.16 over a resistivity span of 0 to 1200 Ωm.

$$R_{g3} = \frac{\rho_g}{2\pi \cdot D} \cdot \left(\ln\left(\frac{8 \cdot D}{d}\right) - 1 \right) \cdot \frac{1}{n} \cdot \left(1 + \frac{d}{2 \cdot D_C} + \frac{d}{D_C} \cdot \sum_{i=1}^{i=n/2-1} \frac{1}{\sin(\frac{\pi \cdot i}{n})} \right) \quad (5.22)$$

ρ_g – soil resistivity

D – the depth of rod(s) in the soil; usually D = 9 m (= 6 × 1.5 m)

d – the electrode diameter d = 0.02 m

n – number of rods; n =13

D_C – diameter of circle = tank diameter + 2 m spacing from the tank

The circular grounding rods are usually connected at multiple points to the tank shell, which represents parallel connections. At a resistivity of 1200 Ωm, the resistance of the rods is 11.78 Ω, a simple parallel connection with the base plate resistance of 10 Ω gives an overall resistance of 5.41 Ω. For a soil resistivity value of 50 Ωm, the resistance of the rods is 0.491 Ω and when connected in parallel with the base plate resistance of 0.4167 Ω, the overall resistance is 0.225 Ω. For the simulations in Simulink, two overall grounding values of 10 Ω as the recommended maximum value for lightning protection and a second case with a low grounding resistance of 0.225 Ω were considered to evaluate the effect of grounding, if any, on the simulation results.

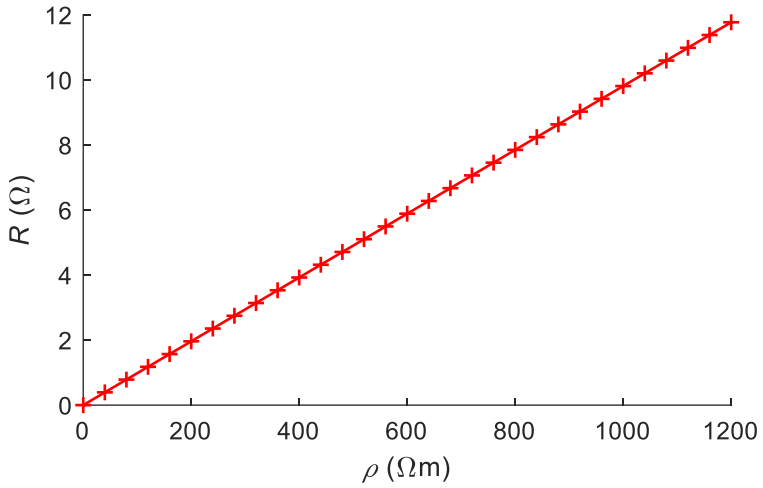

Figure 5.16. Overall grounding resistance of the rods on a circular path

5.4 Modelling of the lightning current in Simulink

The lightning current model applied in this section for the 10/350 µs, 200 kA (pFS), 1/200 µs, 100 kA (nFS) and 0.25/100 µs, 50 kA (nSS) are shown in Figure 5.17, Figure 5.18, and Figure 5.19. The resulting waveforms are displayed in Figure 5.20, Figure 5.21 and Figure 5.22 respectively. The controlled current source in the model has a resistance of 1 MΩ in parallel, which prevents error due to the connection of the block with inductive elements.

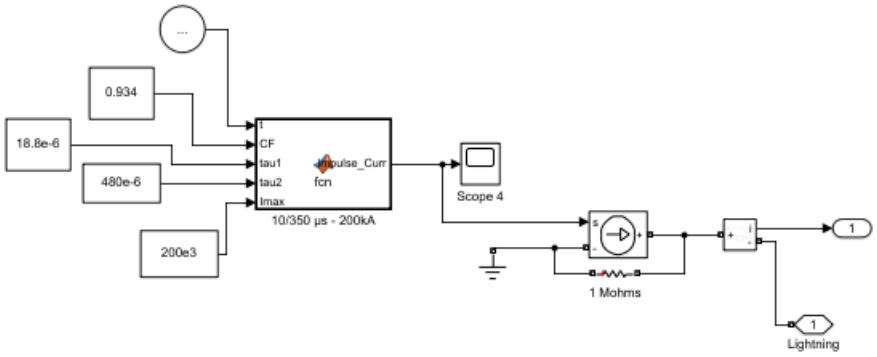

Figure 5.17. 10/350 µs, 200 kA lightning current model

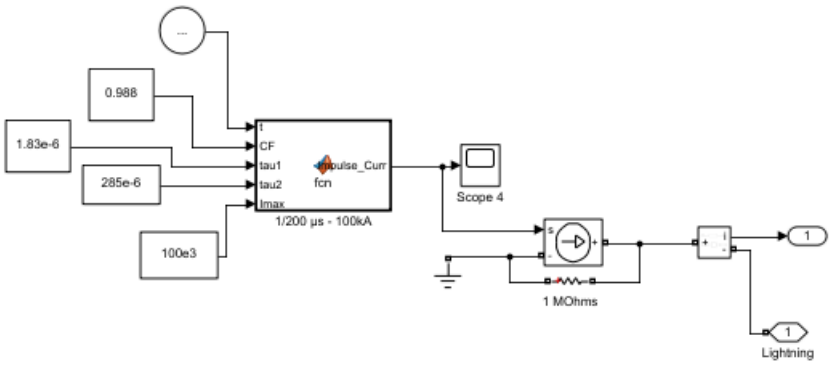

Figure 5.18. 1/200 µs, 100 kA lightning current model

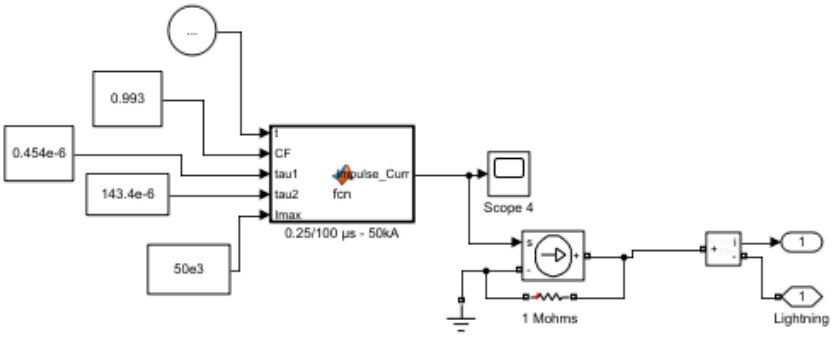

Figure 5.19. 0.25/100 µs, 50 kA lightning current model

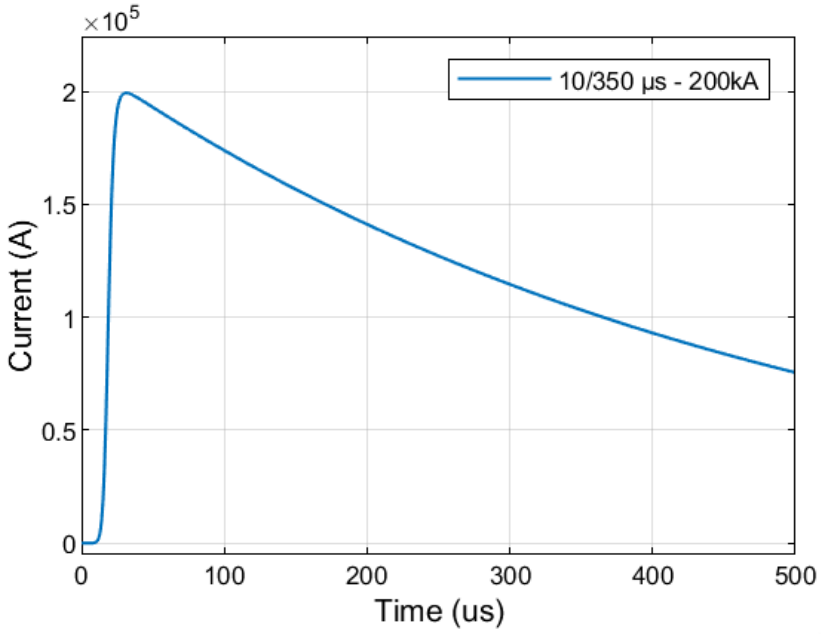

Figure 5.20. 10/350 µs, 200 kA lightning current waveform

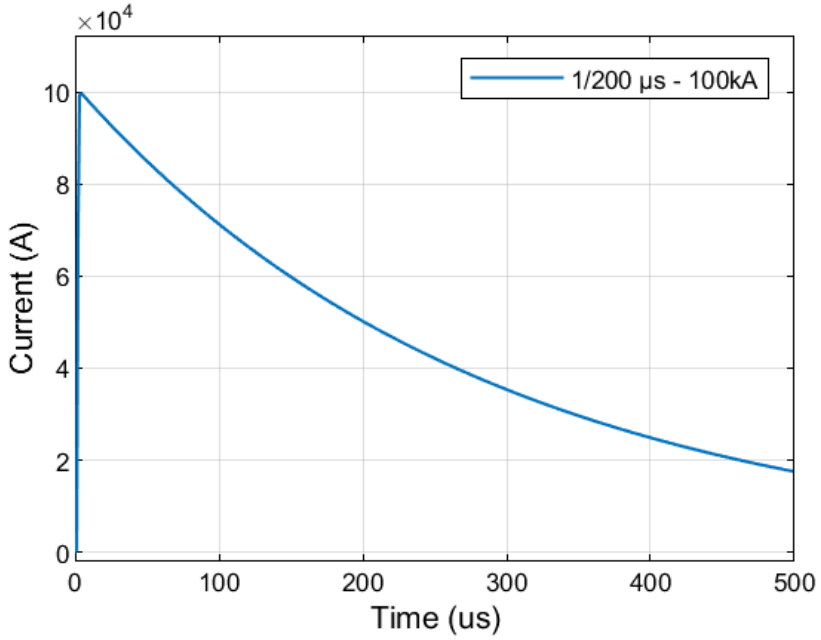

Figure 5.21. 1/200 µs, 100 kA lightning current waveform

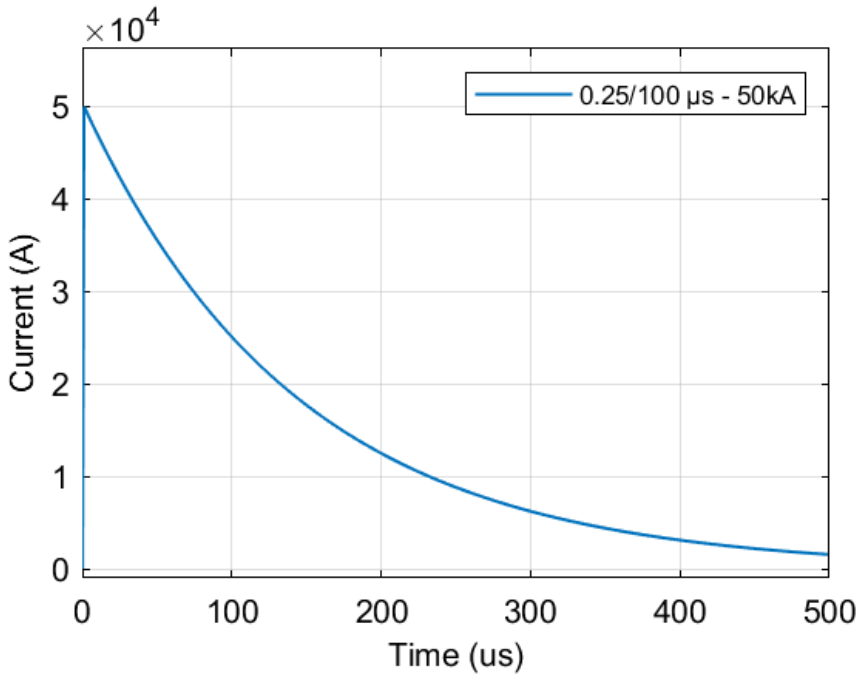

Figure 5.22. 0.25/100 µs, 50 kA lightning current waveform

5.5 Evaluation of the current and voltage distribution on the FRT when lightning strikes

The lightning current Simulink block is connected to the tank's RL mesh model at a point at the top, and the current and voltage distributions along the steel columns are measured, as illustrated in Figure 5.23.

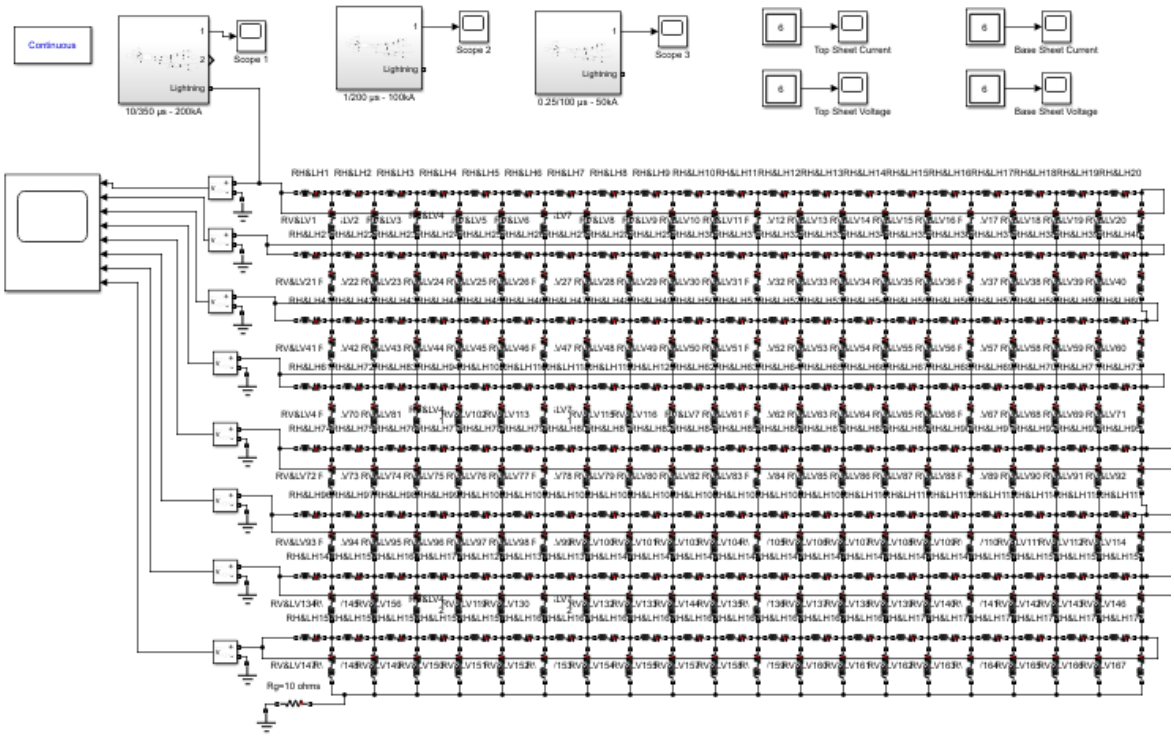

Figure 5.23. Modelling of the lightning current striking the FRT's RL mesh

5.5.1 Evaluating the effect of frequency variations on the current and voltage of the vertical steel columns

A summary comparison of the current and voltage distributions across the steel sections is presented in this section. The lightning waveform is generally said to contain all frequencies based on its spectrum analysis. The results presented here are for the cases when the lightning current frequency is 250 Hz, 437.5 Hz, 25000 Hz, and 250000 Hz by applying their corresponding RL values at the frequency (*f*) from the impedance extraction. For this case, the total grounding resistance R_g at the base of the tank is 0.225 Ω, and the lightning current (10/350 µs, 200kA) strikes a point on the tank rim, as illustrated in Figure 5.23. The voltage at the top of each of the 8 vertical steel sheet rows along the point of strike with respect to the ground is presented in Figure 5.24 (a) to (d) for the four frequencies. The voltage curve largely follows the pulse current. Only at the beginning, there is an additional small inductive voltage peak. A peak voltage of approximately 55 kV is observed at the point of the strike in Figure 5.24 (a). The voltage profiles across the frequencies are quite similar except for the slight reduction in voltage with increasing frequency.

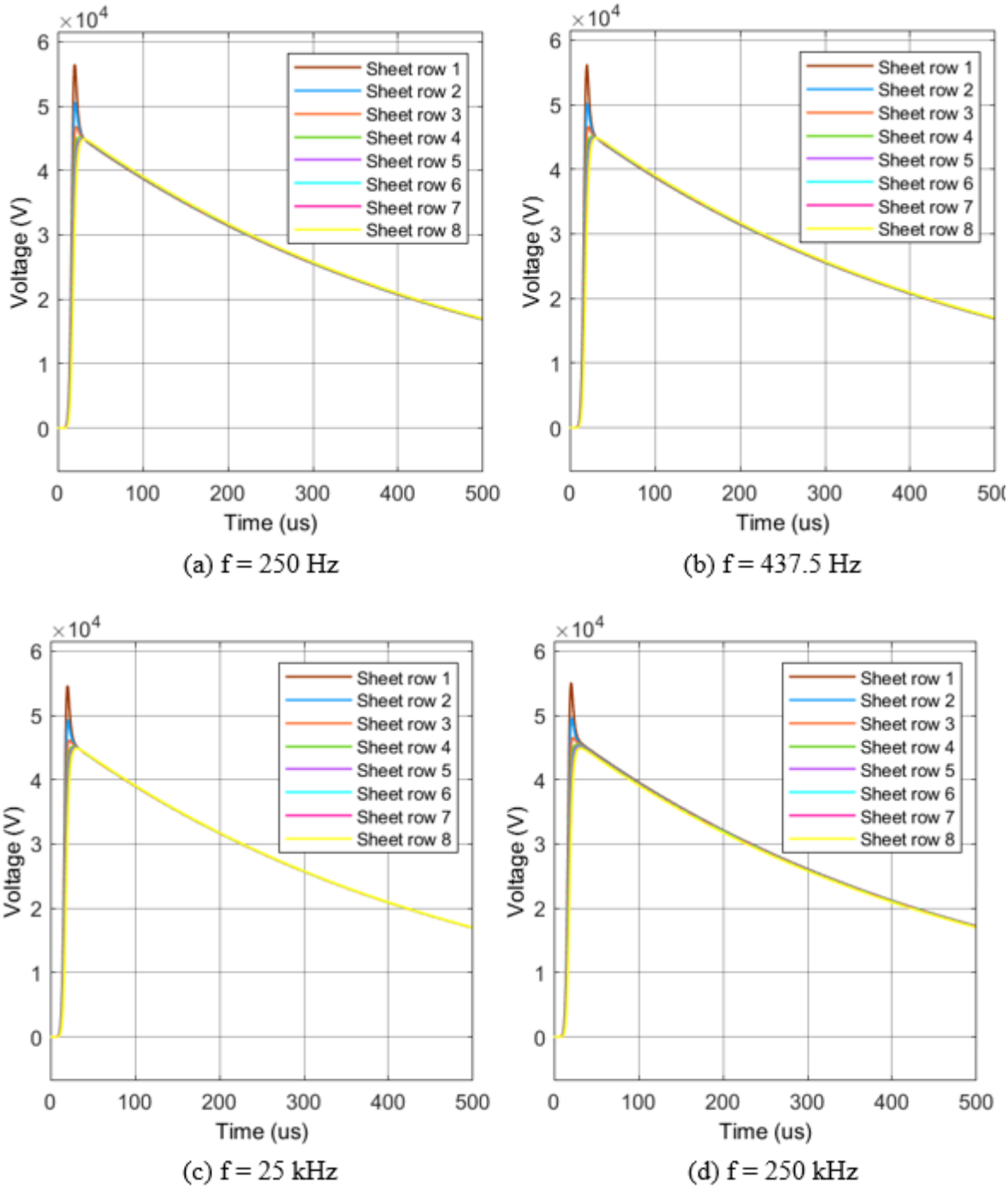

Figure 5.24. The voltage across the vertical steel sections with R_g = 0.225 Ω for the pFS

The voltage across each of the 20 sheets at the topmost sheet (TS) layer is presented in Figure 5.25. The voltage curves show predominantly inductive character, a voltage peak in the front region of the pulse current and low voltage values in the tail region. Across the frequencies, the highest voltage across the sheet struck directly by lightning is 7.2 kV, and this occurred at 250 Hz in Figure 5.25 (a). The next highest voltage level occurred on the two sheets on either side of the struck sheet, and the peak voltage on each of the sheets reduced with increasing distance from the point of strike. As shown in Figure 5.25 (a) to (d), the voltage levels reduced slightly with increasing frequency.

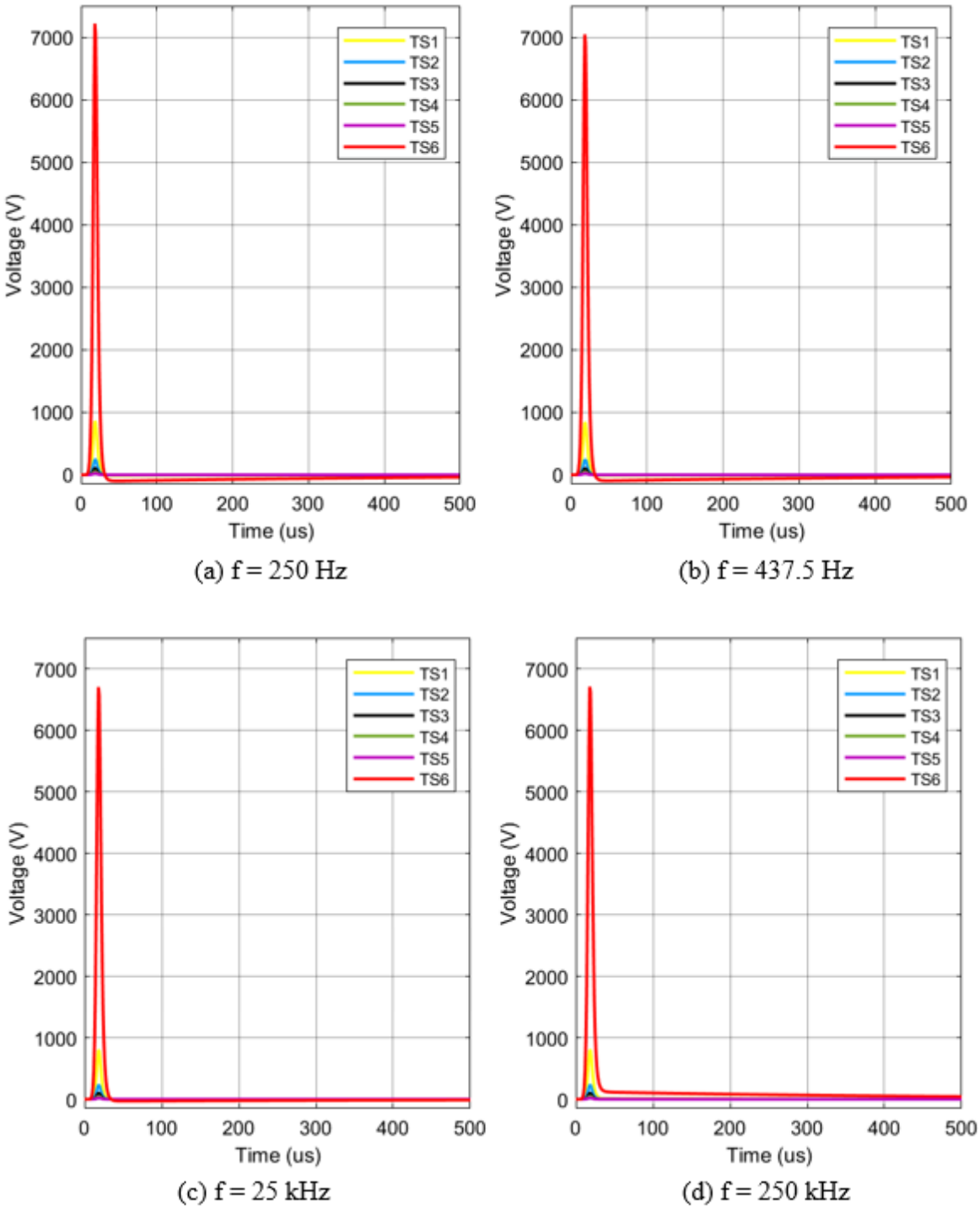

Figure 5.25. The voltage across the 20 top sheets with R_g = 0.225 Ω for the pFS

Figure 5.26 (a) to (d) presents the voltage with respect to ground across each of the 20 steel horizontal sheets at the base of the tank. A peak pulse voltage of about 2400 V is observed at the steel sheet vertically below the strike point in Figure 5.26 (a). The base sheets are 2.5 m high, and they are the sheets most likely to be touched by workers within the tank farm. The base sheet voltage also reduced slightly with increasing frequency. The profiles are quite similar for 250 Hz, 437.5 Hz, 25000 Hz, and 250 kHz, except for slight variations in magnitude.

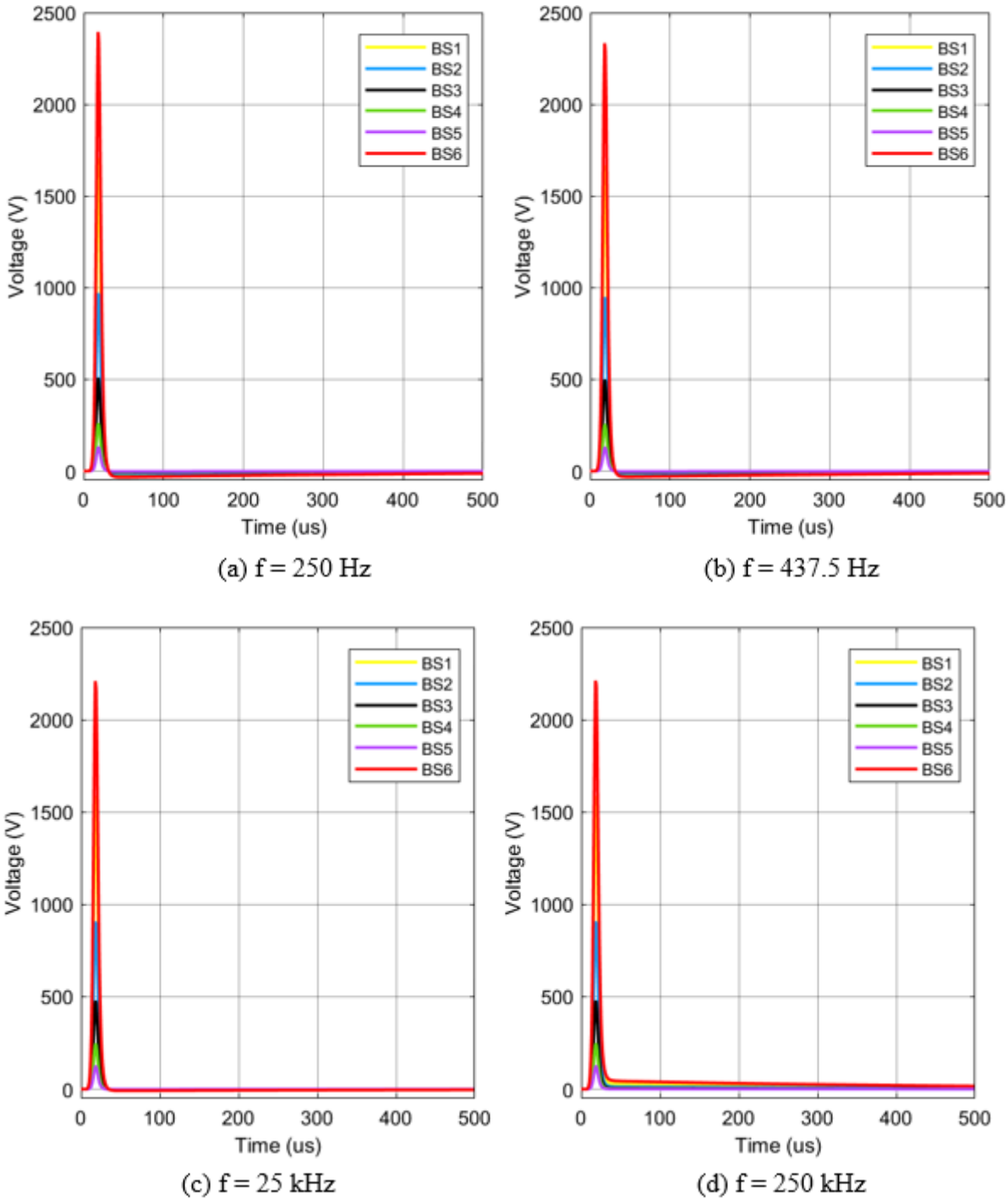

Figure 5.26. The voltage across the 20 base sheets with R_g = 0.225 Ω for the pFS

Figure 5.27 (a) to (d) show the current flowing through each of the 20 steel horizontal sheets at the top of the tank from 250 Hz to 250 kHz. A peak current of 148 kA is observed flowing through the sheet directly struck by lightning, while currents of approximately 20 kA flowed through the sheets on either side of the struck sheet, and lower current magnitudes (< 3 kA) flowed through each of the remaining steel sheets. Figure 5.28 (a) to (d) show the current flowing through each of the 20 steel horizontal sheets at the base of the tank. A peak current of 48 kA can be observed for the base sheet directly below the strike point.

A key observation is that the current distribution at the top of the tank had changed significantly at the tank base. The current is better shared among the sheets at the base of the tank than at the top rim region.

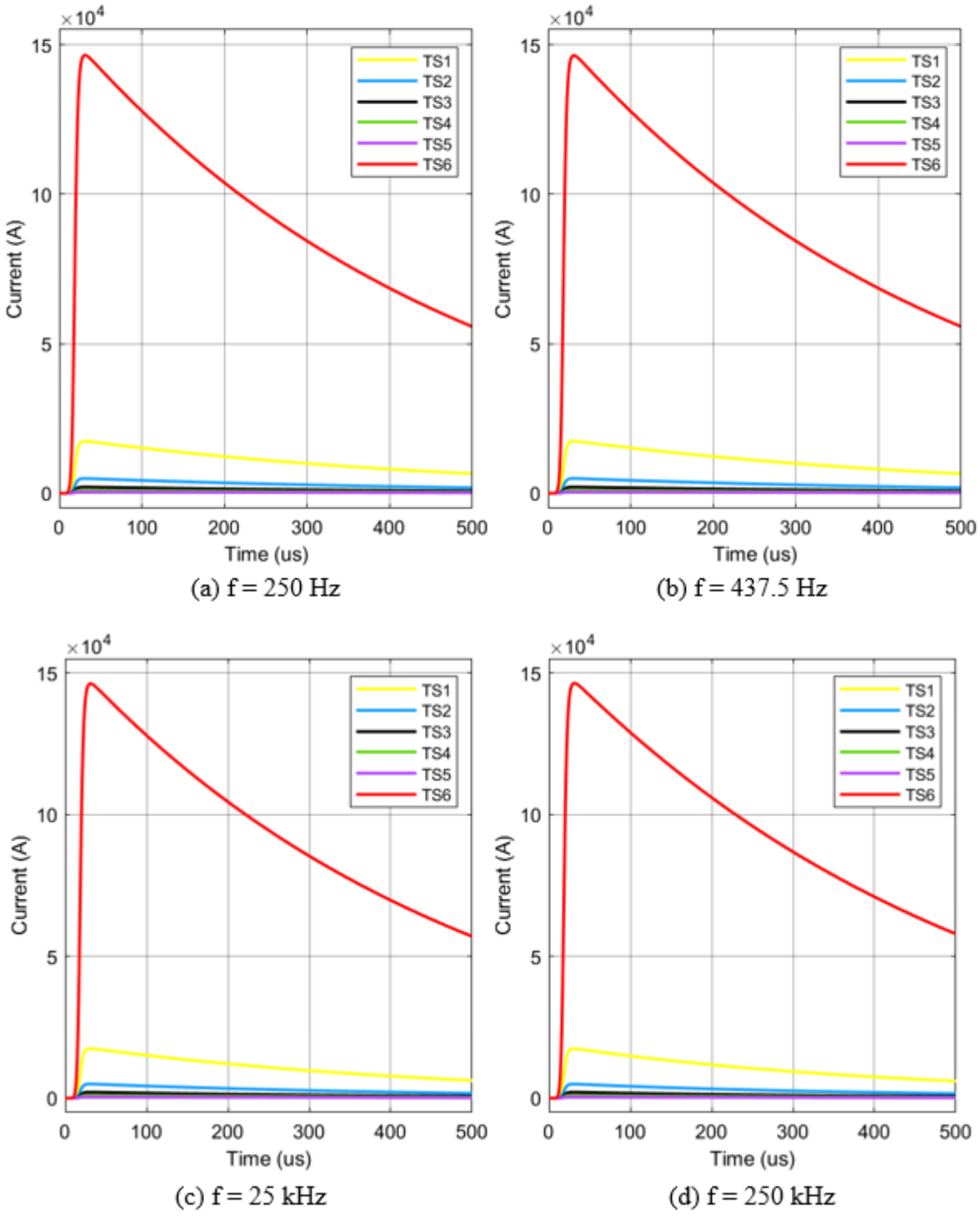

Figure 5.27. The current flowing through each of the 20 top sheets with R_g = 0.225 Ω for the pFS

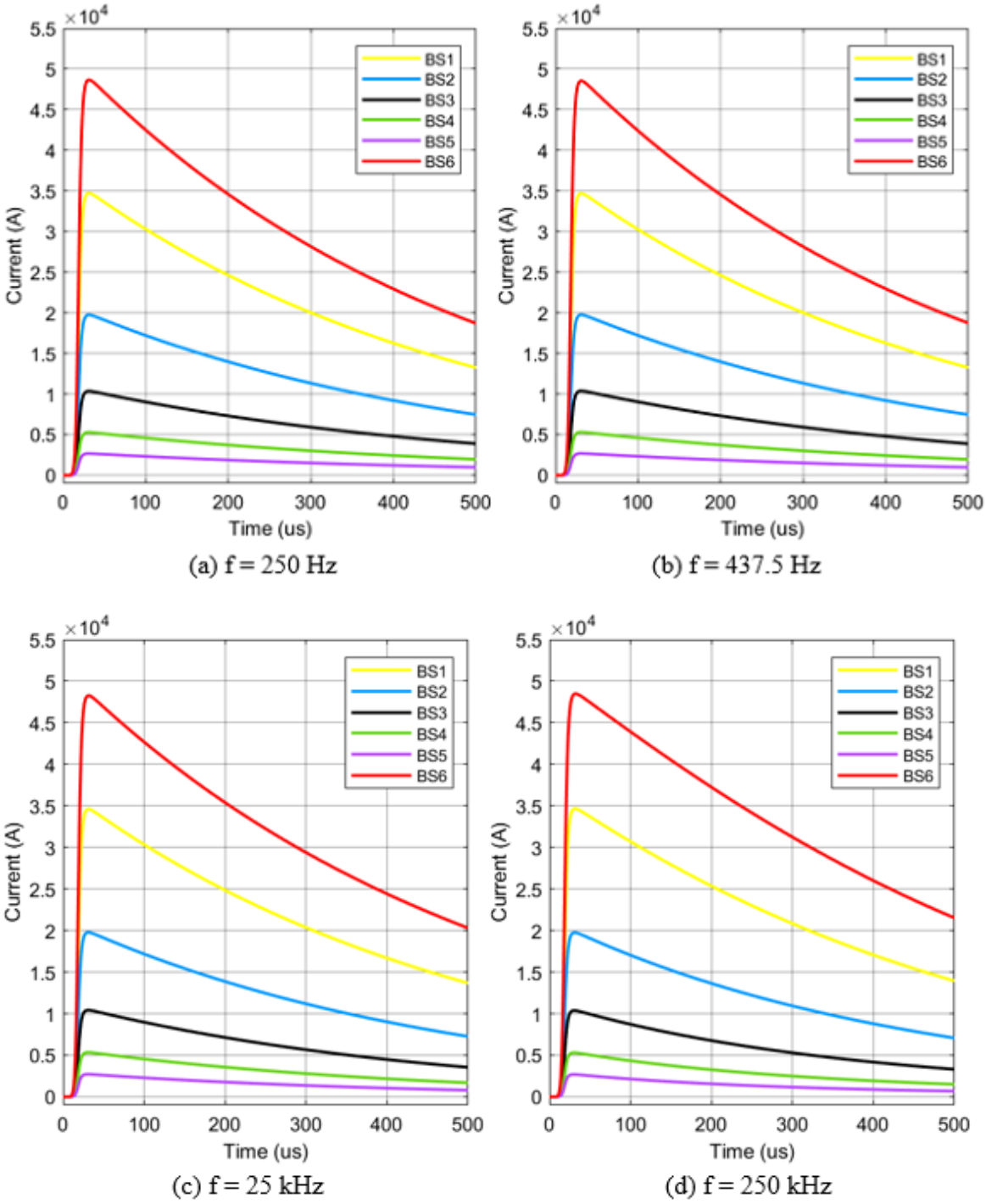

Figure 5.28. The current flowing through each of the 20 base sheets with R_g = 0.225 Ω for the pFS

From the voltage and current profiles, the waveforms for the different frequencies are quite similar. For the rest of the analysis, the pFS will be simulated at 25 kHz, the nFS will be simulated at 250 kHz, and the nSS will be simulated at 1 MHz. The appropriate RL values from the impedance extraction at each frequency will be applied in the simulation.

5.5.2 Evaluating the effect of grounding resistance on the current and voltage of the vertical steel columns

In order to analyse the effect of a high grounding resistance, the resistance is increased from R_g = 0.225 Ω to R_g = 10 Ω which is the maximum recommended grounding resistance for lightning current dissipation.

A closer look at the potential distribution across the vertical steel section at the point of strike within the first 50 µs for R_g = 0.225 Ω and R_g = 10 Ω at 25 kHz as shown in Figure 5.29 (a) and (b) reveals interesting details in terms of the voltage magnitudes. The pulse voltages across the 8 sheets with respect to the ground are different, with a peak of approximately 55 kV at the point of strike for R_g = 0.225 Ω but when R_g = 10 Ω the pulse voltage has reached the magnitude order of 2 × 10^6 V. In the multi-transmission line (MTL) ground model applied by Buccella [170] voltage level of 10^9 V was reported for the no-load case. The peak voltage level across each of the top sheets, as shown in Figure 5.30, and the base sheet voltage, which is shown in Figure 5.31, are approximately equal for both R_g = 0.225 Ω and R_g = 10 Ω.

Figure 5.32 and Figure 5.33 show the current flowing through each of the 20 steel horizontal sheets at the top and the base of the tank at 25 kHz when R_g = 0.225 Ω and R_g = 10 Ω. A comparison between Figure 5.32 (a) and Figure 5.32 (b) shows the difference in the current profile of the top sheets due to the increase in the grounding resistance. The peak current in the profile is approximately 148 kA. A similar profile is presented in Figure 5.33 (a) when R_g = 0.225 Ω and Figure 5.33 (b) when R_g = 10 Ω.

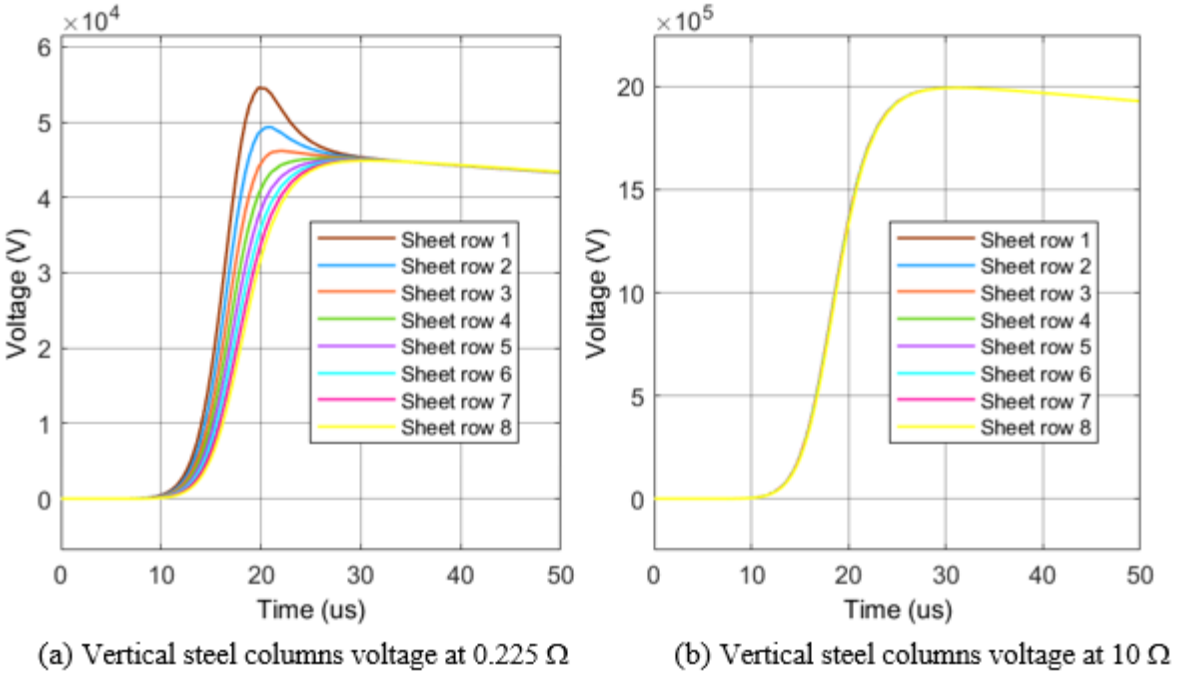

Figure 5.29. Vertical layers of steel voltage at 25 kHz for the pFS

The effect of applying R_g = 0.225 Ω and R_g = 10 Ω is further considered at 25 kHz for 1/200 μs, 100 kA lightning current, i.e., the negative First Stroke (nFS) over a duration of 500 μs.

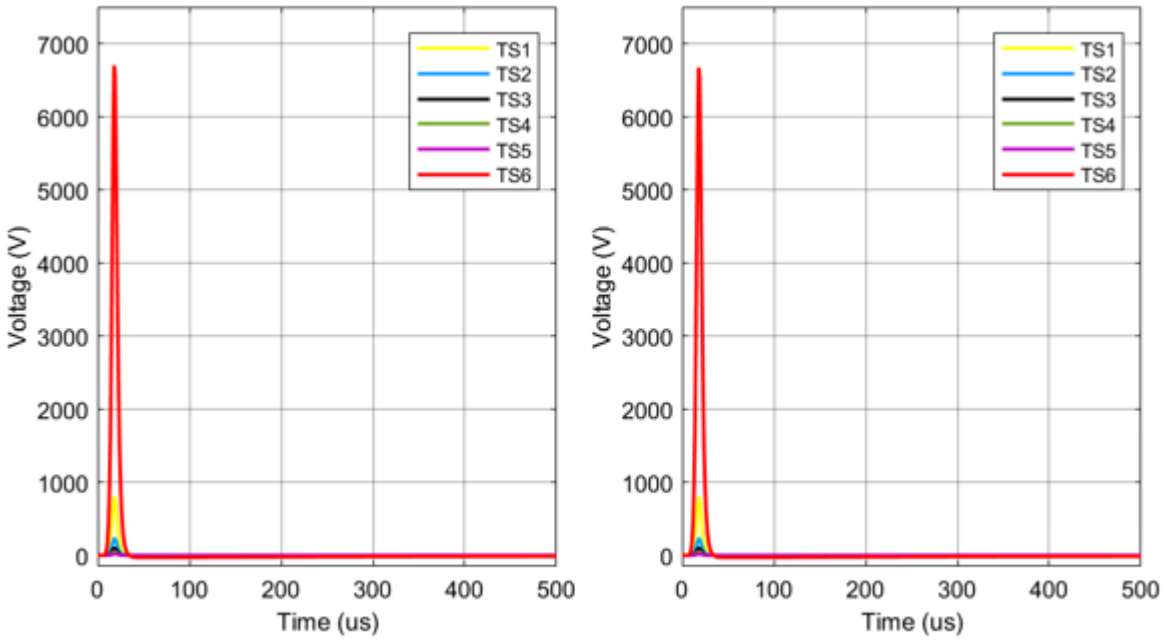

(a) Top sheet voltage at 0.225 Ω (b) Top sheet voltage at 10 Ω

Figure 5.30. The top sheet voltage at 25 kHz for the pFS

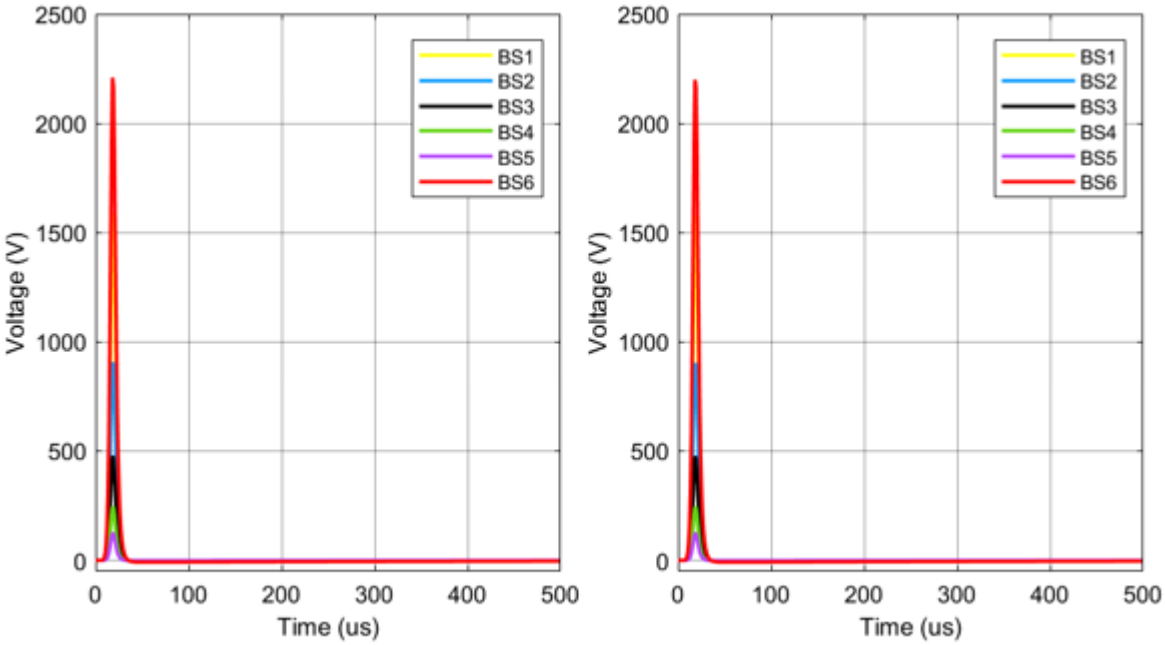

(a) Base sheet voltage at 0.225 Ω (b) Base sheet voltage at 10 Ω

Figure 5.31. The base sheet voltage at 25 kHz for the pFS

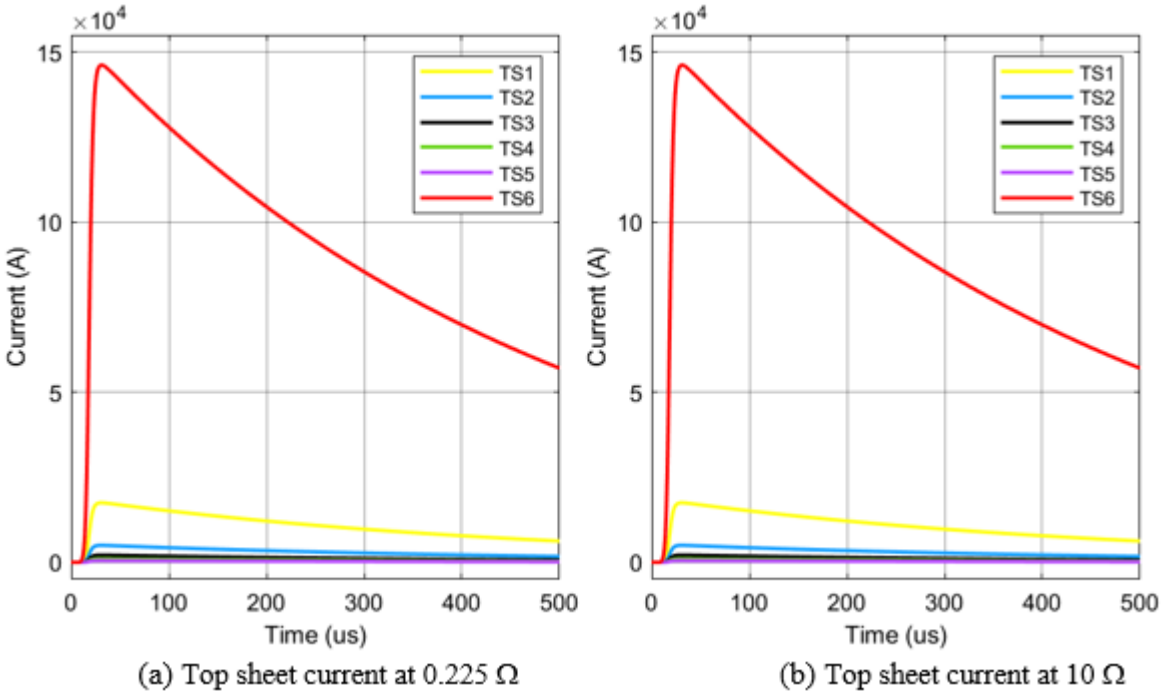

Figure 5.32. The top sheet currents at 25 kHz for the pFS

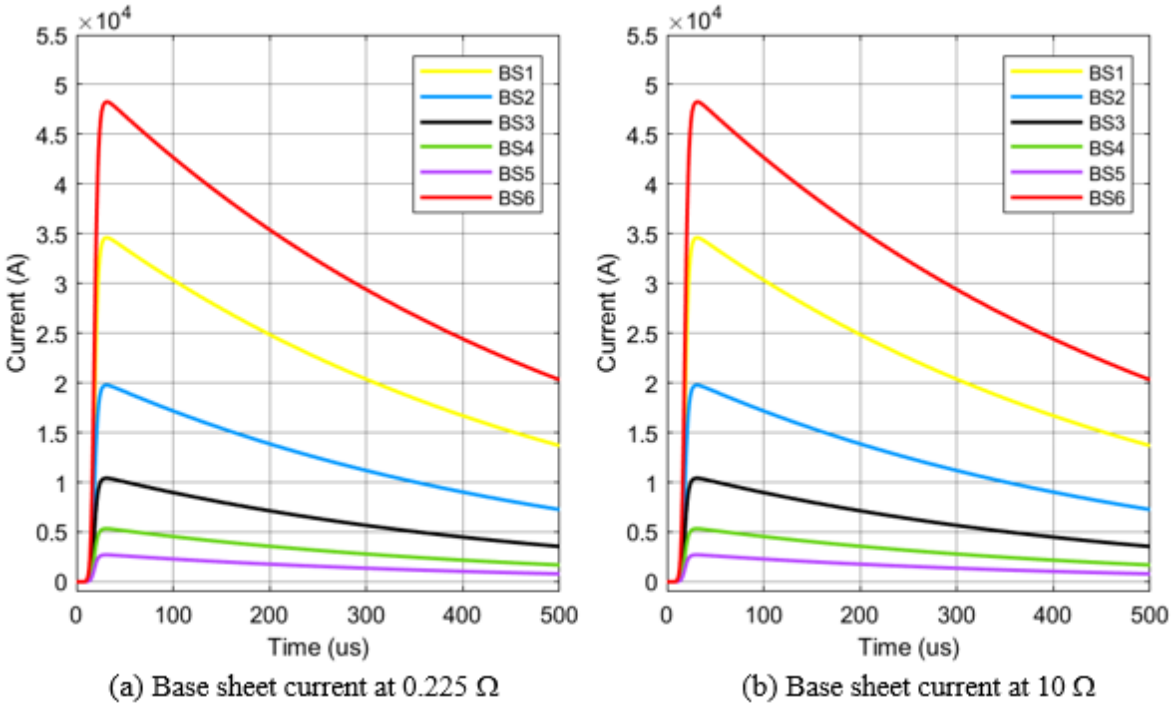

Figure 5.33. The base sheet currents at 25 kHz for the pFS

Figure 5.34 (a) and (b) consider the case of the application of the negative First Stroke lightning current to the FRT. A peak voltage of 153 kV is observed at the point of strike for R_g = 0.225 Ω but when R_g = 10 Ω, the peak voltage rose to 1 × 10^6 V. Also, when R_g = 0.225 Ω, the voltage profile sharply dropped, as shown in Figure 5.35 for the first 6 µs. This indicates a fast voltage change, but when R_g = 10 Ω the voltage is reduced gradually over the 500 µs window. For the top sheet struck by lightning and the next five sheets to one side of the struck point with values that are also symmetrical for the opposite side, the voltage

across the first row of sheets, is approximately equal for both cases, as shown in Figure 5.36 (a) and (b), with a peak voltage of 25 kV on the sheet where the strike terminated. The voltage across the base sheet, i.e., the last row of the sheets, is also approximately equal for both cases, as shown in Figure 5.37 (a) and (b), with a peak voltage of 8.3 kV on the sheet directly vertically below the strike point.

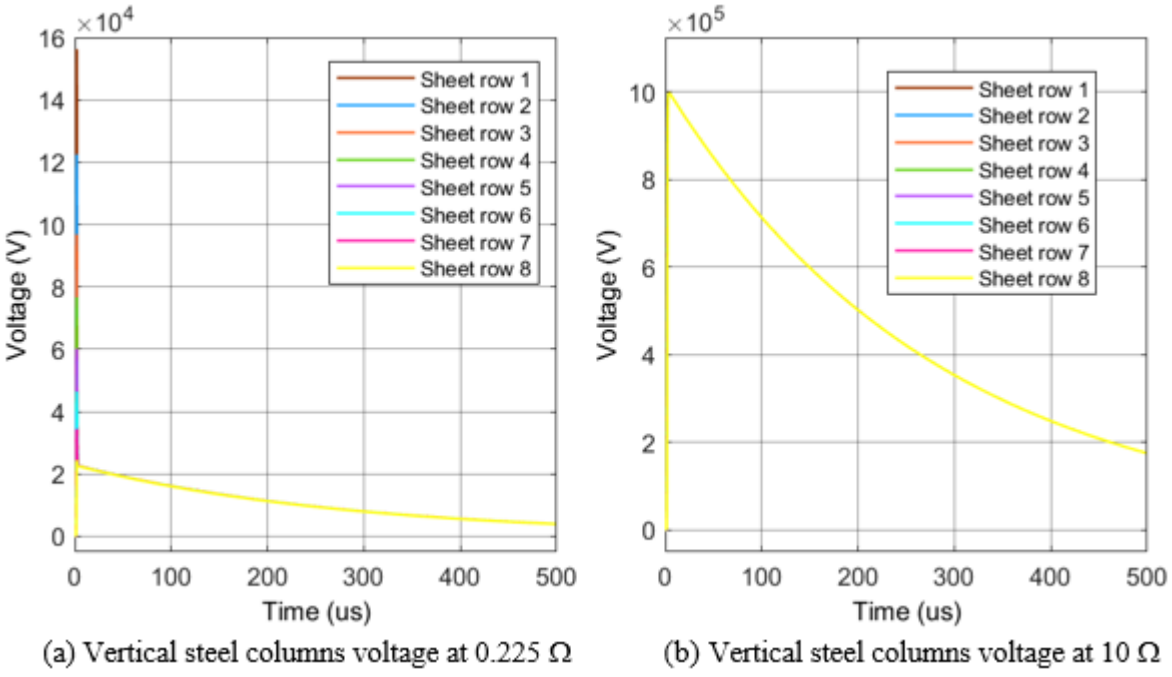

(a) Vertical steel columns voltage at 0.225 Ω (b) Vertical steel columns voltage at 10 Ω

Figure 5.34. Vertical layers of steel sheets voltage at 250 kHz for the nFS

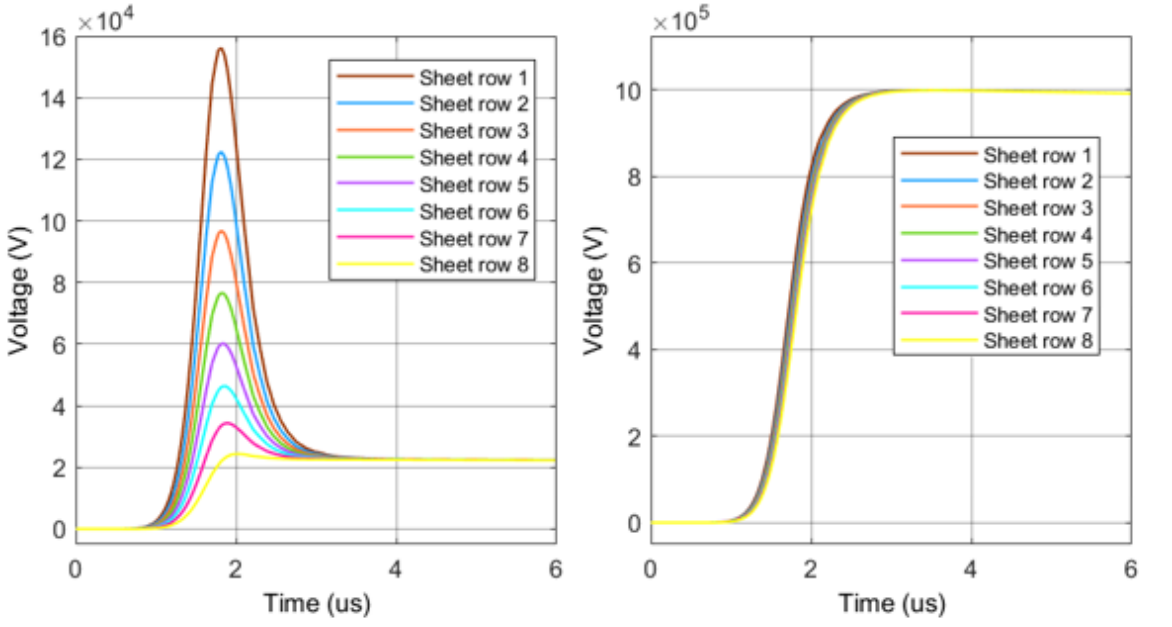

a) Vertical steel columns voltage at 0.225 Ω (b) Vertical steel columns voltage at 10 Ω

Figure 5.35. Vertical layers of steel sheets voltage at 250 kHz for the first 6 μs

The current profile through the top sheets, as illustrated in Figure 5.38 (a) and (b), are also identical for both cases, with a peak of 73 kA flowing through the sheet that was directly struck by lightning. Figure 5.39 (a) and (b) show the current flowing through each of the 20 steel horizontal sheets at the base of the tank for the nFS. The current magnitudes for the two grounding resistances are reasonably similar.

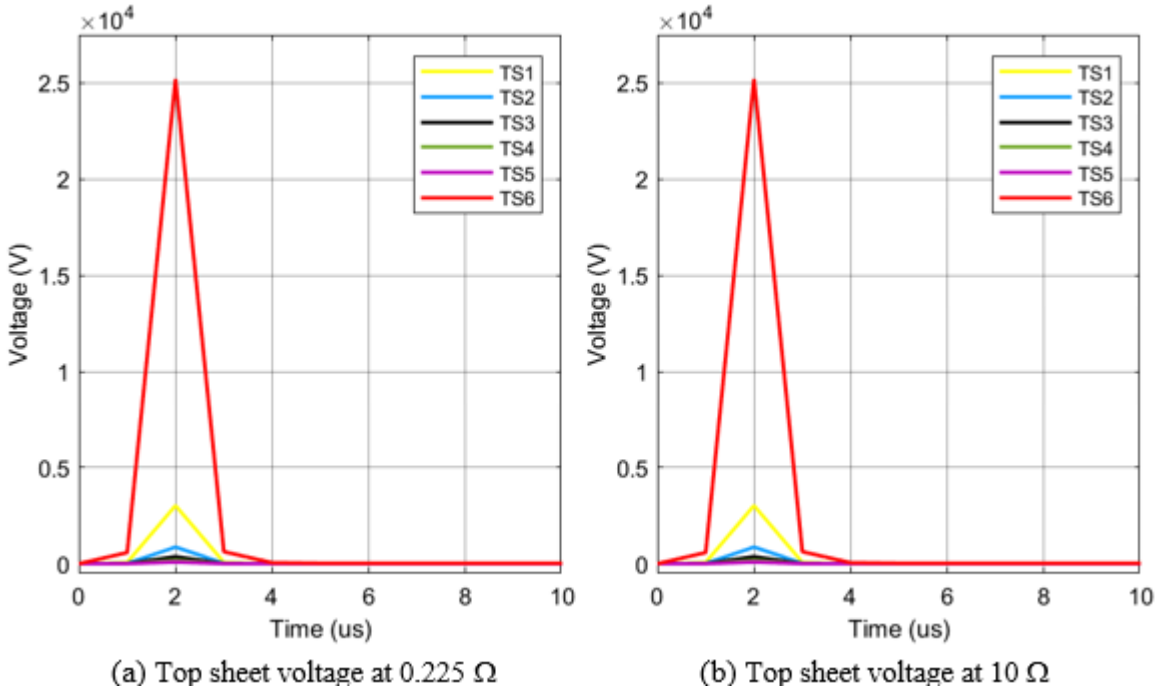

Figure 5.36. The top sheet voltage at 250 kHz for the nFS for the first 10 μs

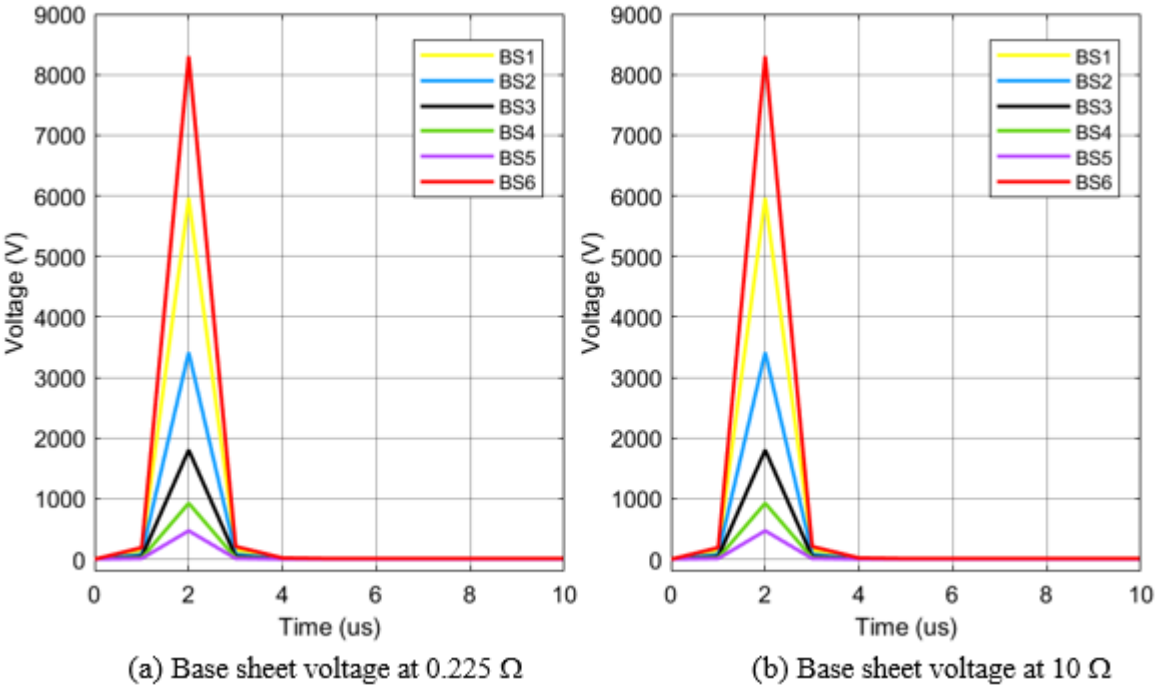

Figure 5.37. The base sheet voltage at 250 kHz for the nFS for the first 10 μs

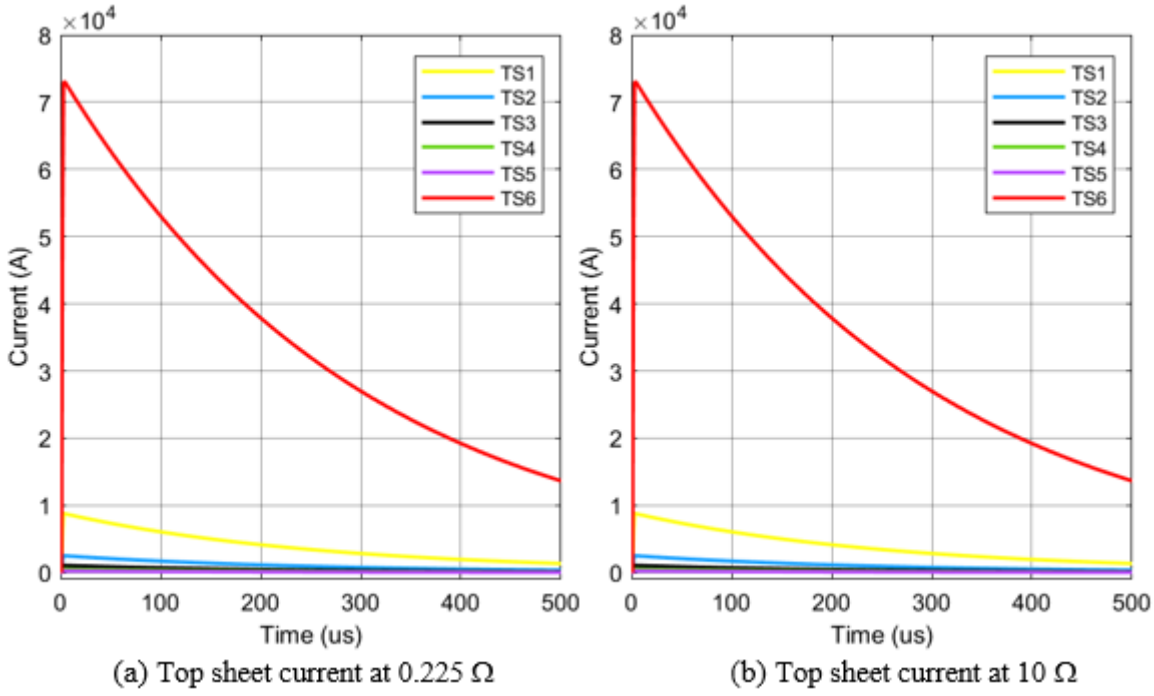

Figure 5.38. The top sheet currents at 250 kHz for the nFS

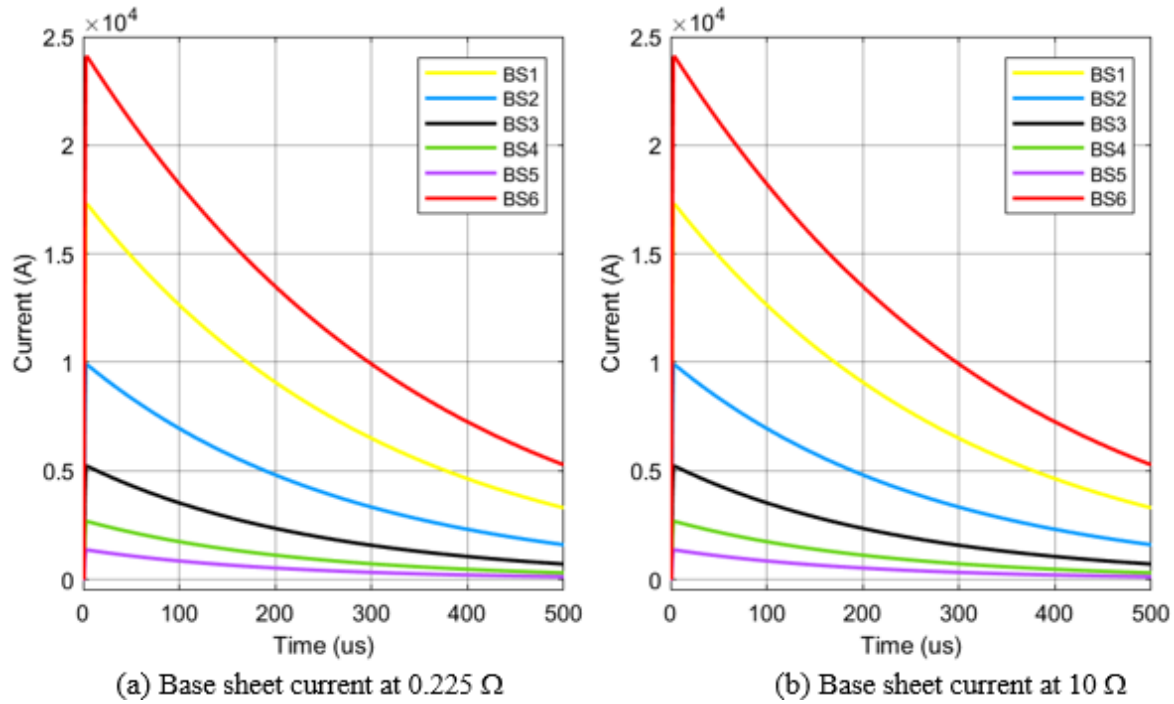

Figure 5.39. The base sheet currents at 250 kHz for the nFS

The effect of applying R_g = 0.225 Ω and R_g = 10 Ω is also considered at 1 MHz for 0.25/100 µs, 50 kA lightning current, i.e., the negative Subsequent Stroke (nSS) over a duration of 500 µs. A peak voltage of 0.3 MV is observed at the point of strike with respect to the ground when R_g = 0.225 Ω and this increased to 0.577 MV when R_g = 10 Ω as shown in Figure 5.40 and Figure 5.41 respectively. For the top sheet section, a peak voltage of 85 V is observed as shown in Figure 5.42 and for the base sheet section, a peak voltage of 31.5 V is observed as shown in Figure 5.43 for both grounding scenarios.

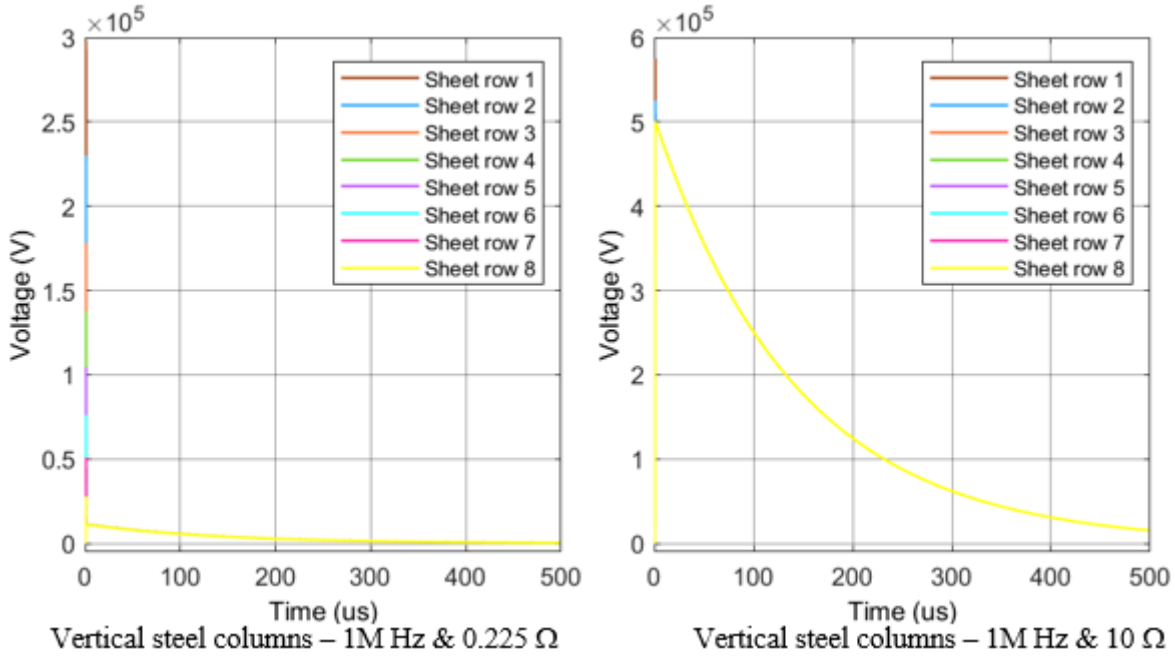

Figure 5.40. Vertical layers of steel sheet voltage at 1 MHz for the nSS

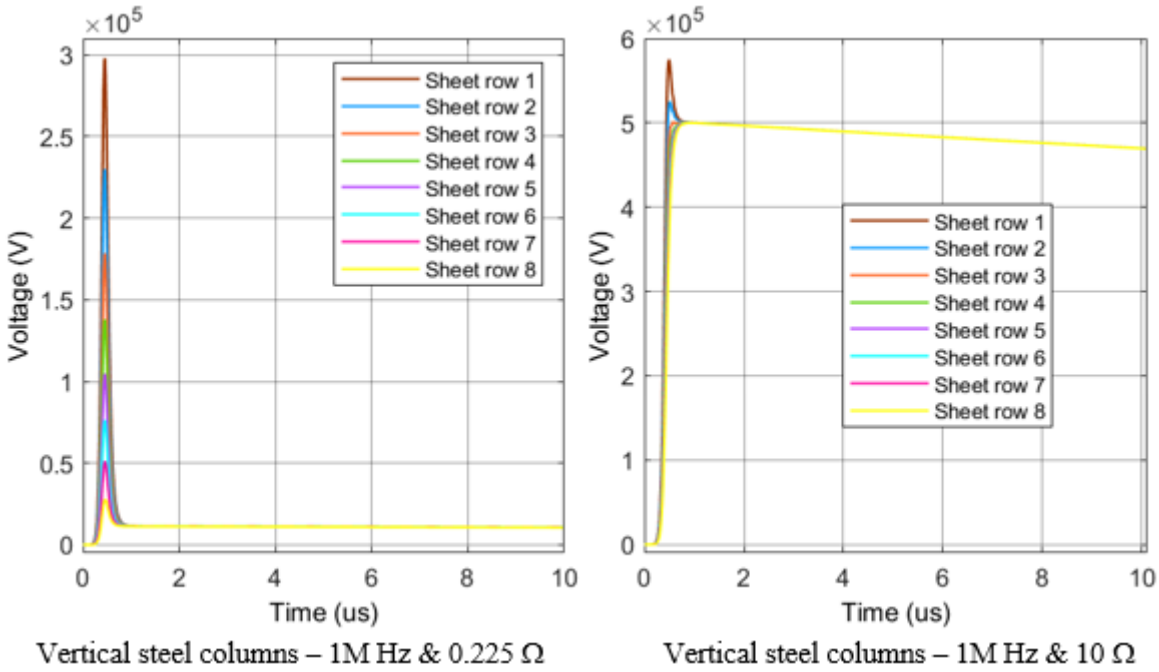

Figure 5.41. Vertical layers of steel sheets voltage at 1 MHz for the nSS for the first 10 μs

A peak current of approximately 36.6 kA flowed through the top sheet as shown in Figure 5.44. For the base sheet, a peak current of approximately 12 kA flowed as shown in Figure 5.45 without a significant difference for when R_g = 0.225 Ω and R_g = 10 Ω.

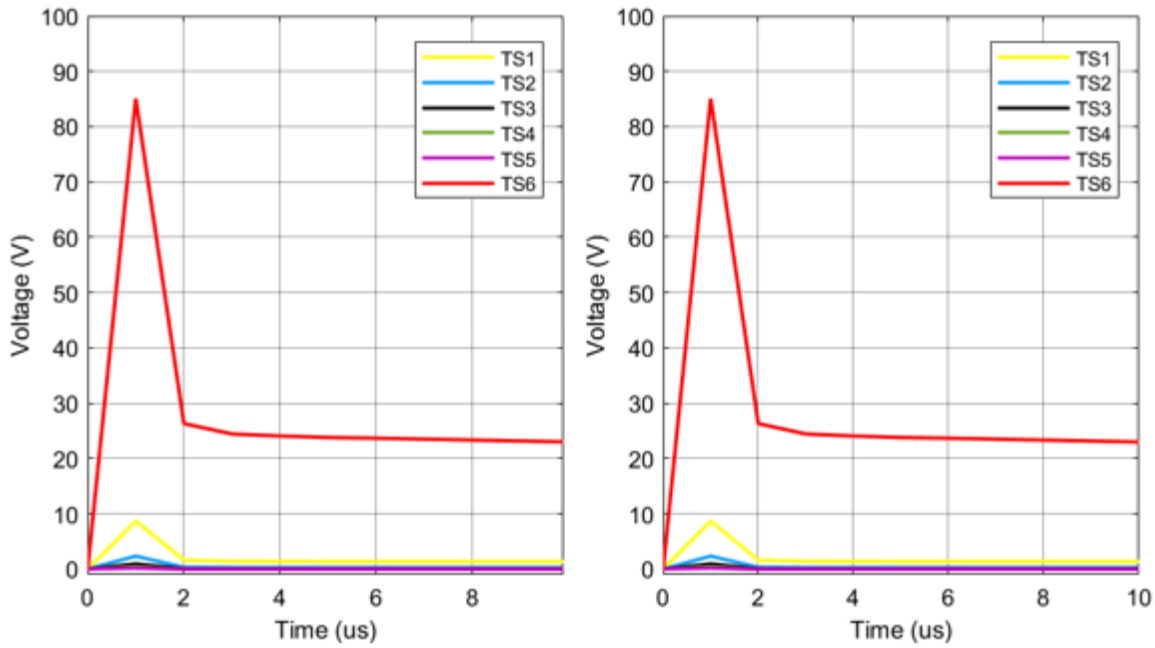

Figure 5.42. The top sheet voltage at 1 MHz for the nSS for the first 10 μs

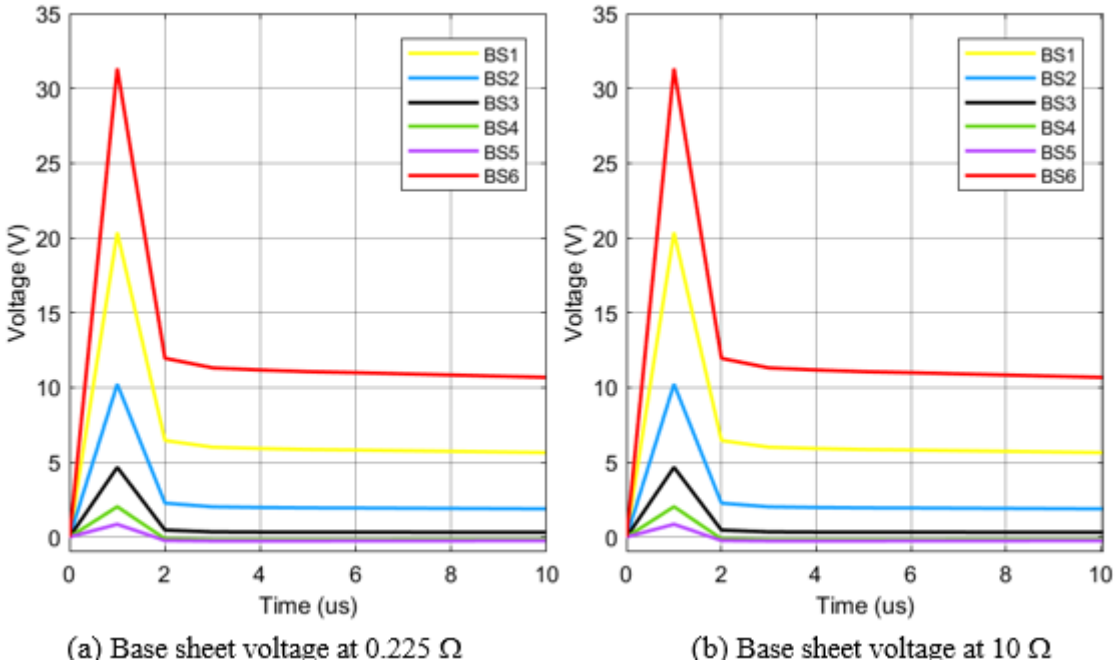

Figure 5.43. The base sheet voltage at 1 MHz for the nSS for the first 10 μs

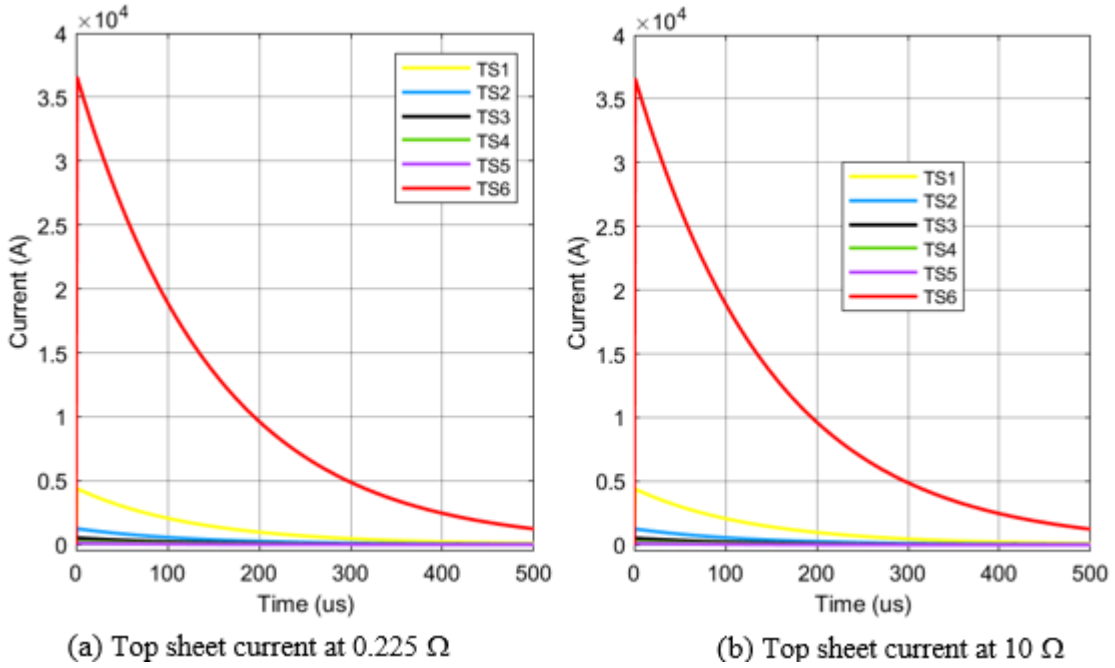

Figure 5.44. The top sheet currents at 1 MHz for the nSS

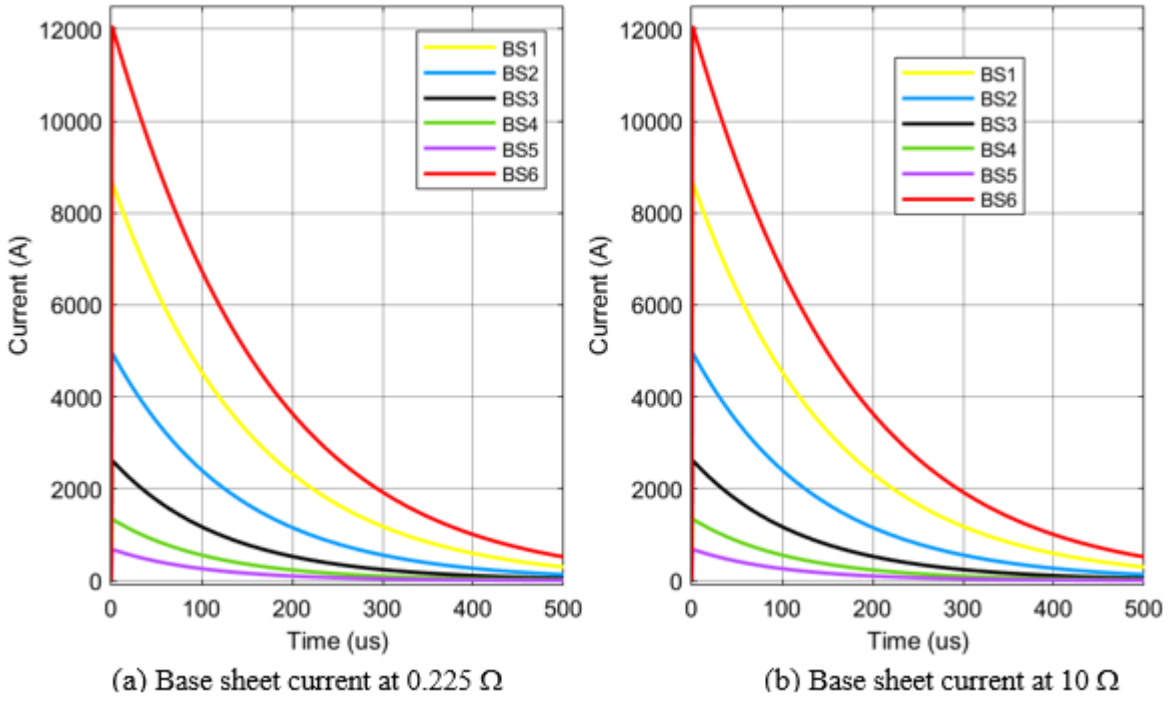

Figure 5.45. The base sheet currents at 1 MHz for the nSS

5.5.3 Evaluating the effects of multiple interconnected flow paths on the steel columns

This section deals with modelling the use of interconnected catenary wires as air terminals above the FRT, which will create parallel paths for the flow of the lightning current when directly struck, as illustrated in Figure 5.46. In this case, the lightning current can flow

through three parallel paths to the rim of the floating roof tank. This will affect the current and voltage distribution across the steel sections of the FRT.

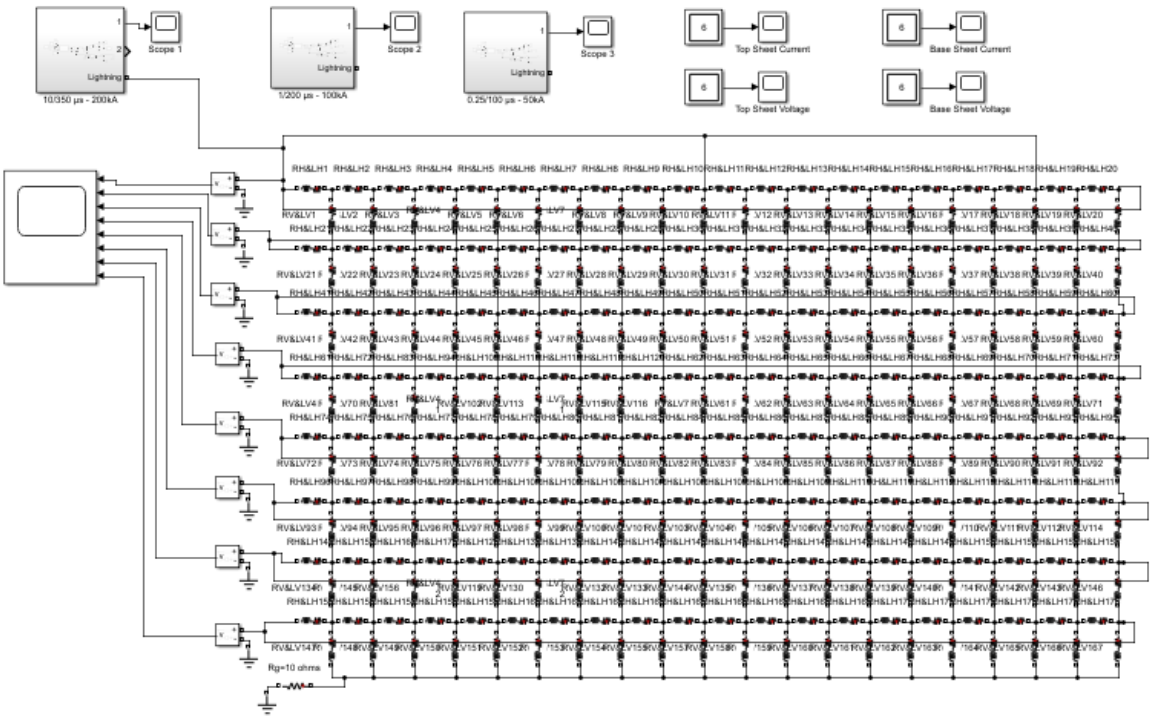

Figure 5.46. Lightning current flowing through interconnected air terminations

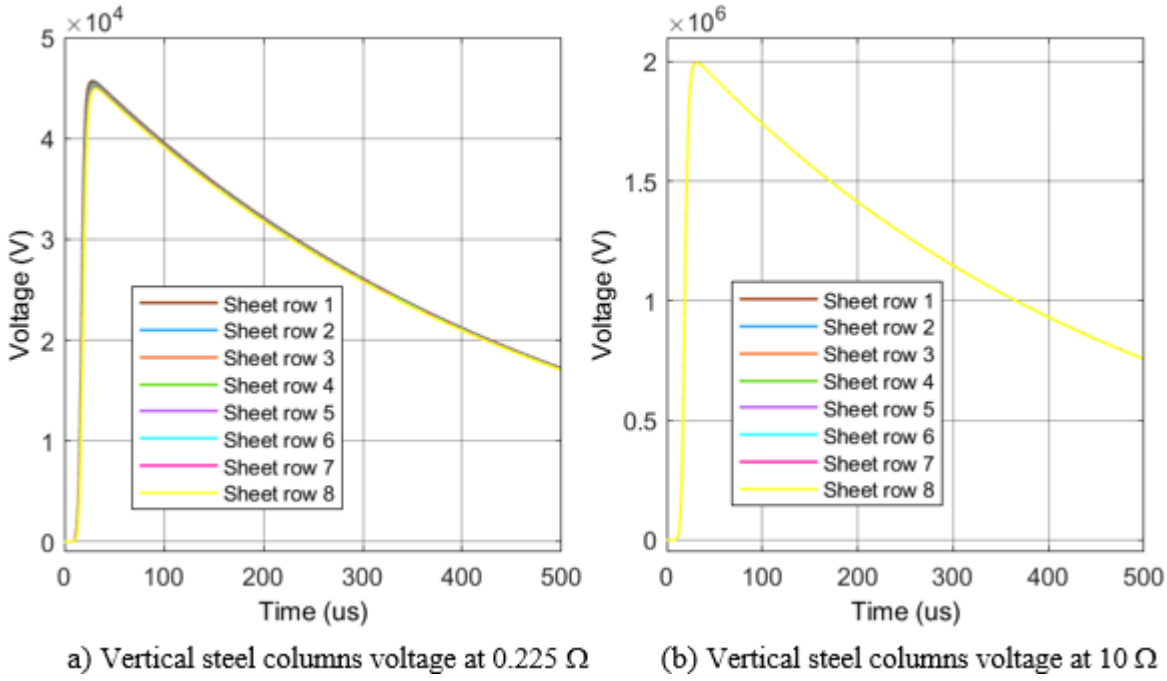

Figure 5.47. The voltage across the vertical layers for interconnected air terminals for the pFS

With the application of 10/350 µs, 200kA lightning current, the availability of three alternative flow paths did not change the voltage profile across the 8 vertical sections of the FRT for R_g = 10 Ω. The result is similar to that of Figure 5.29 (b) with no parallel path, but with a low resistance R_g = 0.225 Ω, there is a significant change in the voltage distribution

as shown in Figure 5.47 (a) compared to the profile in Figure 5.29 (a). The peak voltage had reduced from about 55 kV to 45 kV due to the multiple flow paths.

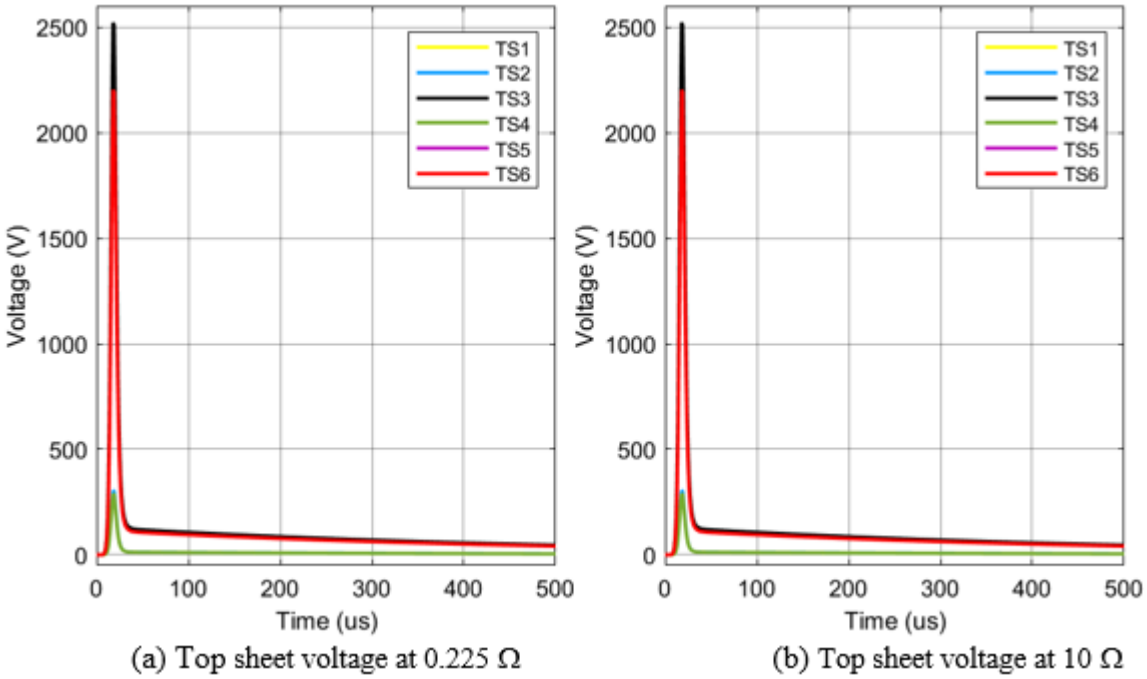

Figure 5.48. The voltage across the top sheets for interconnected air terminals for the pFS

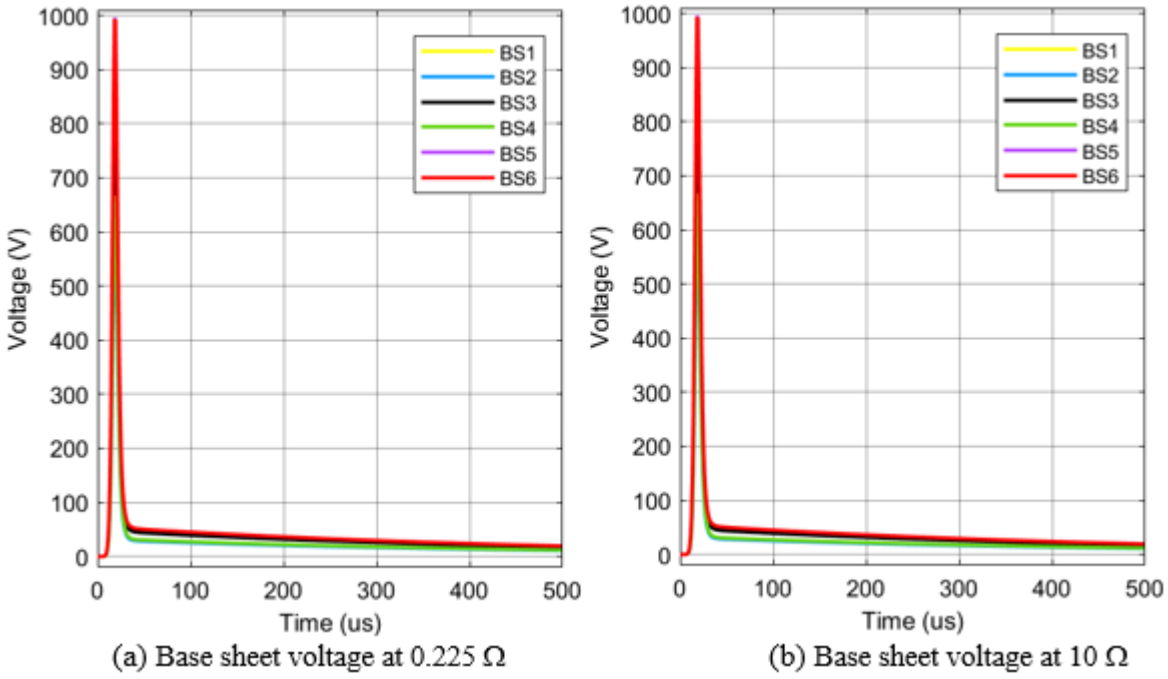

Figure 5.49. The voltage across the base sheets for interconnected air terminals for the pFS

In Figure 5.48, the peak voltage across the top sheets for this case has also reduced to 2.5 kV from 6.7 kV, as shown in Figure 5.30. Figure 5.49 (a) and (b) show a peak voltage of 1 kV across the base sheets of the FRT, and this indicates a reduction from approximately 2.2 kV in Figure 5.31 due to the multiple flow path. Figure 5.50 (a) and (b) show the current flowing

through the rows of sheets at the top of the FRT with the use of multiple paths. When compared with Figure 5.32, the peak current had reduced approximately to 54 kA from 148 kA because the current is better shared among the steel shells due to the multiple flow paths created by the catenary wires. A similar analysis is presented in Figure 5.51 for the base sheet currents with a peak current of 22 kA as compared with 48 kA in Figure 5.33.

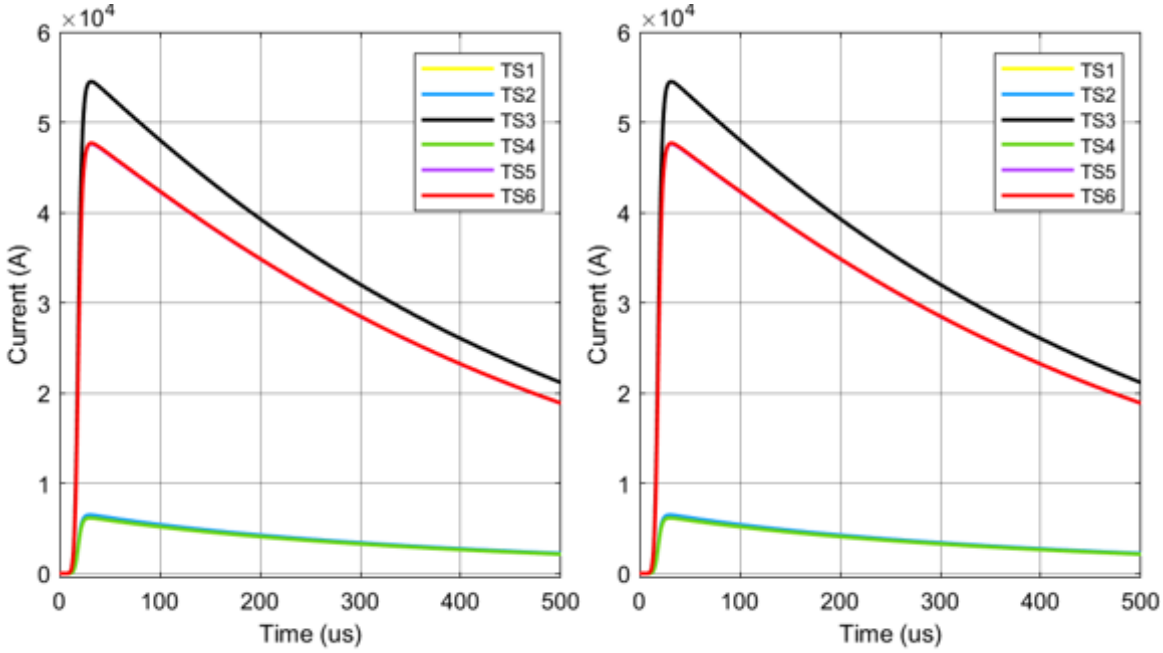

Figure 5.50. The currents through the top sheets for interconnected air terminals for the pFS

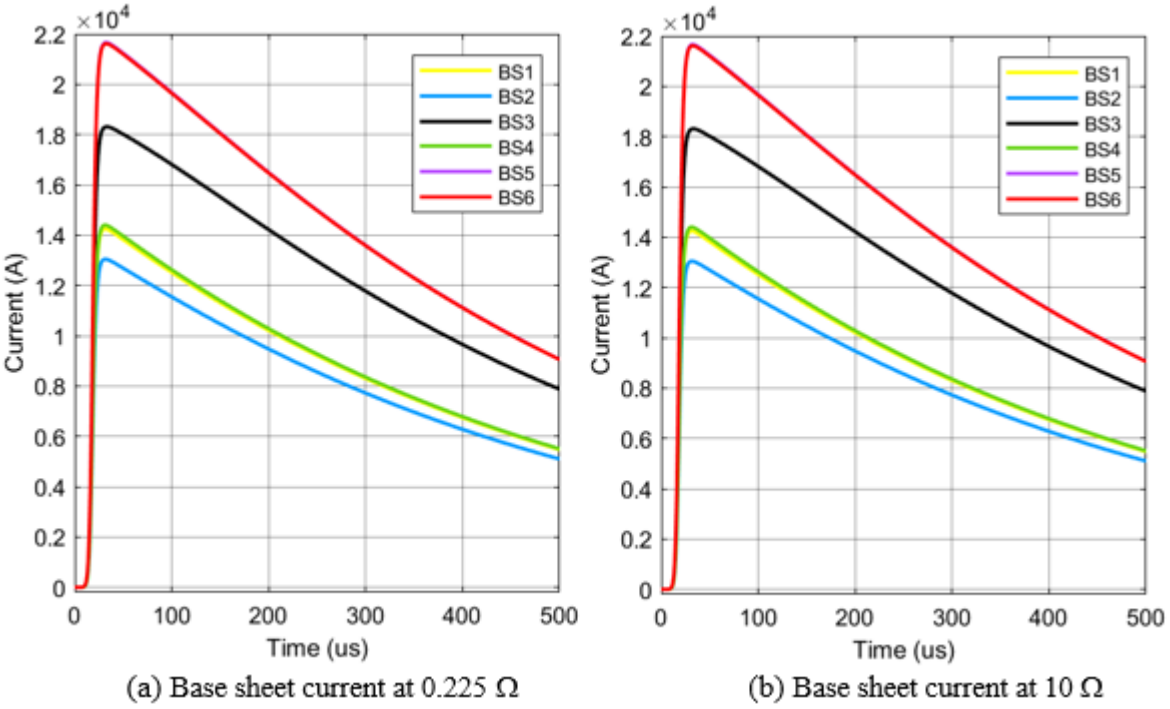

Figure 5.51. The currents through the base sheets for interconnected air terminals for the pFS

5.5.4 Modelling of the shell to roof lightning interaction

The shell and the roof of a FRT are separated by an air gap of about 20 cm. The electrical resistance of air is ideally infinite, but in reality, it depends on factors such as the presence of moisture, vapour and electrical charges. The shell-to-roof air gap needs to be modelled to simulate the effect of the air gap on the electrical voltage build up between the tank shell and the roof, coupled with the tendency of the air gap to break down and conduct when the electric field is sufficient. Air has a starting breakdown electric field of 30 kV/cm which may vary with the air pressure and environmental conditions. For a 20 cm wide air gap, a breakdown voltage of 517.25 kV will be applied according to Hinrichsen [175]. The air gap is modelled with a variable resistance of 1 GΩ before the breakdown occurs, and after the breakdown, the resistance switches to 100 mΩ. Two air gap areas are considered on either side of the roof, at the strike point (Air gap 1) and at the opposite end (Air gap 2). The roof of a FRT, whether a single deck supported with compartmentalised pontoons (buoyant floats) or other designs to keep the roof afloat or the double-deck type, is typically made of carbon steel, aluminium or stainless steel materials for either the non-contact or the full contact type. To estimate the resistance and the inductance of the roof, this study models a simplified, flat plate with a 10 mm thickness, single deck roof of mild steel sheet. The roof is 59.6 m wide with 2 m wide circular pontoons at the edge, as illustrated in Figure 5.52, which shows the setup for extracting the RL parameters of the roof. The resistance and the inductance of the roof obtained from Q3D are plotted in Figure 5.53 across a range of frequencies.

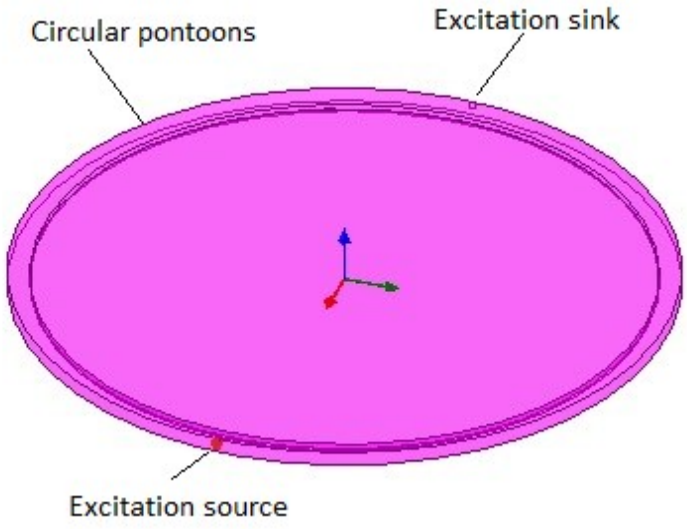

Figure 5.52. A single deck floating roof with pontoons at the edge

At the FRT's shell-roof interface, an electrical breakdown will typically occur at a specific region where the gap voltage is sufficient. For this case, a portion of the shell to roof air gap is approximated as a simple cuboid volume that is 20 cm wide, 0.6 m long and 0.6 m in breadth. Practically, the air gap dielectric properties will vary between pure air and flammable air vapour mixture. In this case, an air dielectric is assumed, as illustrated in

Figure 5.54. The modelled breakdown region has an approximate capacitance (C) of 16 pF and a spark energy (E_c) of 2.14 J.

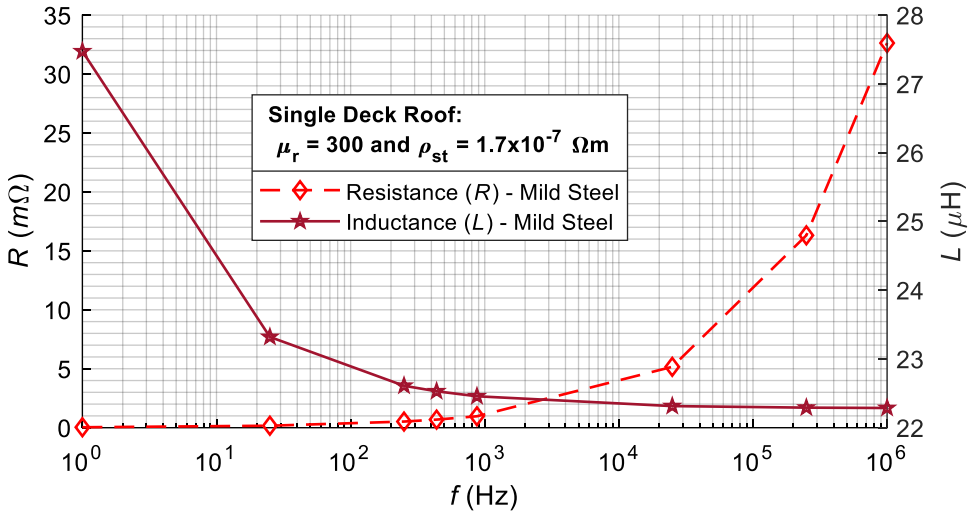

Figure 5.53. The RL values of a single deck floating roof

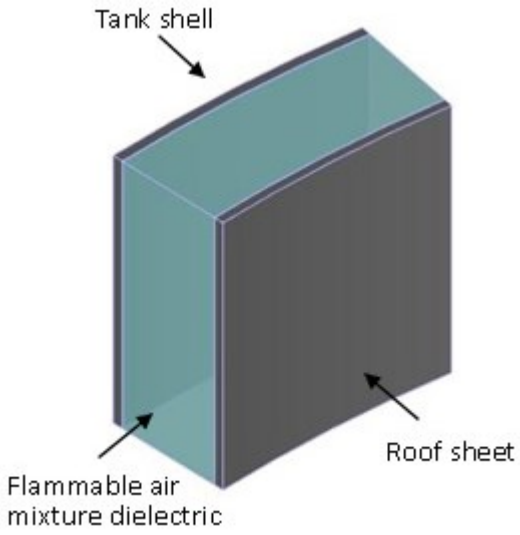

Figure 5.54. Shell-roof air gap capacitance modelling

The permittivity of free space $\varepsilon_0 = 8.854\times10^{-12}$ F/m gives

$$C = \frac{\varepsilon_0 A}{d} = \frac{8.854\times10^{-12}\times0.36}{0.2} = 15.937\times10^{-12} \approx 16\,\text{pF} \tag{5.23}$$

$$E_C = \frac{C\times U^2}{2} = \frac{16\times10^{-12}\times517.25^2\times10^6}{2} = 2.14\,J \tag{5.24}$$

Figure 5.55 shows the RC air gap and RL roof model. The roof is connected between two points on the tank shell's RL model. A is the surface area, and d is the distance between the two perpendicular steel plates.

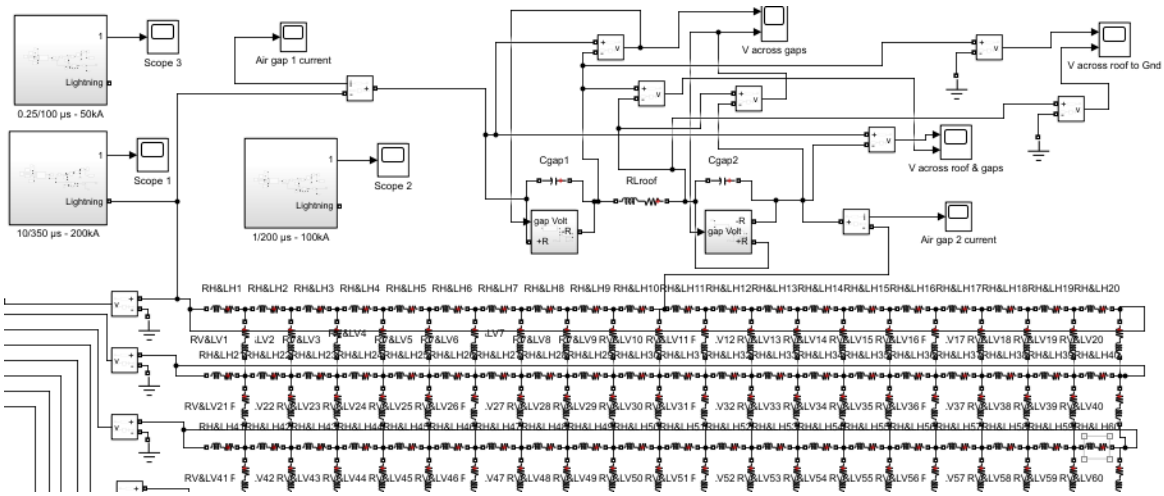

Figure 5.55. A sectional view of the RC air gap and RL roof model

5.5.4.2 A strike to the shell with the lightning current flowing to the roof

A lightning current of 10/350 µs, 200 kA for 500 µs is applied to the tank shell model with RL values at 25 kHz in Figure 5.55 to study the effects on the FRT when the lightning current crosses the air gap from the tank shell to the floating roof. As shown in Figure 5.56 and Figure 5.57, the peak voltage across each of the gaps is approximately 14.4 kV with R_g = 0.225 Ω and R_g = 10 Ω, while the peak voltage across the roof itself is less than 30 mV, but in Figure 5.58, the peak voltage on the roof with respect to the ground is about 45 kV at the point of strike for R_g = 0.225 Ω and 2 MV for R_g = 10 Ω. This shows the danger of having any grounded objects in contact with the floating roof when lightning strikes.

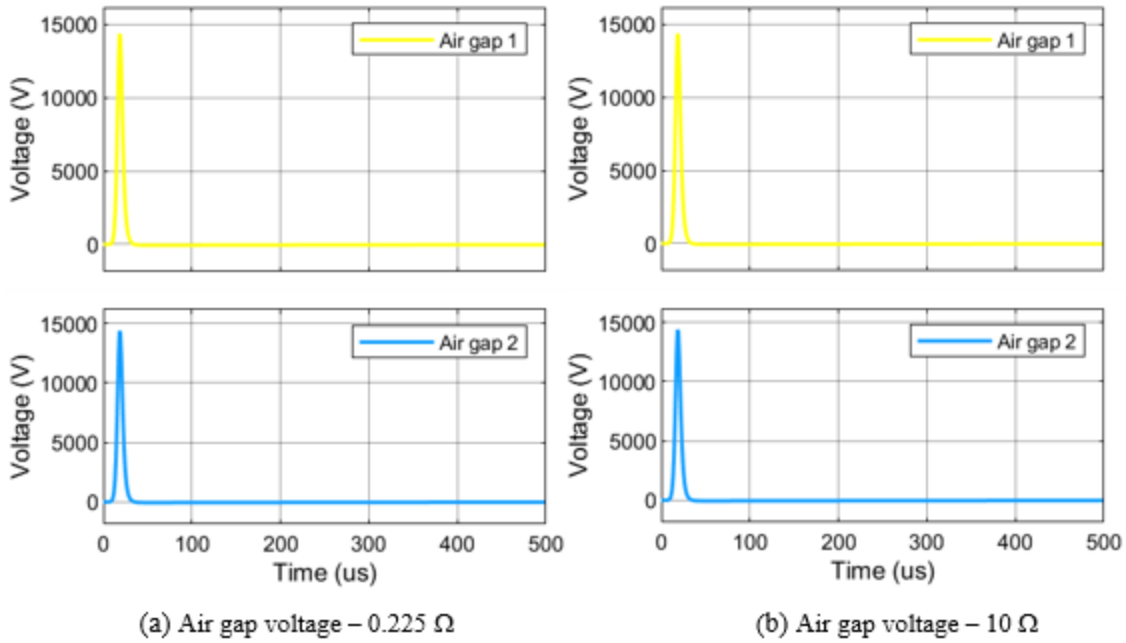

Figure 5.56. The voltage across the air gaps at the strike point and the opposite end for pFS

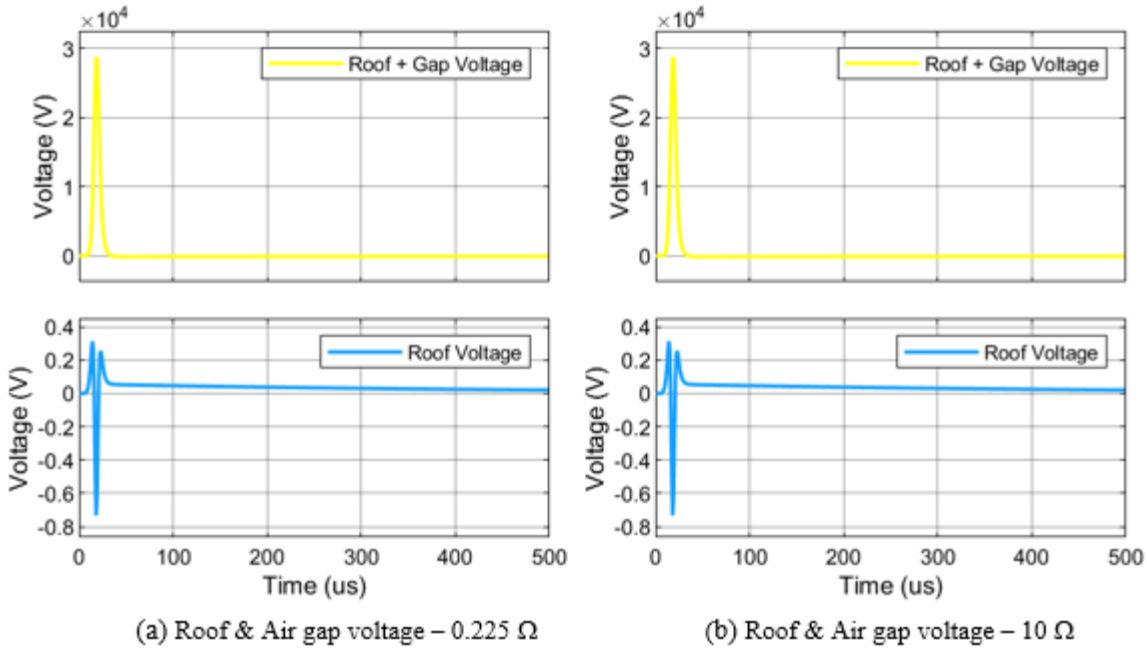

Figure 5.57. The voltage across the air gaps and the roof for pFS

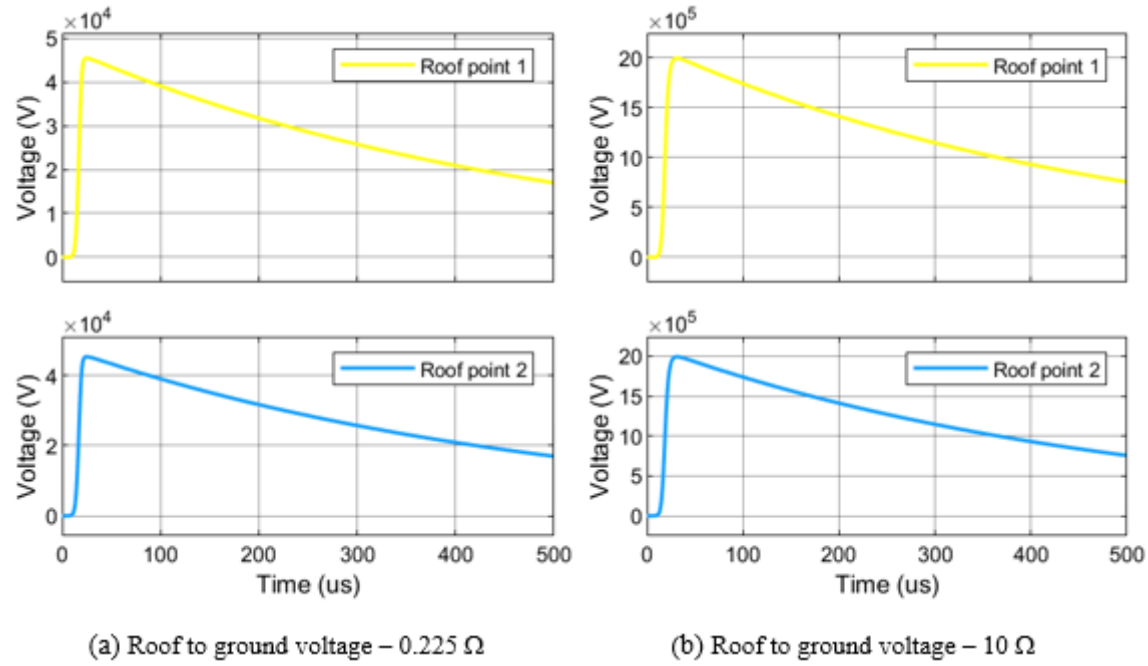

Figure 5.58. The voltage on the roof with the ground as a reference for pFS

A similar result is observed for 1/200 µs, 100 kA at 250 kHz lightning current (nFS), as shown in Figure 5.59 for R_g = 10 Ω. For this case, the peak voltage across the air gap is about 54 kV, but in Figure 5.59 (b), when the voltage on the roof is referenced to the ground, the peak voltage is 1 MV. For 0.25/100 µs, 50 kA at 1 MHz lightning current (nSS), as shown in Figure 5.60 for R_g = 10 Ω. For this case, the peak voltage across the air gap is about 2.2 kV, but in Figure 5.60 (b), when the voltage on the roof is referenced to the ground, the peak voltage is 498 kV at roof point 1 and 501 kV at roof point 2.

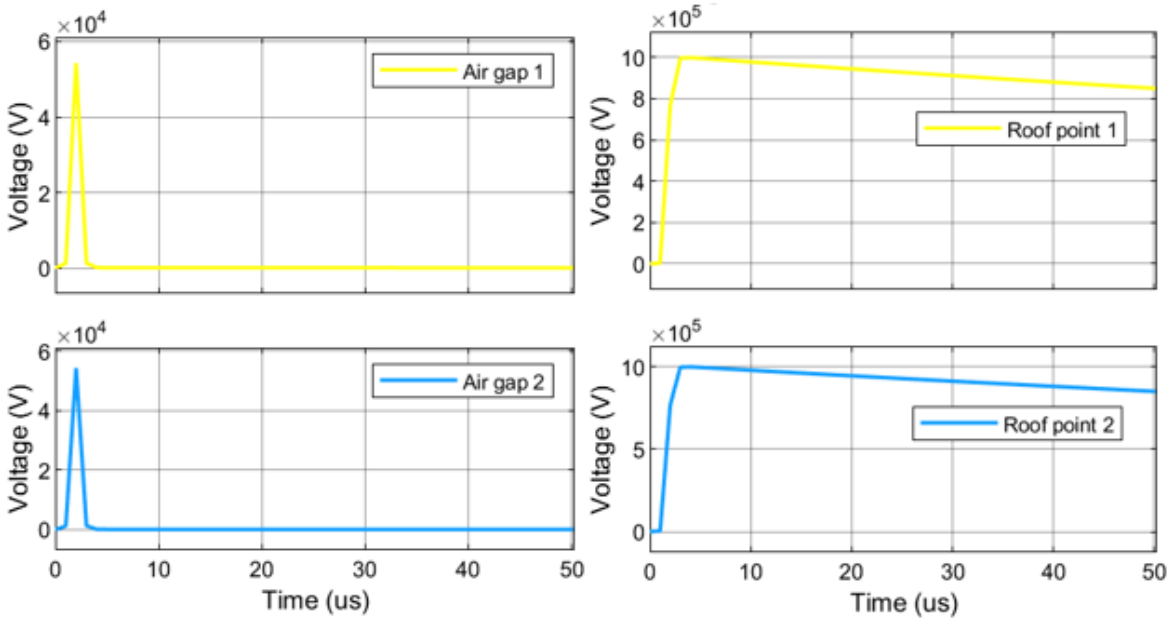

Figure 5.59. The voltage across the air gap and the roof with the ground as a reference for the nFS

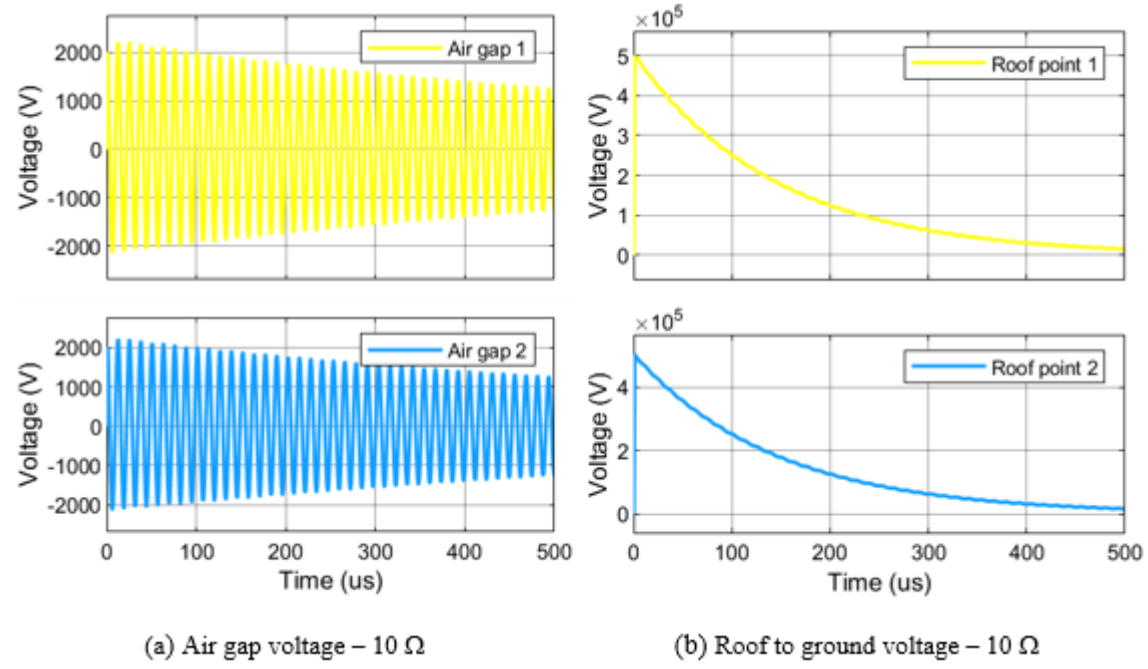

Figure 5.60. The voltage across the air gap and the roof with the ground as a reference for the nSS

5.5.4.3 A strike to the roof with the lightning current flowing to the shell

This section investigates the impact of a direct lightning strike to the roof with two air gaps on either side of the roof. When lightning terminates on the roof, it means that all the lightning current must flow through any available shunts and the air gap to the tank shell. The model is shown in Figure 5.61.

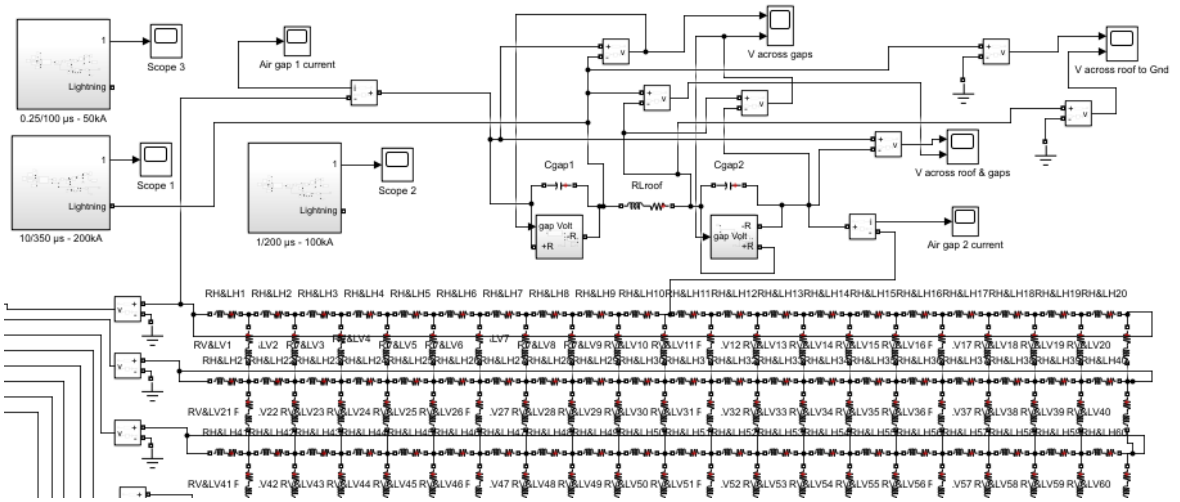

Figure 5.61. Sectional model view for a direct strike to the roof

A lightning current of 10/350 µs, 200 kA for 500 µs is applied to the floating roof with RL values at 25 kHz to study the effects on the FRT when the lightning current crosses the air gap from the tank roof to the shell. As shown in Figure 5.62 and Figure 5.63, the peak positive voltage across air gap 1 and air gap 2 is approximately 211 kV, this voltage is negative for air gap 1 due to the polarity of the voltmeter. while the peak voltage across the roof itself is approximately 34.7 kV with R_g = 0.225 Ω and also when R_g = 10 Ω. In Figure 5.64, the peak voltage on the roof with respect to the ground is about 211 kV at the point of strike and 211 kV at the opposite end with R_g = 0.225 Ω and 2.01 MV at the strike point and 1.99 MV at the opposite end when R_g = 10 Ω. This simulation shows how significantly dangerous it is for all the lightning current to terminate on the isolated floating roof as compared to the results for a direct strike to the tank shell.

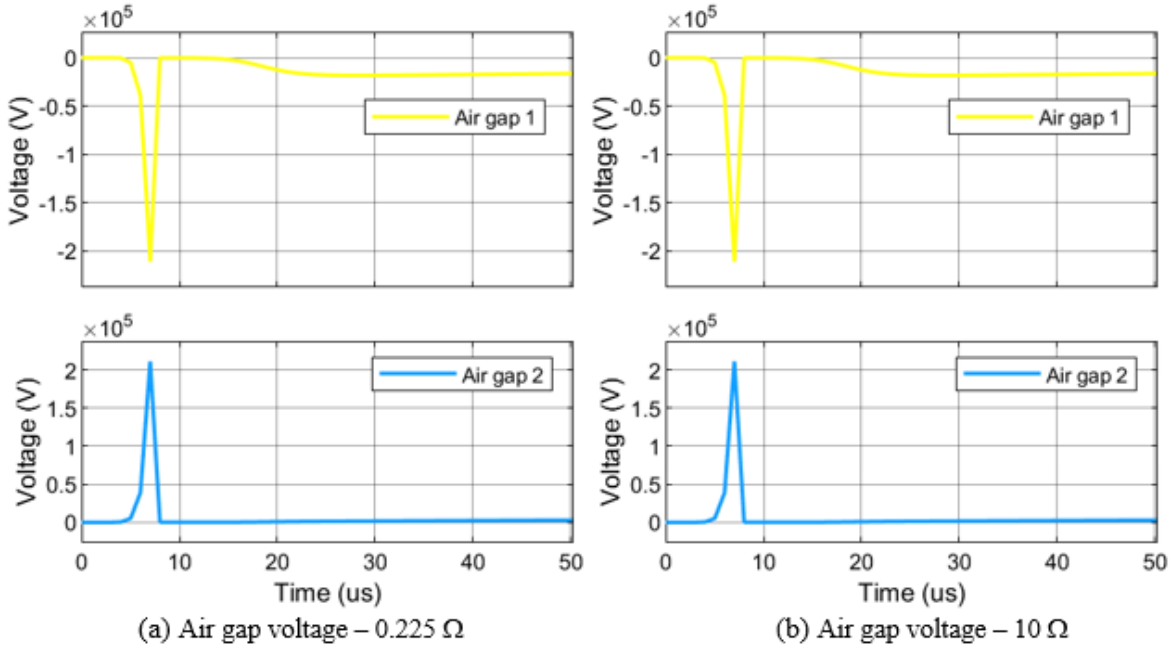

Figure 5.62. The voltage across the air gaps at the strike point and the opposite end for pFS

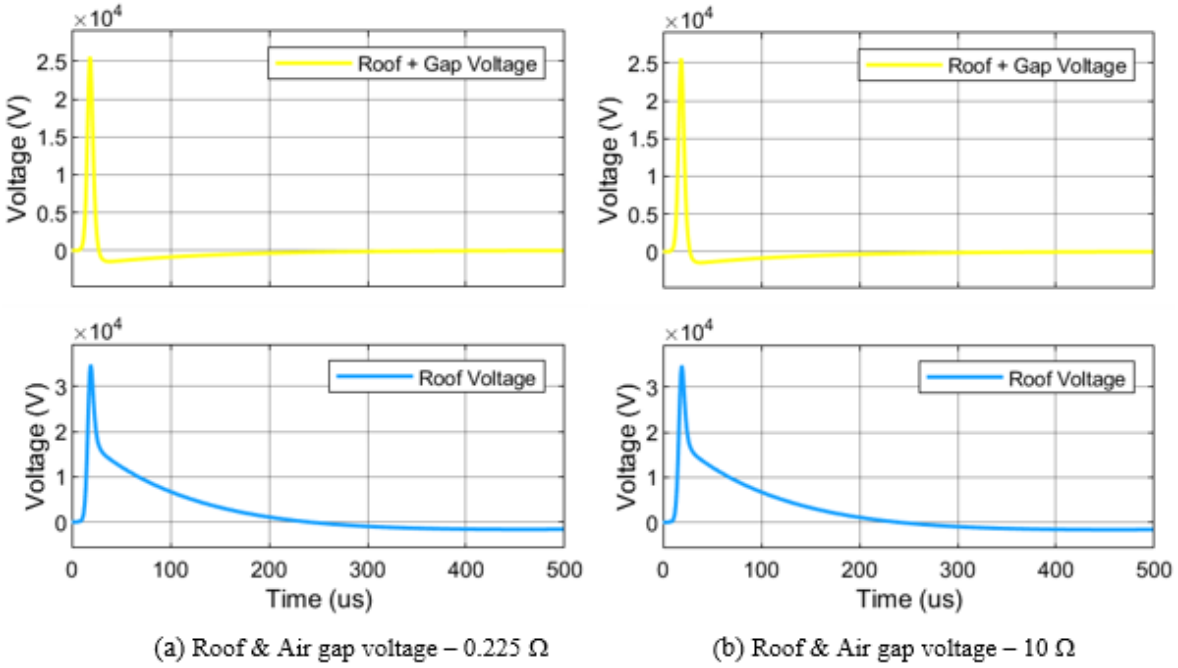

Figure 5.63. The voltage across the air gaps and the roof for pFS

The result for 1/200 µs, 100 kA at 250 kHz lightning current (nFS) is shown in Figure 5.65 for R_g = 10 Ω. For this case, the peak voltage across air gap 1 is about 9.66 kV in the negative direction because the voltage is higher at roof point 1 than the voltage on the opposite point on the tank shell, and 2.6 kV for the air gap 2. The peak voltage to ground at air gap 1 is 1.01 MV and 0.99 MV at air gap 2. The result for 0.25/100 µs, 50 kA at 1 MHz lightning current (nSS) is shown in Figure 5.66 for R_g = 10 Ω. For this case, the peak voltage across air gap 1 is about 4.67 kV in the negative direction, and 0.97 kV for air gap 2, and the peak voltage to ground at air gap 1 is 505 kV and 500 kV at air gap 2.

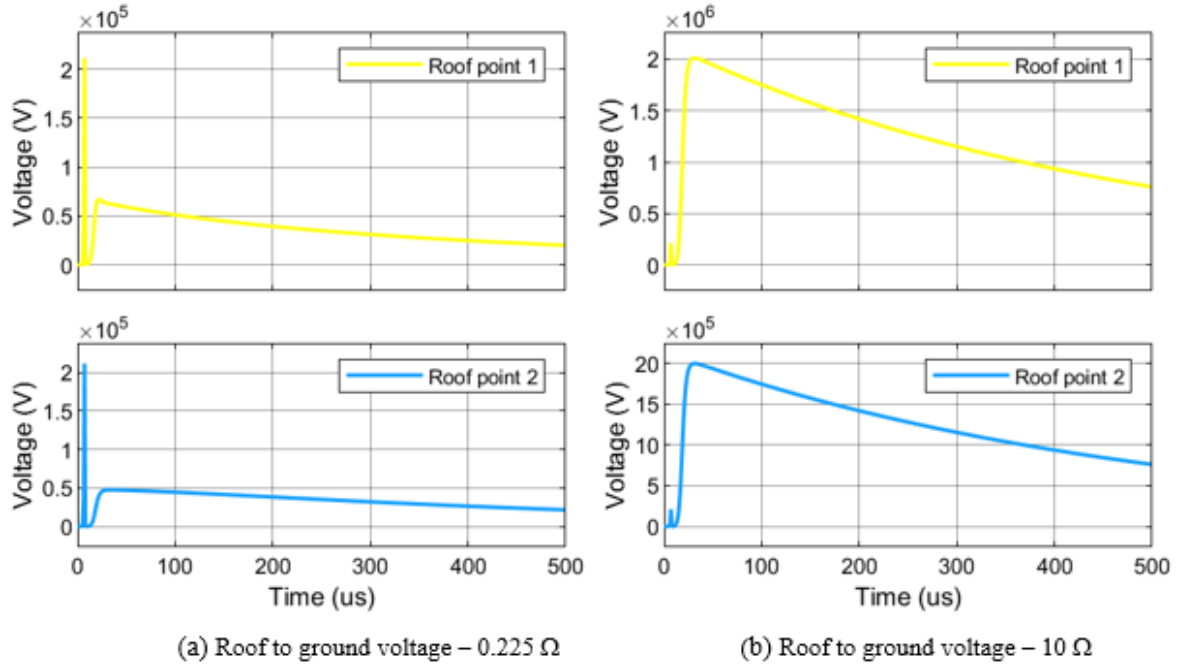

Figure 5.64. The voltage on the roof with the ground as a reference for pFS

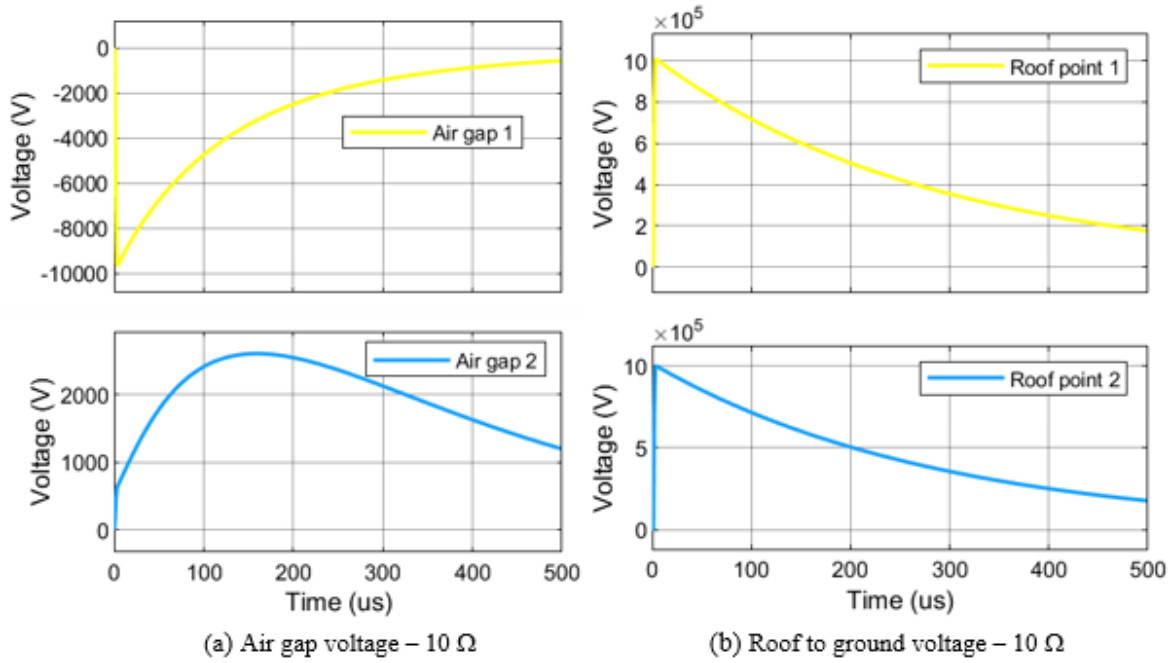

Figure 5.65. The air gap and the roof voltage with the ground as a reference for the nFS

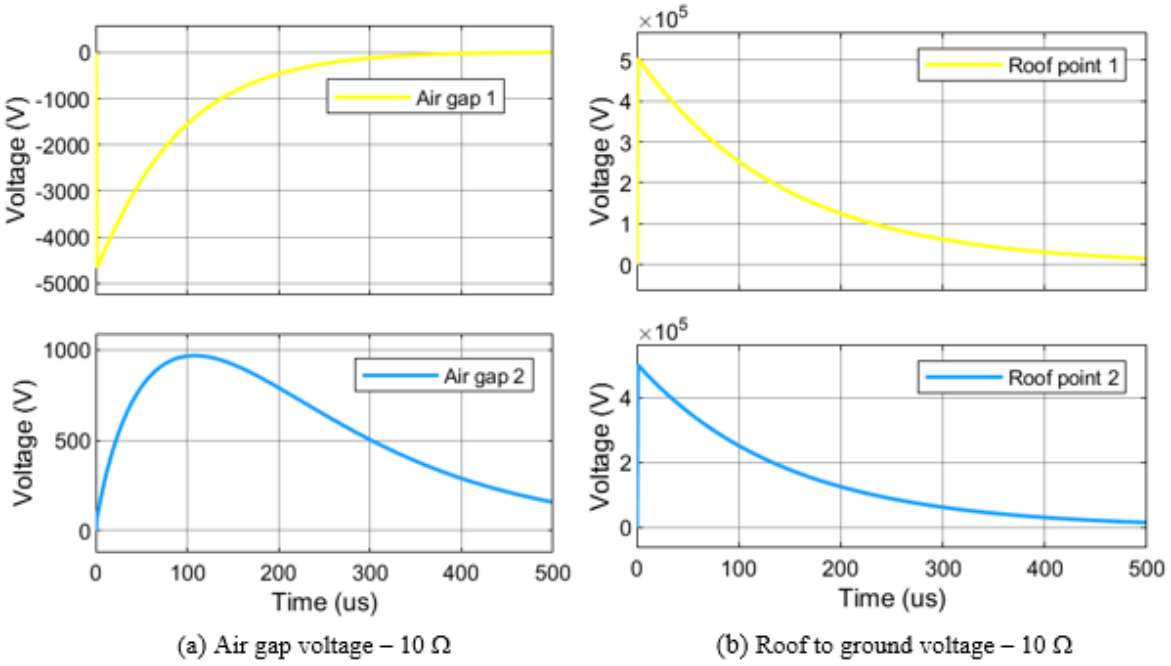

Figure 5.66. The air gap and the roof voltage with the ground as a reference for the nSS

5.5.4.4 The impact of lightning on a pipe connected to a FRT

Previous studies in various forms have investigated the impact of lightning strikes on pipes. The impact of lightning transient voltage on buried pipes and associated corrosion protection systems has been investigated using ATP-EMTP [176]. In a related study, Caulker, et al. [177] determined that a minimum safety distance of 167 cm is required for an impulse current of 40 kA to prevent flashes between pipes within a network of pipes. The induced voltage and the breakdown effect of high voltage transmission lines coupled with lightning

strikes on the breakdown of the protective polyethylene sheath of buried gas pipelines have also been studied [178, 179]. To further investigate the impact of a direct strike on a FRT, this section considers the case of a FRT with a 100 m long pipe section connected directly to the tank shell. The pipe is modelled using pipe data (resistance and inductance per unit metre) of an 8" diameter mild steel pipe modelled in Q3D. The mild steel has an external coating of Fusion Bonded Epoxy (FBE) with a resistance of $3.3 \cdot 10^{13}$ Ω/m and longitudinal coating capacitance of 10.42 pF/cm^2 [176].

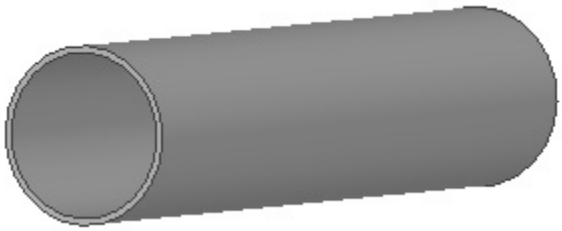

Figure 5.67. 1 m long 8" pipe model in Q3D

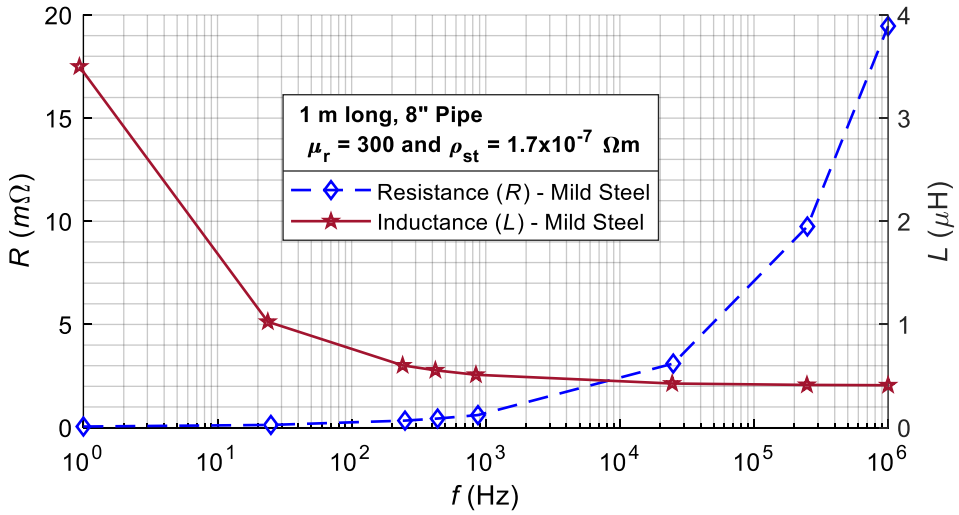

Figure 5.68. The RL values of a 1 m long 8" mild steel pipe

To set up the transient analysis for a FRT connected to a pipe, the impedance of an 8" pipe with an outer diameter of 8.625" (21.91 cm) and an internal diameter of 7.98" (20.27 cm), using the pipe dimensions from ANSI Schedule 40, was extracted on Q3D for a unit meter length of the pipe using mild steel as pipe material [180, 181] as shown in Figure 5.67. The mild steel pipe has a transverse coating capacitance of 28.8 pF/m. The resistance and inductance (*RL*) values across multiple frequencies are presented in Figure 5.68. The pipe in this study is modelled as a surface crude oil pipe that can be grounded at points along its length. There are five welded pipe sections, and each section is 20 m long. Three grounding scenarios are considered in the model. In the first case, the pipe has only one grounding near the tank, i.e., R_{g1}, and in the second case, the pipe has multiple grounding along its length, and it is grounded at three points, i.e., R_{g1}, R_{g2}, and R_{g3} as illustrated in Figure 5.69. For the

third case, the pipe has only one grounding at the far end, i.e., R_{g3}. Each grounding resistance is 0.225 Ω.

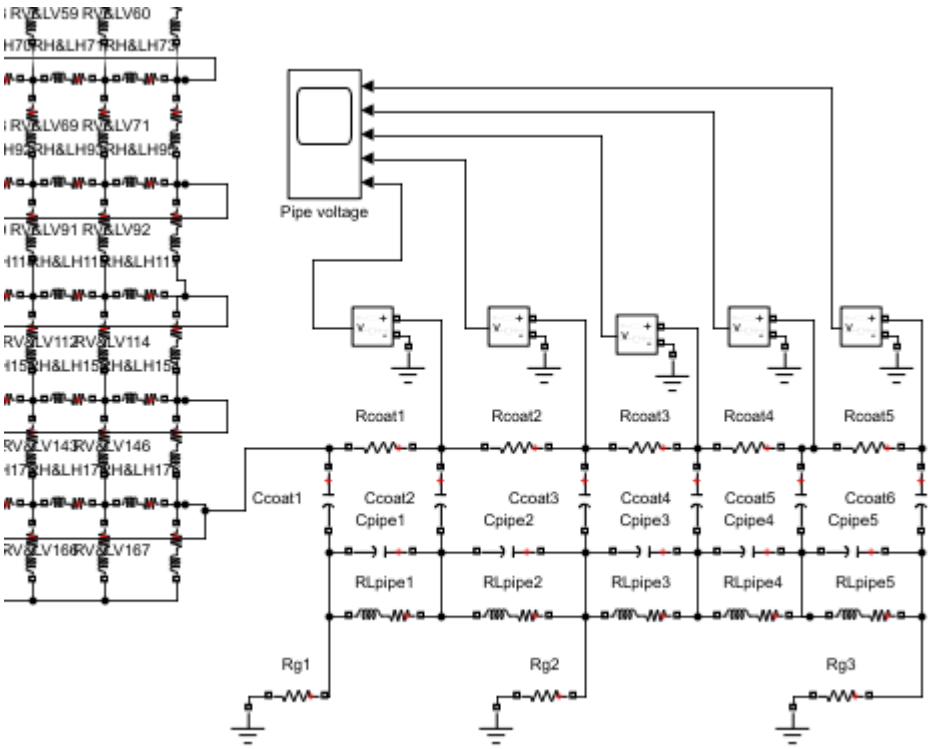

Figure 5.69. Mild steel pipe with multiple grounding along its length

The voltage measured across the 20 top sheets for the three grounding scenarios along the length of the pipe is presented in Figure 5.70 (a) to (c). The voltage measured across the 20 base sheets for the three grounding scenarios is presented in Figure 5.71 (a) to (c). For the base sheets, a significant voltage oscillation can be observed in Figure 5.71 (c) due to the inadequate grounding at the far end of the pipe length. The voltage measured at the intersections of the five connected 20 m pipes is presented in Figure 5.72 (a) to (c). The voltage profiles in Figure 5.72 (a) to (c) are different in voltage magnitudes. In Figure 5.72 (b), the peak voltage at each of the 20 m pipe intersections is lower due to the multiple grounding. Figure 5.72 (c) shows a significant voltage polarity swing with a peak voltage of 19.6 kV at pipe section 1 due to inadequate grounding. These results emphasize the importance of ensuring adequate grounding along the length of a pipe connected to a FRT to reduce voltage oscillations and also the peak lightning voltage along the pipe sections. It is also important to ensure adequate equipotential bonding to nearby metallic structures along the length of the pipe to prevent dangerous voltage differential between parts.

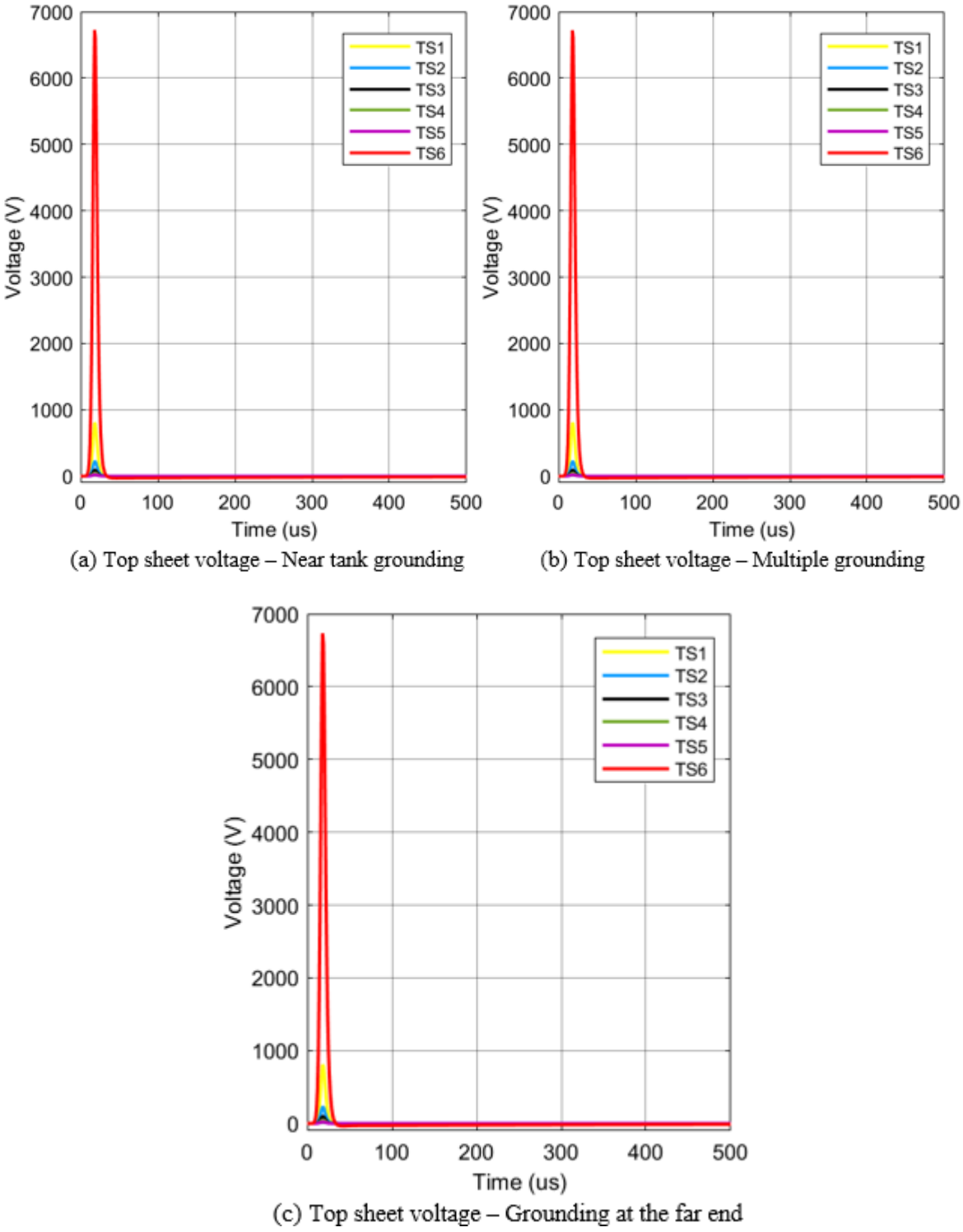

(a) Top sheet voltage – Near tank grounding

(b) Top sheet voltage – Multiple grounding

(c) Top sheet voltage – Grounding at the far end

Figure 5.70. The top sheet voltage with a pipe connected to the FRT for pFS

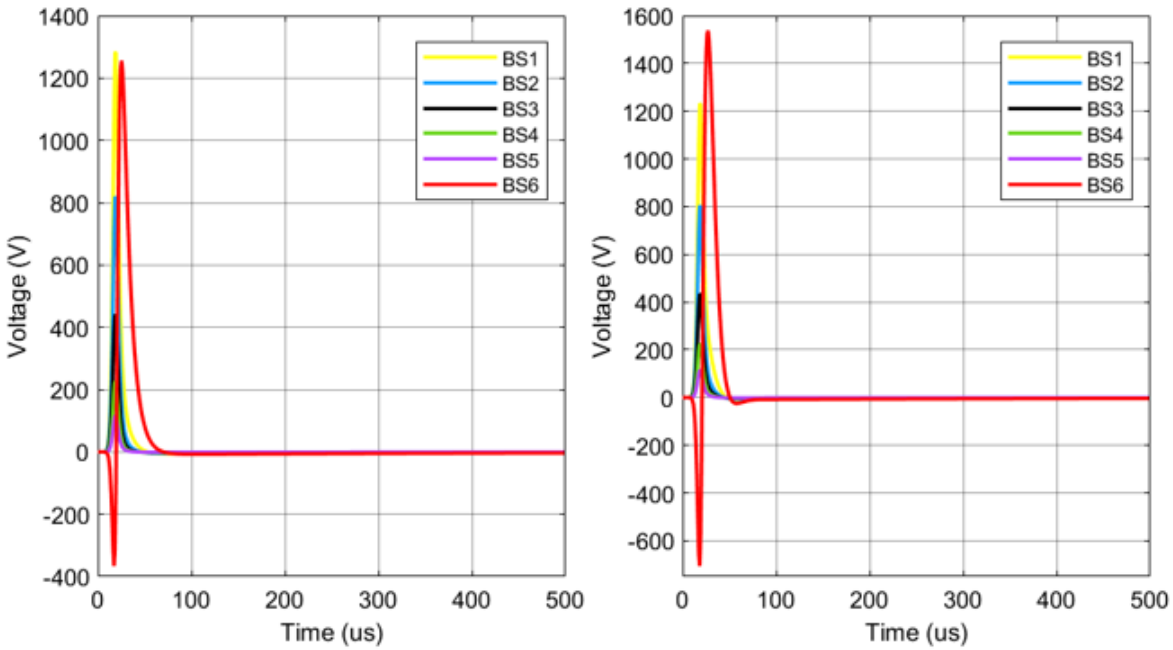

(a) Base sheet voltage – Near tank grounding

(b) Base sheet voltage – Multiple grounding

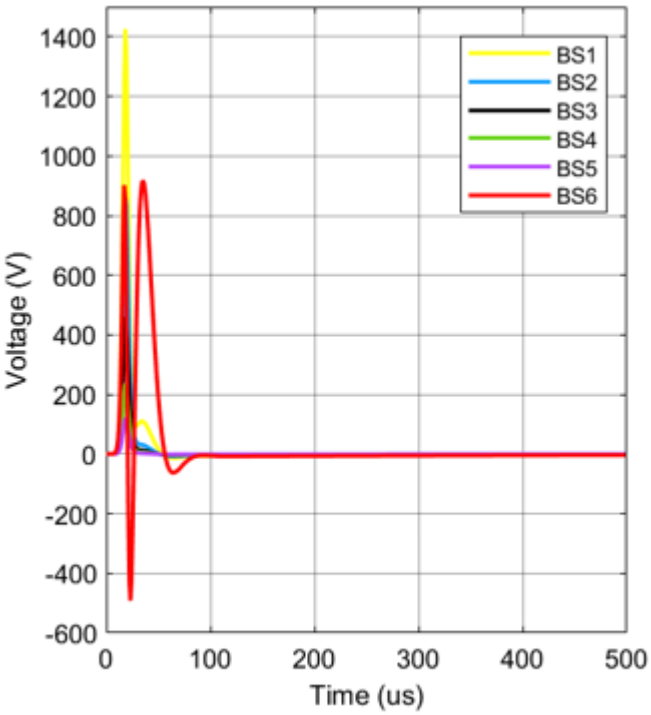

(c) Base sheet voltage – Grounding at the far end

Figure 5.71. The base sheet voltage with a pipe connected to the FRT for pFS

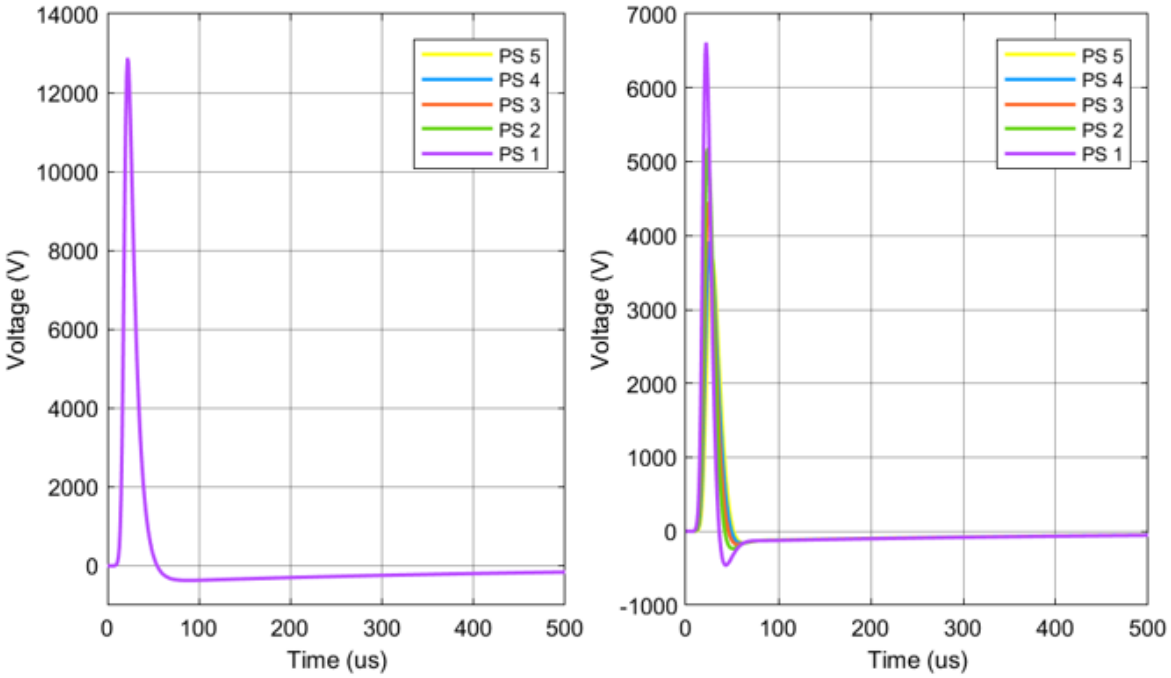

(a) Pipe voltage – Near tank grounding

(b) Pipe voltage – Multiple grounding

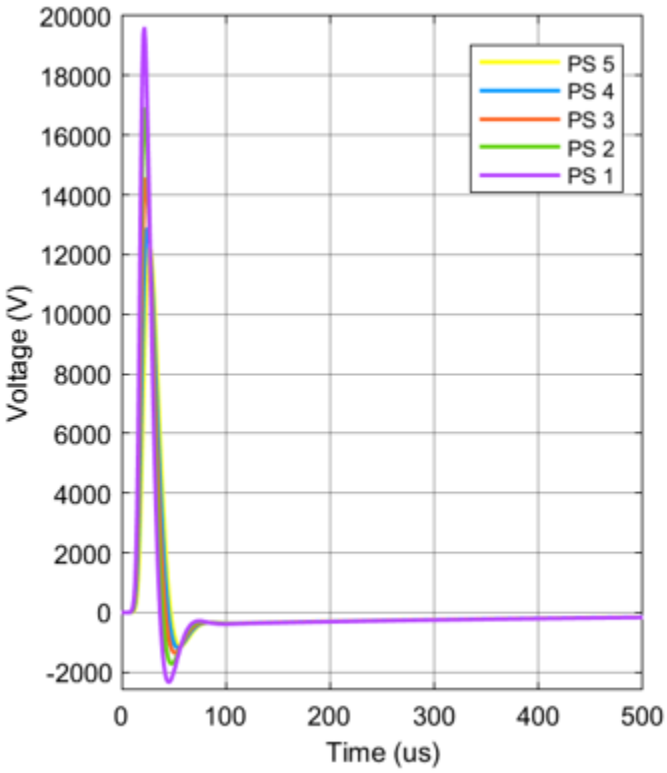

(c) Pipe voltage – Grounding at the far end

Figure 5.72. The voltage at the intersections of the five connected 20 m pipes for pFS

5.6 The implications of the findings

The current and voltage across the shell sheets oscillate as lightning frequency increases significantly in the hundred-kilo hertz range for the positive first stroke lightning current. This can increase the likelihood of voltage induction in nearby metallic structures. Varying voltage potentials, usually within the range of 25 to 60 kV, have been reported by various studies as sufficient to ignite flammable hydrocarbon vapours [182]. With low grounding resistance of 0.225 Ω, a potential of about 55 kV was observed at the strike point, which was reduced to 45 kV by using multiple flow paths via connected wires. These voltage magnitudes emphasise the risk and likelihood of vapour ignition on a FRT. Spark energy with about 0.2 mJ can ignite a flammable vapour if within its explosive limit. This shows that lightning current can indeed induce fire on a FRT if a low resistance path is not provided for the safe dissipation of the current coupled with adequate flammable vapour management using seals.

A direct lightning strike to the floating roof poses the highest risk to a FRT because all the lightning current on the roof must flow to the tank shell via air gaps and shunts, if available. Catenary wires can be used to shield the roof from a direct lightning strike. The use of interconnected catenary air termination is recommended for FRT based on the observations from the simulation results. The peak pulse voltage at various points reduced significantly when the sharing of the lightning current among the sheets improved. Any pipe connected to a FRT should also be grounded at multiple points along its length to reduce the voltage potential across the length of the pipe. Likewise, the overall grounding resistance of a FRT should be preferably maintained below the recommended value of 10 Ω to prevent peak lightning voltage of the order of megavolts across the tank sheets.

6 Results for the conventional LPS models evaluated for a FRT

The results from the RL model simulations of a FRT highlight some critical facts on the impact of a lightning strike on the current and voltage distribution along the steel plates of a FRT. An important fact is that the highest impact occurs at the point of strike, and for each plate level, the highest current flows through the shells that are vertically below the strike point. The current and voltage distributions on each plate can be significantly reduced by creating parallel paths for the lightning current through the use of catenary wires to divert the lightning current to multiple points on the tank shell. Since the highest risk occurs when there is a direct strike to the floating roof itself, an effective LPS should prevent a direct strike to the roof. In this section, these facts are considered in developing various conventional LPS for a FRT which are then evaluated in terms of interception efficiency using DEGM.

6.1 Separation distance calculation for side flash prevention

An appropriate separation distance must be provided to prevent side flashes from a LPS to parts of a structure or an object. NFPA 780 [138] recommends class II LPS for structures containing flammable vapours. According to IEC 62305-3:2010 [183], the required separation distance s is defined in equation 6.1.

$$s = k_i \frac{k_c}{k_m} \cdot l \tag{6.1}$$

Where k_i the induction factor = 0.06 for class II lightning protection.

k_m the material factor = 1 for air.

k_c is the partitioning coefficient.

l in m is the length of the shortest path to ground from the point under consideration.

These calculations are for a 20 m high FRT with 60 m in diameter. For the case of a 33 m high, free-standing lightning protection mast, as shown in Figure 6.1, the whole lightning current flows through the mast, and as such, k_c is 1 and $s = 0.06 \times 1 \times 20 = 1.2$ m.

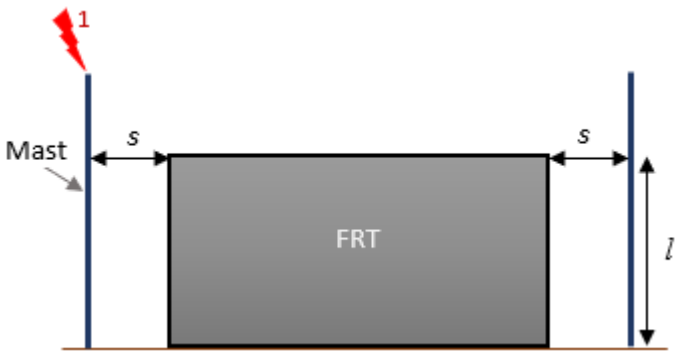

Figure 6.1. Masts installed beside the FRT and separation distance

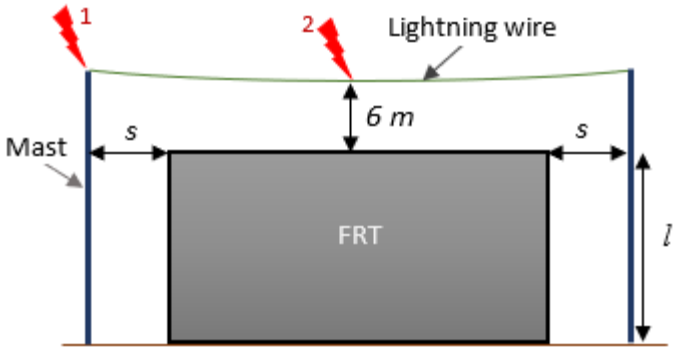

Figure 6.2. A catenary wire supported by masts and separation distance

For a catenary wire supported by 25 m high masts at both ends, as shown in Figure 6.2, the magnitude of the current flow through each mast is influenced by the location of the strike point.

If a lightning strike hits point 1 on top of the mast (Figure 6.2), the shortest current path to the ground is h through the mast. This is referred to as the worst case in terms of current sharing, and for interconnected earthing arrangement (type B), k_c is determined as follows:

$$k_c = \frac{h + c}{2h + c} \tag{6.2}$$

Let the length of the air termination lightning wire c = 64 m

$$k_C = \frac{25 + 64}{2 \times 25 + 64} = 0.7807$$

$s = 0.06 \times 0.7807 \times 20 = 0.937$ m

For strike at point 1, if the grounding is of type A, i.e., isolated single earthing electrodes, but their resistances are comparable, then k_c is 0.66, but if their resistances are different by more than a factor of 2, then k_c is 1. The calculation is as follows:

$s = 0.06 \times 1 \times 20 = 1.2$ m

If a lightning strike hits point 2 at the middle of the lightning wire (Figure 6.2), the shortest current path to the ground is through half of the wire and then through the mast, and k_c is 0.5, $s = 0.06 \times 0.5 \times (25 + 32) = 1.71$ m.

This result implies that the height of the catenary wire above the roof must be higher than 1.71 m at the centre, and the mast must be separated from the FRT by at least 1.2 m. IS 2309: 1989 [184] recommends that the separation distance between a structure and an air termination lightning mast should not be less than 2 m to prevent side flash. For the 60 m FRT, a separation distance of 2 m will be applied between the mast and the tank shell. This distance can be increased for safety reasons to ensure that the stretched arms of a person cannot touch the FRT and the mast simultaneously. Still, due to the usual space constraint in a tank bund wall, the 2 m separation distance is more feasible for implementation.

6.2 Evaluation of various air termination configurations for FRT using DEGM

1) Air terminals installed on the rim of the FRT

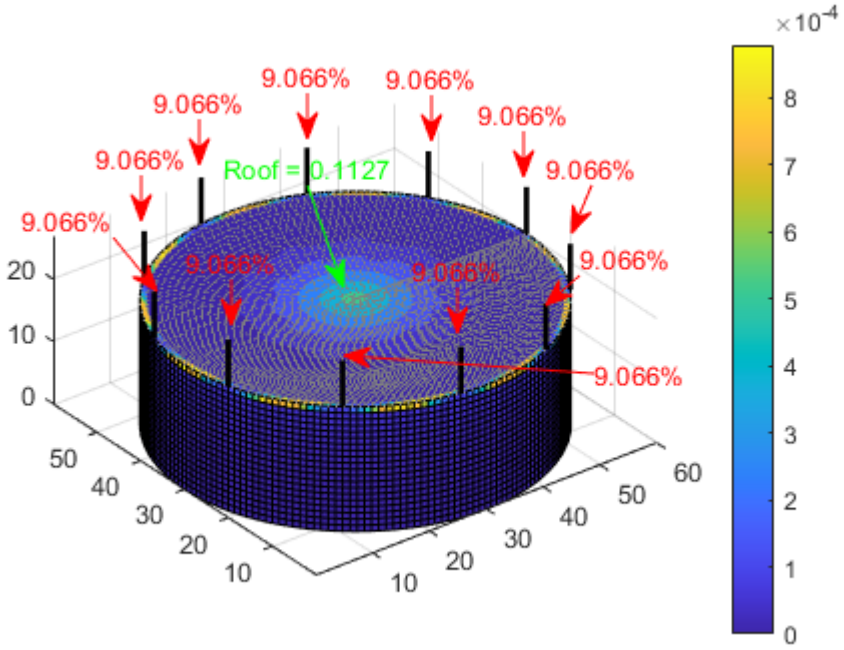

Figure 6.3. The probability of a strike for eleven, 7 m high rods with the roof at the top

Figure 6.3 presents the probability of a direct strike in percentage (%) to a FRT protected by eleven 7 m high air terminals installed on the FRT's rim with the roof at the top. For each rod, the average probability is 9.07%, with an overall lightning interception efficiency of 99.76%. A similar figure is presented in Figure 6.4 for when the roof is in the middle position, with an overall interception efficiency of 99.85%.

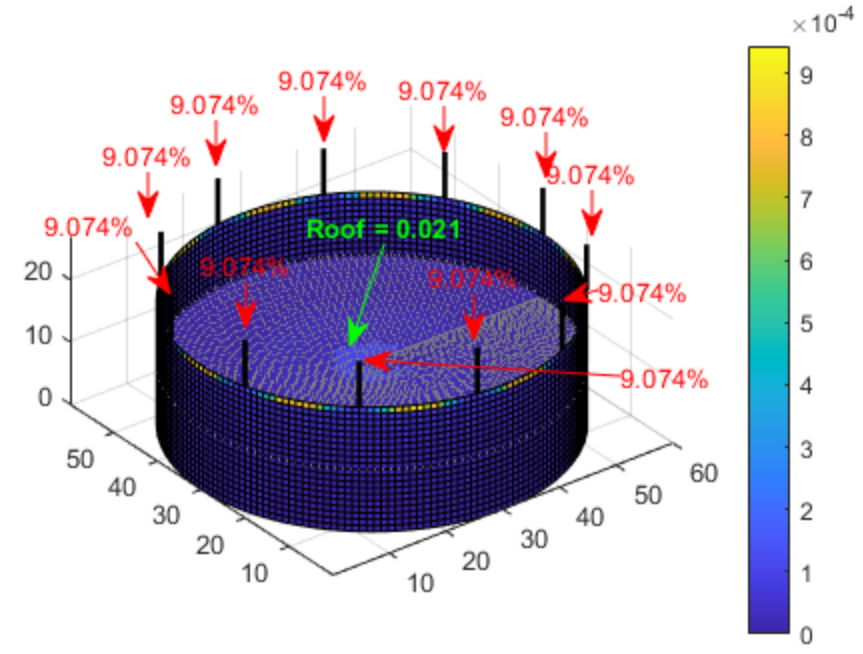

Figure 6.4. The probability of a strike for eleven, 7 m high rods with the roof in the middle

2) Air terminals installed on the rim and on the roof of the FRT

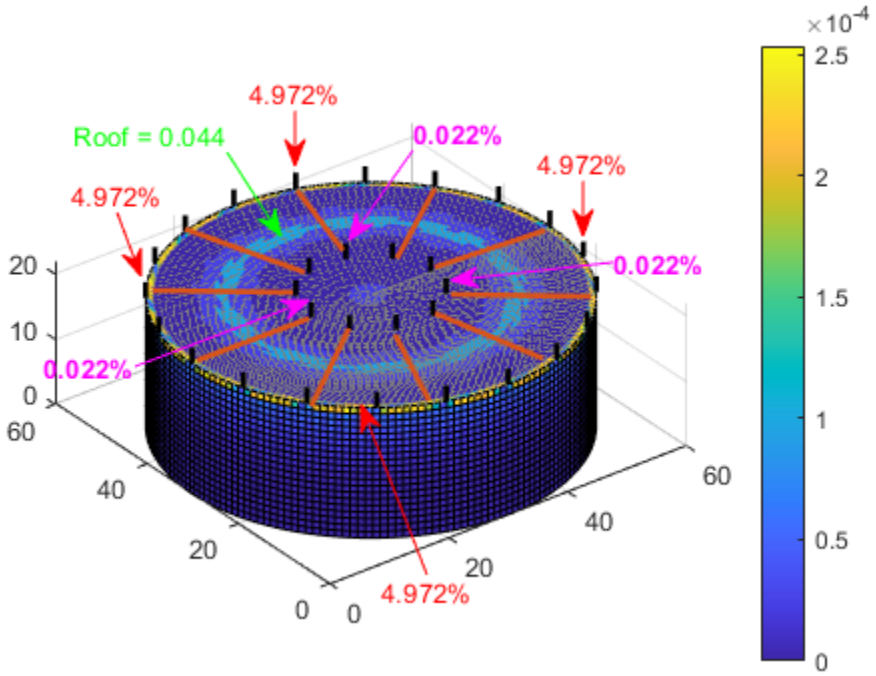

Figure 6.5. The probability of a strike for twenty 2 m high rods on the rim and ten 2 m high rods above the roof with the roof at the top

Stabilizing 7 m high air terminations on the rim of a FRT may create a challenge. Based on this, a modified configuration is considered using a combination of twenty 2 m high rods on the rim of the FRT combined with ten 2 m high rods supported by horizontal insulators above the roof of the FRT, as shown in Figure 6.5 for when the roof is at the top. The insulators will ensure that the lightning current from the rods does not touch any part of the roof. The

lightning current from the rods above the roof will flow via insulated cables attached to the horizontal support insulators. The average probability of a direct strike to each of the rods on the rim is 4.972% and 0.022% for the rods on the roof. The overall lightning interception efficiency of the setup is 99.88%. A similar figure is presented in Figure 6.6 for when the roof is in the middle position. When the roof is in the middle, the overall interception efficiency of the LPS is 99.92%.

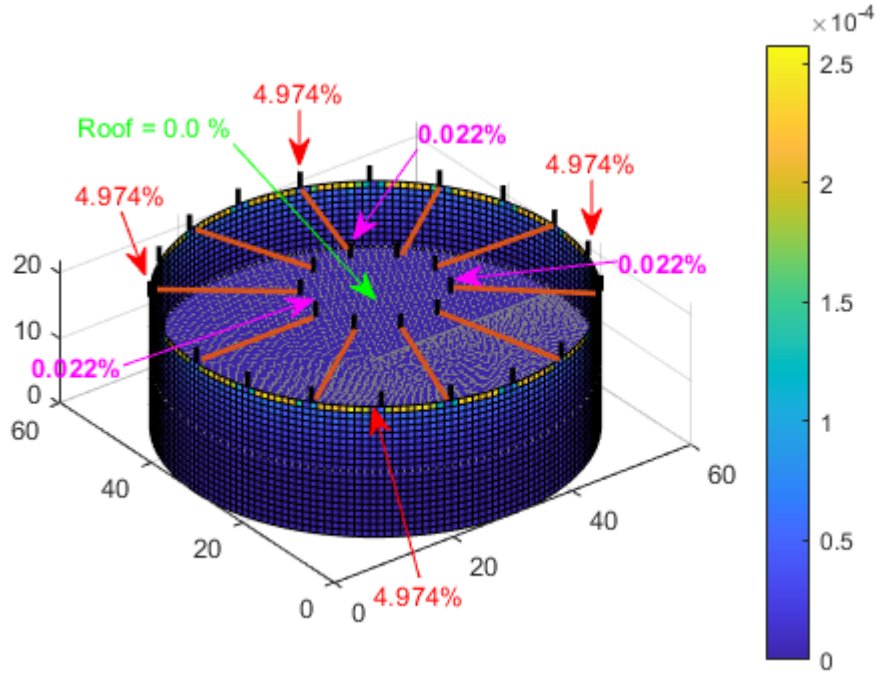

Figure 6.6. The probability of a strike for twenty 2 m high rods on the rim and ten 2 m high rods above the roof with the roof in the middle position

3) Lightning masts installed around the FRT

Lightning protection masts can be used to protect structures underneath their zone of protection from a direct lightning strike. A similar concept is adopted for this case by installing seven masts around the FRT with a separation distance of 2 m to prevent side flashes. The masts completely isolate the path of the intercepted lightning current from the FRT. For each mast, the average probability is 14.23%, and the total interception efficiency of the setup is 99.83%, as shown in Figure 6.7 for when the roof is at the top. A similar figure is presented in Figure 6.8 for when the roof is in the middle position, and for this scenario, the overall interception efficiency of the LPS is 99.84%.

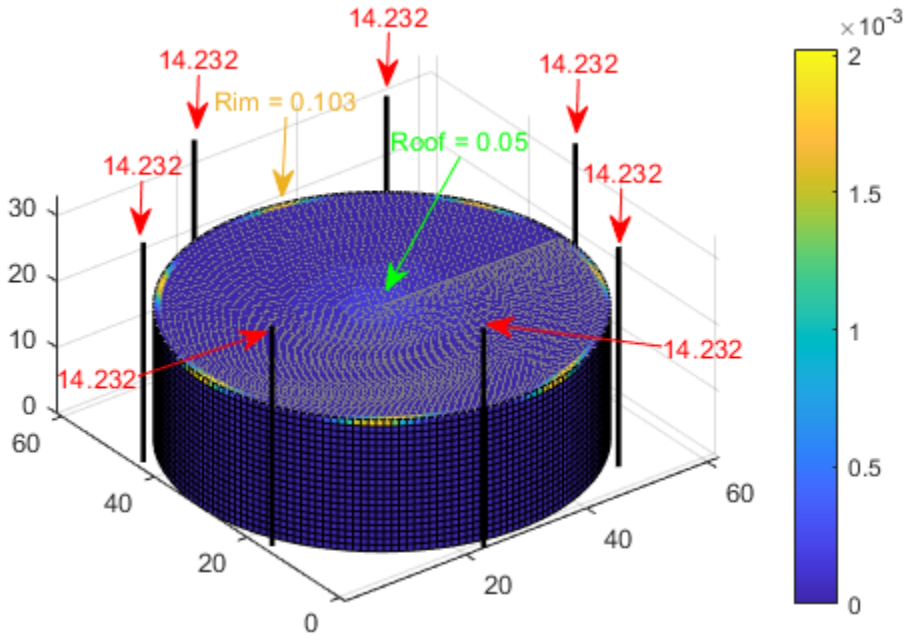

Figure 6.7. The probability of a strike for seven 33 m high masts with the roof at the top

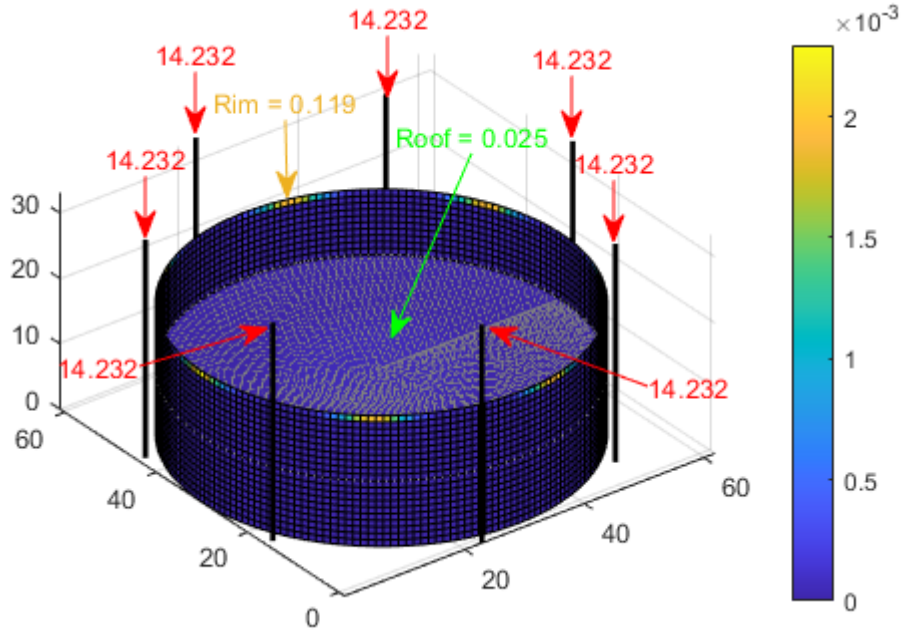

Figure 6.8. The probability of a strike for seven 33 m high masts with the roof in the middle

4) Two crossed catenary wires above the FRT's rim

For this case, two crossed wires 6 m above the FRT are supported by rods positioned on the rim of the FRT to protect the roof from a direct lightning strike. The average probability of a direct strike to each of the catenary wires is 5.55%, the probability of a direct strike to the tip of the support rod is 20.43%, and the total interception efficiency of 92.84%, as shown in Figure 6.9 for when the roof is at the top. A similar figure is presented in Figure 6.10 when the roof is in the middle position. When the roof is in the middle, the total interception efficiency is 92.84%.

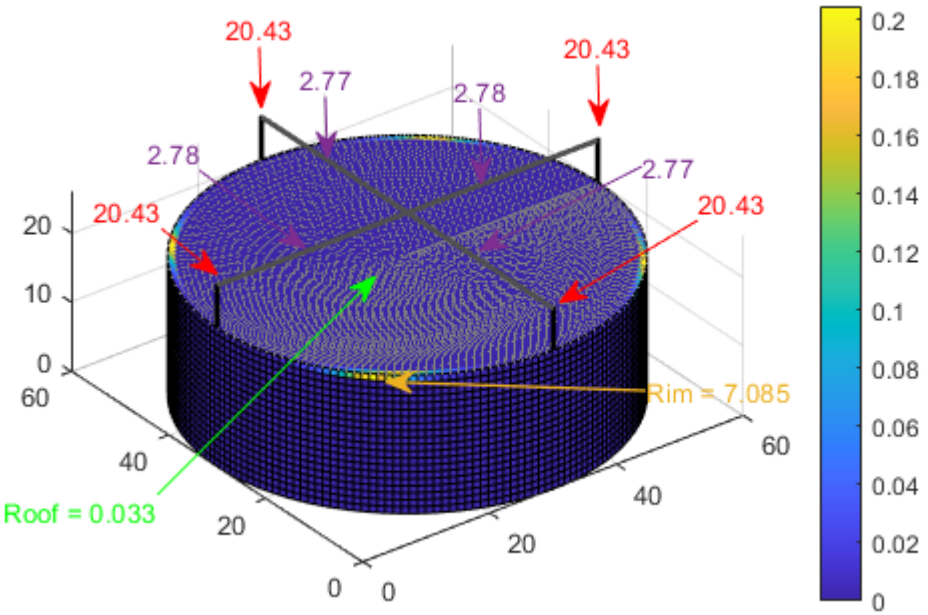

Figure 6.9. The probability of a strike for two 6 m high crossed wires with the roof at the top position

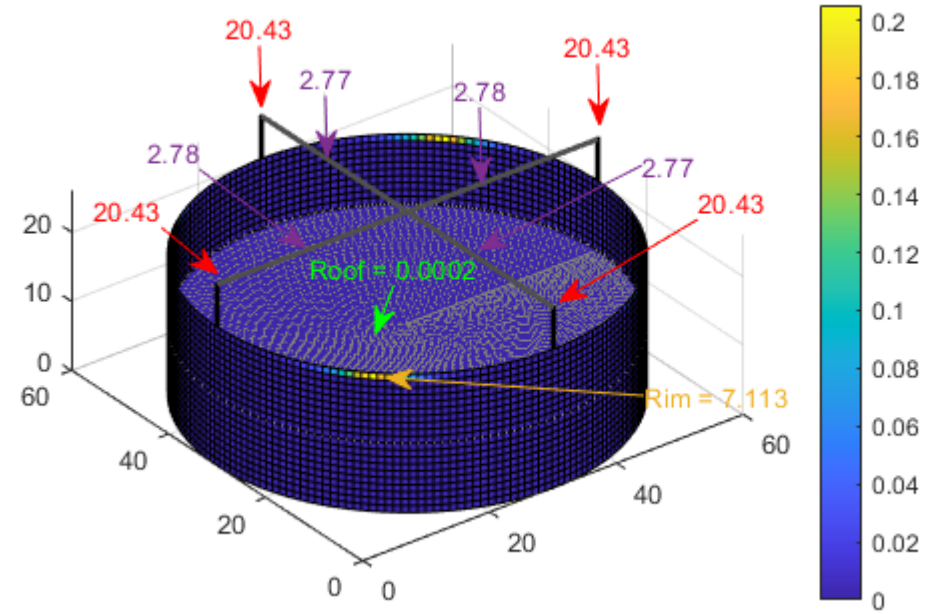

Figure 6.10. The probability of a strike for two 6 m high crossed wires with the roof in the middle position

5) Two crossed catenary wires supported by masts

For this case, two crossed catenary wires are supported by 25 m high masts positioned 2 m away from the FRT to prevent a side flash.

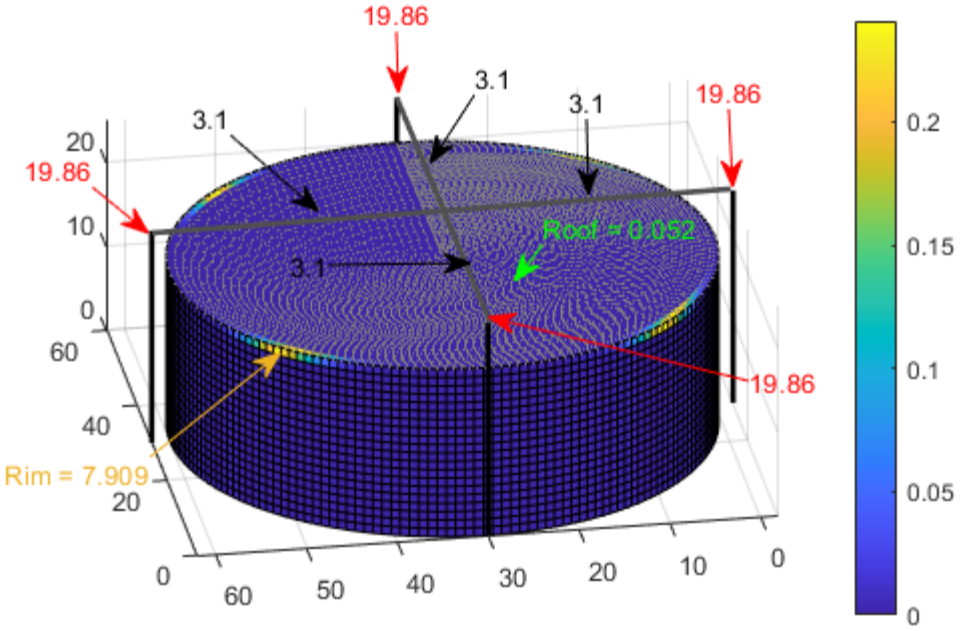

Figure 6.11. The probability of a strike for two 25 m high crossed wires with the roof at the top

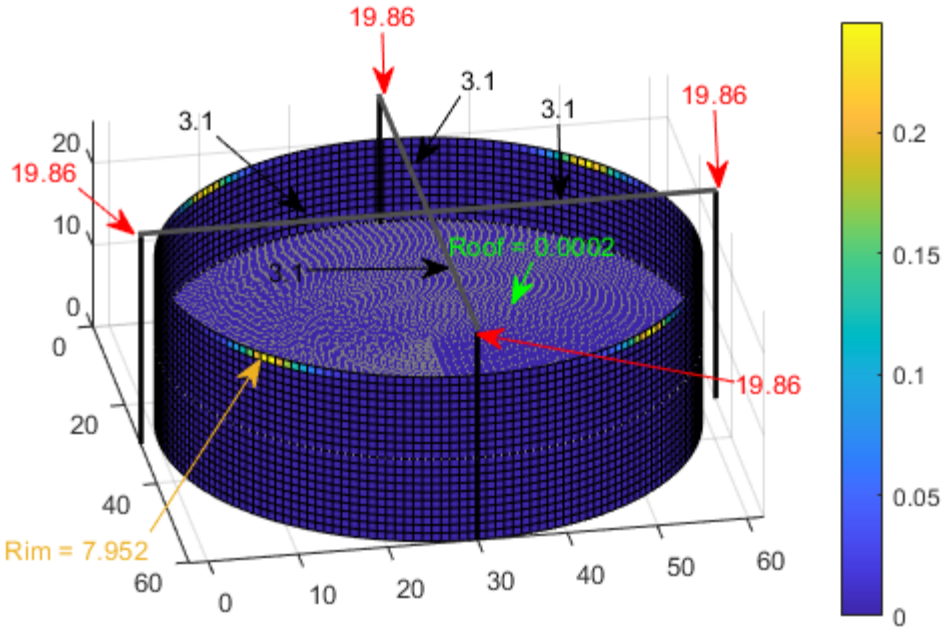

Figure 6.12. The probability of a strike for two 25 m high crossed wires with the roof in the middle

The average probability of a direct strike to each of the catenary wires is 6.2%, and the probability of a direct strike to the tip of the support rod is 19.86%, with an overall interception efficiency of 92.01%, as shown in Figure 6.11 for when the roof is at the top. A similar figure is presented in Figure 6.12 when the roof is in the middle position, with an overall interception efficiency of 92.02%.

6) Two parallel and one crossed wire on the FRT's rim

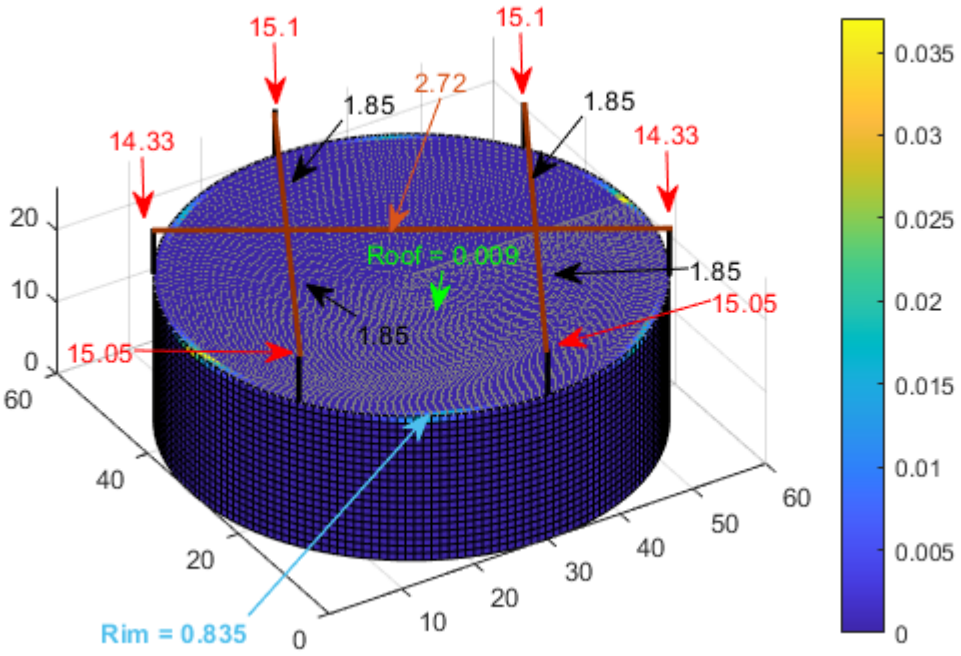

Figure 6.13. The probability of a strike for three, 6 m high crossed wires with the roof at the top

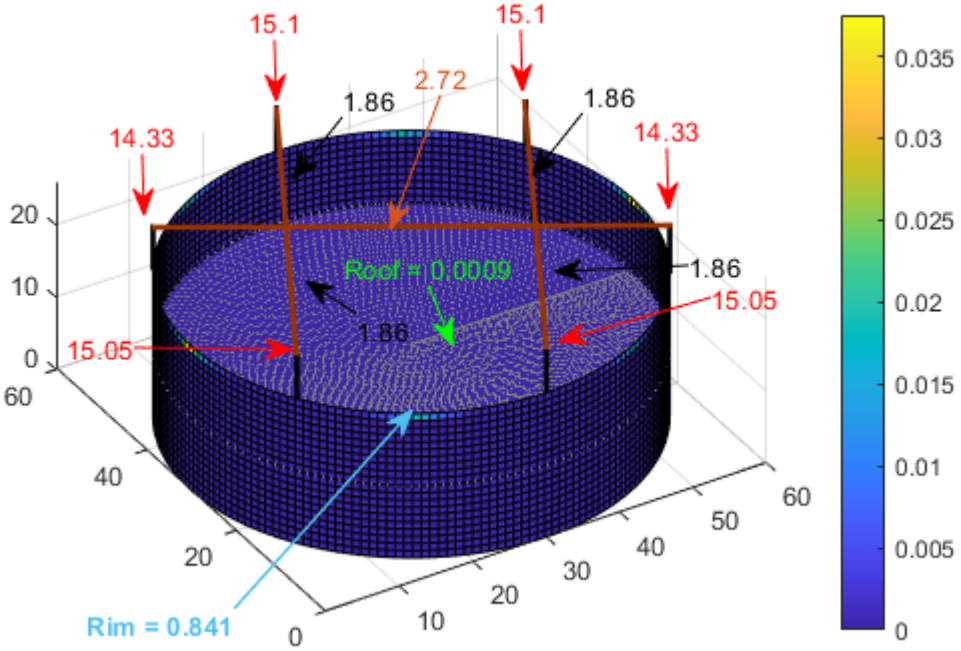

Figure 6.14. The probability of a strike for three, 6 m high crossed wires with the roof in the middle

In this scenario, three catenary wires 6 m above the FRT are supported by rods positioned on the rim of the FRT, with one of the wires crossing the other two. The average probability

of a direct strike to each of the parallel catenary wires is 3.7%, and the average probability of a direct strike to the tip of each of their support rods is 15.3%, while for the third crossed wire, the probability of a direct strike to the catenary wire is 2.72%, and the probability of a direct strike to the tip of its support rod is 14.3%. The total lightning interception efficiency of this arrangement is 99.11%, as shown in Figure 6.13 when the roof is at the top. A similar figure is presented in Figure 6.14 when the roof is in the middle position. The average probability of a direct strike to each of the parallel catenary wires is 3.72%, and the average probability of a direct strike to the tip of their support rod is 15.3%, while for the third crossed wire, the probability of a direct strike to the catenary wire is 2.72%, and the probability of a direct strike to the tip of its support rod is 14.3%. For this case, the total interception efficiency is 99.12%.

7) Two parallel and one crossed catenary wire supported by masts

For this case, the catenary wires are supported by 25 m high masts positioned 2 m away from the FRT to prevent a side flash.

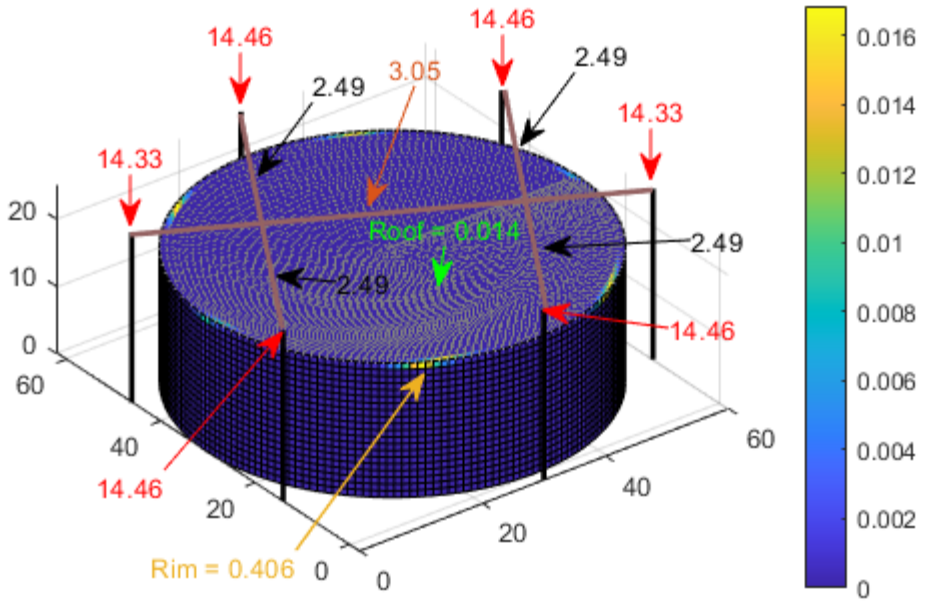

Figure 6.15. The probability of a strike for three 25 m high crossed wires with the roof at the top

The average probability of a direct strike to each parallel catenary wire is 4.98%. The probability of a direct strike to the tip of each of their support rod is 14.46%, while for the crossed wire, the probability of a direct strike to the catenary wire is 3.05%, and the probability of a direct strike to the tip of its support rod is 14.33%. The total lightning interception efficiency is 99.56%, as shown in Figure 6.15 when the roof is at the top. A similar figure is presented in Figure 6.16 for when the roof is in the middle position, and for this case, the total interception efficiency is also 99.56%.

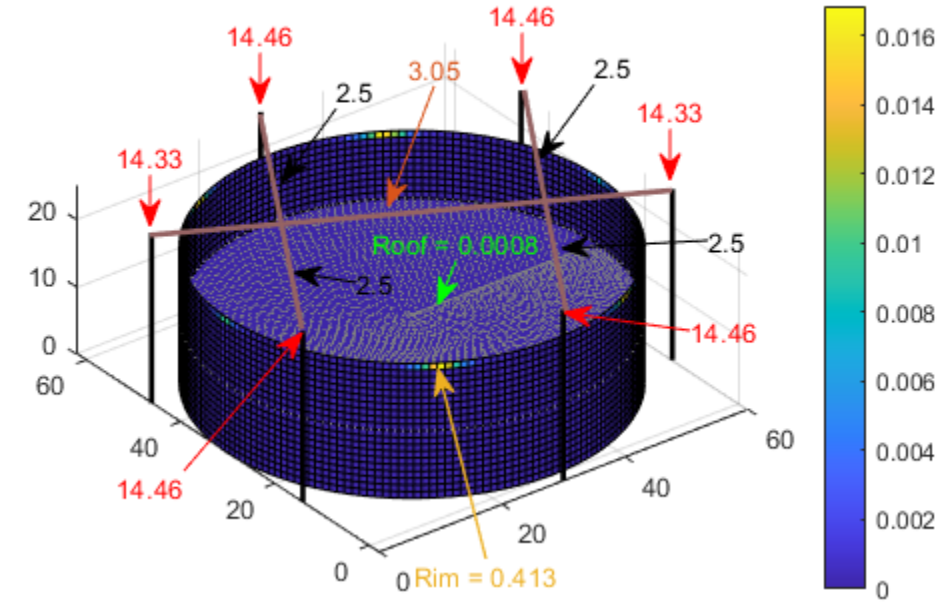

Figure 6.16. The probability of a strike for three 25 m high crossed wires with the roof in the middle

8) Three parallel catenary wires on the FRT's rim

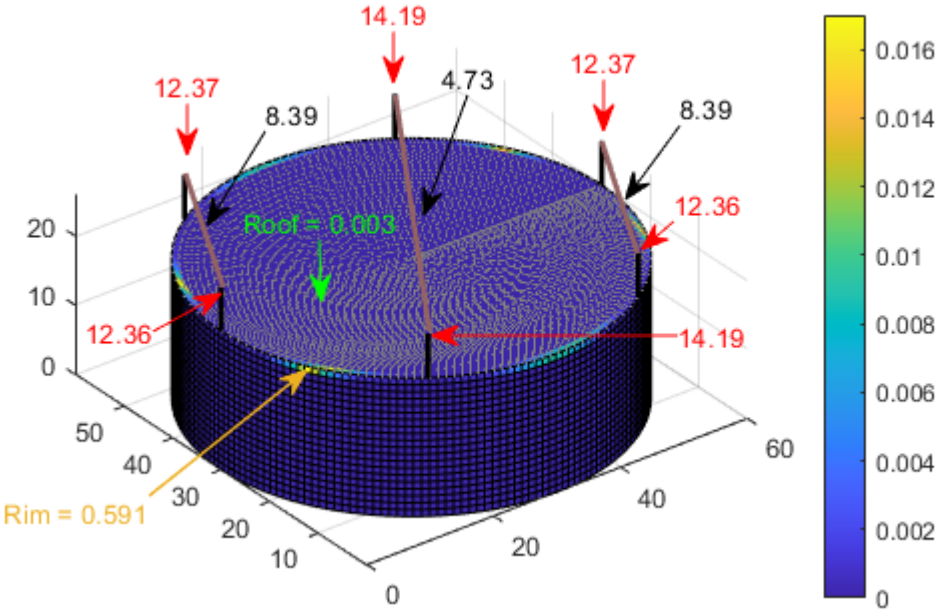

Figure 6.17. The probability of a strike for three 6 m high parallel wires with the roof positioned at the top

In this scenario, three parallel catenary wires 6 m above the FRT are supported by rods positioned on the rim of the FRT. The probability of a direct strike to the middle catenary wire is 4.73%, and the probability of a direct strike to the tip of its support rod is 14.19%. In contrast, for the other two wires, the probability of a direct strike to the catenary wire is 8.39%, and the average probability of a direct strike to the tip of their support rod is 12.37%. This catenary wire arrangement's total lightning interception efficiency is 99.36%, as shown

in Figure 6.17 when the roof is at the top. A similar figure is presented in Figure 6.18 for when the roof is in the middle position, and for this case, the total interception efficiency is also 99.36%.

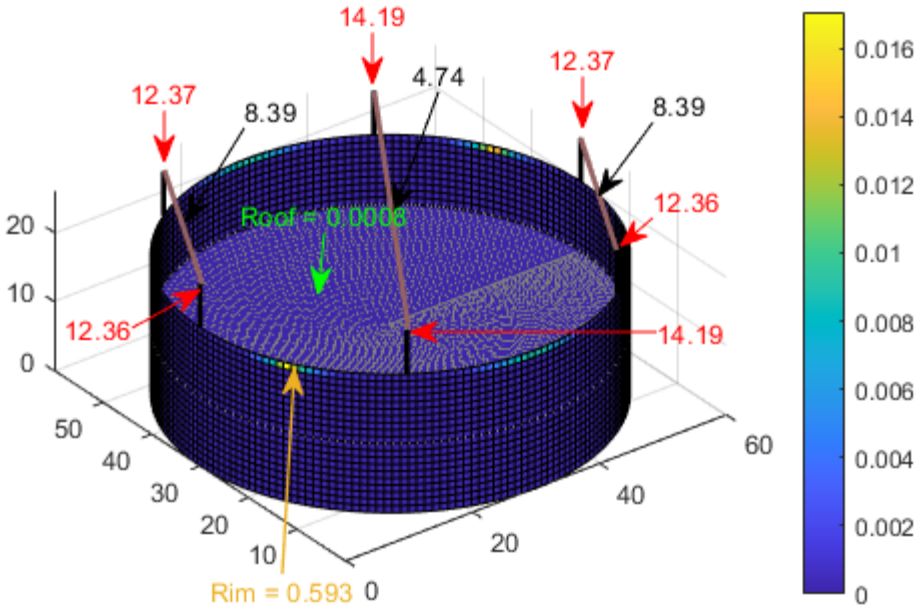

Figure 6.18. The probability of a strike for three 6 m high parallel wires with the roof positioned in the middle

9) Three parallel catenary wires supported by masts

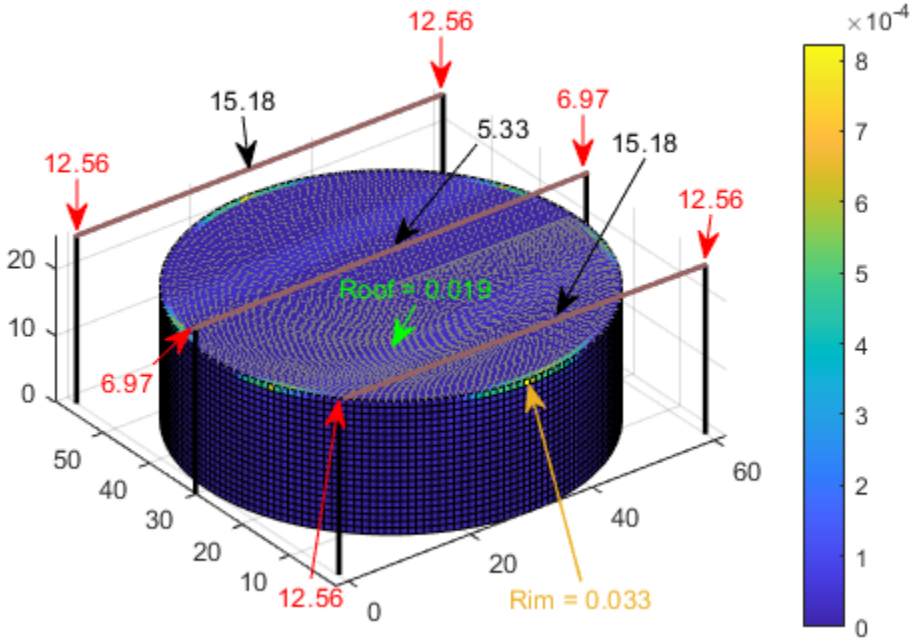

Figure 6.19. The probability of a direct strike for three parallel, 25 m high catenary wires with the roof at the top

For this case, three 25 m high parallel catenary wires are supported by masts positioned beside the FRT. The probability of a direct strike to the middle catenary wire is 5.33%, and the probability of a direct strike to the tip of its support rod is 6.97%, while for the other two wires, the probability of a direct strike to the catenary wires is 15.18%, and the average probability of a direct strike to the tip of their support rod is 12.56%. The total lightning interception efficiency of this arrangement is 99.93%, as shown in Figure 6.19 when the roof is at the top. A similar figure is presented in Figure 6.20 when the roof is in the middle position, and for this case, the total interception efficiency is 99.94%.

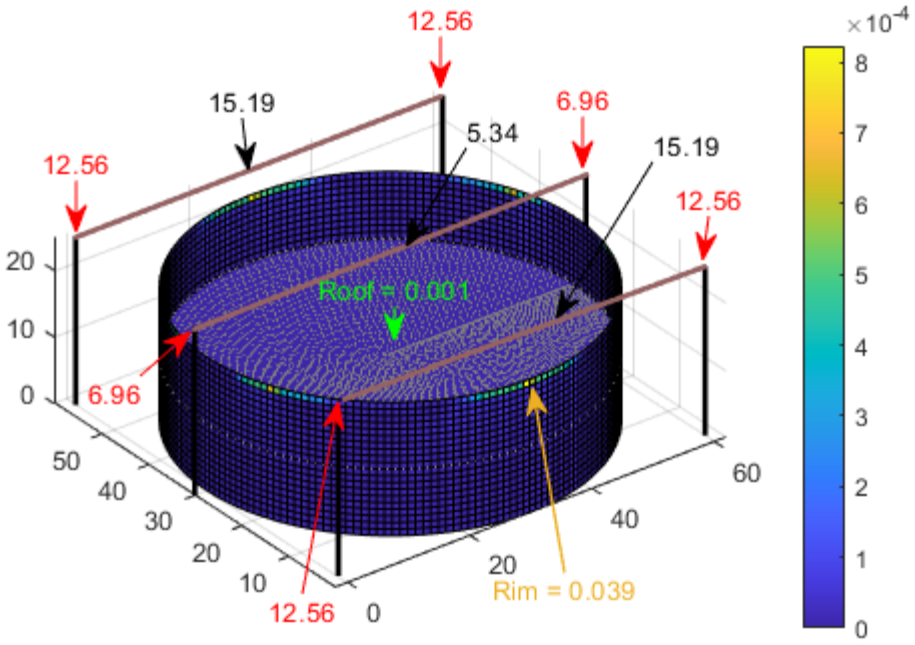

Figure 6.20. The probability of a direct strike for three parallel, 25 m high catenary wires with the roof in the middle position

6.3 A summary of the main attributes of each LPS configuration

Table 6.1. A comparison of the main characteristics of five models with the roof at the top

	Rods on the FRT's rim	**Rods on the rim and above roof**	**Masts around the FRT**	**2 crossed wires on the rim**	**2 crossed wires on masts**
Max roof current (kA)	18.66	3.36	9.43	7.18	6.87
Max rim current (kA)	4.59	3.16	6.19	89.46	104.15
Max wall current (kA)	2.69	2.69	2.69	2.69	2.69
Max current to LPS (kA)	≥ 200	≥ 200	≥ 200	≥ 200	≥ 200
Probability of strike to the roof (%)	0.1127	0.0438	0.0500	0.0331	0.0522
Probability of strike to the rim (%)	0.0849	0.0321	0.1026	7.0853	7.9094
Probability of strike to the FRT wall (%)	0.0392	0.0469	0.0199	0.0428	0.0329
Probability of strike to the LPS (%)	99.76	99.88	99.83	92.84	92.01
Exposure of the roof area	Areas within 8 m to the centre of the roof are exposed to currents from 7.5 kA to 18.7 kA.	Unprotected areas on the roof are exposed to currents ≤ 3.4 kA	Areas within 5 m to the centre of the roof are exposed to currents ≤ 9.4 kA	Unprotected areas on the roof are exposed to currents ≤ 7.2 kA	Unprotected areas on the roof are exposed to currents ≤ 6.9 kA
Exposure of the tank shell	The shell can be struck by low current side flashes.	The shell can be struck by low current side flashes.	Unprotected portions of the shell can be struck by side flashes.	Unprotected portions of the shell can be struck by side flashes and strikes from above.	Unprotected portions of the shell can be struck by side flashes and strikes from above.

Likelihood of spark formation at the rim-seal region of the FRT	Lightning intercepted by the air terminal will direct all the current to a single point on the rim of the FRT. Also, current from strikes to the roof of about 18.7 kA needs to flow through the rim-seal region. Sparking is very likely.	Lightning intercepted by the air terminal will direct all the current to a single point on the rim of the FRT. Also, current from strikes to the roof of about 3.4 kA needs to flow through the rim-seal region. The possibility of sparking is low.	The masts isolate the current paths from the FRT. Also, current strikes of 9.43 kA to the roof are possible. The possibility of sparking is low.	The crossed wires can be connected at the centre to improve current sharing. Portions of the FRT's rim are exposed to high lightning currents of 89.5 kA. The possibility of sparking is very high.	The crossed wires can be connected at the centre to improve current sharing. Portions of the FRT's rim are exposed to high lightning currents of 104.2 kA. The possibility of sparking is very high.
Grounding requirements	The FRT's shell serves as the main grounding for the air terminations. The tank shell can be connected to a grounding ring at the base.	The FRT's shell serves as the main grounding for the air terminations. The tank shell can be connected to a grounding ring at the base.	Each mast must be grounded at the base, and all the earthing points must be connected by an equipotential bonding ring.	The FRT's shell serves as the main grounding for the air terminations. The tank shell can be connected to a grounding ring at the base.	Each mast must be grounded at the base, and all the earthing points must be connected by an equipotential bonding ring.
Space constraint	This does not require additional space within the bund wall area.	This does not require additional space within the bund wall area.	Installing several masts around the FRT requires sufficient space and clearance.	This does not require additional space within the bund wall area.	Installing masts around the FRT requires sufficient space and clearance.

Ease of implementation	Stabilising 7 m high air terminations on the FRT's rim may be mechanically difficult without additional anchoring.	2 m high air terminations can be easily stabilised on the FRT's rim, but supporting the roof terminations via extended insulators may be mechanically difficult without additional anchoring.	Installing seven or more 33 m high masts around each FRT in a tank farm will be tasking, and it will also affect the visual appeal of the facility.	Supporting long protection wires with rods on the FRT's rim without sagging, especially with heavy winds, may be difficult.	Masts can better support catenary wires. Space constraints within the bund walls may be an issue. Also, it may affect the visual appeal of the facility.
Maintenance	This does not require any major maintenance. The resistance of the grounding networks should be checked periodically.	This does not require any major maintenance. The resistance of the grounding networks should be checked periodically.	This does not require any major maintenance. The resistance of the grounding networks should be checked periodically.	The protection wires should be periodically checked for sagging and mechanical stability. The low resistance of the grounding system should be maintained.	The protection wires should be periodically checked for sagging, and the low resistance of the grounding system should be maintained.

Table 6.2. A comparison of the main characteristics of four models with the roof at the top

	2 parallel and 1 crossed wire on the rim	**2 parallel and 1 crossed wire on masts**	**3 parallel wires on the rim**	**3 parallel wires on masts**
Max roof current (kA)	2.06	4.09	2.06	1.87
Max rim current (kA)	27.35	17.54	18.13	6.70
Max wall current (kA)	2.69	2.69	2.69	2.69
Max current to LPS (kA)	≥ 200	≥ 200	≥ 200	≥ 200
Probability of strike to the roof (%)	0.0098	0.0142	0.0029	0.0193
Probability of strike to the rim (%)	0.8351	0.4059	0.5905	0.0326
Probability of strike to the FRT wall (%)	0.0412	0.0235	0.0413	0.0198
Probability of strike to the LPS (%)	99.11	99.56	99.36	99.93

Exposure of the roof area	Unprotected areas on the roof are exposed to currents ≤ 2.1 kA	Unprotected areas on the roof are exposed to currents ≤ 4.1 kA	Unprotected areas on the roof are exposed to currents ≤ 2.1 kA	Unprotected areas on the roof are exposed to currents ≤ 1.9 kA
Exposure of the tank shell	Side flashes and strikes from above can strike unprotected portions of the shell.	Side flashes and strikes from above can strike unprotected portions of the shell.	Side flashes and strikes from above can strike unprotected portions of the shell.	Unprotected portions of the shell can be struck majorly by side flashes.
Likelihood of spark formation at the rim-seal region of the FRT	At least two support rods share any current that hits a protection wire. The crossed wire can be connected to the parallel wires. Strike currents of 27.4 kA can hit exposed areas of the rim. The possibility of sparking is very likely.	The masts isolate the main current paths from the FRT. Strike currents of 17.5 kA can hit exposed areas of the rim. The possibility of sparking is likely.	Two support rods share any current that hits the protection wires. Strike currents of 18.1 kA can hit exposed areas of the rim. Sparking is likely.	The masts isolate the main current paths from the FRT. Strike currents of 6.7 kA can hit exposed areas of the rim. The possibility of sparking is very low.
Grounding requirements	The FRT's shell serves as the main grounding for the air terminations. The tank shell can be connected to a grounding ring at the base.	Each mast must be grounded at the base, and all the earthing points must be connected by an equipotential bonding ring.	The FRT's shell serves as the main grounding for the air terminations. The tank shell can be connected to a grounding ring at the base.	Each mast must be grounded at the base, and all the earthing points must be connected by an equipotential bonding ring.
Space constraint	This does not require additional space within the bund wall area.	Installing masts around the FRT requires sufficient space and clearance around the FRT.	This does not require additional space within the bund wall area.	Installing masts around the FRT requires sufficient space and clearance around the FRT.

Ease of implementation	Supporting long protection wires with rods on the FRT's rim without sagging, especially with heavy winds, may be difficult.	Masts can better support catenary wires. Space constraints within the bund walls may be an issue. Also, it may affect the visual appeal of the facility.	Supporting long protection wires with rods on the FRT's rim without sagging, especially with heavy winds, may be difficult.	Masts can better support catenary wires. Space constraints within the bund walls may be an issue. Also, it may affect the visual appeal of the facility.
Maintenance	The protection wires should be periodically checked for sagging and mechanical stability. The low resistance of the grounding system should be maintained.	The protection wires should be periodically checked for sagging, and the low resistance of the grounding system should be maintained.	The protection wires should be periodically checked for sagging and mechanical stability. The low resistance of the grounding system should be maintained.	The protection wires should be periodically checked for sagging, and the low resistance of the grounding system should be maintained.

Table 6.3. A comparison of the main characteristics of five models with the roof in the middle

	Rods on the FRT's rim	**Rods on the rim and above roof**	**Masts around the FRT**	**2 crossed wires on the rim**	**2 crossed wires on masts**
Max roof current (kA)	4.61	0.00	6.28	1.32	1.32
Max rim current (kA)	4.59	3.16	6.19	89.46	104.15
Max wall current (kA)	2.69	2.69	2.69	2.69	2.69
Max current to LPS (kA)	≥ 200	≥ 200	≥ 200	≥ 200	≥ 200
Probability of strike to the roof (%)	0.0208	0.0000	0.0254	0.00023	0.00019
Probability of strike to the rim (%)	0.0882	0.0328	0.1194	7.1128	7.9518
Probability of strike to the FRT wall (%)	0.0391	0.0469	0.0198	0.0428	0.0329
Probability of strike to the LPS (%)	99.85	99.92	99.84	92.84	92.02

Exposure of the roof area	Areas within 4 m to the centre of the roof are exposed to currents ≤ 4.6 kA.	The roof is completely protected.	Areas within 1 m to the centre of the roof are exposed to currents 6.3 kA.	Unprotected areas on the roof are exposed to currents ≤ 1.3 kA.	Unprotected areas on the roof are exposed to currents ≤ 1.3 kA.
Exposure of the tank shell	Low-current side flashes can strike the shell.	Low-current side flashes can strike the shell.	Side flashes can strike unprotected portions of the shell.	Side flashes and strikes from above can strike unprotected portions of the shell.	Side flashes and strikes from above can strike unprotected portions of the shell.

Table 6.4. A comparison of the main characteristics of four models with the roof in the middle

	2 parallel and 1 crossed wire on the rim	**2 parallel and 1 crossed wire on masts**	**3 parallel wires on the rim**	**3 parallel wires on the masts**
Max roof current (kA)	2.06	1.87	1.32	1.68
Max rim current (kA)	27.35	17.54	18.13	6.70
Max wall current (kA)	2.69	2.69	2.69	2.69
Max current to LPS (kA)	≥ 200	≥ 200	≥ 200	≥ 200
Probability of strike to the roof (%)	0.0098	0.00078	0.00078	0.0013
Probability of strike to the rim (%)	0.8351	0.4134	0.5931	0.0391
Probability of strike to the FRT wall (%)	0.0412	0.0235	0.0413	0.0198
Probability of strike to the LPS (%)	99.11	99.56	99.36	99.94
Exposure of the roof area	Unprotected areas on the roof are exposed to currents ≤ 2.1 kA.	Unprotected areas on the roof are exposed to currents ≤ 1.9 kA.	Unprotected areas on the roof are exposed to currents ≤ 1.3 kA.	Unprotected areas on the roof are exposed to currents ≤ 1.7 kA.
Exposure of the tank shell	Side flashes and strikes from above can strike unprotected portions of the shell.	Side flashes and strikes from above can strike unprotected portions of the shell.	Side flashes and strikes from above can strike unprotected portions of the shell.	Side flashes can strike unprotected portions of the shell.

Based on the comparative analysis of the nine conventional LPS models from Table 6.1, Table 6.2, Table 6.3 and Table 6.4, three models are hereby recommended due to the low lightning current exposure of the roof and the rim and the high lightning strike interception offered by these configurations. The best option is the use of three parallel catenary wires

supported by masts with an interception efficiency of 99.93% when the roof is at the top, with a maximum roof-strike current of 1.866 kA and a maximum rim-strike current of 6.704 kA. This option also provides complete isolation of the lightning current flow path from the FRT. This is followed by the model using air terminals installed on the rim and the roof of the FRT with an interception efficiency of 99.88% when the roof is at the top, with a maximum roof strike current of 3.364 kA, and a maximum rim strike current of 3.155 kA. The model with lightning masts installed around the FRT is the third recommended option, with an interception efficiency of 99.83% when the roof is at the top, with a maximum roof-strike current of 9.43 kA, and a maximum rim-strike current of 6.19 kA.

The use of catenary wires will provide a shield for the roof, thereby preventing lightning from terminating on the protruding support rods on the roof of the FRT, as illustrated in Figure 6.21. Aluminium-clad steel wire can be used as catenary wires because of its higher tensile strength, lighter weight, good conductivity, better corrosion resistance and continuous endurance as compared to galvanised steel wires.

Figure 6.21. Potential attachment points for a lightning strike on the floating roof

7 Conclusion and recommendations

In some FRT storage facilities, a LPS is not required as a primary barrier against lightning strikes on tanks, and this is because the tank itself is considered to be self-protecting due to its steel thickness. Such facilities may continue to operate safely without any major incident because the highest risk occurs when there is a direct strike to the roof of a FRT. The likelihood of a direct strike to the roof is generally less than 26%, even for a 100 m diameter tank when the roof is at the top, as revealed using DEGM. Since most tanks will not even be filled to their full capacity most of the time, the roof is further protected, and when the roof is in the middle position, the likelihood of a direct strike is less than 5%. For tanks located in regions with a low number of thunderstorm days per year or where severe lightning current magnitudes are rare, such facilities may continue to operate without any major lightning fire incident. This can be erroneously interpreted as "no protection at all is an adequate protection method". This culture is not an optimal and safe practice for high-risk lightning locations.

7.1 Reducing transient potential differences on and around the FRT

It is very vital to prevent the development of transient potential differences between the various components of the FRT, appurtenances, instrumentation and other equipment attached to the FRT by equipotential bonding. Likewise, all ground electrodes for the FRT or LPS masts must be connected by a closed equipotential ring. Metallic pipes within the bund wall must also be grounded along its length, and the grounding electrodes should be connected to the grounding network or grid within the tank facility. This extensive grounding and bonding will serve as a secondary barrier to mitigate any negative effect of a lightning strike within the storage tank facility. Like shunts, mechanical shoe-type seals have also been associated with sparking, and alternatives should be deployed. In compliance with API recommendations, modern FRTs should ensure an insulation rating of 1 kV and greater for conductive seal assembly components that are non-fully submerged. The LPS for a FRT must have good electrical continuity with very low impedance (resistance and inductance).

7.2 Surge and transient voltage protection

A lightning strike on a structure can trigger surges and transient voltages, which can have destructive effects on electrical equipment and sensitive electronics due to the resultant electromagnetic pulse. According to EN 61643-11 and IEC 61643-11 standards, surge protective devices are classified into Type 1 for handling lightning wave currents of 10/350 μs, Type 2 for handling surge wave currents of 8/20 μs and Type 3 SPDs, which are meant for sensitive devices and are designed to handle 8/20 μs current and 1.2/50 μs voltage waves.

Surge protection systems should be provided for incoming power cables and instrumentation lines within the tank farm. Surge protective devices located within Zone 0 and Zone 1 explosive zones of the FRT should be intrinsically safe for such operations. A potential surge protection scheme for a FRT situated in a storage tank facility is illustrated in Figure 7.1.

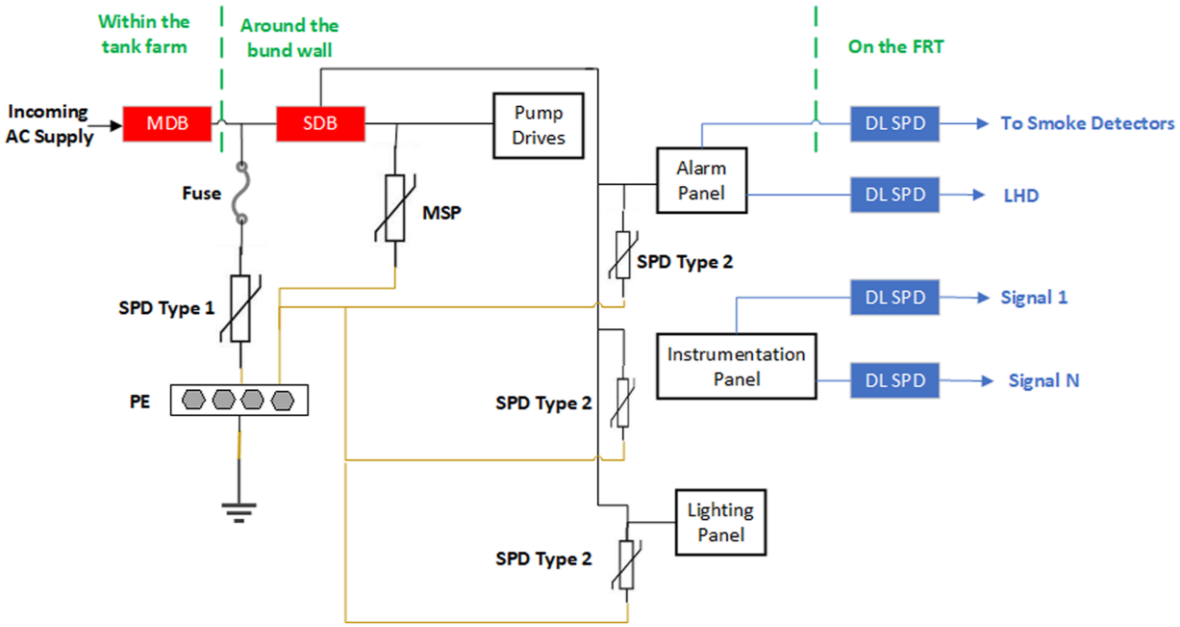

Figure 7.1. A surge protection scheme for a FRT

In Figure 7.1, MDB is the main distribution board that is connected to the main alternating current (AC) incoming line, SDB is the sub-distribution board, MSP stands for motor surge protection, PE is the protective earthing conductor, DL SPD represents the data line surge protective device and LHD stands for linear heat detector.

7.3 Maintenance issues in a FRT facility

Beyond having a good LPS in a tank farm as a vital requirement for fire prevention, the maintenance culture and the operational practices in a tank farm are essential factors that can determine if the LPS installed will be reliable and not eventually fail. A LPS that is well designed may not be very reliable if there are excess flammable fumes around it due to the high likelihood and ease of ignition when intercepting a lightning strike. Poor operational practices such as the prolonged bypass of automatic control systems, which may result in a tank overfilling, also constitute a risk. Inadequate staff training and safety awareness within a tank farm can negatively impact how the LPS components are handled and maintained.

This section highlights typical issues in a FRT facility that can aggravate the lightning risk within the facility. Figure 7.2 shows a section of the roof-shunt interface with a missing rim seal. By implication, the level of flammable vapour concentration around and escaping from this area will be very high. This portends a great risk when lightning terminates within the region, as the risk of an induced fire is significantly high because rich flammable vapour sufficient for ignition will be readily available to start and support any resulting fire. It is

important to always ensure that rim seals of the appropriate type (primary and secondary seals, electrically insulated seal assembly components etc.) are installed. A three-layer seal arrangement can also be implemented, as illustrated in Figure 7.3.

Figure 7.2. Missing rim seal on a FRT

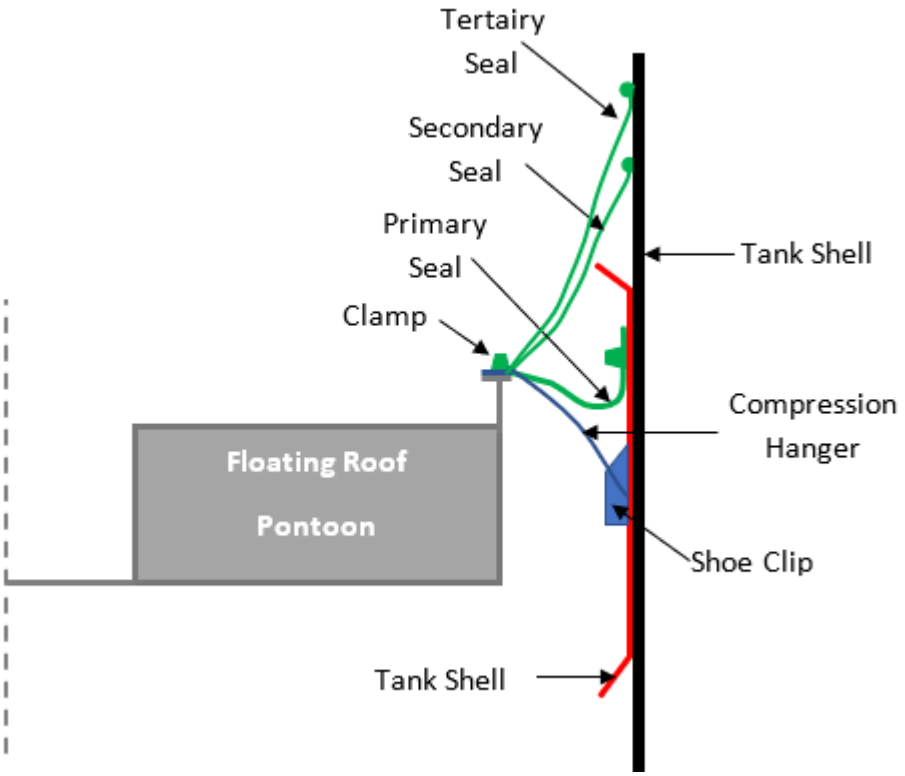

Figure 7.3. Three layers of the seal arrangement

The pictures in Figure 7.4 show a paper tape wrapped on the earth cable and a disconnected cable from the grounding clamp on the tank. Paper tape is not ideal insulation for a conductor carrying lightning current. Any thermal effect of the lightning current around the terminal can easily sear the paper. The disconnected earth cable from the tank's earth log is a failure in the line of defence, and this ought to be rectified.

Figure 7.4. Poor grounding cable management

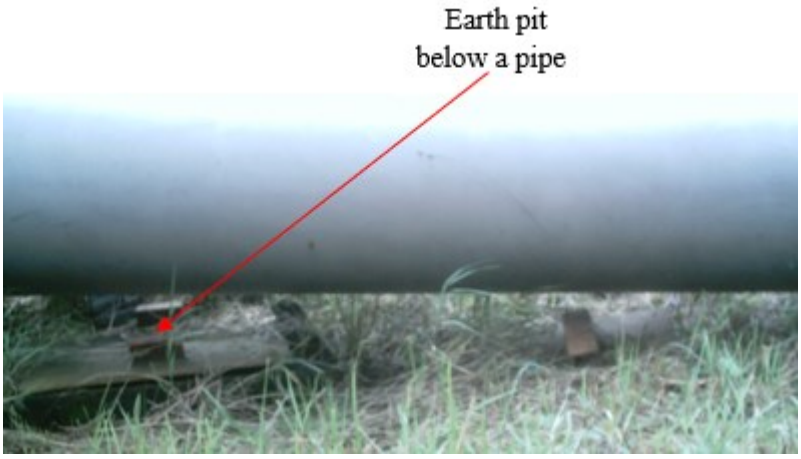

Figure 7.5. Improper grounding pit location

The ability of a conventional LPS to sink lightning current is affected by the effective impedance of the current flow path. The overall resistance of the grounding system is therefore important. It is essential to carry out a periodic test on the grounding system, e.g., the fall-off-potential test (FOPO), to keep track of the grounding system's ability to sink lightning current. It is important to provide adequate grounding for any LPS, and in a FRT facility, it is not only the number of grounding points that is important but also the location of such points. As shown in Figure 7.5, the inspection pit for an earth rod is positioned underneath a pipe, thereby preventing easy access to the earth rod for inspection and testing purposes. This may be due to improper planning from the onset or later retrofit pipe installation, which was not in the initial design. Since there is a space constraint within a tank’s bund wall, installing retrofit equipment, pipes and even LPS masts may be challenging if not well planned.

Cable routing and management are also crucial for ensuring Lightning Electromagnetic Pulses (LEMP) management within a flammable zone. In Figure 7.6 and Figure 7.7, cables are shown dangling around the steel stairs of a FRT. This is not ideal, and the wire loops may result in high voltage induction around that tank region when lightning strikes.

Figure 7.6. Sprawled cables around the tank shell

Figure 7.7. Cables dangling on the FRT's stairway

Oil spillage on the roof should be prevented or adequately cleaned to avoid ignition in the event of a lightning strike. Poor vapour management is as critical as the high-energy lightning current. Flammable vapour emission coupled with the ready availability of oxygen in the atmosphere is a potential disaster waiting for the source of ignition to complete the fire triangle. In Figure 7.8, the oil spill shown on the floating roof around the stairway is undesirable, especially as there are some unintended spark gaps along the steel stairway and its contact points with the roof. Ensuring the absence of flammable fuel-air vapour around the rim seal region and the exposed surface of the roof is vital for lightning safety.

Figure 7.8. Oil spills on the roof

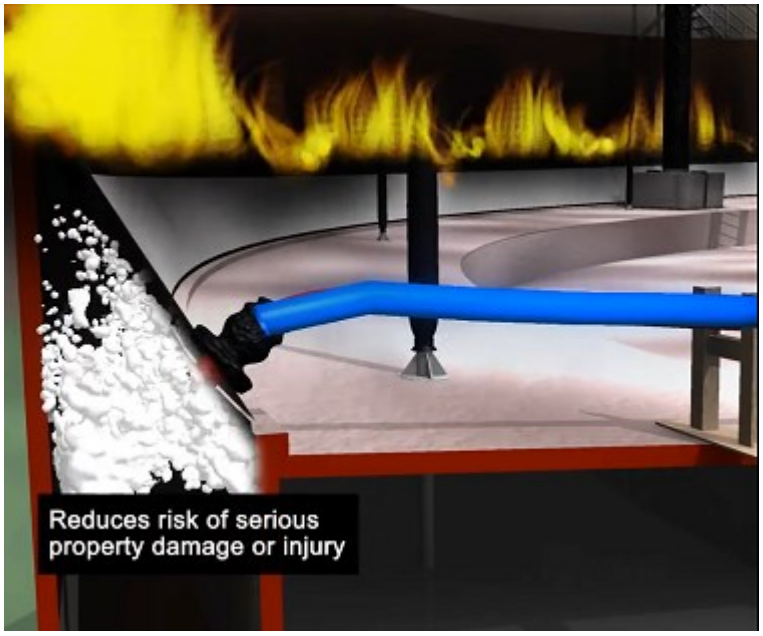

Figure 7.9. A system for delivering foam to the rim seal region [185]

A tank fire is undesirable, but there must be adequate firefighting equipment coupled with well-trained manpower to respond appropriately on time in the event of a fire. Fixed and mobile firefighting systems should be installed on and around FRTs. Modern fire extinguishing foam pourers such as the Mesa foam delivery system, as shown in Figure 7.9, can be installed to extinguish fires around the rim seal area.

Preventing lightning-induced tank fires can be achieved by a simple recommendation of ensuring flammable vapour containment and providing a safe pathway for the flow of lightning current. The following should be ensured in a FRT facility:

1) FRTs should have rim seals installed, and those with only a primary seal should be replaced with a double seal to reduce, if not eliminate, flammable fuel-air vapour escape.

2) Since shunts are inadequate, a LPS should be installed on a FRT, especially in tropical regions that experience severe lightning activities and significant lightning current magnitudes.
3) An adequate plant earthing network or grid should be available and connected to the FRT's LPS earthing points. Also, equipment, pipes, metallic conduits and cable trays should be appropriately bonded.
4) All corroded earth cable logs and studs should be cleaned or replaced.
5) A program for periodic earth resistance checks of earthing systems should be implemented and compliance monitored.
6) The yearly inspection of FRTs should include integrity checks of the LPS system components.
7) API recommendation on ensuring an insulation rating of 1 kV and greater for conductive seal assembly components that are non-fully submerged should be implemented on modern FRTs.
8) Proper cable segregation should be ensured in separating power and sensitive instrument or signal lines.
9) Remove unused cables and also avoid the use of excessive cable lengths within the bund wall. All dangling cables should be properly braced.

7.4 Challenges and potential study extension areas

In the course of this PhD study, challenges came up at various phases, and some of these challenges discussed below also create opportunities for future related studies.

1) The period of this PhD study coincided with the peak period of the COVID-19 pandemic in Germany. Previous plans to conduct study visits to FRT facilities in Germany were no longer feasible.
2) This study applied analytical techniques and computer simulations to evaluate various aspects of the FRT. FRTs are large structures which can be up to 100 m in diameter in some cases, and FRT models used for experimental purposes are usually like 2 m to 5 m in diameter. The lightning current generators available at the research cluster are designed for generating high lightning currents. The biggest generator has a small aperture for studying small devices. Vertical high-voltage generators will be required to research lightning interception by FRTs. Also, there is no special funding available for this doctoral study for producing such a big FRT model and various LPS models proposed for experimental studies. Likewise, analysis in external laboratories with high voltage generators will also require appropriate funding. Even if the LPS models can be experimentally evaluated, another challenge is the extent to which the result from a miniature model in the lab can be interpreted for an actual large FRT under natural lightning.

3) The inadequacy of shunts has been established with various recommendations to remove them from FRTs. Future research looking into the design and experimental verifications of the different conductive shell-to-roof links can help provide an effective alternative and possibly develop a commercial product.

4) This study has improved the DEGM concept to reduce the impacts of numerical errors and also speed up the computation time. A significant challenge with the current status is that the DEGM implementation is programming intensive, requiring about 1500 lines of intricate MATLAB codes per structure, depending on the complexity and the number of air terminals. The structures evaluated in the study are cuboids and cylindrical tanks with simple geometry that equations can define. Applying the technique for complex structures or any aesthetic, multi-shaped modern building will be very tasking to implement.

7.5 Conclusion

Designing and implementing safe and efficient LPS for a FRT requires an adequate understanding and evaluation of the various ways a lightning strike affects a FRT, as demonstrated in this study. Lightning can strike a FRT directly or indirectly. The effects of an indirect strike on adjacent grounds and structures can be mitigated by equipotential bonding and the use of SPDs. A direct strike requires appropriate channelling of the lightning current via safe paths to the ground. Lightning-induced tank fire is a significant threat to petroleum storage facilities and requires legitimate defences to prevent a recurrence.

The probability of a direct strike to a meshed FRT surface is evaluated using DEGM. First, the accuracy of the DEGM is enhanced to create an improved DEGM (IDEGM) by eliminating numerical errors and superfluous space points, which gave a significant simulation time advantage that decreased from over 20 hours to less than 30 minutes for a FRT. A factor termed K_{P2C} for converting PDF to CDF has been developed and applied to improve the computational accuracy of the numerical DEGM. FRT evaluation using DEGM reveals that the FRT's rim region has the highest probability of being hit by a lightning strike as a function of the diameter and the height of the tank. For a 20 m high FRT with a radius of 20 m and with its roof at the most elevated position, the probability of a direct strike to the rim areas is 95%. This increases to 99% when the roof is in the middle position. This result shows that the rim region is a critical area on a FRT, and it confirms the historical observation that about 95% of FRT fires start at the rim seal region.

Resistance (R) and inductance (L) modelling of a FRT struck by lightning revealed that a voltage level of about 55 kV can develop at the strike point on the rim. Flammable vapours can be ignited by voltage levels of 25 – 60 kV, as reported by various studies, and this shows that lightning can indeed induce fire on a FRT if the fire triangle is complete. A lightning current of 10/350 μs, 200 kA for 500 μs applied to the floating roof with RL values at 25 kHz to study the effects on the FRT when the lightning current crosses the air gap from the tank

roof to the shell revealed that the peak voltage across the air gap is approximately 211 kV with a voltage of 34.7 kV across the roof when the grounding resistance is 10 Ω but when the current flows from the tank shell to the roof, the air gap voltage is 14.4 kV. This result shows that a direct strike to the floating roof creates the highest level of risk because all the lightning current hitting the roof must flow to the shell via the air gap and any available shunts. Preventing lightning from directly hitting the floating roof is vital for ensuring the lightning safety of a FRT. Also, the use of connected, multiple catenary wires to intercept the lightning strike significantly reduces the peak voltage along the sections of the tank's shell.

The best of the nine LPS models proposed in this study can prevent a direct strike to the floating roof by using three parallel catenary wires supported by masts. This design has an interception efficiency of 99.93% when the roof is at the top, with a maximum roof-strike current of 1.9 kA. The second recommended option is a LPS model using air terminals installed on the rim and the roof of the FRT with an interception efficiency of 99.88% when the roof is at the top, with a maximum roof strike current of 3.4 kA. The third recommended option involves the use of lightning masts installed around the FRT with an interception efficiency of 99.83% when the roof is at the top, with a maximum roof-strike current of 9.4 kA.

Poor operational practices and maintenance culture can cause a well-designed LPS to fail. Efforts must be geared towards ensuring good operational and safe practices within a flammable fuel storage tank farm. Staff must be adequately trained with appropriate scenario drills and demonstrations to ensure incident readiness, and safety measures and interventions must be periodically reviewed, revised and improved if necessary.

References

[1] O. S. Peters, "Protection of life and property against lightning," *Technologic Papers of the Bureau of Standards,* 1915.

[2] Z. Flisowski and P. Sul, "Individual assessment of the lightning hazard of building objects as a guarantee of their proper protection," *Electric Power Systems Research,* vol. 178, 2020.

[3] A. Galván Diego, "Lightning protection of high-risk installations: petrochemical plants," in *Lightning: Science, Engineering, and Economic Implications for Developing Countries*, C. Gomes, Ed., ed Singapore: Springer Singapore, pp. 173-201, 2021.

[4] P. Moshashaei, S. S. Alizadeh, L. Khazini, and M. Asghari-Jafarabadi, "Investigate the causes of fires and explosions at external floating roof tanks: A comprehensive literature review," *Journal of Failure Analysis and Prevention,* vol. 17, pp. 1044-1052, 2017.

[5] K. Jung, D. Shim, and D. Son, "Review about the lightning protection system for ground facilities of anti-aircraft weapons system," *Journal of the Korea Institute of Military Science and Technology,* vol. 24, pp. 339-347, 2021.

[6] Z. M. Leksana, Suhariyanto, and F. D. Wijaya, "Evaluation of implementation of external lightning protection system: case study on the military radar tower," in *3rd International Conference on Information Technology, Information System and Electrical Engineering (ICITISEE)*, pp. 164-168, 2018.

[7] Y. Shuyu, X. Wei, and S. Zheng, "Study on application of random bidirectional discharge model in risk assessment of lightning disaster at airport," in *34th International Conference on Lightning Protection (ICLP)*, pp. 1-4, 2018.

[8] C. Karch, F. Heidler, and C. Paul, "Protection of aircraft radomes against direct lightning strikes -An overview," *Atmosphere,* vol. 12, p. 1141, 2021.

[9] T. Kai, K. Yamamoto, and S. Sumi, "Lightning protection for power cables connected to aviation lights on an airport runway," in *International Symposium on Lightning Protection (XIV SIPDA)*, pp. 157-161, 2017.

[10] M. S. M. Nasir, M. Z. A. Ab-Kadir, M. A. M. Radzi, M. Izadi, N. I. Ahmad, and N. H. Zaini, "Lightning performance analysis of a rooftop grid-connected solar photovoltaic without external lightning protection system," *PLoS ONE,* vol. 14, 2019.

[11] J. C. Hernández, P. G. Vidal, and F. Jurado, "Lightning and surge protection in photovoltaic installations," *IEEE Transactions on power delivery,* vol. 23, pp. 1961-1971, 2008.

[12] Z. Yao, Z. Li, Z. Kaifang, Z. Tong, and Z. Liang, "Dynamic striking distance and electrical geometrical model of wind turbine blades based on lightning physics," *The Journal of Engineering,* vol. 2017, pp. 2298-2302, 2017.

[13] J. Birkl, E. Shulzhenko, J. Kolb, and M. Rock, "Approach for evaluation of lightning current distribution on wind turbine with numerical model," in *33rd International Conference on Lightning Protection (ICLP)*, pp. 1-8, 2016.

[14] H. Persson and A. Lönnermark, "Tank fires-Review of fire incidents 1951-2003," SP Swedish National Testing and Research Institute, Borås2004.

[15] P. Moshashaei, S. S. Alizadeh, M. A. Jafarabadi, and L. Khazini, "Prioritizing the causes of fire and explosion in the external floating roof tanks," *Journal of Failure Analysis and Prevention,* vol. 18, pp. 1587-1600, 2018.

[16] T. Kletz, "Chapter 5 - Storage tanks," in *What Went Wrong?: Case Histories of Process Plant Disasters and How They Could Have Been Avoided*, 5th ed, pp. 97-121, 2009.

[17] A. Tatematsu, H. Motoyama, and A. Tanigawa, "Application of the FDTD-based simulation code VSTL REV to the lightning surge analysis of a nuclear power plant," *Electric Power Systems Research,* vol. 178, 2020.

[18] N. Petrov, G. Petrova, and F. D'alessandro, "Quantification of the probability of lightning strikes to structures using a fractal approach," *IEEE Transactions on Dielectrics and Electrical Insulation,* vol. 10, pp. 641-654, 2003.

[19] P. N. Mikropoulos and T. E. Tsovilis, "Interception Probability and Proximity Effects: Implications in Shielding Design Against Lightning," *IEEE Transactions on Power Delivery,* vol. 25, pp. 1940-1951, 2010.

[20] IEC 62305-1:2010, *Protection against lightning – Part 1: General principles*

[21] F. Heidler, W. Zischank, Z. Flisowski, C. Bouquegneau, and C. Mazzetti, "Parameters of lightning current given in IEC 62305-background, experience and outlook," in *29th International Conference on Lightning Protection*, p. 26, 2008.

[22] M. El-Samanody, A. Ghorab, and A. S. Noaman, "Design and study of floating roofs for oil storage tanks," *Mechanics and Mechanical Engineering,* vol. 21, 2017.

[23] R. Zinke, F. Köhler, A. Klippel, U. Krause, and B. Leitl, "Emissions of volatile hydrocarbons from floating roof tanks and their local dispersion: Considerations for normal operation and in case of damage," *Journal of Loss Prevention in the Process Industries,* vol. 66, p. 104179, 2020.

[24] D. W. Skaf and T. Lervolino, "Atmospheric storage tank emission estimates: understanding the calculation basis and effects of uncertainty in meteorological inputs," *Journal of Environmental Engineering,* vol. 145, p. 04019089, 2019.

[25] A. I. Adekitan and M. Rock, "Performance investigation of lightning protection systems for floating roof tanks in Nigeria," in *13. VDE Blitzschutztagung*, Aschaffenburg, pp. 71-77, 2019.

[26] J. I. Chang and C.-C. Lin, "A study of storage tank accidents," *Journal of Loss Prevention in the Process Industries,* vol. 19, pp. 51-59, 2006.

[27] E. Renni, E. Krausmann, and V. Cozzani, "Industrial accidents triggered by lightning," *Journal of Hazardous Materials,* vol. 184, pp. 42-48, 2010.

[28] A. Necci, F. Argenti, G. Landucci, and V. Cozzani, "Accident scenarios triggered by lightning strike on atmospheric storage tanks," *Reliability Engineering & System Safety,* vol. 127, pp. 30-46, 2014.

[29] C. Breitweiser, "AST Lightning Protection - API 545 Update," in *API Storage Tank Conference*, Fort Worth, Texas, 2008.

[30] V. Sharma, A. Nandan, and N. A. Siddiqui, "Study and analysis of storage tank hazards and its mitigation measures using bow tie diagram," *Research & Reviews: Journal of Engineering and Technology,* vol. 7, 2018.

[31] T. Wei, X. Qian, and M. Yuan, "Quantitative risk assessment of direct lightning strike on external floating roof tank," *Journal of Loss Prevention in the Process Industries,* vol. 56, pp. 191-203, 2018.

[32] Y. Liu, Z. Fu, A. Jiang, Q. Liu, and B. Liu, "Analysis of the effect on the large floating roof oil tanks struck by indirect lightning based on FDTD," in *International Conference on Lightning Protection (ICLP)*, pp. 911-916, 2014.

[33] S. Haigh, P. Leichauer, M. Scanlon, and B. Burrows, "Mitigation of the lightning hazard for above ground hydrocarbon floating roof storage tanks," *Hazards XXI: Process Safety and Environmental Protection in a Changing World Symposium Series 155,* 2009.

[34] V. Cooray, *An Introduction to Lightning*: Springer Netherlands, 2015.

[35] J. Stevens and K. Hansen, 2013, Global lightning activity. *NASA Earth Observatory*. Available: https://earthobservatory.nasa.gov/images/85600/global-lightning-activity

[36] M. Akinyemi, A. Boyo, M. Emetere, M. Usikalu, and O. Olawole, "Lightning a Fundamental of Atmospheric Electricity," in *International Conference on Environment Systems Science and Engineering*, pp. 47–52, 2014.

[37] E. M. Emetere, "Lightning as a Source of Electricity: Atmospheric Modeling of Electromagnetic Fields," *International Journal of Technology,* vol. 8, pp. 508-518, 2017.

[38] D. W. Zipse, *Lightning Protection Systems: Advantages and Disadvantages* vol. 30, 1993.

[39] V. Rakov, "A review of positive and bipolar lightning discharges," *Bulletin of the American Meteorological Society,* vol. 84, pp. 767-776, 2003.

[40] J. Birkl, A. Kern, G. Diendorfer, and S. Thern, "Extremely high lightning peak currents," in *34th International Conference on Lightning Protection (ICLP)*, pp. 1-7, 2018.

[41] D. Johari, V. Cooray, M. Rahman, P. Hettiarachchi, and M. M. Ismail, "Characteristics of leader pulses in positive ground flashes in Sweden," *Electric Power Systems Research,* vol. 153, pp. 3-9, December, 2017.

[42] A. Kalair, N. Abas, and N. Khan, "Lightning interactions with humans and lifelines," *Journal of Lightning Research,* vol. 5, pp. 11–28, 2013.

[43] M. Rock, "Protection of Selected Cases: PV Systems, Wind Turbines and Railway Systems," in *Lightning: Science, Engineering, and Economic Implications for Developing Countries*, C. Gomes, Ed., ed Singapore: Springer Singapore, pp. 203-261, 2021.

[44] F. Rachidi, M. Rubinstein, J. Montanya, J. L. Bermudez, R. Sola, G. Sola*, et al.*, *A review of current issues in lightning protection of new-generation wind-turbine blades* vol. 55, 2008.

[45] N. M. Nor, S. Abdullah, S. Reffin, N. Agbor, N. A. Rahman, N. Abdullah*, et al.*, "Determination of critical electric field and recommended earth resistance values," *International Review of Electrical Engineering,* vol. 12, 2017.

[46] W. Rison, "Experimental validation of conventional and nonconventional lightning protection systems," in *Power Engineering Society General Meeting*, pp. 2195-2200, 2003.

[47] A. J. Eriksson, "Lightning and tall structures," *Transactions South Africa. The SA Institute of Electrical Engineering,* vol. 69, pp. 238-252, 1978.

[48] K. Arzag, Z.-E. Azzouz, and B. Ghemri, "Lightning Return Stroke Current Analysis Using Electromagnetic Models and the 3D-FDTD Method," *Journal of Electrical Systems,* vol. 13, pp. 160-168, 2017.

[49] T. Ogasawara, Y. Hirano, and A. Yoshimura, "Coupled thermal–electrical analysis for carbon fiber/epoxy composites exposed to simulated lightning current," *Composites Part A: Applied Science and Manufacturing,* vol. 41, pp. 973-981, August, 2010.

[50] V. A. Rakov and M. A. Uman, *Lightning: Physics and Effects*: Cambridge University Press, August 2003.

[51] SAE ARP 5412, "Aircraft lightning environment and related test waveforms, aerospace recommended practice" 1999.

[52] A. Adoghe, A.F. Agbetuyi, A. Abdulkareem, J. Olowoleni, and C. Awosope, "Review of lightning protection standard in building structures in Nigeria," *IOSR Journal of Electrical and Electronics Engineering,* vol. 9, pp. 51-54, 2014.

[53] A. Ghavamian, M. R. Maghami, S. Dehghan, and C. Gomes, "Concerns of corrosive effects with respect to lightning protection systems," *Engineering Failure Analysis,* vol. 57, pp. 434-443, 2015.

[54] G. Ala and M. L. D. Silvestre, "A simulation model for electromagnetic transients in lightning protection systems," *IEEE Transactions on Electromagnetic Compatibility,* vol. 44, pp. 539-554, 2002.

[55] A. M. Mousa and P. Eng, "War of the Lightning Rods," *Electricity Today,* 2004.

[56] M. Uman and V. Rakov, "A critical review of nonconventional approaches to lightning protection," *Bulletin of the American Meteorological Society,* vol. 83, pp. 1809-1820, 2002.

[57] I. A. Adekitan, Isaac Samuel, Bukola Adetokun, and T. Shomefun, "Monte Carlo simulation approach to soil layer resistivity modelling for grounding system design," *International Journal of Applied Engineering Research,* vol. 12, pp. 13759-13766, 2017.

[58] R. H. S. Soeprapto, "Modelling lightning strike on overhead lines for the analysis of back flashover using electromagnetic transient program (EMTP)," *International Review of Electrical Engineering,* vol. 9, 2014.

[59] D. Muller-Hillebrand, "The protection of houses by lightning conductors—An historical review," *Journal of the Franklin Institute,* vol. 274, pp. 34-54, July, 1962.

[60] R. N. Covert, "Protection of buildings and farm property from lightning," *Farmers' Bulletin No. 1512,* 1926.

[61] J. M. Tobias, C. L. Wakefield, L. W. M. Strother, V., and J. Covino, "The basis of conventional lightning protection technology: A review of the scientific development of conventional lightning protection technologies and standards," 2001.

[62] Committee on Atmospheric and Space Electricity of the American, "Scientific basis for traditional lightning protection systems," The American Geophysical Union, 2001.

[63] W. J. Smith, "Efficacy of Lightning Rods," 1915.

[64] E. M. Bazelyan and Y. P. Raizer, *Lightning physics and lightning protection,* . Bristol, England: Institute of Physics Publishing, 2000.

[65] A. Mousa and K. D. Srivastava, "A revised electrogeometric model for the termination of lightning strokes on ground objects," in *International Aerospace and Ground Conference on Lightning and Static Electricity*, Oklahoma, pp. 342-352, 1988.

[66] Z. Hartono and I. Robiah, "Review of studies of ESE & CTS in Malaysia," in *17th International Symposium EMC*, Zurich, 2006.

[67] Z. A. Hartono and I. Robiah. (Nov 15, 2021). *Conventional and un-conventional lightning air terminals: An overview*. Available: http://ground.co.kr/PGS_forum/forum_20090818.html

[68] Electrical Knowhow. (2013, 24-May-2022). *Non-conventional lightning protection system – part two*. Available: http://www.electrical-knowhow.com/2014/02/Charge-Transfer-Lightning-Protection-System.html

[69] T. C. Marshall and M. Stolzenburg, "Voltages inside and just above thunderstorms," *Journal of Geophysical Research: Atmospheres,* vol. 106, pp. 4757-4768, 2001.

[70] Roy B. Carpenter Jr. and M. N. Drabkin, Lightning Strike Protection. Available: https://www.academia.edu/7120069/Lightning_Strike_Protection

[71] M. M. Drabkin, C. Y. A. Mui, and Ong Lai Mun, "Lightning protection of tall structures thunderbolt and lightning very very fright'ning?," *The Electrical Engineer,* vol. XLIV 3rd Quarter, pp. 27-30, 2014.

[72] N. L. Aleksandrov, E. M. Bazelyan, J. R. B. Carpenter, M. M. Drabkin, and P. R. Yu, "The effect of coronae on leader initiation and development under thunderstorm conditions and in long air gaps," *Journal of Physics D: Applied Physics,* vol. 34, p. 3256, 2001.

[73] N. L. Aleksandrov, E. M. Bazelyan, R. B. Carpenter, M. M. Drabkin, and Y. Raizer, "Prospects for reliability improvement of lightning protection owing to long-duration injection of space charge into atmosphere," in *Proceedings of 26th International Conference on Lightning Protection*, Poland, 2002.

[74] N. L. Aleksandrov, E. M. Bazelyan, M. M. Drabkin, R. B. Carpenter, and Y. P. Raizer, "Corona discharge at the tip of a tall object in the electric field of a thundercloud," *Plasma Physics Reports,* vol. 28, pp. 953-964, 2002.

[75] R. B. Carpenter and R. Auer, "Lightning and surge protection of substations," in *35th Rural Electric Power Conference,* , pp. B6/1-B615, 1991.

[76] Federal Aviation Administration, "Lightning protection multpoint discharge systems tests Orlando, Sarasota, and Tampa, Florida," presented at the FAATC T16 Power Systems Program, Final Rep. ACN-210, 1989.

[77] R. B. Bent and S. K. Llewellyn, "An investigation of the lightning elimination and strike reduction properties of dissipation arrays," Atlantic Science Corp. Indialantic, FL, 1976.

[78] A. M. Mousa, "Validity of the lightning elimination claim," in *Power Engineering Society General Meeting*, pp. 2213-2218, 2003.

[79] W. Rison, "There is no magic to lightning protection: charge transfer systems do not prevent lightning strikes," *New Mexico Institute of Mining and Technology, Langmuir Laboratory for Atmospheric Research,* 2002.

[80] W. Durrett, "Dissipation arrays at Kennedy space center," *Review of Lightning Protection Technology for Tall Structures,* vol. 449, pp. 24-52, 1977.

[81] U.S. Air Force, "Review of lightning protection technology for tall structures," November 6, 1975.

[82] A. M. Mousa, *The applicability of lightning elimination devices to substations and power lines* vol. 13, 1998.

[83] Lightning Protection Institute. (2005, April) IEEE terminates Projects P1576 on CTS lightning protection. *LPI Tech Letter*.

[84] TSTLP. (2022). *Early streamer emission air terminal*. Available: https://www.tslpro.com/smt-ese-air-terminal-13.html

[85] A. M. Mousa, "Failure of the collection volume method and attempts of the ese lightning rod industry to resurrect it," *Journal of Lightning research,* vol. 4, pp. 118-128, 2012.

[86] N. Allen, K. Cornick, D. Faircloth, and C. Kouzis, "Tests of the 'early streamer emission' principle for protection against lightning," *IEE Proceedings-Science, Measurement and Technology,* vol. 145, pp. 200-206, 1998.

[87] J. Dubin. (2005). *Reactions towards Mr Abdul Mousa statements*. Available: https://www.scribd.com/document/84045585/Reactions-Towards-Mr-Abdul-Mousa-Statement

[88] M. Becerra and V. Cooray, "Laboratory experiments cannot be utilized to justify the action of early streamer emission terminals," *Journal of Physics D: Applied Physics,* vol. 41, p. 085204, 2008.

[89] S. McIvor, R. Carpenter, and M. Drabkin, "Evaluation of early streamer emission air terminals," ed: ITEM, 1998.

[90] R. Kithil and O. Alzamora, 2013, Dynasphere ESE air terminals: Issues deserving consideration. Available: http://lightningsafety.com/nlsi_lhm/ESEIssuesDeservingConsideration.pdf

[91] Z. A. Hartono, "Clear Evidence of Lightning Strikes to a Building Installed with Multiple ESE Air Terminals," in *35th International Conference on Lightning Protection (ICLP) and XVI International Symposium on Lightning Protection (SIPDA)*, pp. 1-6, 2021.

[92] O. Beierl and R. Brocke, "Wirkungsweise niederimpedanter isolierter Ableitungen," presented at the VDE/ABB-Blitzschutztagung, Aschaffenburg, Germany, 2017.

[93] C. Moore, G. Aulich, and W. Rison, "Measurements of lightning rod responses to nearby strikes," *Geophysical research letters,* vol. 27, pp. 1487-1490, 2000.

[94] C. Bouquegneau, "A critical view on the lightning protection international standard," *Journal of electrostatics,* vol. 65, pp. 395-399, 2007.

[95] K. Chrzan and Z. Hartono, "Inefficacy of radioactive terminals and early streamer emission terminals," *XIIIth International Sympos. High Voltage Engineering,* p. 86, 2003.

[96] R. H. Golde, *Lightning protection*: Edward Arnold (Publishers) Ltd., 1973.

[97] Z. A. Hartono and I. Robiah, 2010, The Bell Tower Incident. Available: http://www.lightningsafetyalliance.com/documents/Sigolsheim+bell+tower+incident_rev1.pdf

[98] C. Cixuan, X. Guangrun, and X. Zifeng, "Thc semiconductor lightning current duration extender (SLE)," presented at the 24th International Conference on Lightning Protection (ICLP), United Kingdom, 1998.

[99] Y. Zhang, M. Chen, Y. Du, and X. Liu, "Phenomena of parallel discharges and flashovers in lightning triggered to conventional and non-conventional lightning rods," *IEEJ Transactions on Fundamentals and Materials,* vol. 126, pp. 531-535, 2006.

[100] C. Chen, G. Xie, and Z. Xie, "An introduction to semiconductor lightning current duration extender," presented at the IEEE Power Engineering Society Winter Meeting. , 2000.

[101] G. Xie, C. Chen, Y. Chen, X. Wen, and J. Yu, "Theory and practice of semiconductor lightning eliminator," in *Proceedings of EMPD '98. 1998 International Conference on Energy Management and Power Delivery (Cat. No.98EX137)*, pp. 532-537 vol.2, 1998.

[102] G. Xie, C. Chen, X. Wen, J. Wang, Y. Zhang, J. Yu*, et al.*, "Analysis of test results on rocket triggered lightning to lightning rod and semiconductor lightning eliminator," *High Voltage Eng.,* vol. 32, p. 11, 2006.

[103] X. Liu, K. Jiang, and J. Xiong, "The application of current-limiting lightning rods on high-rise buildings," in *11th Asia-Pacific International Conference on Lightning*, pp. 1-4, 2019.

[104] Y. Zhang and X. Liu, "Experiment of artificially triggered lightning to lightning rod and semiconductor lightning eliminator," presented at the International Conference on Atmospheric Electricity (ICAE), France, 2003.

[105] A. I. Adekitan and M. Rock, "Lightning exposure of oil tanks with changing roof position," presented at the XII Russian-German Raw Materials Conference, Saint-Petersburg, 2019.

[106] M. S. Mannan, K. Krishna, R. E. Sanders, C. A. Brown, G. K. Lee, M. Sawyer*, et al.*, "Chapter 22 - Storage," in *Lees' Loss Prevention in the Process Industries (Fourth Edition)*, S. Mannan, Ed., 4 ed Oxford: Butterworth-Heinemann, pp. 1889-1985, 2012.

[107] Nexus Alliance, *Shell intensive training programme (SITP 2) phase 1 operations module 3 manual*, 2008.

[108] A. Kulikov and S. Chekardovskiy, "Improving the safety of operation of tanks with a floating roof in the winter period," in *IOP Conference Series: Materials Science and Engineering*, p. 012010, 2018.

[109] Chemical Strategies. (2019). *Flammable liquids classes & categories*. Available: https://chemicalstrategies.com/flammable-liquids-classes-and-categories/

[110] M. S. Hildebrand, G. G. Noll, and W. T. Hand, *Above ground bulk storage tank emergencies*, 2 ed.: Jones & Bartlett Learning, 2019.

[111] Geldof. (2018). *7 double walled tanks, dome & internal floating roof*. Available: https://www.geldof.be/?portfolio=7-double-walled-tanks-dome-internal-floating-roof-28624

[112] R. Zinke, F. Köhler, and U. Krause, "Long-term emission measurements at a floating roof tank for gasoline storage," *Journal of Loss Prevention in the Process Industries,* vol. 55, pp. 152-161, 2018.

[113] Float Tek. (2022). *Tank Seal*. Available: http://www.float-tek.com/en/product.php?act=list&cid=10

[114] Eco Tank Systems. (2022). *Primary mechanical shoe seal*. Available: https://www.ecotanksystems.in/vapourcontrolsystem.html

[115] DEHN + SÖHNE, *Lightning protection guide*, 2014.

[116] D. Wu and Z. Chen, "Quantitative risk assessment of fire accidents of large-scale oil tanks triggered by lightning," *Engineering failure analysis,* vol. 63, pp. 172-181, 2016.

[117] Pictures and images of France. (2005). *Aftermath of the Buncefield oil terminal fire*. Available: https://www.reddit.com/r/ImagesOfFrance/comments/3w4yqh/aftermath_of_the_buncefield_oil_terminal_fire/

[118] R. Ritchie, "Предотвращение возгорания резервуаров для хранения нефтепродуктов," *Нефтегазовые технологии,* pp. 101-104, 2010.

[119] B. Q. Liu, H. Y. Hu, Q. Z. Liu, T. T. Zhang, and X. Gao, "Research on shunts spark discharge in the oil and gas space of floating roof tank," *Insulators and Surge Arresters,* pp. 86-89, 2012.

[120] API-RP 545-A, "Verification of lightning protection requirements for above ground hydrocarbon storage tanks," 2009.

[121] A. I. Adekitan and M. Rock, "Lightning induced fires: A case study of floating roof tanks," presented at the XII Russian-German Raw Materials Forum: Youth Day, St Petersburg, Russia, 2019.

[122] L. B. Huang, W. Y. Chai, and W. Y. Li, "Research on the safety of secondary spark discharge to oil/gas area induced by lightning," *Static Electron,* vol. 10, pp. 45-47, 1995.

[123] Y. Liu, Z. Fu, A. Jiang, Q. Liu, and B. Liu, "FDTD analysis of the effects of indirect lightning on large floating roof oil tanks," *Electric Power Systems Research,* vol. 139, pp. 81-86, 2016.

[124] H. E. Sueta, L. E. Caires, V. Teixeira, M. Shigihara, and G. F. Burani, "Protection of fuel storage tanks against lightning-Experimental developments and risk analysis," in *Asia-Pacific International Conference on Lightning (APL)*, 2015.

[125] Lastfire, 2016, Lastfire boilover research – practical lessons learned. *(3)*. Available: http://www.lastfire.co.uk/uploads/LASTFIRE%20BOILOVER%20LESSONS%20Issue%203%20December%202016.pdf

[126] A. Adekitan and M. Rock, "The undesirable interaction of lightning strike and floating roof tanks," in *35th International Conference on Lightning Protection (ICLP) and XVI International Symposium on Lightning Protection (SIPDA)*, pp. 1-8, 2021.

[127] Health and Safety Executive, *HSG176: The storage of flammable liquids in tanks*, 2015.

[128] T. Kletz, "Chapter 13 - Tank trucks and cars," in *What Went Wrong? Case Histories of Process Plant Disasters and How They Could Have Been Avoided*, 5 ed: Butterworth-Heinemann, pp. 237-245, 2009.

[129] E. Wami, W. Onunwor, O. Chisa, and D. Jimmy, "Design of a floating roof crude oil storage tank of 100,000 bpd capacity and prototype fabrication," *Journal of Scientific and Engineering Research,* vol. 4, pp. 318-329, 2017.

[130] API-RP 545, "Recommended practice for lightning protection of aboveground storage tanks for flammable or combustible liquids," 2009.

[131] A. I. Adekitan, "Lightning protection of floating roof tanks," *American Journal of Engineering Research,* vol. 2, pp. 11-21, 2013.

[132] H. Hu and Q. Liu, "Research on lightning sparks discharge and protection measures of large floating roof tank," presented at the International Conference on Lightning Protection (ICLP), 2012.

[133] M. Guthrie, N. Blanch, A. Rousseau, and F. Vincennes, "Lightning related ignition mechanism and associated protection techniques for storage applications," presented at the 9th Global Congress on Process Safety, San Antonio, Texas, 2013.

[134] J. A. Lanzoni, "Improving Lightning Safety of Petroleum Storage Tanks," Lightning Eliminators and Consultants2009.

[135] Lightning Eliminators and Consultants, 2016, RGA 750 retractable grounding assembly. Available: https://www.hydrocarbons-technology.com/products/rga750/

[136] B. Denov and R. Zoro, "Lightning protection system for oil and gas installation case on cilacap area at Central Java, Indonesia," in *6th International Conference on Electrical Engineering and Informatics (ICEEI)*, pp. 1-7, 2017.

[137] M. F. Khan, 2019, Explore the hazard associated with rolling stairs at floating roof tank. Available: https://www.linkedin.com/pulse/explore-hazard-associated-rolling-stairs-floating-roof-fahad-khan

[138] NFPA-780, "Standard for the installation of lightning protection systems," 2017.

[139] B. Liu, J. Anfeng, and Z. Fu, "Scale model experiment for the study of lightning-induced spark discharge on large floating roof oil tanks," in *International Conference on High Voltage Engineering and Application*, pp. 81-84, 2012.

[140] F. Zhang, H. Jiang, and C. Zhang, "Study of charging nitrogen to external floating roof tank to prevent rim-seal fires from lightning," *Procedia Engineering,* vol. 71, pp. 124–129, 2014.

[141] H. Sueta, L. Caires, V. Teixeira, G. Burani, M. Shigihara, G. Ansiliero*, et al.*, *Llightning protection of above ground fuel storage tanks*, 2014.

[142] E. Degaev and D. Korolchenko, "Improving Fire Protection of Pontoon Tanks or Floating Roof Tanks," *MATEC Web of Conferences,* vol. 117, p. 36, 2017.

[143] X. Ren, Z. Fu, N. Yan, and W. Sun, "Analysis and experimental investigation of direct lightning protection for floating roof oil tanks," *Electric Power Systems Research,* vol. 94 pp. 134–139, 2012.

[144] X. Ren, Z. Fu, N. Yan, and W. Sun, "Analysis and experimental investigation of direct lightning protection for floating roof oil tanks," in *7th Asia-Pacific International Conference on Lightning*, pp. 762-766, 2011.

[145] H. Sueta, M. Shigihara, L. Caires, and G. Burani, "Experimental verifications of direct lightning protection in flammable liquid storage tanks: Cases of carbon-steel and aluminum geodesic domes," presented at the International Symposium on Lightning Protection (XIV SIPDA), 2017.

[146] D. A. Galván and C. Gomes, "Protection of oil storage tanks against direct lightning strikes: Self protection scheme or standalone LPS?," in *International Symposium on Lightning Protection (XII SIPDA)*, pp. 309-313, 2013.

[147] X. Z. Meng, G. M. Liu, and C. Li, "Study on intelligent fire fighting system for large external floating-roof tank," *DEStech Transactions on Materials Science and Engineering,* 2016.

[148] Y. Wang, M. Liu, F. Liu, C. Zhao, D. Zhao, F. Han*, et al.*, "Research on the effect of wall corrosion and rim seal on the withdrawal loss for a floating roof tank," *Environmental Science and Pollution Research,* vol. 25, pp. 18434-18442, 2018.

[149] V. Cooray, "Attachment of lightning flashes to grounded structures," in *Lightning Electromagnetics*, ed: Institution of Engineering and Technology, 2012, pp. 765-787.

[150] I. Ullah, M. N. R. Baharom, H. Ahmad, F. Wahid, H. M. Luqman, Z. Zainal*, et al.*, "Smart Lightning Detection System for Smart-City Infrastructure Using Artificial Neural Network," *Wireless Personal Communications,* vol. 106, pp. 1743-1766, 2019.

[151] M. Becerra, F. Román, and V. Cooray, "Lightning attachment to common structures: is the rolling sphere method really adequate?," presented at the 29th International Conference on Lightning Protection (ICLP), Uppsala, Sweden, 2008.

[152] Z. Hartono, I. Robiah, and M. Darveniza, "A database of lightning damage caused by bypasses of air terminals on buildings in Kuala Lumpur, Malaysia," in *Proc. of the 6th International Symposium on Lightning Protection, Santos, Brazil*, 2001.

[153] Z. A. Hartono and I. Robiah, "A study of non-conventional air terminals and stricken points in a high thunderstorm region," in *25th International Conference on Lightning Protection,*, pp. 357-361, 2000.

[154] T. Horvath, "Relation between the radius of the rolling sphere and the probability of lightning stroke," presented at the 18th International Conference on Lightning Protection, Munich, Germany, 1985.

[155] A. Kern, C. Schelthoff, and M. Mathieu, "Probability of lightning strikes to air-terminations of structures using the electro-geometrical model theory and the statistics of lightning current parameters," presented at the 30th International Conference on Lightning Protection (ICLP), 2010.

[156] M. Hannig, V. Hinrichsen, R. Hannig, and R. Brocke, "An analytical consideration on the striking probability and the total amount of strikes to simple structures according to standardized regulations," presented at the International Conference on Lightning Protection (ICLP), 2014.

[157] A. I. Adekitan and M. Rock, "The impact of space point definition on dynamic electro-geometrical model of lightning strike probability," *Electric Power Systems Research,* vol. 184, p. 106336, 2020.

[158] V. Rakov, "Lightning parameters for engineering applications (keynote speech)," presented at the Asia-Pacific International Symposium on Electromagnetic Compatibility, 2010.

[159] V. A. Rakov, "Lightning discharge and fundamentals of lightning protection," *Journal of Lightning Research,* vol. 4, pp. 3-11, 2012.

[160] A. I. Adekitan and M. Rock, "A further look at dynamic electro-geometrical model: Its fundamentals and implementation," *Ain Shams Engineering Journal,* vol. 11, pp. 651-658, 2020.

[161] A. Kern, C. Schelthoff, and M. Mathieu, "Calculation of interception efficiencies for air-terminations using a dynamic electro-geometrical model," presented at the International Symposium on Lightning Protection (SIPDA), Fortaleza, Brazil, 2011.

[162] A. I. Adekitan, "Improving the computational accuracy of the dynamic electro-geometrical model using numerical solutions," *Scientific Reports,* vol. 12, pp. 1-13, 2022.

[163] M. Hannig, V. Hinrichsen, and R. Brocke, "Determination of the probability function of lightning peak currents on flat ground," presented at the International Symposium on Lightning Protection (XIV SIPDA), 2017.

[164] W. Dodd, *Lightning and petroleum storage tanks: a scientific exposition of the manner by which lightning causes tank fires, with helpful suggestions and means of protection (classic reprint)*: Forgotten Books, 2018.

[165] API 650, (2007). *Welded steel tanks for oil storage (11 ed.)*.

[166] F. H. Budisatrio, B. Denov, Suwarno, S. Hidayat, A. S. Wisnu, and R. Zoro, "Tropical lightning strike potential as a cause of oil tank fire in Indonesia," in *2021 3rd International Conference on High Voltage Engineering and Power Systems (ICHVEPS)*, pp. 451-456, 2021.

[167] R. Zoro, "Tropical lightning current parameters and protection of transmission lines," *International Journal on Electrical Engineering and Informatics,* vol. 11, pp. 506-514, 2019.

[168] F. Heidler and J. Cvetić, "A class of analytical functions to study the lightning effects associated with the current front," *European transactions on electrical power,* vol. 12, pp. 141-150, 2002.

[169] M. Kamon, C. Smithhisler, and J. White, (1996). *FastHenry user's guide*.

[170] C. Buccella, "Computation of the transient voltage distribution caused by direct lightning on flammable liquid containers," in *Conference Record of the 1999 IEEE Industry Applications Conference. Thirty-Forth IAS Annual Meeting (Cat. No.99CH36370)*, pp. 421-428 vol.1, 1999.

[171] Z. Tan, "Theory on resistance of m × n cobweb network and its application," *International Journal of Circuit Theory and Applications,* vol. 43, pp. 1687-1702, 2015.

[172] IEEE Std 80, (2013). *IEEE guide for safety in AC substation grounding*.

[173] BS 7430, (2011). *Code of practice for protective earthing of electrical installations*.

[174] G. F. Tagg, *Earth resistances*. London: George Newnes, 1964.

[175] V. Hinrichsen, 2009, (December 12, 2022). Lecture series on high-voltage technology. *TU Darmstadt (2009/10)*. Available: https://www.mikrocontroller.net/attachment/276777/hst_v_09.pdf

[176] K. Bhumkittipich, B. Topradith, and T. Suwanasri, "Analysis of lightning phenomena for underground petroleum pipeline system," *Energy Procedia,* vol. 34, pp. 148-158, 2013.

[177] D. Caulker, H. Ahmad, and M. Mohamed Ali, "Effect of lightning induced voltages on gas pipelines using ATP-EMTP program," in *2008 IEEE 2nd International Power and Energy Conference*, pp. 393-398, 2008.

[178] L. Czumbil, D. Micu, D. Stet, and H. Nouri, "Induced voltages in metallic pipelines due to lightning strikes to nearby power lines," 2020.

[179] A. Elgayar and Z. Abdul-Malek, "Induced voltages on a gas pipeline due to lightning strikes on nearby overhead transmission line," *International Journal of Electrical and Computer Engineering (IJECE),* vol. 6, p. 495, 2016.

[180] ASTM A53, 2020, Standard specification for pipe, steel, black and hot-dipped, zinc-coated, welded and seamless.

[181] Engineering ToolBox. (2003, June 10, 2022). *ANSI Schedule 40 Steel Pipes - Dimensions*. Available: https://www.engineeringtoolbox.com/ansi-steel-pipes-d_305.html

[182] H. Walmsley, "Threshold potentials and discharge charge transfers for the evaluation of electrostatic hazards in road-tanker loading," *Journal of electrostatics,* vol. 26, pp. 157-173, 1991.

[183] IEC 62305-3:2010, *Protection against lightning – Part 3: Physical damage to structures and life hazard*.

[184] IS 2309, 1989, Protection of buildings and allied structures against lightning - code of practice.

[185] Mesa ETP. (2013, May 15, 2022). *Foam Delivery System for Floating Roof Tanks*. Available: https://www.youtube.com/watch?v=ceyIhuMq92A

[186] NASA/MSFC, 2016, Global lightning image. Available: https://ghrc.nsstc.nasa.gov/lightning/images/browse/mission.png

[187] T. Horvath, "The protected space proved to be an undefined term," in *International Conference on Lightning Protection (ICLP)*, pp. 1-7, 2012.

[188] CIGRÉ, "Guide to procedures for estimating the lightning performance of transmission lines," Report of CIGRÉ Working Group 01 Lightning vol. 1, 1991.

[189] CIGRÉ, Lightning parameters for engineering applications, 2013.

[190] IEEE Working Group on Lightning Performance of Transmission Lines, "A simplified method for estimating lightning performance of transmission lines," IEEE Trans. Power App. Syst., vol. PAS-104, pp. 919–932, April, 1985.

Appendices

Appendix A: Lightning current

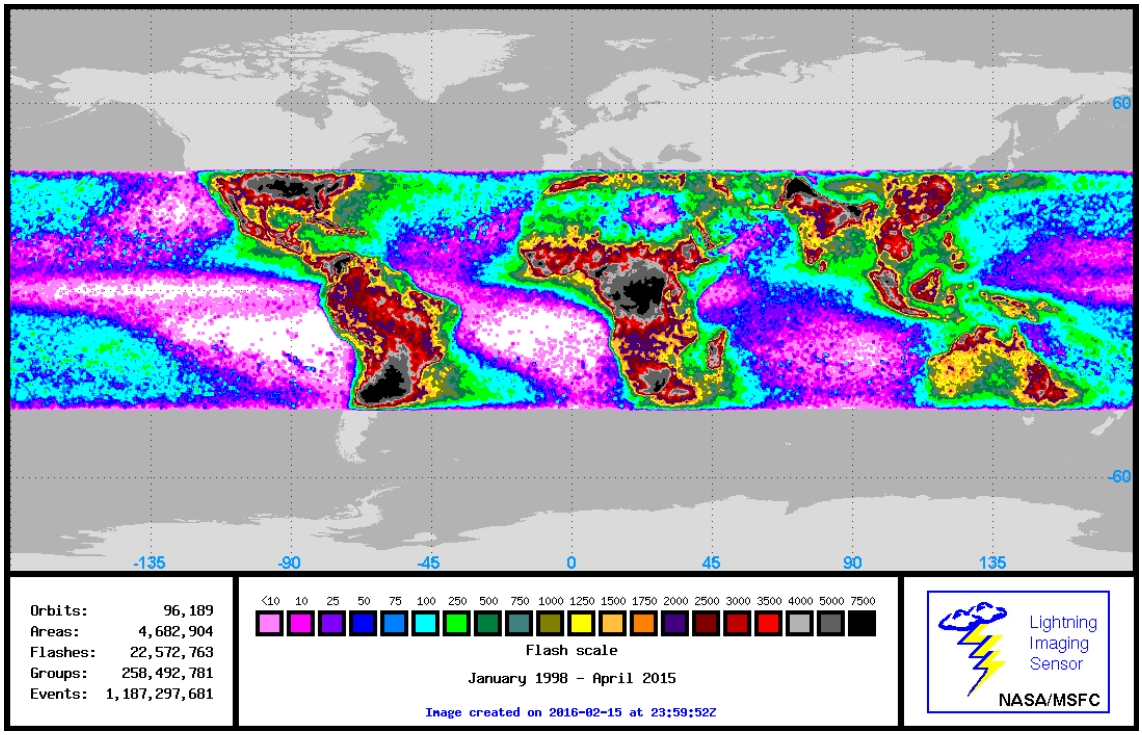

Figure A.1: Global lightning distribution as captured by the lightning imaging sensor (LIS) from January 1998 to April 2015 [186]

Table A.1: Lightning parameters according to API [120]

Component A (First Return Stroke)		**Component C (Continuing Current)**	
Peak amplitude	200 kA (+10 %)	Amplitude	200 A to 800 A
Action integral	2×10^6 A^2 s (±20 %) (in 500 µs)	Charge transfer	200 C (±20 %)
Duration	≤ 500 µs	Duration	0.25 s to 1 s
Component B (Intermediate Current)		**Component D (Subsequent Return Stroke)**	
Max. charge transfer	10 C (±20 %)	Peak amplitude	100 kA (±10 %)
Average amplitude	2 kA (±20 %)	Action integral	0.25×10^6 A^2 s (±20 %) (in 500 µs)
Duration	≤ 5 ms	Duration	≤ 500 µs

Table A.2: Comparison of the parameters of the methods for designing air terminations [20, 187]

Class of LPS	Mesh size	Rolling sphere radius	Minimum current (I_m)	Peak current (Ip)	Pr ($i > I_m$)	Pr ($i \leq I_p$)
I	5 x 5 m	20 m	3 kA	200 kA	0.99	0.99
II	10 x 10 m	30 m	5 kA	150 kA	0.97	0.98
III	15 x 15 m	45 m	10 kA	100 kA	0.91	0.97
IV	20 x 20 m	60 m	16 kA	100 kA	0.84	0.97

Table A.3: Lightning Protection Level (IEC 62305-1)

Peak Current	Protection Level	Interception Efficiency	Rolling sphere radius
3 kA	I	99%	20 m
5 kA	II	97%	30 m
10 kA	III	91%	45 m
16 kA	IV	84%	60 m

Table A.4: Comparison of the lightning current parameters

	IEC 62305-1 [20]		**CIGRE – Guide procedure** [188]			**CIGRE – Lightning Parameters** [189]		
	Mean (μ) kA /σ_{log}	β (σ_{log} ×2.3026)		Mean (μ) kA	β	Mean (μ) kA	σ_{log}	β (σ_{log} ×2.3026)
First negative short (20 %)	61.1 /0.576	1.3269	Shielding Failure Domain (I < 20kA)	61	1.33	30kA	0.265	0.6102
First negative short (80 %)	33.3 /0.263	0.6058	Backflash Domain (I > 20kA)	33.3	0.605			
Subsequent negative short	11.8 /0.233	0.5365	Subsequent stroke	12.3	0.53	12kA	0.265	0.6102
First positive short (single)	33.9 /0.527	1.2135	Positive stroke	Disregard in normal lightning studies		35kA	0.544	1.2526

σ_{log} = Standard deviation of $\log_{10}$ of peak current; $\beta = \sigma_{log} \times 2.3026$

IEEE distribution, the probability of exceeding current I

$$P(I) = \frac{1}{1+\left(\frac{I}{31}\right)^{2.6}}$$ in per unit for I in kA up to 200 kA [159, 190]

The peak-current distribution for subsequent strokes adopted by the IEEE (IEEE Std 1243-1997; IEEE Std 1410-2010) [189]

$$P(I) = \frac{1}{1+\left(\frac{I}{12}\right)^{2.7}}$$ where I is in kA

Appendix B: Separation distance

$$s = k_i \cdot \frac{k_c}{k_m} \cdot l$$

Where:

s is the separation distance

k_i depends on the class of LPS selected (induction factor)

k_c depends on the geometric arrangement (partitioning coefficient)

k_m depends on the material used in the point of proximity (material factor) and

l [m] is the length along the air-termination system or down conductor from the point where the separation distance is to be determined to the next equipotential bonding or earthing point.

The following tables are sourced from Tables 11, 12 and 13 from IEC 62305-3 [181] standard.

Table B.1: Comparison of the induction factor of the relevant class of LPS

Class of LPS	k_i
I	0,08
II	0,06
III and IV	0,04

Table B.2: The material factor

Material	k_m
Air	1
Concrete, bricks, wood	0,5
In using other insulating materials, construction guidance and the value of k_m is usually provided by the manufacturer. For additional information on insulating stand-offs, see IEC TS 62561-8. NOTE When there are several insulating materials in series, it is a good practice to use the lower value for k_m	

Table B.3: The partitioning coefficient

Number of down-conductors *n*	k_c
1 (only in the case of an isolated LPS)	1
2	0,66
3 and more	0,44
Values of Table 13 apply for all type B earthing arrangements and for type A earthing arrangements, provided that the earth resistance of earth electrodes do not differ by more than a factor of 2. If the earth resistances of single earth electrodes differ by more than a factor of 2, k_c = 1 is to be assumed.	

The partitioning coefficient k_c, for two masts with spanned wire

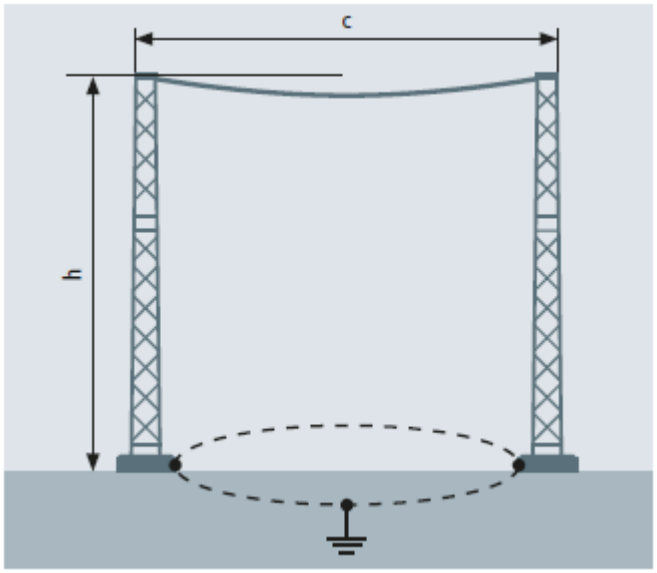

Figure B.1: Determination of k_c for two masts with spanned cable and a type B earthing [115]

The following formula is for calculating the factor k_c for a two-mast setup

$$k_c = \frac{h + c}{2h + c}$$

Where:

h is the length of the down conductor (i.e., the height of the mast)

c is the distance between the air-termination supporting masts

Declaration

I certify that I prepared the submitted thesis independently without undue assistance of a third party and without the use of others than the indicated aids. Data and concepts directly or indirectly taken over from other sources have been marked stating the sources.

When selecting and evaluating materials, no persons helped me.

Further persons were not involved in the content-material-related preparation of the thesis submitted. In particular, I have not used the assistance against payment offered by consultancies or placing services (doctoral consultants or other persons). I did not pay any money to persons directly or indirectly for work or services which are related to the content of the thesis submitted.

So far, the thesis has not been submitted identically or similarly to an examination office in Germany or abroad.

I have been notified that any incorrectness in the submitted above-mentioned declaration is assessed as an attempt to deceive and, according to § 7 para. 10 of the PhD regulations, this leads to a discontinuation of the doctoral procedure.

(Place, Date) Aderibigbe Adekitan